Statistical Mechanics of Self-Gravitating Systems in General Relativity JURY

Giuseppe Alberti

Université Fédérale
Toulouse Midi-Pyrénées

THÈSE

En vue de l'obtention du

DOCTORAT DE L'UNIVERSITÉ DE TOULOUSE

Délivré par : *l'Université Toulouse 3 Paul Sabatier (UT3 Paul Sabatier)*

Présentée et soutenue le *17/11/2017* **par :**

GIUSEPPE ALBERTI

Statistical Mechanics of Self-Gravitating Systems in General Relativity

---

JURY

DINH PHUONG MAI	Professeur (Président)	Université de Toulouse 3
ALASTUEY ANGEL	Directeur de Recherche (Rapporteur)	ENS de Lyon
LAVALLE JULIEN	Chargé de Recherche (Rapporteur)	Université de Montpellier
SIRE CLÉMENT	Directeur de Recherche (Invité)	Université de Toulouse 3
CHAVANIS PIERRE-HENRI	Chargé de Recherche (Directeur de Thèse)	Université de Toulouse 3

École doctorale et spécialité :
SDM : Physique - COR 02
Unité de Recherche :
Laboratoire de Physique Théorique (UMR 5626)
Directeur de Thèse :
Pierre-Henri CHAVANIS
Rapporteurs :
Angel ALASTUEY et *Julien LAVALLE*

Köpekten Kurda sevği ile

"Considerate la vostra semenza:
fatti non foste a viver come bruti,
ma per seguir virtute e canoscenza."

"Pensez à ce que vous êtes :
point n'avez été faits pour vivre comme des brutes,
mais pour rechercher la vertu et la connaissance."

"Consider well the seed that gave you birth:
you were not made to live your lives as brutes,
but to be followers of worth and knowledge."

Dante Alighieri, Divina Commedia,
Inferno XXVI, vv. 118-120

Ringraziamenti

Giunto alla fine di questo percorso, è doveroso ringraziare alcune persone che ne hanno fatto parte. Primariamente, desidero ringraziare il mio relatore di tesi di Dottorato, Pierre-Henri CHAVANIS, per avermi mostrato un modo di fare ricerca che non conoscevo. Voglio altresì ringraziare i revisori Angel ALASTUEY e Julien LAVALLE, non solo per aver accettato di leggere e correggere il manoscritto, ma anche per i preziosi consigli datemi durante il nostro cordiale scambio di opinioni e mail. Estendo questi ringraziamenti al presidente della commissione Mai DINH PHUONG e a Clément SIRE.

Un pensiero in particolare lo rivolgo anche a Malika BENTOUR, segretaria dell'LPT, per avermi aiutato, in questi tre anni, ad affrontare la burocrazia quotidiana. In seno all'LPT, voglio ringraziare la mia informatica di fiducia Sandrine LE MAGOARU, per aver risposto a tutte le mie "domande tecniche". Ho sempre apprezzato il tuo modo gentile di fare. Un'altra persona che non posso esimermi dal non ringraziare è Pina ROMANIELLO, per aver ascoltato e risposto ai dubbi avuti durante questi tre anni con dei preziosi consigli.

Voglio ringraziare il mio ex-collega ed amico Tristan BENOIST, non solo per aver condiviso l'ufficio nell'anno 2016 ma anche, e soprattutto, per avermi dato le sue impressioni quando gli parlavo del mio lavoro. Allo stesso tempo, voglio dedicare un pensiero a Wei-Lin TU, per l'amicizia e la lealtà dimostrata. A loro, aggiungo un ringraziamento a Lucie PERQUIS, François COPPENS, Lidice CRUZ RODRIGUEZ, Sergio SASTRE CASCÓN, Anna SALVIONI, Silvia ARCUCCI, Lisa Cazalens e Ludovic COATANTIEC.

Una menzione speciale va a Cyril SARRIEU, per avermi prestato il computer il giorno della presentazione e per le lunghe chiacchierate notturne (in particolare durante la primavera 2017). Un piccolo pensiero voglio rivolgerlo a Raquel SÁNCHEZ RODRIGUEZ, per avermi sostenuto durante l'estate 2017. Ho molto apprezzato quel che ci siamo detti per spalleggiarci, parlando anche di prospettive di vita successive al Dottorato.

Ripensando al periodo estivo consacrato alla stesura della tesi, non posso non esimermi dal dedicare alcune righe alle mie studentesse del progetto “Equilibrio e Struttura di una Stella Omogenea”, Alice DAUTEZAC, Louise MARIOTON e Julie PUYO, per avermi ridato entusiasmo, per avermi aiutato nella stesura del riassunto in francese della tesi e per il bel rapporto instaurato, una volta conclusasi la nostra esperienza professionale. Non potendo dimenticare le lunghe e spesso “vivaci” conversazioni avute, conversazioni che spesso Alice e Louise rinunciavano a seguire, mi permetto di dedicare una riga in più a Julie e di ringraziarla nuovamente.

Un’altra persona da non dimenticare è Citlali CABRERA GUTERRIEZ che, benché conosciuta a fine 2016, si è rivelata essere una presenza importante durante questo percorso triennale. Da una messicana ad un’altra, non potrei mai dimenticare Sara AYALA MARISCAL, che ha avuto un’esperienza di dottorato, per certi versi, molto simile alla mia. Grazie per i nostri pranzi all’UPSIDUM nei quali si passava dal serio al faceto con naturalezza.

Non avrei mai conosciuto Sara se non fosse stato per Jordi ROYES MIR e Melisa del BARRIO REDONDO, che mi hanno accompagnato fino all’estate 2016. Ricordo ancora, con piacere, quando Jordi non voleva che parlassimo spagnolo ed eravamo costretti ad avere conversazioni dapprima in inglese e poi in francese. Da una coppia di amici ad un’altra, come dimenticare Timothée POUSSARD e Seyran DEMIRBAŞ, per tutta la positività e l’allegria che mi hanno trasmesso da quando abbiamo iniziato a frequentarci. È raro trovare qualcuno col quale ci si capisce così bene dal primo istante.

Ci sono state delle persone che mi hanno accompagnato durante questo periodo tolosano sin dal suo inizio. Voglio rivolgere un pensiero a Guillaume BORDEAU del laboratorio IMRCP, ringraziandolo per avermi parlato sempre in maniera franca ed onesta e per i suoi consigli. Affianco a Guillaume, non dimentico Claire LAFOSSAS, che ringrazio per la sua gentilezza.

Un piccolo gruppo di amici si è formato il 24 Ottobre 2014, giorno d’accoglienza dei dottorandi. Con grande soddisfazione e felicità, questo gruppo continua ancora a proseguire la sua reciproca relazione. Un grazie speciale a Andreas GAVRIELIDES, Suhail USMANI e Florian WODLEI, non solo per i tre anni intensi trascorsi, ma anche per il sostegno reciproco che ci siamo offerti. Aggiungo una riga in più per Florian, non potendo dimenticare le nostre cene improvvisate all’ultimo momento.

Il giorno della presentazione dei dottorandi dell’IRSAMC, all’inizio di Ottobre 2014, ho conosciuto i miei primi amici di Tolosa. Non avrei mai potuto dimenticare Juan SANZ GARCÍA e Maria Francesca EVARISTI, che mi hanno aiutato nel difficile periodo iniziale, quando nulla sembrava funzionare. Di Juan non dimentico le nostre lunghe conversazioni all’IRSAMC, l’aiuto reciproco quando un programma non funzionava o quando uno dei due aveva bisogno di un parere su un calcolo od altro. Di Maria Francesca non dimentico le nostre cene del venerdì quando, rientrando insieme a Juan, avevo

l'impressione di fare parte della vostra piccola famiglia.

Voglio dedicare le ultime righe di questi ringraziamenti alla mia famiglia, in particolare ai miei genitori Luigi Rocco ALBERTI e Nunzia REGINA, per avermi permesso di scegliere, consapevolmente e liberamente, d'intraprendere il percorso di vita iniziato, anni fa, con i miei studi universitari. Un ringraziamento a mia sorella gemella Rita ALBERTI, per il rapporto che ci lega sin da bambini, rapporto dal quale traggo sempre una nuova linfa, che mi consente di andare avanti.

Infine, voglio ringraziare mia sorella Marianna ALBERTI perché, se non fosse stato per lei, quel 31/10/2013 non sarei mai andato ad assistere all'evento in Aula Magna all'Università La Sapienza che mi ha poi permesso di venire a Tolosa e ottenere il titolo di Dottore di Ricerca. A te dedico questo lavoro. Grazie.

Remerciements

A l'issue de ce parcours, c'est juste de remercier certaines personnes qui en ont fait partie. D'abord, je désire remercier mon directeur de thèse de Doctorat, Pierre-Henri CHAVANIS, pour m'avoir montré une manière de faire la recherche que je ne connaissais pas. Je veux aussi remercier les rapporteurs Angel ALASTUEY et Julien LAVALLE, ne pas seulement pour avoir accepté de lire et corriger le manuscrit, mais aussi pour les suggestions qu'ils m'ont données pendant notre cordial échange d'opinions et de mails. J'adresse ces remerciements au président du jury Mai DINH PHUONG et à Clément SIRE.

Je tourne une pensée particulière aussi à Malika BENTOUR, secrétaire du LPT, pour m'avoir aidé, durant ces trois ans, à faire face aux tâches administratives quotidiennes. Au sein du LPT, je veux remercier mon informaticienne de confiance Sandrine LE MAGOAROU, pour avoir répondu à toutes mes "questions techniques". J'ai toujours apprécié ta manière gentille de faire. Une autre personne que je ne peux pas me soustraire de ne pas remercier c'est Pina ROMANIELLO, pour avoir écouté et répondu aux doutes eus pendant ces trois ans avec des précieux conseils.

Je veux remercier mon ancien collègue et ami Tristan BENOIST, ne pas seulement pour avoir partagé le bureau pendant l'année 2016 mais aussi, et surtout, pour m'avoir donné ses impressions quand je lui parlais de mon travail. En même temps, je veux adresser une pensée à Wei-Lin TU, pour l'amitié et la loyauté montrée. Ensemble avec eux, je rajoute un remerciement à Lucie PERQUIS, François COPPENS, Lidice CRUZ RODRIGUEZ, Sergio SASTRE CASCÓN, Anna SALVIONI, Silvia ARCUCCI, Lisa Cazalens et Ludovic COATANTIEC.

Une mention spéciale va à Cyril SARRIEU, pour m'avoir prêté l'ordinateur le jour de la soutenance et pour les longues conversations nocturnes (en particulier pendant le printemps 2017). Je veux destiner une petite pensée à Raquel SÁNCHEZ RODRIGUEZ, pour le support réciproque pendant l'été 2017. J'ai beaucoup apprécié ce que l'on s'est dit pour nous épauler, en parlant aussi des perspectives de vie

successives au Doctorat.

En repensant à la période estivale consacrée à la rédaction de la thèse, je ne peux pas me soustraire de dédier quelques lignes aux étudiantes du projet “Equilibre et Structure d’une Etoile Homogène”, Alice DAUTEZAC, Louise MARIOTON et Julie PUYO, pour mavoir redonné enthousiasme, pour m’avoir aidé dans la rédaction du résumé en français de la thèse et pour le rapport que l’on a instauré, une fois conclue notre expérience professionnelle. En ne pouvant pas oublier les longues et souvent “vives” conversations eues, conversations que parfois Alice et Louise renonçaient à suivre, je me permets de dédier une ligne en plus à Julie et de la remercier de nouveau.

Une autre personne à ne pas oublier c’est Citlali CABRERA GUTERRIEZ qui, bien que connue à la fin de l’année 2016, s’est révélée être une présence importante pendant ce parcours triennal. D’une mexicaine à une autre, je ne pourrais jamais oublier Sara AYALA MARISCAL, qui a eu une expérience de doctorat, d’un côté, très similaire à la mienne. Merci pour nos repas à l’UPSIDUM dans lesquels on passait du sérieux au facétieux avec naturalité.

Je n’aurais jamais connu Sara s’il n’avait pas été pour Jordi ROYES MIR et Melisa del BARRIO REDONDO, qui m’ont accompagné jusqu’à l’été 2016. Je me souviens encore, avec plaisir, quand Jordi ne voulait pas que l’on se parle en espagnol et on était obligé d’avoir des conversations d’abord en anglais et ensuite en français. D’un couple d’amis à un autre, comment oublier Timothée POUSSARD et Seyran DEMIRBAŞ, pour toute la positivité et l’allégresse qui m’ont donné, depuis que l’on a commencé de se fréquenter. C’est rare de trouver quelqu’un avec lequel on s’entend si bien du premier moment.

Ils y ont été des personnes qui m’ont accompagné dans cette période toulousaine à partir du début. Je veux adresser une pensée à Guillaume BORDEAU du laboratoire IMRCP, en lui remerciant de m’avoir toujours parlé de façon franche et honnête et pour ses conseils. A côté de Guillaume, je n’oublie pas Claire LAFOSSAS, que je remercie de sa gentillesse.

Un petit groupe d’amis s’est formé le 24 Octobre 2014, journée d’accueil des doctorants. Avec grande satisfaction et grand bonheur, ce groupe continue encore à suivre sa relation réciproque. Un merci particulier à Andreas GAVRIELIDES, Suhail USMANI et Florian WODLEI, ne pas seulement pour les trois ans intensifs passés mais aussi pour le soutien réciproque que l’on s’est offert. Je rajoute une ligne en plus pour Florian, en ne pouvant pas oublier nos dîners improvisés au dernier moment.

Le jour de la présentation des doctorants de l’IRSAMC, en début Octobre 2014, j’ai connu mes premiers amis de Toulouse. Un remerciement particulier à Juan SANZ GARCÍA et Maria Francesca EVARISTI, qui m’ont aidé dans la difficile période initiale, quand il semblait que rien marchait. Par rapport à Juan, je me souviens de nos longues conversations à l’IRSAMC, de l’aide réciproque lorsqu’un

programme ne marchait pas ou lorsqu'un de deux avait besoin d'un avis sur un calcul ou autres. Par rapport à Maria Francesca, je n'oublie pas nos dîners du vendredi quand, en rentrant ensemble avec Juan, j'avais l'impression de faire partie de votre petite famille.

Je veux dédier les dernières lignes de ces remerciements à ma famille, à mes parents Luigi Rocco ALBERTI e Nunzia REGINA, pour m'avoir permis de choisir, consciemment et librement, d'entreprendre le parcours de vie commencé, il y a des ans, avec mes études universitaires. Un remerciement à ma sœur jumelle Rita ALBERTI, pour le rapport qui nous lie à partir de l'enfance, rapport duquel je tire toujours une nouvelle lymphe, qui me permet d'avancer.

Enfin, je veux remercier ma sœur Marianna ALBERTI car, s'il n'avait pas été pour elle, ce 31/10/2013 je ne serais jamais allé à assister à l'événement dans l'Aula Magna à l'Université La Sapienza qui m'a ensuite permis de venir à Toulouse et obtenir le grade de Docteur de Recherche. A toi je dédie ce travail. Merci.

Contents

1

Introduction

Among the four (three after the electro-weak unification [93]) natural forces present in nature, gravity is the most enigmatic, because of its peculiar nature. Classically, gravity is described in the same way as electrostatic forces, by means of a potential which is inversely proportional to the distance from the body creating the gravity, the "gravitational charge". Nevertheless, differently from electromagnetic forces, a quantum generalization of gravity is very complex and actually far from its complete solution [162]. The main reason of this difficulty can be explained by virtue of the extreme weakness of the gravity, in comparison with the other forces present in nature.

This fact can be clearly seen if we consider two elementary particles (e.g. two protons) and compute the ratio of the gravitational to the electrostatic forces acting on them. The result of this evaluation shows that the gravitational force is $\sim 10^{-37}$ times weaker than the electrostatic one, implying that the detection of gravitational effects, at the typical scales of quantum mechanics, is very hard. The energy necessary to this purpose, indeed, is of the order of the Planck mass (10^{19} GeV/c^2 $\sim 10^{-5}$ g), which cannot be achieved, at the present time, in the laboratories. In order to better understand the properties of gravity, working with sources having a high amount of "gravitational charge" becomes fundamental: that is why gravity is mainly investigated within the realm of Astrophysics.

As it is well known, according to the intensity of the gravitational fields, the law describing the behaviour of this force changes. In classical physics, the Newtonian law of gravity works properly within systems as the planetary one or at galactic scales. However there exists a wide literature, concerning the comprehension and the description of gravity, consisting of theories alternative to the Newtonian paradigm. Among the proposals advanced, we mention here the pioneering papers of Milgrom [142], Sanders [167] and Kuhn & Kruglyak [125] (see also Ref.[21]). These works, arosen as

alternatives to the Dark Matter (hereafter DM) conjecture, propose modofications to Newton's law of universal gravitation (see Ref.[10]).

Nevertheless, a large number of phenomena cannot be described by means of Newtonian gravity. If we want, for example, to study systems such as Neutron Stars or work at Cosmological scales, we have to turn to General Relativity (hereafter GR), the theory of the gravity formulated by Einstein at the beginning of last Century [190, 75, 168], which introduces the concept of space-time[1].

At the same time, it is possible to provide a second description of astrophysical systems, by using the typical language of the thermodynamics. The presence of gravity is indeed responsible of some particular features, not appearing in other kinds of systems, that can be explained within this schematization. One of the most important examples, in this sens, is represented by the gravo-thermal catastrophe [5, 132, 133, 115, 53] in Globular Clusters (hereafter GCs). The origin of this phenomenon resides in the tendency of the stars to "collapse" to the central nucleus [20]. Nevertheless this feature, related to the negativity of the heat capacity[2] (a consequence of the *inequivalence* of the statistical ensembles), is not an exclusive property of self-gravitating systems but, more generally, of systems characterized by long range interactions [36, 69, 35].

It is possible to realize this statistical-thermodynamical description if, analogous to the usual kinetic theory of gases, we imagine a stellar cluster as a gas which "molecules" are represented by the stars (see Sec. 1.1). According to this scheme, stellar systems can be seen as the extension, to the gravitational case, of the perfect gas model. A rigorous description and comprehension of the properties of self-gravitating systems within this thermodynamical framework requires turnig out to the tools provided by statistical mechanics. Historically, the first theoretical models used to describe astrophysical systems as a self-gravitating Boltzmann gas. Nonetheless, in order to avoid the infinite mass problem (see Sec. 1.2), these proposals have been modified (Ref.[26] and references therein).

This preliminar sketch, about the literature on the thermodynamics of self-gravitating systems, gives the idea that a lot of open questions are still unanswered. The present work aims at studying, from a thermodynamical point of view, a self-gravitating and spherically symmetric fermionic configuration, in a general relativistic framework. To take into account the different regimes, the treatise will be

[1] There also exists a wide literature regarding alternative theories to GR. Historically, one of the first attempts was made by Dirac [71], who constructed a Cosmological theory based on some "numerical coincidences". His goal was to show that the gravitational constant G was a (slow) decreasing function of time (see also Ref.[87]). Another more intriguing model, advanced by Brans & Dicke [33, 37], discusses the possibility of making a modified relativistic theory of gravitation incorporating in a coherent way Mach's principle. For the implications of a generalized Brans-Dicke theory in high energy particles physics see Ref.[174].

[2] In the following, we will use indifferently heat capacity or specific heat.

performed in the most general case, without particular restrictions.

In the remaining part of this introductive Chapter, we will accompany the reader to the understanding of the main historical steps leading authors to the discovery of the existence of the so called "gravitational phase transition". In Sec. 1.1 we briefly review the observational properties of some self-gravitating systems in Astrophysics, such as degenerate stars or GCs. In Sec. 1.2 we initiate the historical review about the theoretical models, by discussing the case of the systems made of classical particles (i.e. isothermal gas sphere). Therefore, in Sec. 1.3, we pass to the quantum generalization of the models analyzed in Sec. 1.2, by discussing the nature of the phase transition. In Sec. 1.4 we present the extensions, to the realm of GR, of the proposals discussed in the two preceding Sections. In Sec. 1.5, finally, we show the idea, the goal and the methodology of the present work.

1.1. Self-Gravitating Systems in Astrophysics

A self-gravitating[3] system is a gas in equilibrium, which the only forces acting on are the pressure and the gravitational attraction. Consequently, no other external forces affect the system, that can be considered isolated. In the following, we will make use of this assumption.

The first example of a self-gravitating system is represented by a generic star, i.e a spherical object in thermal equilibrium where the gravity (leading the object to collapse) is balanced by the radiation pressure produced within the nucleus, where nuclear reactions set in [92, 65, 116, 146]. Observationally, thanks to the radiation sent by the star, we can get all the informations about its structural parameters and its chemical composition. Further, observations enable us to distinguish among the different types of stars. At the present time, we know well the general properties of stars and their evolutive path: nevertheless, a lot of phenomena are not yet clarified [134, 112, 145].

In particular, there is a class of stellar objects (representing the final states of the evolutive path of stars), which properties are well understood, that is White Dwarfs stars (hereafter WDs), Neutron Stars (hereafter NSs) and Black Holes (hereafter BHs). These three categories are theoretically known since the beginning of last Century, thanks to the seminal works of Schwarzschild [170], Fowler [83], Chandrasekhar [40, 41] and Oppenheimer & Volkoff [150] (see Secs. 1.3 and 1.4). Within a more general framework, we can describe WDs and NSs in a unified approach, by schematizing them as "compact degenerate stars" (Narain *et al.* [144]).

[3]Self-gravitation is the process by which the individual constituents of a large body are held together by the combined gravity of the object as a whole. Without it, stars, stellar clusters, galaxies, and groups and clusters of galaxies would all expand and dissipate. It also plays a role on even larger scales, being responsible for the deceleration of the the cosmic expansion until fairly recently in cosmological time (the Universe is currently accelerating in its expansion).

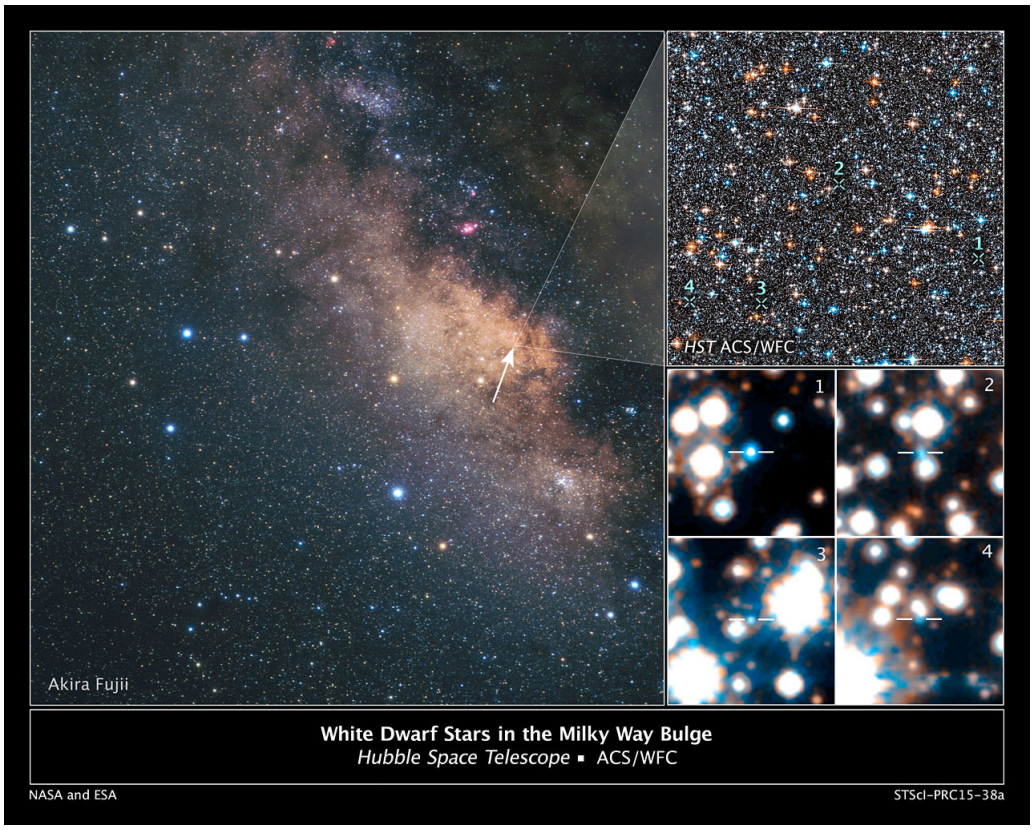

Figure 1.1: ***Left Panel****: View of the Milky Way's central bulge, seen in the direction of the constellation of the Sagittarius.* ***Upper Right Panel****: Sagittarius Window Eclipsing Extrasolar Planet Search field, (SWEEPS), a survey in the galactic bulge located 26000 lyr away.* ***Lower Right Panel****: Sample of 4 out of the 70 brightest WDs in the Milky Way's bulge (Hubble Space Telescope).*

From an observative point of view, WDs[4] are stars having planetary dimensions and masses of the order of Solar mass[5] (the relative mean density is about 10^6 g cm^{-3}). These stars are characterized by a compact core, formed by helium or heavier elements, surrounded by an atmosphere where electrons or lighter elements than those present in the core (according to the chemical composition of the stars) are in. These stars, such as NSs, can be considered "dead", because they have ceased the production of energy via the nuclear reactions. WDs are destined to continuously cool down, till their extinction [186, 123]. In addition, we observe that WDs, as NSs, have the tendency to stay in binary systems.

NSs, by contrast, are smaller than WDs (the typical radius is around $R \sim 10\,km$) but their mass, such as WD, is of the order of the mass of the Sun[6], by implying that the associated average densities

[4]The discovery of WD dates back to 1914, when Adams observed Sirius β, the binary companion of Sirius α (see Ref.[171]).

[5]The value of the Solar mass is $M_\odot = 1.989 \times 10^{33}\,g$.

[6]Actually the most massive NS is the pulsar PSR J0348+0432 (discovered by Antoniadis and collaborators [3]), which

Figure 1.2: *Composite image of the Galaxy NGC 1275, also known as Perseus A, lies at the centre of Perseus Galaxy Cluster. NGC 1275 is an active galaxy, well-known for its radio source (Perseus A), and is a strong emitter of X-rays, due to the presence of the supermassive BH in its centre (Hubble Space Telescope).*

are of the order of 10^{15} g cm^{-3}. As their name indicates, this kind of stars is mainly formed by free neutrons, not anymore bound in atomic nuclei. NSs are the result of Supernovae explosions, as it was originally argued by Baade & Zwicky [13, 14], and they have been discovered, for the first time, in 1967 when Bell & Hewish [19, 102] found regular radio pulses from the pulsar PSR B1919+21 (for more historical details see Ref.[171]).

BHs represent the last possible self-gravitating configuration achievable in Nature. They are distinguished by the other astrophysical objects because of their ability to attract all the matter surrounding them and, even, the electromagnetic radiation. They can be stationary (in this case we talk about Schwarzschild's BH) or rotating (also called Kerr's BH, see Ref.[89]) and, according to the amount of mass, authors talk about supermassive BHs[7]. Supermassive BHs may be in quiet mode (e.g. that at the centre of Milky Way) or active mode (e.g. Active Galactic Nuclei or Quasars). Starting from this

mass is $M \simeq 2.2 M_{\odot}$.

[7]This last category of BHs is very important, because supermassive BHs are supposed to be at the center of galaxies [9]. Anyway, this scenario is not the unique. In fact, when a fermionic gas cools down a critical temperature, it condenses and forms a "fermions ball" which can mimic the behaviour of supermassive BHs [188, 189], see also Sec. 1.3.

scenario, it has been possible to derive a thermodynamical description for BHs [18, 16, 96]. Because of the quadratic behaviour of relativistic equations, there exist the "anti-BHs", that is the White Holes (firstly theorized by Novikov [147, 148]). In this work, however, we do not consider this kind of systems.

The objects till now mentioned can be viewed as "particles gases". Nevertheless, also stars in stellar clusters can be seen as the particles of a gas. Thanks to this analogy, also stellar systems can be studied by means of a statistical approach (the stars are considered as point mass particles). Among the different types of the stellar systems, the most important examples are represented by Galaxies and GCs. These two categories of stellar systems have different structural and evolutive properties. Galaxies are generally big systems (the typical size are $1 \div 100$ kpc)[8], popoulated by $10^9 \div 10^{11}$ stars and are classified, according to their morphology (Hubble classification), as elliptical, lenticular, spiral (barred or regular) and irregular (there are also sub-classification in each category, see e.g. Ref.[166]). The masses of the Galaxies vary from $10^9\, M_\odot$ (Dwarf Elliptical Galaxies) to $10^{12}\, M_\odot$ (Giant Elliptical Galaxies). As the stars, Galaxies have the tendency to stay in binary systems or clusters (the Milky Way, e.g., is in the Local Group of Galaxies).

GCs are smaller than Galaxies and populated by around 10^5 stars. GCs live inside Galaxies and their appearance is, as suggested by the name, a globule. The stars populating this kind of systems have the same age and present the same level of metallicity. Nevertheless, the masses can vary in a very large range [90]. This mass spread is at the basis of the phenomenon of the mass-segregation [17], leading the system to the gravo-thermal catastrophe (see below). The age of GCs, due to the properties of the stars above mentioned, can be evaluated by means of the isochrone lines in the Hertzsprung-Russell (HR) diagram [187].

Because of the different dynamics of the stars inside, Galaxies and GCs present a dissimilar evolutive path. The distinction is made by means of some characteristic times that can be successively compared with the ages (τ_{life}). Generally, by assuming that the stellar system is isolated[9], the movement of stars is influenced by the mutual interactions among each other. These "gravitational encounters", unlike scatterings among classical point mass particles, do not require a "contact" among the stars.

The cumulative effect of these encounters can drastically change the original orbit of a star, that is the orbit determinable by the gravitational potential of the cluster. The relaxation time τ_{rel} is defined

[8]The parsec (pc) is defined as the distance at which one astronomical unit (AU) subtends an angle of one arcsecond. In terms of other distance units we have 1 pc = 3.26 lyr = 3.086×10^{18} cm.

[9]This assumption can work as a first approximation but it is not rigorous, for example, for GCs. In this case, indeed, the orbits of stars feel the solicitations of the Galaxy where the GC is in. In addition, the presence of the Galaxy is responsible of tidal actions and the evaporation of stars [176].

Figure 1.3: *The Sombrero galaxy, Messier 104 (M104), named in this way because of its resemblance to the broad rim and high-topped Mexican hat. The galaxy's hallmark is a brilliant white, bulbous core encircled by the thick dust lanes comprising the spiral structure of the galaxy. As seen from Earth, the galaxy is tilted nearly edge-on (Hubble Space Telescope).*

as the time interval necessary for a substantial modification of the orbit of a star. When the system gets this characteristic time, the distribution of the velocities becomes Maxwellian. We have [26]

$$\tau_{rel} = \frac{N}{8 \ln N} \tau_{cross} \,, \tag{1.1}$$

where the ratio $N/8 \ln N$ represents the number of encounters such that $\Delta v^2 \sim v^2$ (v^2 is the mean quadratic velocity of the stars and Δv^2 its variation). Moreover N is the number of stars and τ_{cross} is the crossing time, defined as the time that a star needs to cross the entire system. A good estimate of τ_{cross} is given by $\tau_{cross} \sim R_h/v$, where R_h is the half mass radius[10] (i.e. the radius of the sphere containing half of the mass of the cluster). These times depend on the global dynamical effects and they give an idea of the time-scale necessary for significant modifications in the structure of the cluster. If $\tau_{rel} < \tau_{life}$ the system is collisional, vice-versa collisionless. For GCs we have $\tau_{cross} << \tau_{rel} < \tau_{life}$, by implying that they are collisional[11]; for (Elliptical) Galaxies we have $\tau_{cross} << \tau_{life} < \tau_{rel}$, by implying that they are collisionless[12]. According to the intensity of the gravitational fields, we observe that WDs, Galaxies and GCs are Newtonian; NSs and BHs general relativistic.

[10]The definition of the crossing time can be also modified by using, for example, the tidal radius R_t. Anyway, other typical size-scales can be used, e.g. referring to the surface density. For more details see Ref.[176].

[11]Typical values: $\tau_{cross} \sim 1.5 \times 10^7$ yr, $\tau_{rel} \sim 10^9$ yr, $\tau_{life} \sim 1.3 \times 10^{10}$ yr.

[12]Typical values: $\tau_{cross} \sim 1.3 \times 10^8$ yr, $\tau_{life} \sim 10^{10}$ yr, $\tau_{real} \sim 2 \times 10^{10}$ yr.

1.2. Thermodynamical Description: Classical Systems

As we have seen in the previous Section, the typical astrophysical systems are populated by a large number of elements. It is thus possible to imagine these systems as gases which total volume can be divided in microcells. By analogy with the kinetic theory of gas, these microcells are small compared to the typical dimensions of the system but large enough to include a sufficient amount of particles. Each microcell is chacterized by an infinitesimal volume $d^3\vec{r}\,d^3\vec{q}$, where $\vec{r}$ and $\vec{q}$ are, respectively, the position and the momentum of each particle within the microcell. The occupation number of each microcell is defined as

$$dn(t) = f(\vec{r},\vec{q},t)d^3\vec{q}d^3\vec{r}\,, \tag{1.2}$$

where $f = f(\vec{r},\vec{q},t)$ represents the distribution function (hereafter DF) of the system, which gives the probability to find a particle having position and momentum in the interval $[\vec{r},\vec{r}+d\vec{r}]$ and $[\vec{q},\vec{q}+d\vec{q}]$, respectively, at the time t. The DF associated with the system depends on the nature of the gas (e.g. collisional or not). In order to get the right functional form of the DF, we need an equation governing its evolution in time. Assuming that the interaction among the particles is exclusively a function of the position $\vec{r}$ (condition verified in the case of a stellar system), we get the evolution equation for the DF (for more details see Refs.[105, 26]), i.e. the Boltzmann equation

$$\frac{df}{dt} = \frac{\partial f}{\partial t} + \frac{q}{m}\cdot\nabla_r f - \nabla_r\Phi\cdot\nabla_q f = \Gamma(f)\,. \tag{1.3}$$

In the foregoing expression, $\Gamma = \Gamma(f)$ is the collisional term, allowing us to distinguish the nature of the fluid. Moreover Φ is the potential describing the interaction among the particles (gravitational in the case here considered) and m the mass of the particle (i.e. the star).

The dynamical study of long range systems (such as gravitational systems) cannot be achieved analytically, since the large number of particles prevents the integration of the equations. For this reason many authors resort to the mean field approximation. In this framework, for a given test particle, the field due to the binary interactions with the remaining ones is replaced with the field generated by the continuous matter distribution compatible with the particles distribution. The relative fluctuations are reduced because of the large number of particles and the local mean field dominates the individual field generated by the particles close to the test particle.

For Galaxies, clearly, we have $\Gamma = 0$ and Eq.(1.3) becomes (Vlasov Equation)

$$\frac{\partial f}{\partial t} + \frac{q}{m}\cdot\nabla_r f - \nabla_r\Phi\cdot\nabla_q f = 0 \qquad \Longleftrightarrow \qquad \frac{df}{dt} = 0\,. \tag{1.4}$$

For GCs, of course, the collisional term deos not vanish. An explicit evaluation of Γ can be obtained by means of the local approximation[13]. Let us consider a test star of mass m into a volume of phase space $d^3\vec{r}\,d^3\vec{q}$ and a flux of field stars of mass m_a colliding with this volume. The difference between the number of field stars that are going to scatter and the number of field stars that have already scattered the test star gives $\Gamma(f)$. Then, invoking the Fokker-Planck approximation (see Ref.[26]), the Boltzmann equation reduces to the Fokker-Planck equation

$$\frac{df(x,t)}{dt} = \frac{1}{\tau_{rel}}\frac{1}{x^2}\frac{\partial}{\partial x}\left\{2x\mathcal{G}(x)\left[\frac{\partial f(x,t)}{\partial x} + \frac{2m}{m_a}xf(x,t)\right]\right\}. \tag{1.5}$$

In the foregoing expression τ_{rel} is the relaxation time defined in Sec. 1.1 while $x = v/\sqrt{2}\sigma$ (v is the velocity of the test star and σ is the one-dimensional velocity dispersion of the field stars). Furthermore, the function $\mathcal{G}(x)$ is defined by

$$\mathcal{G}(x) = \frac{1}{2x^2}\left[\mathrm{erf}(x) - \frac{2x^2}{\sqrt{\pi}}e^{-x^2}\right], \tag{1.6}$$

and it is obtained evaluating the diffusion coefficients that characterize the collisional term $\Gamma(f)$ ($\mathrm{erf}(x)$ is the error function). Solution of Eq.(1.5) is King DF (see below). Regarding collinsionless systems, we can show that they are equivalent to the isothermal gas sphere (for more details see Ref.[26]). This last one is described by Boltzmann DF

$$f = Ae^{-E/k_BT}, \tag{1.7}$$

where E represents the *relative energy* of the star (defined as the algebraic sum of kinetic and potential energy) and T the temperature of the system. Moreover, k_B is the Boltzmann constant and A a normalization factor. In order to determine the gravitational equilibrium, we have to solve the Poisson equation

$$\nabla^2\phi = 4\pi G\rho = 4\pi Gmn = 4\pi Gm\int f d^3\vec{q}, \tag{1.8}$$

where ϕ indicates the gravitational potential, $\rho = mn$ is the mass density of the system and G the gravitational constant. In the case of a spherical system Eq.(1.8), after some algebraic manipulations, reduces to the Emden equation [41]

$$\frac{1}{\xi^2}\frac{d}{d\xi}\left(\xi^2\frac{d\psi}{d\xi}\right) = e^{-\psi}, \tag{1.9}$$

[13]It is assumed that the gravitational encounters are weak enough to not alter the positions of the star.

with the boundary conditions $\psi(0) = \psi'(0) = 0$ (prime indicates the derivative with respect to ξ). There exist two solutions of Eq.(1.9). The first one satisfies the boundary conditions and can be obtained numerically [45]. The second one can be obtained analytically

$$e^{-\psi} = \frac{2}{\xi^2}\,. \tag{1.10}$$

Thanks to the previous result, we get the density profile

$$\rho = \frac{\sigma^2}{2\pi G r^2} \qquad \text{where} \qquad \sigma^2 = \frac{k_B T}{m}\,, \tag{1.11}$$

which is singular at the centre. Moreover, there is a second problem. Let be the mass

$$M = \int_0^r 4\pi\rho r'^2 dr' = \frac{2\sigma^2}{G} r\,. \tag{1.12}$$

The reader can easily see that, in the limit $r \to \infty$, the mass (1.12) is a diverging quantity. Because astrophysical objects have finite dimensions, it arises the necessity to find out a way to spatially bind the system. To this purpose, two strategies are possible.

The first one consists in encapsulating the stellar gas within a box which dimensions are fixed *a priori*. Apparently, there is no a physical reason justifying the introduction of the box. Nevertheless, a physical argument can be found by considering the effects of tidal streams. Nonetheless, in spite of this conceptual problem, in this work we use the box model.

The second one consists in "cutting" the matter in the momentum phase space, i.e. modifying the DF by means of a limiting configuration energy. The spatial limitation of the system comes out as a natural consequence of the presence of this "cut-off" energy. In this framework, King's models [118, 119, 120] represent the first attempt well reproducing the behaviour of GCs. The system is assumed to be described by a lowered Maxwell-Boltzmann DF

$$f = \begin{cases} A\,(e^{-E/\sigma^2} - e^{-\epsilon_c/\sigma^2}) & \text{if} \qquad E \leq \epsilon_c\ , \\ 0 & \text{if} \qquad E > \epsilon_c\ , \end{cases} \tag{1.13}$$

where E represents the energy of a single star in the cluster and ϵ_c is the cut-off energy. Further, $\sigma^2 = k_B T/m$ and it is related to the velocity dispersion of stars (A is a normalization constant). The cut-off energy can be also seen as a measure of the escape velocity v_e associated with a GC. In fact, stars having a velocity larger than v_e are able to leave the system, which evaporates[14]. In addition, Eq.(1.13) is solution of the Fokker - Planck equation (1.5).

[14]For a detailed description of this process and the implications related to the Hénon paradox see Refs.[98, 185, 66].

A thermodynamical description by directly applying Eq.(1.13) is not possible, because the King DF does not describe systems in thermodynamical equilibrium, differently from Maxwell-Boltzmann DF. In order to achieve a statistical mechanical description, it is necessary to modify the DF (1.13) by introducing an effective potential. In this way, the evolution of King models can be treated as a succession of quasi-equilibrium states, analogous to the usual thermodynamics.

The effective potential is a screen potential which restricts the phase space of the available velocities for the stars and takes into account the effect of the tidal forces on the system [84, 140, 141, 136]. In addition, the effective potential also solves the discrepancy problem (see Refs. [114, 139].)

Let us now go back to the box models. The first investigations about thermodynamical instabilites in systems formed by classical particles began with Antonov, who showed that no global entropy maxima exist if $ER/GM^2 < -0.335$ [5, 6, 8, 7, 131] (see below). The fate of the system is thus to undergo a gravitational collapse. The physical reason of such instability comes from the negativity of heat capacity. To show it, let us consider the kinetic energy K that, by analogy with the perfect gas, we write as

$$K = \frac{3}{2} N k_B T \,, \tag{1.14}$$

where N represents the number of stars and T the mean temperature of the system. The virial theorem for a steady state isolated system (see Ref.[26]) writes

$$2K + W = 0 \qquad \Longleftrightarrow \qquad W = -2K \,, \tag{1.15}$$

where W represents the potential energy. Consequently, the total energy E of the system is

$$E = K + W = -K = -\frac{3}{2} N k_B T \,. \tag{1.16}$$

From the foregoing expression we can get the heat capacity, being

$$C_V = \frac{dE}{dT} = -\frac{3}{2} N k_B < 0 \,. \tag{1.17}$$

The specific heat (1.17) is therefore negative, implying that one has to extract energy from the system to heat up it. This feature[15] is not restricted to isolated systems but it holds also for bound systems within boxes [132]. In order to see the consequences of Eq.(1.17), let us discuss the model of Lynden-

[15] For a detailed discussion about the properties of systems presenting negative heat capacity and its link with stellar nuclei see Ref.[32].

Bell & Wood [133]. Here, a self-gravitating ideal gas within a spherical[16] and permeable container of dimension R_b is considered. Differently from Eq.(1.15), the virial theorem writes

$$2K + W = 3P_bV_b = 4\pi P_bR_b^3\,, \tag{1.18}$$

where P_b is the pressure at the boundary and V_b indicates the total volume of the spherical container. The total energy is

$$E = K + W = 4\pi P_bR_b^3 - K = 4\pi P_bR_b^3 - \frac{3}{2}Nk_BT\,. \tag{1.19}$$

From the foregoing expression, we see that even bound self-gravitating systems have negative heat capacity. We stress that, in the limit $R_b \to +\infty$, the isothermal gas sphere is recovered (see Ref.[133]). The stability analysis is carried out by Lynden-Bell & Wood through the series of equilibria, i.e. by studying the behaviour of the $\beta = \beta(E)$ curve [where $\beta = 1/(k_BT)$], which is represented in Fig. 1.4. By means of the turning point method of Poincaré (see Refs.[113, 53]), we know that the stability changes are related to the extremal points of the curve. Moreover, if the curve rotates clockwise (anti-clockwise) a mode of stability is lost (gained).

Since the curve $\beta = \beta(E)$ [or, as represented in the figure, $\eta = \eta(\Lambda)$, see Eq.(1.27)] offers a representation of both temperature and energy, three types of analysis can be carried out. A first one, keeping constant the energy E and the volume V_b (microcanonical description, see Refs.[151, 152]); a second one, keeping constant the temperature T and the volume V_b (canonical description, see Ref.[45]); a third one, keeping constant the temperature and the pressure P_b (isobaric description, see Refs.[30, 73, 48])[17]. Let us further define the important parameter

$$\mathcal{R} = \frac{\rho(r=0)}{\rho(r=R_b)} = \frac{\rho_0}{\rho_b}\,, \tag{1.20}$$

which is called density contrast and gives a measure of the concentration (i.e. homogeneity) of the system. According to Eq.(1.20), $\mathcal{R} \geq 1$ always. Moreover, large values of $\mathcal{R}$ indicate that the system has a core-halo structure, being the matter more concentrated at the center than at the edge. Vice-versa, values of $\mathcal{R}$ close to the unity indicate a homogeneous system. Along the $\beta = \beta(E)$ curve there are several critical points, but we restrict our analysis only to four (for the others see Refs. [133, 104]). According to the value of the density contrast, we have:

[16] As pointed out by Antonov [5], only spherical systems can correspond to local entropy maxima.

[17] In particular, in Refs.[151, 152, 45, 48] the stability of isothermal spheres has been studied by solving an eigenvalue equation, related to the second order variations of the thermodynamical potential.

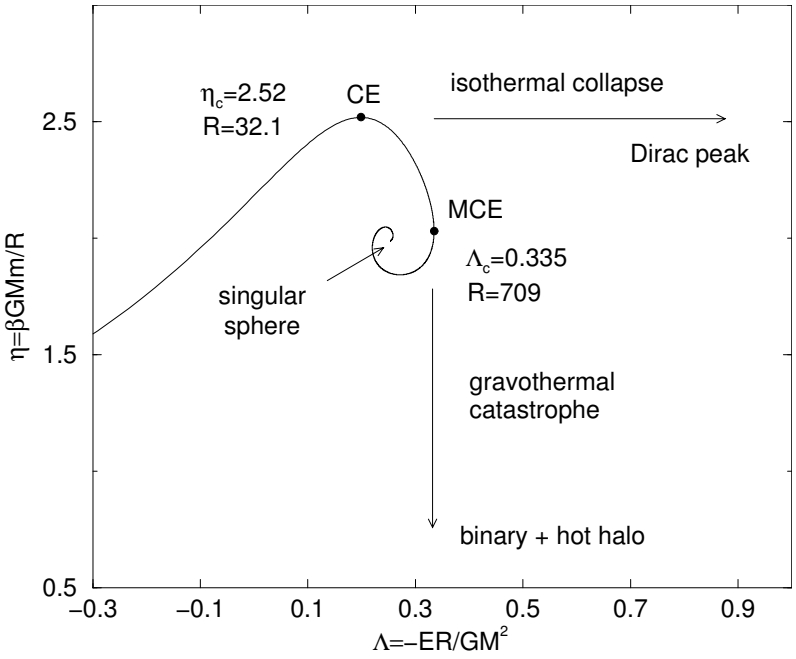

Figure 1.4: *Series of equilibria of classical self-gravitating isothermal spheres. For $\Lambda > \Lambda_c$ or $\eta > \eta_c$, the system is not anymore in equilibrium and undergoes a collapse (from Chavanis [53]).*

1 $\mathcal{R} = 6.8$: equivalence between gravitational and thermal energy (point B in Ref.[26], not represented in Fig. 1.4). The system is still in its gaseous phase.

2 $\mathcal{R} = 14.1$: onset of the thermal instability at constant pressure, i.e. the system undergoes an isobaric collapse [30, 73] (not represented in Fig. 1.4).

3 $\mathcal{R} = 32.125$: onset of the thermal instability at constant volume, i.e. the system undergoes an isothermal collapse in the canonical ensemble (point *CE* in Fig. 1.4). All the mass of the system is concentrated in a small core (Dirac peak, see Ref.[53] and references therein). The heat capacity becomes infinite. The reverse normalized temperature achieves the value $\eta_c = 2.52$ (Emden temperature).

4 $\mathcal{R} = 708.61$: onset of the gravo-thermal instability (Antonov instability), i.e. the system undergoes a collapse in the microcanonical ensemble (point *MCE* in Fig. 1.4). The system takes a core-halo structure: a small "cold" core is surrounded by a hot halo ([53] and references therein). The normalized energy achieves the value $\Lambda_c = 0.335$ (Antonov limit).

Moreover, in the region $32.125 < \mathcal{R} < 708.61$, the heat capacity is negative. However, we know that in the canonical ensemble, by definition, the heat capacity is positive because related to energy fluctuations (see, e.g., Ref.[105]). To solve this paradox, Thirring [179, 101, 100, 99] firstly pointed

out that, for long range systems, the statistical ensembles are generally *inequivalent*. The region with negative specific heat is allowed in the microcanonical ensemble and forbidden in the canonical ensemble. In this last case, the region of negative specific heat is replaced by an isothermal collapse.

In the microcanonical ensemble the instability sets in for $\mathcal{R} = 708.61$: points before this one are stable configurations. Conversely, in the canonical ensemble the instability sets in for $\mathcal{R} = 32.125$. Points after this one represent unstable physical solutions, implying that the stable points in the microcanonical ensemble cannot be reached in the canonical one.

In the microcanonical ensemble, the points until *MCE* are local entropy maxima (LEM) and correspond to stable physical solutions. Points after *MCE* are unstable saddle points. In the canonical ensemble, similarly, we find that points placed before *CE* are local minima (LFm) of Helmholtz free energy (hereafter simply free energy) and represent stable states whereas points after *CE* are unstable saddle points.

By means of the steepest descent technique, Horwitz & Katz [104] improved the results obtained in the original Lynden-Bell & Wood scenario. They concluded that spherically symmetric clusters are thermodynamically unstable if the density contrast $\mathcal{R} > 1.58$, which implies that the stability is a property of the homogeneous systems. As the reader can notice, this value is noticeably lower than that found by Antonov.

This discrepancy is explained because the states before the point *MCE* (and, equivalently in the canonical ensemble, before *CE*) are only *metastable*: indeed, they are not global entropy maxima (global minima of free energy in the canonical ensemble). However, in spite of their nature, these states are longlived (see Ref.[53] and references therein).

Conclusions about the onset of thermodynamical instability can be also drawn by means of the linear perturbation analysis. As firstly emphasized by Chavanis [45] (and successively confirmed by Sormani & Bertin [175]), the gravothermal catastrophe might reduce to Jeans instability. Similar studies, including effects due to the presence of the Cosmological Constant Λ or, by considering the Vector Resonant Relaxation (VRR), can be found in Refs.[11, 12, 161].

In the case of rotating protoplanet accretion disks, by including slower dynamical processes in the interaction among the particles and using a power-like distribution, the onset of the gravitational instability can be determined (see Ref.[124]).

1.3. Thermodynamical Description: the Case of Fermions

Fermions are particles introduced by Enrico Fermi in 1926 [81], in order to explain the electronic properties of metals[18] (for more details see Ref.[91]). By omitting the calculations for a formal derivation (see e.g. Refs.[126, 105]), we write the Fermi-Dirac statistics as

$$f = \frac{g}{h^3} \frac{1}{e^{(E-\mu)/k_B T} + 1} \,. \tag{1.21}$$

In the previous equation, E represents the energy of single particle, T the temperature of the gas, μ the chemical potential[19] and $g = 2s + 1$ is the multiplicity of quantum states (s being the spin). Fermions are distinguished from bosons[20] because of the nature of the wavefunction, being antisymmetric under particles exchange. This behaviour is relevant in the limit $T \to 0$, when Pauli exclusion principle [153, 31] is manifest. At low temperatures, indeed, any fermion is allowed to occupy only one energy level. Therefore, the DF (1.21) takes the form

$$f = \begin{cases} g/h^3 & \text{if} \qquad q \leq q_F \ , \\ 0 & \text{if} \qquad q > q_F \ , \end{cases} \tag{1.22}$$

where q_F represents the maximum accessible value of the particle momentum (Fermi momentum [105]). In Chap. 3 we will extensively study systems described by Eq.(1.22). When the fermionic gas reaches very low temperature, it is called degenerate because the particles tend to go to the lowest energy levels possible, by then filling all the levels up to ϵ_F. The equation of state (hereafter EOS) for the degenerate Fermi gas can be written as [105]

$$PV = \frac{2}{3} U \,, \tag{1.23}$$

where P represents the pressure, V the volume of the gas and U the internal energy. Eq.(1.23) displays Pauli exclusion principle: indeed, it is necessary to contain the gas with external walls because the pressure does not vanish.

[18] Some months later Paul A. M. Dirac [70] arrived, following a different reasonement, to the same result of Fermi (for more details see Ref.[91]).

[19] The chemical potential is defined such that, for any variation dN of the particles number, the energy changes by μdN, being $\mu = (\partial U/\partial N)_{S,V}$ (S and V are, respectively, the entropy and the volume of the gas, see Refs.[126, 105]).

[20] There are several proposals for boson stars or, more generally, self-gravitating bosonic configurations with astrophysical applications. One of the most intruiguing feature is represented by the possibility to schematize NSs, for example, as Cooper pairs of neutrons (see, e.g., Refs.[106, 110, 57, 56]). However, in this work, we do not consider this kind of particles.

Historically, the first theoretical description of WDs (Fowler [83]), used the result previously shown. More in details, Fowler referred to a WD star as a degenerate electron gas surrounding a core mainly made of ionized Helium nuclei[21]. The equilibrium of the structure is guaranteed by the balance between the degeneracy pressure (1.23) of the electrons and the gravity of the core. Successively Chandrasekhar [40, 41] improved Fowler's original proposal, by including special relativistic corrections in the EOS and arriving to evaluate a (maximal) limiting mass for WDs [169, 43] (see Chap. 3)

$$M_{Ch} = \frac{5.75}{\mu_e^2} M_\odot \,. \tag{1.24}$$

In the foregoing expression μ_e is the mean weight per electron[22] and it is related to the chemical composition of WD (see Refs.[94, 95, 121]). The original Chandrasekhar's scenario has been later improved by taking into account the variety of the nature of WDs, according to the chemical composition [156, 155] or by also considering, for example, the action of magnetic fields [68, 67] (see also Refs.[82, 163]). At the same time, it is important to mention proposals advancing the existence of a minimal mass for WDs, which is $M_{KAPBK} \sim 0.17 M_\odot$ (Kilic *et al.* [117]).

To seek for a thermodynamical description of fermionic self-gravitating systems, we need to relax the condition $T = 0$. Similarly to the isothermal gas sphere, the study can be carried out by considering truncated (i.e. cut-off energy), box or approximated models ([135], see below), because Fermi-Dirac statistics presents the infinite mass problem. The historical motivation for truncated models arose from the DM scenario. Ruffini & Stella [165] firstly pioneered a modification of Fermi-Dirac statistics introducing, in analogy with King DF (1.13), a maximal energy. In this way Eq.(1.21) becomes

$$f = \frac{g}{h^3} \frac{1 - e^{(E-\epsilon_c)/k_B T}}{e^{(E-\mu)/k_B T} + 1} \qquad \text{if} \qquad E \leq \epsilon_c \,, \qquad\qquad f = 0 \qquad \text{otherwise} \,. \tag{1.25}$$

The DF (1.25) has been later obtained by Chavanis [44], who solved the Fokker-Planck equation taking into account Pauli exclusion principle[23]. It is important to understand the relation between the Fermi energy ϵ_F and the cutoff energy ϵ_c, when $T \to 0$. Due to the presence of ϵ_c, we know that the energy variation (due to a single particle) cannot be larger than the cutoff energy, i.e. $\partial U / \partial N \leq \epsilon_c$. Recalling the definition of the chemical potential, we have $\mu \leq \epsilon_c$. In the fully degenerate case, $\mu = \epsilon_F$ [105]

[21] Electrostatic considerations prevent the existence of this model. For this reason, Fowler hypothesized the local charge neutrality and ignored the contribution of the electrostatic forces, as a first approximation.

[22] The molecular mean weight μ_I is defined as the mass per unit mole of material, or, alternatively, the mean mass of a particle in Atomic Mass Units (AMU).

[23] More precisely, the Fokker-Planck equation solved by Chavanis is conceptully different from the usual Fokker-Planck equation (1.5). In his work, indeed, Chavanis used the Maximum Entropy Production Principle (MEPP) [44, 50, 49].

which implies $\epsilon_F \leq \epsilon_c$. Moreover, in the interval between ϵ_F and ϵ_c the density in phase space is zero. This means that, in the fully degenerate case, we have $\epsilon_F = \epsilon_c$ [137].

A thermodynamical description in terms of Eq.(1.25) is complicated to perform, because the link between the cut-off energy and the thermodynamic functions is not trivial. However, in spite of this complexity, Chavanis *et al.* [58, 59] studied thermodynamical instabilities (both of types, microcanonical and canonical) for fermionic systems described by Eq.(1.25). Such as box models (see below), truncated models exhibit phase transitions. Further, in the non-quantum limit [in this case Eq.(1.25) recovers Eq.(1.13)], the authors obtained the critical values of energy and temperature for the onset of the instabilities (the shape of the series of equilibria is very similar to that of the box models).

An alternative to this description is represented by the proposal of Membrado *et al.* [135], consisting of a trapezoidal approximation of Fermi-Dirac DF

$$\mathcal{G}(\epsilon) = \begin{cases} 1 & \text{if} \quad 0 \leq E < \mu - 1/2\beta' \ , \\ \frac{1}{2} - \beta'(E-\mu) & \text{if} \quad \mu - 1/2\beta' \leq E < \mu + 1/2\beta' \ , \\ 0 & \text{if} \quad E \geq \mu - 1/2\beta' \ , \end{cases} \tag{1.26}$$

being $\beta' = 1/(2\pi k_B T)$ [the other symbols have the same meaning of Eq.(1.25)]. Thanks to Eq.(1.26), Membrado *et al.* derived analytical expressions (up to terms T^2) for total energy, radius of the system, density and pressure.

By using a model consisting of two stars, Padmanabhan [151, 152, 53] showed the occurrence of the phase transition in the canonical ensemble. In his work, Padmanabhan assumed that the stars were hard spheres of radius $a/2$, confined within a spherical box of dimension R. The key parameter in this description is the cut-off parameter R/a. It is found that, in the series of equilibria diagram, the region of the negative specific heat is more and more pronounced for small values of a. At the same time, the model does not exhibit the microcanonical phase transition.

To make the link with the results of Chap. 5, we are going to discuss in more detail the model of Chavanis [47] (see also Chavanis & Sommeria [63]). The fermionic system is placed within a spherical box of size R. The appropriate parameters to represent and study the caloric curve[24] are defined by

$$\Lambda = -\frac{ER}{GM^2} \, , \qquad \eta = \frac{GMm}{k_B T R} \, , \tag{1.27}$$

Λ and η being, respectively, the normalized energy and normalized reverse temperature. The definitions (1.27) are the same given in Ref.[133]. The function $\eta = \eta(\Lambda)$ is parameterized by the following

[24]The caloric curve is only a part of the series of equilibria, because consisting only of stable and metastable states. This means that the phase transition does not occurs in practice (see Ref.[53]).

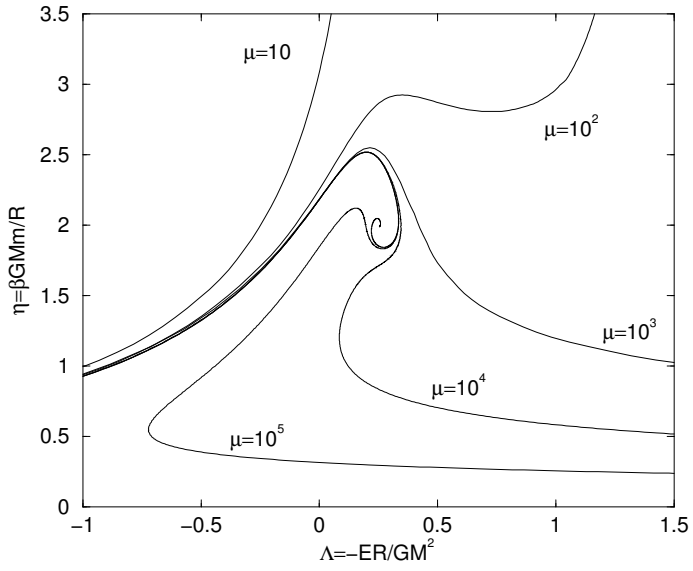

Figure 1.5: *Equilibrium phase diagram for the self-gravitating Fermi gas with different values of the degeneracy parameter μ_d. The inclusion of the degeneracy has the effect of unwinding the spiral obtained in the case of Boltzmann statistics. When the value of μ_d is reduced, the shape of the series of equilibria drastically changes until the extinction of the phase transition (from Chavanis [45]).*

parameter, called by Chavanis "degeneracy parameter" μ_d (which should not be confused with the "usual" degeneracy parameter $\theta = \mu/k_BT$):

$$\mu_d = \eta_0\sqrt{512\pi^4 G^3 M R^3}\,, \qquad \text{where} \qquad \eta_0 = \frac{gm^4}{h^3}\,. \tag{1.28}$$

According to the definition (1.28), the non-quantum limit is recovered for $\mu_d \to +\infty$ (i.e. $h \to 0$). Differently from the case of classical systems, the series of equilibria of the fermionic systems (see Fig. 1.5) present new features. In his accurate analysis, in particular, Chavanis focused his attention on two specific values of μ_d, to emphasize the exhibition of the microcanonical ($\mu_d = 10^5$) and canonical ($\mu_d = 10^3$) phase transition (represented, respectively, in Figs. 1.6 and 1.7).

Concerning the microcanonical ensemble, the caloric curve has a "Z-shape" (Fig. 1.6). The spiralic behaviour typical of classical system has been replaced by a phase transition (for a fixed value of the energy there are more than one solution) dividing the caloric curve in a gaseous (upper branch, points A) and a condensed phase (lower branch, points C). The curve presents two critical values of the energy, corresponding to the gravo-thermal catastrophe (Λ_c) and to the formation of the condensed phase (Λ_*). The presence of the two collapses is associated with the disappearance of the metastable phase [47, 53].

As we will see in Sec. 5.5, points forming the gaseous phase present smooth density profiles (see also

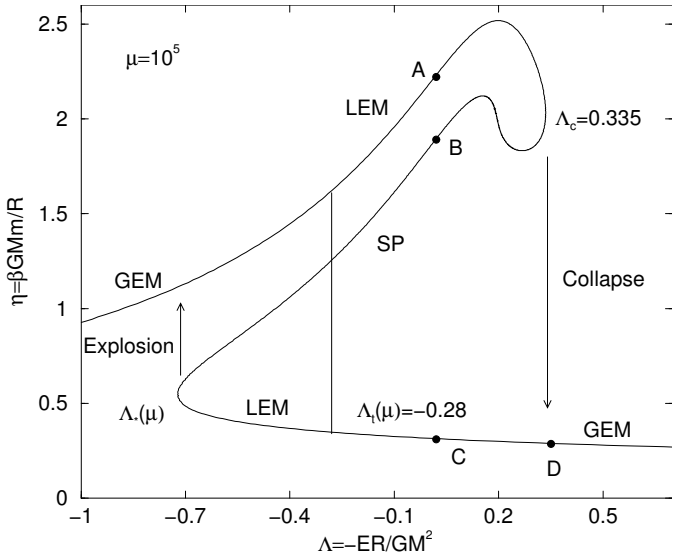

Figure 1.6: *Equilibrium phase diagram for the self-gravitating Fermi gas with a degeneracy parameter* $\mu_d = 10^5$*. Points A form the "gaseous" phase whereas points C form the "condensed" phase. Points B are unstable saddle points (SP). Due to the existence of metastable states, for* $\Lambda \geq \Lambda_c$*, a gaseous configuration undergoes a gravothermal catastrophe (collapse) and for* $\Lambda \leq \Lambda_*$*, a condensed configuration undergoes an explosion.* Λ_t *(see below) indicates the transition energy, where the stable (metastable) gaseous (condensed) configurations become metastable (stable) (from Chavanis [53]).*

Ref.[63]) and they are global entropy maxima (GEM) for $\Lambda < \Lambda_t$ (Λ_t being the transition energy) and local entropy maxima (LEM) for $\Lambda > \Lambda_t$. Conversely, the points forming the condensed phase have a core-halo structure and, according to the value of the transition energy Λ_t, they are LEM for $\Lambda < \Lambda_t$ and GEM $\Lambda > \Lambda_t$ (see Ref.[47] and Sec. 5.5). The transition energy Λ_t can be obtained by a vertical Maxwell construction. The equivalence of the areas determined by the Maxwell plateau connecting the gaseous (on the right of Λ_t) and the condensed (on the left of Λ_t) phase. The equivalence of the areas can be expressed as

$$\int_{\eta'}^{\eta'''} (\Lambda - \Lambda_t)\, d\eta \neq 0\,, \tag{1.29}$$

where η' and η''' are the reverse temperatures of the two phases at the transition energy Λ_t (for more details see Ref.[53]). To be more specific, the LEM states are *metastable*. This means that metastable configurations in the gaseous phase are destined to collapse whereas, metastable condensed configurations undergo an explosion. As pointed out by Chavanis [52], the metastable states are very longlived. A good estimate of their lifetime, close to the critical point, is [52]

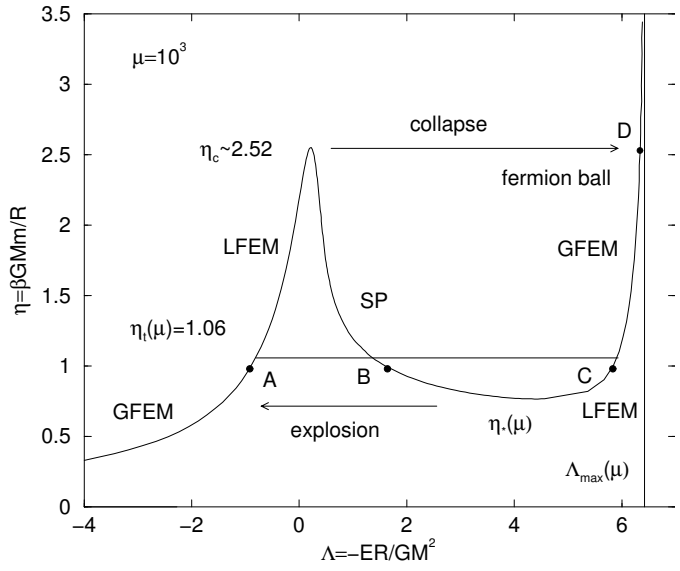

Figure 1.7: *Equilibrium phase diagram for the self-gravitating Fermi gas with a degeneracy parameter* $\mu_d = 10^3$*. Points A form the "gaseous" phase whereas points C form the "condensed" phase. Points B are unstable saddle points (SP). Due to the existence of metastable states, for* $\eta \geq \eta_c$*, a gaseous configuration undergoes an isothermal collapse and for* $\eta \leq \eta_*$*, a condensed configuration undergoes an explosion.* η_t *(see below) indicates the transition temperature, where the stable (metastable) gaseous (condensed) configurations become metastable (stable) (from Chavanis [53]).*

$$\tau_{life} \sim e^{2\lambda' N(\Lambda_c - \Lambda)^{3/2}}, \qquad \lambda' = 0.863159... \tag{1.30}$$

The term $2\lambda'(\Lambda_c - \Lambda)^{3/2}$ corresponds to the entropy barrier ΔS near the critical point Λ_c. The entropy barrier is determined by the difference between the entropy of the metastable state and the entropy of the saddle point. Being exponentially proportional to the particles number N, the lifetime τ_{life} diverges in the thermodynamical limit $N \to +\infty$: for this reason, we argue that these metastable states could exist.

By now considering the canonical ensemble, we see that the caloric curve presents an "N-shape" (Fig. 1.7). Here the distinction between the gaseous and the condensed phase is more evident. Such as the microcanonical ensemble, there exists a critical point identified by $\eta = \eta_c = 2.52$ (reverse Emden temperature) leading the system to the collapse. The gaseous phase is formed by the branch of points having $\eta < \eta_c$, which are global or local minima of free energy, according to their position with respect to the reverse temperature transition η_t. Then, after η_c, the caloric curve consists of a descending part and the points forming it are unstable saddle points. The stability is gained a second time when the temperature reaches a minimum at $\eta = \eta_*$, which corresponds to the condensed phase.

We stress that, between the points $\Lambda(\eta_c) = \Lambda_{gas}$ and $\Lambda(\eta_*) = \Lambda_{cond}$ (see Secs. 5.4 - 5.5), the specific heat is negative (from a microcanonical point of view). Similarly to the microcanonical ensemble, we can get an estimate of the lifetime of the metastable states

$$\tau_{life} \sim e^{2\lambda N(\eta_c - \eta)^{3/2}}, \qquad \lambda \simeq 0.16979815... \tag{1.31}$$

where the term $2\lambda(\eta_c - \eta)^{3/2}$ corresponds to the free energy barrier ΔF near the critical point η_c. The free energy barrier is determined by the difference between the free energy of the metastable state and the free energy of the saddle point. In addition, metastable gaseous (condensed) configurations collapse (explode) if $\eta > \eta_c$ ($\eta < \eta_*$). After η_* the caloric curve reaches the minimal accessible energy Λ_{max}: at this point the temperature diverges (i.e. $\eta \to +\infty$, corresponding to $T \to 0$), indicating that we have recovered the full degeneracy. The points forming the condensed phase, differently from those of the gaseous phase, have a structure similar to WDs, i.e. consisting of a degenerate nucleus not anymore surrounded by the atmosphere, having been swallowed (a more detailed discussion, for both microcanonical and canonical ensembles, can be found in Ref.[53]). Analogous to the microcanonical ensemble, the transition temperature η_t can be obtained by a horizontal Maxwell construction.

An interesting application of this model is represented by the "fermions balls" [188, 189, 23]. When the semidegenerate (i.e. nondegenerate) gas is cooled down below a critical temperature (i.e. the transition temperature where the free energies of the gaseous and the condensed phases are equal), the condensed phase naturally emerges. As above explained, this condensed fermionic gas has a structure similar to a WD below "its own Chandrasekhar's limiting mass" M_{Ch}, which is called a cold star (see also Ref.[144]). As pointed out by Bilić & Viollier [23, 22, 24], the condensation is accompanied by a big release of energy in a time scale of the order of the free fall time $\tau_{ff} \simeq [R^3/(GM)]^{1/2}$ (see Ref.[26]). If we consider a fermionic gas made of particles of rest mass of $10 \div 20\, keV/c^2$, the corresponding mass of the condensed sphere can range in the interval $10^6 \div 10^9\, M_\odot$. Being this mass compatible with the BH masses supposed to be at the centre of Galaxies, we can argue that these cold stars (which formation took place in the early Universe) could provide a good theoretical framework to describe galactic buldges. However, observational constraints seem to exclude this hypothesis and the related scenario, by instead supporting the BH hypothesis (Genzel *et al.*, [86]).

The nature of the transition phase can depend not only on the kind of gas, but also on other effects. A detailed description by taking into account the dimensions of the workspace has been studied by Chavanis [51, 54] (see also Ref.[172] for the case of Brownian particles). In his work, he considered a fermionic system in D-dimensions ($1 \leq D \leq 10$). It has been found that, for $D \geq 4$, the quantum pressure cannot balance the gravitational attraction, by implying that systems in four or more

dimensions should collapse.

The inclusions of rotations has consequences on the onset of the instabilities and the occurrence of gravitational phase transitions. As shown by Chavanis & Rieutord [60], although the shape of the series of equilibria is maintained (both of types, N and Z), rotations can alter the critical values of temperature and energies. Moreover in the non-quantum limit, since the critical energy Λ_c decreases with rotation, the gravitational collapse occurs sooner than in the non-rotating case. Further, beyond the fermionic model, a description of self-gravitating systems can be obtained by means of Tsallis DF ([62, 111] and references therein) or by considering systems made by hard spheres in gravitational interaction [39].

1.4. Thermodynamics and General Relativity

The models mentioned up to this point have been studied in the framework of Newtonian gravity. However, relativistic corrections at astrophysical scales are not negligible and have to be taken into account although, for GCs or Galaxies, these effects are unimportant. At the same time, from a theoretical point of view, it is fundamental to provide a framework enabling us to describe the thermodynamics of self-gravitating systems in GR.

The first historical application of the Fermi gas model in GR concerned NSs, leading to the discovery of the well known Oppenheimer-Volkoff (OV) limiting mass [150]. The two authors moved from Chandrasekhar's model for WDs and studied the general relativistic version[25] of such model. This study predicts the existence of a limiting configuration, the OV limit[26] (analogous to Chandrasekhar limit)

$$M_{OV} = 0.71 M_{\odot}\,, \qquad R_{OV} = 9.16 km\,. \tag{1.32}$$

Historically, the extension of WD model to GR was not immediate (for a detailed discussion see Refs.[192, 31]). Oppenheimer & Volkoff, indeed, assumed that a NS was a degenerate core made of neutrons, analogous to the fermions balls previously analyzed. This model, however, is too simplistic and does not provide the correct description of a NS.

A more precise idea about the structure of NSs arrived some decades later. Consequently, the evaluation of the limiting mass also changed. Theoretically, we know that the maximum mass of a NS *cannot*

[25] For an elegant and formal derivation of the equations governing the gravitational equilibrium, the Tolman-Oppenheimer-Volkoff (TOV) system, see Refs.[183, 190].

[26] One year before (1938), Oppenheimer & Serber derived a lower limiting value for NS (Oppenheimer-Serber limit), corresponding to $M_{OS} = 0.17 M_{\odot}$ [149].

be larger than $M_{RR} = 3.2M_\odot$ (Rhoades & Ruffini [158]). This estimate must not be interpreted as a limiting mass but, rather, as an *asymptotic* value. In this sens, a theoretical explanation for the mass of the pulsar PSR J0348+0432 (see above) is difficult to find, because the EOS regulating the matter inside the NS is unknown.

A proposal has been suggested by Drago *et al.* [72], considering two separate families of compact stars: hadronic stars (with a soft EOS) and quark stars (with a stiff EOS). A second explanation, by means of thermodynamic arguments, has been advanced by Roupas [160]. In his paper, by including thermal contributions to the gravitational stability, Roupas derived an upper mass limit for NSs which value is $M_R = 2.43M_\odot$. Alternatively, the inclusion of some anisotropies in the particles momenta distribution could explain such high mass ([138] and references therein). Out of the fermionic paradigm, Chavanis & Harko [57] considered the possibility of modeling NSs as BEC stars. In this case, the limiting mass can be expressed as

$$M_{CH} = 0.436\,\kappa M_\odot \qquad \text{where} \qquad \kappa = \Big(\frac{a}{1fm}\Big)^{1/2}\Big(\frac{m}{2m_n}\Big)^{-3/2}. \tag{1.33}$$

In the foregoing expression, a is the scattering lenght, m the mass of the boson forming the BEC star and m_n the neutron mass. For $\kappa = 5$, Eq.(1.33) yields $M_{CH} = 2.18M_\odot$, which is compatible with the mass of PSR J0348+0432.

The investigation about the link between Thermodynamics and GR started with Tolman [182]. Nevertheless, the general relativistic generalizations to the models described in Secs. 1.2 and 1.3 arrived later. Parallely to Antonov's studies, the first investigations about the structure (see, e.g., Ruffini & Bonazzola [164]) and the dynamical stability (Refs.[109, 107, 108, 76, 77, 78, 178]) of relativistic clusters began.

Even for relativistic systems the question about their spatial confinement arises. By considering truncated models, Bisnovatyi - Kogan *et al.* [28, 29] studied the stability of equilibrium models described by a Maxwellian DF. By means of three different methods (sequence of models with fixed cut-off parameter, constant specific entropy, conservation of adiabatic invariant), the authors obtained an estimate of the (normalized) temperature for the onset of the instability, which is $k_BT_c/mc^2 = 0.223$. In addition, thanks to the central redshift versus temperature diagram, authors classified the configurations obtained according to their stability (both thermodynamical and dynamical).

An interesting analysis for what concerns the stability of isothermal spheres in GR has been made by Chavanis [46]. More precisely, he put special relativistic effects in a Newtonian framework by finding a critical value of mass-energy above which no equilibrium state is possible. However, by also considering a gas described by an EOS of the kind $P = q\epsilon$ (q is a free dimensionless parameter in the interval

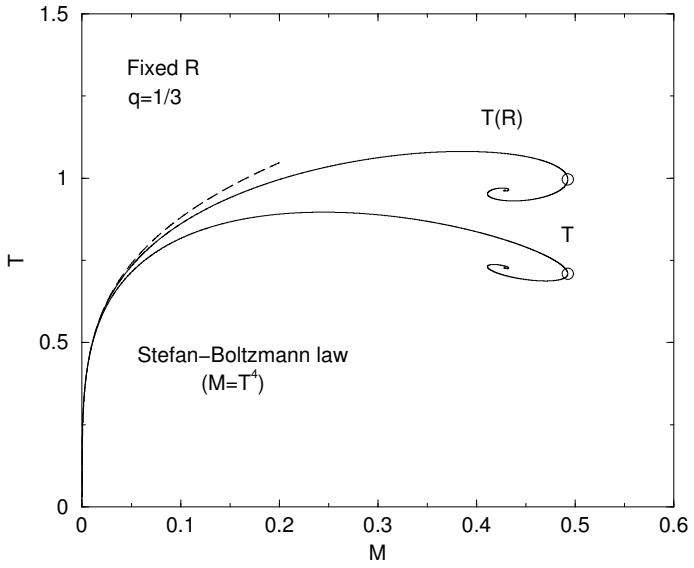

Figure 1.8: *Temperature diagram for the high energy instabilities. When general relativistic effects are taken into account, the curve forms a spiral and deviates from the Stefan-Boltzmann law (from Chavanis [55]).*

$[0, 1]$), he obtained a description of NSs cores ($q = 1/3$). In a subsequent work [55] (see Fig. 1.8), Chavanis completed his previous investigations by determining the limiting mass (and the associated density contrast) of a self-gravitating radiating sphere in a box[27]. These results will be obtained in Sec. 4.2.2, where we will consider the isothermal relativistic gas sphere in the ultrarelativistic limit.

An improvement in the theoretical understanding, has been provided by Roupas [159]. In his work, he considered the contribution of high and low energy to gravothermal instabilities. High energy instabilities correspond to the thermal radiation (already studied by Chavanis in Refs.[46, 55]). In the series of equilibria, as we will see, the radiation gives origin to a second spiral (see Sec. 4.4). Low energy instabilities, by contrast, represent the general relativistic generalization of Antonov's instability. He also found a limiting configuration (corresponding to the $\mathcal{N}_{max}$ configuration defined in Sec. 4.4), having a relativistic origin[28].

Although the behaviour of a cluster with cutoff is very similar to that in a box [27], the models are

[27]In his model, Chavanis considered the case of a gas formed by ultra-relativistic particles which EOS is $P = \epsilon/3$ and which $\mu = 0$, corresponding to photons.

[28]In Chap. 4 we analyze the case of the isothermal spheres in GR, by using a method different from that used by Roupas. He determined the equilibrium configuration by means of the intersections between the 3-dimensional function $\xi = 2GNm/Rc^2$ and the perpendicular plane obtained for a fixed value of ξ. Moreover, he found some critical parameters not appearing in our model, because of the scaling GNm/Rc^2 (see Sec. 4.2). We stress that we have obtained our results independently of Roupas.

different from a thermodynamical point of view. Truncated configurations are *always* thermodynamically unstable whereas, as we know, box models become unstable after the Antonov limit (in the microcanonical ensemble, see Ref.[27]).

The models above discussed refer to systems formed by classical particles. A quantum generalization, in order to study the occurrence of the gravitational phase transition, is more recent. Bilić & Viollier [24, 25] extended to GR the Thomas-Fermi model precedingly studied in the realm of Newtonian gravity [23]. In their work, they have shown the occurrence of the phase transition in the canonical ensemble, but only for a particular configuration below the OV limit. Moreover, they did not obtain the phase transition in the microcanonical ensemble.

1.5. Objectives of This Work

The aim of this work is to obtain a detailed description of phase transitions in self-gravitating systems in a general relativistic framework. We move from the work of Bilić & Viollier [25] and we study a static fermionic configuration, formed by N particles of mass m placed within a box of fixed dimensions. In contrast to Bilić & Viollier, we study a wider variety of cases by varying the size of the box, the intensity of the gravitational fields and the level of degeneracy.

Since we are interested in the effects induced by gravity in a thermodynamic system, we neglect the contributions coming from other interactions: particles interact only gravitationally. This assumption can only work as a simplifying approximation, because the nature of astrophysical systems is more complex. For example, if we want to study the equilibrium and the internal structure of a NS, we should, in principle, account for strong interactions, but this goes beyond the scope of the present study.

The thesis is organized as follows. In Chap. 2 we present the general formalism and deduce the equations governing the gravitational equilibrium. Further we show that, in the limit of weak gravitational fields, we recover the Thomas-Fermi model in Newtonian gravity. In Chap. 3 we focus our attention on the degenerate fermionic configurations, by studying the gravitational equlibrium and the dynamical stability of such configurations. In Chap. 4 we consider the non-quantum limit of Fermi-Dirac statistics (i.e. Botzmann statistics), which allows us to extend to GR the Newtonian models considered in Sec. 1.2 and complete the investigations discussed in Sec. 1.4. In Chap. 5, finally, we describe the nature of the phase transitions of the general relativistic self-gravitating fermionic gas.

2

General Formalism

This Chapter can be seen as the link between the historical introduction and the discussion of the results of our study, that will be presented in Chaps. 3, 4 and 5. By taking into account the most general case, we derive here the main relations describing a fermionic system (the limiting situations at low and high temperature will be extensively studied in Chaps. 3 and 4).

Sec. 2.1 is devoted to the deduction of the equations of the gravitational equilibrium (TOV system). However, we do not provide a detailed deduction of the TOV system starting from Einstein's field equations (the reader can find it in Ref.[190]). In Sec. 2.2 the attention is focused on the definition of the thermodynamic quantities, namely the density-state number, the energy density, the pressure, the entropy and the free energy. We also introduce the variables that will be used in the subsequent analysis (e.g. α, see below).

In order to be independent of physical constants and dimensions and to have a more suitable form for the numerical resolution, in Sec. 2.3, the equations are put in dimensionless form. In the end, in Sec. 2.4, we recover the Newtonian limit.

2.1. Equations of the Gravitational Equilibrium

As we know, the dynamics of a system in GR is described by Einstein's field equations [126]

$$G_{\mu\nu} = R_{\mu\nu} - \frac{1}{2} R g_{\mu\nu} = \frac{8\pi G}{c^4} T_{\mu\nu} \,, \tag{2.1}$$

where $G_{\mu\nu}$ is the Einstein tensor, being a linear combination between Ricci $R_{\mu\nu}$ and metric $g_{\mu\nu}$ tensor (R is the scalar curvature, i.e. the trace of the Ricci tensor with respect to the metric, see Ref.[126]).

$T_{\mu\nu}$ is the stress-energy tensor. The metric tensor $g_{\mu\nu}$ is defined by

$$ds^2 = g_{\mu\nu}dx^\mu dx^\nu \tag{2.2}$$

where ds^2 represents the line element, i.e. the distance between two infinitely close points in the space-time. We now specify to the case of a static configuration within a spherical box of fixed dimensions R, filled up by N particles having the same mass m. Due to the symmetries of the problem[1], the line-element correctly describing this system is given by

$$ds^2 = \Big(1 - \frac{2GM}{rc^2}\Big)c^2dt^2 - \Big(1 - \frac{2GM}{rc^2}\Big)^{-1}dr^2 - r^2(d\theta^2 + \sin^2\theta d\phi^2)\,, \tag{2.3}$$

which corresponds to the well known Schwarzschild's solution [170, 126, 190]. In the foregoing expression, M represents the total mass (more precisely the mass energy, that is the sum of rest mass and internal energy) of the system (the other symbols have their usual meaning). Eq.(2.3) can be obtained by solving Einstein's field equations outside the source, i.e. when

$$G_{\mu\nu} = 0\,. \tag{2.4}$$

At large distances from the system, i.e. $r \to +\infty$, the metric (2.3) is asymptotically flat and reduces to the Minkowskian one

$$ds^2 = c^2dt^2 - dr^2 - r^2(d\theta^2 + \sin^2\theta d\phi^2)\,. \tag{2.5}$$

According to Eq.(2.5), an observer located very far from the body does not feel the gravitational field generated by the body itself and the gravitational potential can be described by the well known formula $\phi \sim -GM/r$. Let us now consider the interior solution, implying that $T_{\mu\nu} \neq 0$. By virtue of the symmetries of the problem, the stress-energy tensor is diagonal and takes the form

$$T_{\mu\nu} = (\epsilon + P)u_\mu u_\nu + Pg_{\mu\nu}\,, \tag{2.6}$$

where ϵ and P represent, respectively, the energy density the pressure and u_μ is the covariant 4-velocity. Einstein's field equations give [42]

$$\frac{d(re^{-\lambda})}{dr} = 1 - \frac{8\pi G}{c^4}\epsilon r^2\,, \tag{2.7}$$

$$\frac{e^{-\lambda}}{r}\frac{d\nu}{dr} = \frac{1 - e^{-\lambda}}{r^2} + \frac{8\pi G}{c^4}P\,, \tag{2.8}$$

[1] For a more detailed derivation see Ref.[190].

$$\frac{dP}{dr} = -\frac{P+\epsilon}{2}\frac{d\nu}{dr}\,. \tag{2.9}$$

$\lambda = \lambda(r)$ and $\nu = \nu(r)$ are functions of the radial coordinate r. In particular, λ is related to the mass energy of the body by the relation [139]

$$e^{\lambda} = \Big(1 - \frac{2GM_r}{rc^2}\Big)^{-1}\,, \tag{2.10}$$

where, differently from the exterior solution, M_r represents the mass-energy of the sphere (concentric to that encapsulating the gas) of radius $r < R$ and corresponds to the total mass energy M only when $r = R$. By eliminating the presence of ν via Eqs.(2.8), (2.9) and (2.10), we get the equation for the pressure gradient [190]

$$\frac{dP}{dr} = -\frac{GM_r\epsilon}{r^2c^2}\Big(1 + \frac{4\pi Pr^3}{M_rc^2}\Big)\Big(1 + \frac{P}{\epsilon}\Big)\Big(1 - \frac{2GM_r}{rc^2}\Big)^{-1}\,. \tag{2.11}$$

From the foregoing expression we see that, differently from the Newtonian gravity (see below), the pressure gives an additional contribution to the mass-energy (first term in parenthesis).

Dimensionally, since the pressure is an energy density, the term $4\pi Pr^3$ plays the role of an *effective mass* to be added to the term M_rc^2. This means that, if we consider a shell between r and $r + dr$, the effective mass attracting the matter is made by two contributions. The presence of the pressure has the effect of enhancing this effective mass[2]. Eq.(2.11) is solved together with the conservation equation of the mass-energy

$$\frac{dM_r}{dr} = \frac{4\pi\epsilon r^2}{c^2}\,. \tag{2.12}$$

Writing $\epsilon = \rho c^2$ in Eq.(2.11), we have

$$\frac{dP}{dr} = -\frac{GM_r\rho}{r^2}\Big(1 + \frac{4\pi Pr^3}{M_rc^2}\Big)\Big(1 + \frac{P}{\rho c^2}\Big)\Big(1 - \frac{2GM_r}{rc^2}\Big)^{-1}\,. \tag{2.13}$$

As noted by Weinberg [190], the terms in parenthesis can be seen as the relativistic corrections to the equation of hydrostatic equilibrium in Newtonian gravity. In fact, in the limit $c \to +\infty$, these terms become negligible and Eq.(2.13) takes the form

$$\frac{dP}{dr} = -\frac{GM_r\rho}{r^2}\,, \tag{2.14}$$

which corresponds to the hydrostatic equilibrium in Newtonian gravity. At the the same time, Eq.(2.12) becomes

[2]This effect is called *regeneration of the pressure*. For an interesting discussion about the solutions in total generality of TOV system see Ref.[173].

$$\lim_{c\to+\infty}\frac{dM_r}{dr}=\frac{4\pi\epsilon r^2}{c^2}=\frac{4\pi\rho c^2 r^2}{c^2}=4\pi\rho r^2\,. \tag{2.15}$$

corresponding to the usual mass conservation equation in Newtonian gravity. Thus, the equilibrium of a static fluid in GR is described by the following pair of equations, the Tolman-Oppenheimer-Volkoff (TOV) system[3], that we rewrite as[4]

$$\begin{aligned}\frac{dP}{dr}&=-\frac{G}{c^4}\frac{(M_r c^2+4\pi P r^3)(P+\epsilon)}{r^2}\Big(1-\frac{2GM_r}{rc^2}\Big)^{-1}\,,\\ \frac{dM_r}{dr}&=\frac{4\pi\epsilon r^2}{c^2}\,,\end{aligned} \tag{2.17}$$

with the conditions $P(0)=P_0$ and $M_r(0)=0$. The system (2.17) can be solved if there exists an EOS of the form $P=P(\epsilon)$. In this work, however, we follow the formalism outlined in Ref.[24]. For this reason, we define the new variable

$$\xi=e^{\nu/2}=\sqrt{1-\frac{2GM_r}{rc^2}}\,. \tag{2.18}$$

The equation governing the evolution of ξ along the system can be obtained from Eq.(2.9)

$$\frac{d\xi}{dr}=\frac{e^{\nu/2}}{2}\frac{d\nu}{dr}=\frac{\xi}{2}\frac{d\nu}{dr}=-\frac{\xi}{P+\epsilon}\frac{dP}{dr}\,. \tag{2.19}$$

If we now substitute the first of the TOV system (2.17), we obtain

$$\frac{d\xi}{dr}=\frac{G}{c^4}\frac{\xi(M_r c^2+4\pi P r^3)}{r^2}\Big(1-\frac{2GM_r}{rc^2}\Big)^{-1}\,. \tag{2.20}$$

Eq.(2.20), together with the second of Eqs.(2.17), forms the pair of equations that must be solved to get the variation of the functions P, ϵ and M_r along the system. Together with these quantities, we need also to compute the baryonic number N. The reason resides in the fact that, in the framework of the Thomas-Fermi model (i.e. the model used in the present work), the caloric curve is obtained for a fixed value of N. Following Weinberg [190], we write the baryonic number as

$$N=\int_0^R 4\pi n e^{\lambda/2} r^2 dr=\int_0^R 4\pi n r^2\Big(1-\frac{2GM_r}{rc^2}\Big)^{-1/2}dr\,, \tag{2.21}$$

[3]Tolman [181, 183] derived the equations that have been applied by Oppenheimer & Volkoff to NSs [150].

[4]The TOV system has an analytical solution [143] in the ultrarelativistic limit (i.e. when the internal energy of the fluid dominates the rest mass component):

$$\epsilon=\frac{3c^4}{56\pi G r^2}\,. \tag{2.16}$$

In this approximation, the EOS describing the fluid is $P=\epsilon/3$ (see Sec. 4.2.2).

where n is the density state number (or, equivalently, the rest mass density, up to a factor m). As noticed by Landau & Lifshitz [126], the integration (2.21) is performed by using the element volume of the metric (2.3) $dV = 4\pi e^{\lambda/2} r^2 dr$ whereas, in Eq.(2.12), we have $dV = 4\pi r^2 dr$. This difference displays the mass deficit of the body. The TOV system formed by Eqs.(2.20) and (2.12) is solved with the following boundary conditions

$$\xi(R) = \sqrt{1 - \frac{2GM}{Rc^2}}\,, \qquad M_r(0) = 0\,. \tag{2.22}$$

As pioneered by Tolman & Ehrenfest [180, 184], both the temperature and the chemical potential, inside a body, are not constant but depend on the metric. At the equilibrium, for a configuration in a static gravitational field, we have [122]

$$dP = \frac{N_r}{V}\Big(d\mu_r - \mu_r \frac{dT_r}{T_r}\Big) + (P + \epsilon)\frac{dT_r}{T_r}\,. \tag{2.23}$$

In the foregoing expression[5], analogous to the mass (2.12), the subscript r indicates that we are placed within the sphere of radius $r < R$. Moreover, N_r is the particle number within this sphere which volume is $V = \int_0^r 4\pi e^{\lambda/2} r'^2 dr'$. The chemical potential μ_r present in Eq.(2.23) is defined as

$$\mu_r = \mu_{NR} + mc^2\,, \tag{2.24}$$

where μ_{NR} represents the nonrelativistic chemical potential [24]. Substituting Eq.(2.9) in Eq.(2.23), we get

$$\frac{N_r}{V}\Big(d\mu_r - \mu_r \frac{dT_r}{T_r}\Big) + (P + \epsilon)\Big(d\nu + 2\frac{dT_r}{T_r}\Big) = 0\,. \tag{2.25}$$

The preceding identity must be identically fulfilled for every value of ϵ, P and N_r: so we have

$$\frac{dT_r}{T_r} = -\frac{d\nu}{2} \qquad \Longleftrightarrow \qquad T_r e^{\nu/2} = T e^{\nu_R/2}\,, \tag{2.26}$$

where $T = T_R$ indicates the temperature measured by an infinitely removed observer and $e^{\nu_R/2}$ is given by the first of (2.22). The preceding relation, thus, yields $Te^{\nu/2} = const.$, which is the well-known Tolman condition [180, 182]. Thanks to Eqs.(2.25) and (2.26), further, we have

$$\frac{d\mu_r}{\mu_r} = \frac{dT_r}{T_r} \qquad \Longleftrightarrow \qquad \mu_r e^{\nu/2} = \mu e^{\nu_R/2}\,, \tag{2.27}$$

where, similar to the temperature, $\mu = \mu_R$ is the chemical potential at the infinity. From the previous relation, moreover, we find that $\mu/T = const.$ (see Sec. 2.2). Eq.(2.26) shows that, in GR, the

[5] Eq.(2.23) can be derived by combining the Gibbs-Duhen relation and Einstein's field equations.

condition of "isothermality" under thermodynamical equilibrium in gravitational field can never be satisfied. More precisely, the isothermality is recovered at the infinity, where an observer measures the temperature evaluated at the edge $T = T_R$, being constant for $r > R$. According to the formalism outlined in this work, the conditions on temperature and chemical potential are

$$\mu_r = \frac{\mu}{\xi}, \qquad T_r = \frac{T}{\xi}\,. \tag{2.28}$$

2.2. Definition of Thermodynamic Quantities

The relations obtained in the previous Section have general validity and do not depend on the EOS describing the fluid. However, in this work, we consider a fermionic system. The DF (1.21) does not formally change but, now, the temperature and the chemical potential are defined by Eqs.(2.28). Consequently, we have

$$f = \frac{g}{h^3}\frac{1}{e^{(E-\mu_r)/k_B T_r}+1}\,. \tag{2.29}$$

The thermodynamic quantities, by means of the DF (2.29), are

$$n = \int f d^3\vec{q} = \frac{g}{h^3}\int \frac{d^3\vec{q}}{e^{(E-\mu_r)/k_B T_r}+1}\,, \tag{2.30}$$

$$\epsilon = \int f E d^3\vec{q} = \frac{g}{h^3}\int \frac{E d^3\vec{q}}{e^{(E-\mu_r)/k_B T_r}+1}\,, \tag{2.31}$$

$$P = \frac{1}{3}\int f\vec{q}\frac{\partial E}{\partial \vec{q}}\, d^3\vec{q} = \frac{g k_B T_r}{h^3}\int \ln\Big[1+e^{(\mu_r - E)/k_B T_r}\Big] d^3\vec{q}. \tag{2.32}$$

n is the number density of particles, ϵ the total mass-energy density and P the pressure. The quantities (2.30), (2.31) and (2.32) are local function of the radial coordinate r, via the conditions (2.28). To perform the integration, we have to express the kinetic energy E in terms of the momentum q. By means of the special relativistic definition of the kinetic energy, one has

$$E = \sqrt{m^2c^4 + q^2c^2} = mc^2\sqrt{1+y^2} \qquad \text{where} \qquad y = \frac{q}{mc}\,. \tag{2.33}$$

Now, by passing to the polar coordinates in the momentum phase space, we write the volume element as $d^3\vec{q} = 4\pi q^2 dq = 4\pi m^3 c^3 y^2 dy$. In addition, by introducing a new set of variables defined as follows

$$\alpha = \frac{\mu}{k_B T}, \qquad \xi = \frac{|\mu|}{mc^2}\frac{1}{\sqrt{\Phi+1}}, \qquad z = e^{-\alpha}\,, \tag{2.34}$$

the expressions of the thermodynamic quantities (2.30), (2.31) and (2.32) become

$$n = \frac{4\pi g m^3 c^3}{h^3} \int_0^\infty y^2 \Big(z e^{|\alpha| \sqrt{\frac{y^2+1}{\Phi+1}}} + 1 \Big)^{-1} dy \,, \tag{2.35}$$

$$\epsilon = \frac{4\pi g m^4 c^5}{h^3} \int_0^\infty y^2 \sqrt{y^2+1} \Big(z e^{|\alpha| \sqrt{\frac{y^2+1}{\Phi+1}}} + 1 \Big)^{-1} dy \,, \tag{2.36}$$

$$P = \frac{4\pi g m^4 c^5}{3h^3} \int_0^\infty \frac{y^4}{\sqrt{y^2+1}} \Big(z e^{|\alpha| \sqrt{\frac{y^2+1}{\Phi+1}}} + 1 \Big)^{-1} dy \,. \tag{2.37}$$

We note that, in their work, Bilić & Viollier [24] implicitely assumed that the chemical potential could get only positive[6] values whereas, rather, μ can be both negative and positive. In the following, we prefer to work with α instead of μ. According to the value of α, there are two limiting situations

$$\begin{cases} \alpha \to +\infty : & \textit{Full Degeneracy Limit}, \\ \alpha \to -\infty : & \textit{Classical Limit}. \end{cases} \tag{2.38}$$

The first limit means that the chemical potential is very large compared to the temperature, i.e. $\mu \gg k_B T$. The second limit, vice-versa, means that the chemical potential is very small compared to the temperature, i.e. $\mu \ll k_B T$ (and also negative). We address the reader to Chaps. 3 and 4 for a detailed study of these two limiting situations. The variable z defined in Eq.(2.34) can be seen as the inverse of the fugacity [105].

The variable Φ, defined by the second equality (2.34), corresponds to the gravitational field. From Eq.(2.34) we see that $\Phi > -1$. For a fixed value of the chemical potential, there are three different limiting cases:

$$\begin{cases} \Phi \to +\infty & \Longrightarrow & \xi \to 0 \\ \Phi \to -1 & \Longrightarrow & \xi \to +\infty \\ \Phi \to 0 & \Longrightarrow & \xi \to |\mu|/mc^2 \end{cases} \tag{2.39}$$

For large and positive values of Φ, we have that ξ is infinitesimal. By remembering that $\xi = e^{\nu/2}$ [see Eq.(2.18)], we have $e^{\nu/2} \to 0$, implying that $r \to R_S = 2GM/c^2$ (R_S is the Schwarschild's radius). So, in the limiting situation of large and positives gravitational fields, the system approaches the BH configuration. In this sens we refer to this case as the "Schwarzschild" limit.

The limit $\Phi \to -1$ comes out from the parametrization used [see Eq.(2.34)]. Since ξ is divergent in this limit, we see that the intensity of the gravitational fields is very high. Small values of Φ, by contrast, indicate that we are recovering the Newtonian gravity. In fact, $\xi \to |\mu|/mc^2$ implies that the

[6] For an explanation about the link between the sign of μ and the kind of statistics used, see Ref.[159].

gravitational field is constant[7] (we have indeed $e^{\nu/2} \to 1$, up to a numerical factor). The free energy F is defined as

$$F = Mc^2 - TS\,, \tag{2.40}$$

where Mc^2 is the total energy of the system and S represents its entropy. This last one can be evaluated starting from the First Principle of the Thermodynamics

$$dU = T_r dS - PdV + \mu_r dN\,. \tag{2.41}$$

Isolating the entropy and writing $dU = \epsilon dV$, we have

$$dS = \frac{P+\epsilon}{T_r}dV - \frac{\mu_r}{T_r}dN = \frac{\xi(P+\epsilon)}{T}dV - \frac{\mu}{T}dN\,, \tag{2.42}$$

where we have used Eq.(2.28). Integrating all over the configuration

$$S = \frac{1}{T}\int \xi(P+\epsilon)dV - \frac{\mu}{T}\int dN = \frac{1}{T}\int_0^R 4\pi\xi(P+\epsilon)r^2\Big(1-\frac{2GM_r}{rc^2}\Big)^{-1/2}dr - \frac{\mu}{T}N\,. \tag{2.43}$$

Substituting the definitions (2.34) of α and Φ we have

$$S = \frac{k_B|\alpha|}{mc^2}\left[\int_0^R \frac{4\pi(P+\epsilon)r^2dr}{\sqrt{\Phi+1}\sqrt{1-\frac{2GM_r}{rc^2}}} - \mathrm{sgn}(\alpha)Nmc^2\right]. \tag{2.44}$$

Now, substituting Eq.(2.43) in Eq.(2.40), we get the final expression of the free energy

$$F = Mc^2 + \mu N - \frac{|\mu|}{mc^2}\int_0^R \frac{4\pi(P+\epsilon)r^2dr}{\sqrt{\Phi+1}\sqrt{1-\frac{2GM_r}{rc^2}}}\,. \tag{2.45}$$

Further, by means of the definition (2.34) of Φ, we rewrite the TOV system (2.20)-(2.12) in the following way

$$\begin{aligned} \frac{d\Phi}{dr} &= -\frac{2G}{c^4}\frac{(\Phi+1)(M_rc^2+4\pi Pr^3)}{r^2}\Big(1-\frac{2GM_r}{rc^2}\Big)^{-1}\,, \\ \frac{dM_r}{dr} &= \frac{4\pi\epsilon r^2}{c^2}\,. \end{aligned} \tag{2.46}$$

The system in the form (2.46) is solved with the conditions $\Phi(0) = \Phi_0 > -1$ and $M_r(0) = 0$.

[7] More precisely, we have

$$\xi \sim \frac{|\mu|}{mc^2}\Big(1 - \frac{\Phi}{2} + \frac{3}{8}\Phi^2 + ...\Big)$$

.

2.3. Dimensionless Relations

To have a more suitable form for the numerical integration, in this Section we are going to put the relations derived in Secs. 2.1 and 2.2 in dimensionless form. To do that, we define the characteristic quantities associated with the variables previously defined, that is

$$r = r_*\tilde{r}\,, \qquad n = n_*\tilde{n}\,, \qquad \epsilon = \epsilon_*\tilde{\epsilon}\,, \qquad P = P_*\tilde{P}\,, \qquad M = M_*\tilde{M}\,, \qquad N = N_*\tilde{N}\,. \tag{2.47}$$

The variables with the subscript $*$ represent the characteristic quantities (keeping the physical dimensions) while the variables with the superscript $\sim$ the dimensionless ones. Let us substitute the definitions (2.47) in the TOV system (2.46): we have

$$\begin{aligned} \frac{d\Phi}{dr} &= -\frac{GM_*}{r_*c^2}\frac{2(\Phi+1)}{\tilde{r}^2}\Big(\tilde{M}_r + \frac{P_*r_*^3}{M_*c^2}4\pi\tilde{P}\tilde{r}^3\Big)\Big(1-\frac{GM_*}{r_*c^2}\frac{2\tilde{M}_r}{\tilde{r}}\Big)^{-1}\,, \\ \frac{d\tilde{M}_r}{d\tilde{r}} &= \frac{\epsilon_*r_*^3}{M_*c^2}4\pi\tilde{\epsilon}\tilde{r}^2\,. \end{aligned} \tag{2.48}$$

From previous relations we choose

$$\frac{GM_*}{r_*c^2} = 1\,, \qquad M_* = \frac{\epsilon_*r_*^3}{c^2}\,, \qquad P_* = \frac{M_*c^2}{r_*^3} = \epsilon_*\,. \tag{2.49}$$

From the first equality (2.49) we recognize the Schwarzschild scale lenght and, looking at the third, we see that the pressure has a gravitational effect. Let us now consider the thermodynamic quantities: by writing the Planck constant as $h = 2\pi\hbar$, we have

$$n = \frac{gm^3c^3}{2\hbar^3}\frac{1}{\pi^2}\int_0^\infty y^2\Big(ze^{|\alpha|\sqrt{\frac{y^2+1}{\Phi+1}}}+1\Big)^{-1}dy = n_*\tilde{n}\,. \tag{2.50}$$

$$\epsilon = \frac{gm^4c^5}{2\hbar^3}\frac{1}{\pi^2}\int_0^\infty y^2\sqrt{y^2+1}\Big(ze^{|\alpha|\sqrt{\frac{y^2+1}{\Phi+1}}}+1\Big)^{-1}dy = \epsilon_*\tilde{\epsilon}\,, \tag{2.51}$$

$$P = \frac{gm^4c^5}{2\hbar^3}\frac{1}{3\pi^2}\int_0^\infty \frac{y^4}{\sqrt{y^2+1}}\Big(ze^{|\alpha|\sqrt{\frac{y^2+1}{\Phi+1}}}+1\Big)^{-1}dy = P_*\tilde{P}\,. \tag{2.52}$$

From the previous relations we define the characteristic particle number density n_*, energy density ϵ_* and pressure P_* as

$$n_* = \frac{gm^3c^3}{2\hbar^3}\,, \qquad \epsilon_* = \frac{gm^4c^5}{2\hbar^3} = mn_*c^2\,, \qquad P_* = \epsilon_*\,. \tag{2.53}$$

According to Eqs.(2.50), (2.51), (2.52) and (2.53), the dimensionless particle number density $\tilde{n}$, energy density $\tilde{\epsilon}$ and pressure $\tilde{P}$ are defined as

$$\tilde{n} = \frac{1}{\pi^2}\int_0^\infty y^2\Big(ze^{|\alpha|\sqrt{\frac{y^2+1}{\Phi+1}}}+1\Big)^{-1}dy\,. \tag{2.54}$$

$$\tilde{\epsilon} = \frac{1}{\pi^2}\int_0^\infty y^2\sqrt{y^2+1}\Big(ze^{|\alpha|\sqrt{\frac{y^2+1}{\Phi+1}}}+1\Big)^{-1}dy\,, \tag{2.55}$$

$$\tilde{P} = \frac{1}{3\pi^2}\int_0^\infty \frac{y^4}{\sqrt{y^2+1}}\Big(ze^{|\alpha|\sqrt{\frac{y^2+1}{\Phi+1}}}+1\Big)^{-1}dy\,. \tag{2.56}$$

Now, by combining Eqs.(2.49) and (2.53), we get the definition of r_*

$$r_* = \sqrt{\frac{2\hbar^3}{gGm^4c}} = \sqrt{\frac{2}{g}}\sqrt{\frac{\hbar^3}{Gc}}\frac{1}{m^2}\,. \tag{2.57}$$

Thanks to Eq.(2.57), we can define all the other characteristic quantities in terms of r_*

$$\begin{aligned} &n_* = \frac{c^2}{Gmr_*^2}\,, \quad \epsilon_* = P_* = mn_*c^2 = \frac{c^4}{Gr_*^2} \\ &N_* = n_*r_*^3 = \frac{c^2r_*}{Gm}\,, \quad M_* = \frac{\epsilon_* r_*^3}{c^2} = mn_*r_*^3 = mN_* = \frac{c^2r_*}{G} \end{aligned} \tag{2.58}$$

[the definition of N_* comes from Eq.(2.21)]. In this way, Eqs.(2.48) and (2.21), in dimensionless form, become

$$\begin{aligned} &\frac{d\Phi}{d\tilde{r}} = -\frac{2(\Phi+1)(\tilde{M}_r+4\pi\tilde{P}\tilde{r}^3)}{\tilde{r}^2}\Big(1-\frac{2\tilde{M}_r}{\tilde{r}}\Big)^{-1}\,, \\ &\frac{d\tilde{M}_r}{d\tilde{r}} = 4\pi\tilde{\epsilon}\tilde{r}^2\,, \end{aligned} \tag{2.59}$$

$$\tilde{N} = \int_0^{\tilde{R}} 4\pi\tilde{n}\tilde{r}^2\Big(1-\frac{2\tilde{M}_r}{\tilde{r}}\Big)^{-1/2}d\tilde{r}\,. \tag{2.60}$$

Following the same procedure, we can obtain the dimensionless expressions of the entropy (2.44) and the free energy (2.45). Starting from the entropy, we have

$$\begin{aligned} &S = \frac{k_B|\alpha|}{mc^2}\epsilon_* r_*^3\left[\int_0^{\tilde{R}}\frac{4\pi(\tilde{P}+\tilde{\epsilon})\tilde{r}^2d\tilde{r}}{\sqrt{\Phi+1}\sqrt{1-\frac{2\tilde{M}_r}{\tilde{r}}}} - \frac{N_*mc^2}{\epsilon_* r_*^3}\,\mathrm{sgn}(\alpha)\tilde{N}\right] = \\ &= k_BN_*|\alpha|\Big[I_S - \mathrm{sgn}(\alpha)\tilde{N}\Big] = S_*\tilde{S}\,, \end{aligned} \tag{2.61}$$

where $S_* = k_BN_*$ and $\tilde{S} = |\alpha|[I_S - \mathrm{sgn}(\alpha)\tilde{N}]$. Thanks to previous result, the free energy is

$$F = M_*c^2\Big(\tilde{M} - \frac{TS_*}{M_*c^2}\tilde{S}\Big) = M_*c^2\Big(\tilde{M} - \frac{k_BT|\alpha|}{mc^2}\tilde{S}\Big) = F_*\Big(\tilde{M} - \tilde{T}|\alpha|\tilde{S}\Big)\,, \tag{2.62}$$

where we have defined the energy unit $F_* = M_* c^2$ and the Tolman temperature [159] $\tilde{T} = k_B T/mc^2$. The foregoing relation allows us to obtain an expression for the Tolman temperature in terms of the mass and the radius of the system. Be

$$\frac{k_B T|\alpha|}{mc^2} = \frac{|\mu|}{mc^2} = \xi_R\sqrt{\Phi_R + 1} = \sqrt{\Phi_R + 1}\sqrt{1 - \frac{2\tilde{M}}{\tilde{R}}}\,, \tag{2.63}$$

where we have used Eqs.(2.34) and (2.22). Isolating the temperature on the l.h.s. of the foregoing expression, we have

$$\tilde{T} = \frac{k_B T}{mc^2} = \frac{\sqrt{\Phi_R + 1}}{|\alpha|}\sqrt{1 - \frac{2\tilde{M}}{\tilde{R}}}\,. \tag{2.64}$$

Substituting in Eq.(2.62), we get the dimensionless expression of the free energy

$$\tilde{F} = \frac{F}{F_*} = \tilde{M} - \sqrt{\Phi_R + 1}\sqrt{1 - \frac{2\tilde{M}}{\tilde{R}}}\tilde{S}\,. \tag{2.65}$$

According to Eq.(2.57) the characteristic length depends on the fundamental constants G, c and $\hbar$. This suggests that we can express the characteristic quantities in terms of Planck's units. Because of the presence of the particle mass m in Eq.(2.57), it seems reasonable to use the Planck Mass[8] M_{Pl}, defined by

$$M_{Pl} = \sqrt{\frac{\hbar c}{G}} = 2.176 \times 10^{-5}\, g = 1.222 \times 10^{19}\frac{GeV}{c^2}\,. \tag{2.66}$$

Introducing the Planck mass (2.66) in Eq.(2.57), we have [24]

$$r_* = \sqrt{\frac{2}{g}}\frac{\hbar M_{Pl}}{m^2 c} = 1.3185 \times 10^{10}\sqrt{\frac{2}{g}}\left(\frac{15\, keV}{mc^2}\right)^2\, km\,. \tag{2.67}$$

By using Eq.(2.67), the characteristics quantities M_*, N_* and F_* are

$$M_* = \sqrt{\frac{2}{g}}\frac{M_P^3}{m^2}\,, \qquad N_* = \sqrt{\frac{2}{g}}\frac{M_P^3}{m^3}\,, \qquad F_* = \sqrt{\frac{2}{g}}\frac{M_P^3 c^2}{m^2}\,. \tag{2.68}$$

2.4. The Newtonian Limit $\Phi \to 0$

In this section we consider the case $\Phi \to 0$, corresponding to the weak field limit. Moreover the particles are nonrelativistic. This implies that the kinetic energy (2.33) becomes

[8] We could also use the Planck Length $R_{Pl} = \sqrt{G\hbar/c^3} = 1.616 \times 10^{-33}\ cm$ but, because of its smallness, its employement would not be practical.

$$\frac{E}{mc^2} = \sqrt{1+y^2} \sim mc^2\Big(1 + \frac{y^2}{2} - \frac{y^4}{8} + ...\Big) = mc^2 + \frac{q^2}{2m} + ... \tag{2.69}$$

In addition, thanks to Eq.(2.18), we get

$$\xi = e^{\nu/2} \sim 1 - \frac{GM_r}{rc^2} + ... = 1 + \frac{\phi}{c^2} + ... \tag{2.70}$$

The exponential term in the Fermi - Dirac distribution function (2.29) becomes

$$\frac{e^{\nu/2}E - \mu}{k_BT} \sim \frac{1}{k_BT}\Big(1 + \frac{\phi}{c^2} + ...\Big)\Big(mc^2 + \frac{q^2}{2m} + ...\Big) - \frac{\mu_{NR} + mc^2}{k_BT} = \frac{q^2}{2mk_BT} + \frac{m\phi}{k_BT} - \frac{\mu_{NR}}{k_BT} \tag{2.71}$$

where we have used Eq.(2.24). Substituting the foregoing expression in the thermodynamic quantities (2.30), (2.31) and (2.32), one has

$$n \sim \frac{4\pi g}{h^3}\int_0^\infty q^2\left[\exp\Big(\frac{q^2}{2mk_BT} + \frac{m\phi}{k_BT} - \frac{\mu_{NR}}{k_BT}\Big) + 1\right]^{-1} dq \tag{2.72}$$

$$\epsilon = \rho c^2 \sim \frac{4\pi g mc^2}{h^3}\int_0^\infty q^2\left[\exp\Big(\frac{q^2}{2mk_BT} + \frac{m\phi}{k_BT} - \frac{\mu_{NR}}{k_BT}\Big) + 1\right]^{-1} dq\,, \tag{2.73}$$

$$P \sim \frac{4\pi g}{3m}\int_0^\infty q^4\left[\exp\Big(\frac{q^2}{2mk_BT} + \frac{m\phi}{k_BT} - \frac{\mu_{NR}}{k_BT}\Big) + 1\right]^{-1} dq\,. \tag{2.74}$$

The previous expressions correspond to the expressions of the thermodynamic quantities in Newtonian gravity (see Refs.[23, 47]). Moreover Eq.(2.73) implies $\rho = mn$. In the limit of weak gravitational fields, Eq.(2.20) becomes

$$\frac{1}{c^2}\frac{d\phi}{dr} \sim \frac{GM_r}{r^2c^2}\Big(1 + \frac{\phi}{c^2} + ...\Big)\Big(1 + \frac{4\pi Pr^3}{M_rc^2}\Big)\Big(1 + \frac{GM_r}{rc^2} + ...\Big) = \frac{GM_r}{r^2c^2}\,, \tag{2.75}$$

where we have used Eq.(2.70). Simplifying the terms in c^2 we get

$$\frac{d\phi}{dr} = \frac{GM_r}{r^2}\,. \tag{2.76}$$

If we now isolate M_r on the r.h.s. of Eq.(2.76), derive both members and substitute Eq.(2.15), we obtain [ρ is defined by Eq.(2.73), implying that $M_r = N_rm$]

$$\frac{1}{r^2}\frac{d}{dr}\Big(r^2\frac{d\phi}{dr}\Big) = 4\pi G\rho\,, \tag{2.77}$$

which corresponds to the Poisson equation for the (classical) gravitational field ϕ. In Newtonian gravity, the volume element becomes

$$dV = 4\pi e^{\lambda/2} r^2 dr = \frac{4\pi r^2 dr}{\sqrt{1-\frac{2GM_r}{rc^2}}} \sim 4\pi r^2 \Big(1 + \frac{GM_r}{rc^2} + \frac{3GM_r^2}{2r^2c^4} + ...\Big) dr \simeq 4\pi r^2 dr \tag{2.78}$$

Thanks to the previous result and using Eq.(2.70), the entropy (2.43) becomes

$$\begin{aligned} S \simeq \frac{1}{T}\int_0^R 4\pi(P+\epsilon)\Big(1+\frac{\phi}{c^2}+...\Big)r^2 dr - \frac{(\mu_{NR}+mc^2)N}{T} \sim \frac{1}{T}\int_0^R 4\pi P r^2 dr + \\ + \frac{Mc^2}{T} + \frac{1}{T}\int_0^R 4\pi\rho\phi r^2 dr - \frac{\mu_{NR}N}{T} - \frac{Mc^2}{T}\,, \end{aligned} \tag{2.79}$$

that is

$$S = \frac{1}{T}\int_0^R 4\pi P r^2 dr - \frac{W}{T} - \frac{\mu_{NR}N}{T}\,. \tag{2.80}$$

where W represents the gravitational energy of the body (see Ref.[190]). Consequently, the free energy (2.45) is

$$F = Nmc^2 + \mu_{NR}N + W - \int_0^R 4\pi P r^2 dr\,, \tag{2.81}$$

that corresponds to the expression of the free energy in the Newtonian Thomas-Fermi model (up to the term Nmc^2).

3

Full Degeneracy Limit: the Case $T = 0$

In this Chapter we focus our attention on the degenerate fermionic configurations. As we have seen in Sec. 1.3, the Pauli exclusion principle is manifest and fermions tend to fill all the energy levels up to the Fermi energy. As we shall see, differently from the fermions at $T \neq 0$, degenerate configurations do not need external walls to be spatially bound. The existence of the Fermi energy, indeed, guarantees the spatial limitation of the gas (see Sec. 3.2.1).

Several authors [83, 41, 150, 144] have studied the degenerate self-gravitating Fermi gas model to explain the properties of WDs and NSs. In this Chapter, in particular, we extend the original work of Chandrasekhar & Tooper [43]. In their paper, the two authors have studied the case of a WD regarded as a gas made of helium nuclei[1] and degenerate electrons.

he model of Chandrasekhar & Tooper (CT in the following) depends on a parameter, namely q, defined as the ratio $m_e/(\mu_e H)$ (m_e and H are, respectively, the electron and the hydrogen mass and μ_e is the molecular mean weight, see Sec. 1.3.). However, they have considered a specific value of q. In this Chapter we complete their previous investigation by considering all the values that the parameter q can take. We emphasize that we neglect the contributions of other interactions (such as electromagnetic or strong interactions) that must be taken into account in a more precise and realistic description of both WDs and NSs. Furthermore, only in this Chapter, we use the formalism outlined in Refs.[41, 43].

In Sec. 3.1 we discuss the EOS of a degenerate Fermi gas, defining the rest mass density, the pressure and the energy density[2]. Then, we proceed to the study of equilibrium and stability of such configurations, by separating between the Newtonian (Sec. 3.2) and the general relativistic (in Sec. 3.3)

[1] Because of the typical values of pressure and temperature of the core, the helium atoms are expected to be completely ionized.

[2] We restrict ourselves to on gas of fermions formed by spin 1/2 particles. According to Eq.(1.22) this implies $g = 2$.

regimes. As we shall see in Appendix D, the study of the dynamical properties of the degenerate configurations is linked to the description of the series of equilibria that will be analyzed in Chap. 5. In Sec. 3.4 we provide some applications of the models advanced.

3.1. Equation of State

According to the explanations above given, we rewrite the Fermi-Dirac DF (1.22) as follows

$$f = \begin{cases} 2/h^3 & \text{if} \qquad p \leq p_0 \ , \\ 0 & \text{if} \qquad p > p_0 \ , \end{cases} \tag{3.1}$$

where p_0 is the Fermi momentum. The rest mass density ρ and the pressure P are defined by[3]

$$\rho = mn = m \int f \, d^3\vec{p} = \frac{8\pi m}{h^3} \int_0^{p_0} p^2 dp = \frac{8\pi m p_0^3}{3h^3} \, , \tag{3.2}$$

$$P = \frac{1}{3} \int f \vec{p} \cdot \frac{\partial E}{\partial \vec{p}} \, d^3\vec{p} = \frac{8\pi}{3h^3} \int_0^{p_0} \frac{dE}{dp} p^3 \, dp \, , \tag{3.3}$$

where $E = E(p)$ represents the kinetic energy of a particle having momentum p [see Eq.(2.33)]. Further, the energy density ϵ is written as the sum of the rest mass and the internal energy density[4] u, defined as follows

$$u = \int fE \, d^3\vec{p} = \frac{8\pi}{h^3} \int_0^{p_0} Ep^2 dp = \frac{8\pi}{3h^3} p_0^3 E(p_0) - P \, , \tag{3.4}$$

where, in the last passage, we have performed an integration by parts. Consequently, we write

$$\epsilon = \rho c^2 + u \, . \tag{3.5}$$

Now, using the expression of the kinetic energy (2.33) and introducing the variable

$$x = \frac{p_0}{mc} \, , \tag{3.6}$$

the preceding equations become

$$\rho = \frac{8\pi m^4 c^3}{3h^3} x^3 \, , \tag{3.7}$$

$$P = \frac{\pi m^4 c^5}{3h^3} f(x) \, , \tag{3.8}$$

[3] Analogous to Sec. 2.2, the distribution of momenta is assumed to be spherically symmetric.

[4] In this model, the internal energy is assumed to be only kinetic.

$$u = \frac{\pi m^4 c^5}{3h^3} g(x)\,, \tag{3.9}$$

$$\epsilon = \frac{8\pi m^4 c^5}{3h^3}\Big[x^3 + \frac{1}{8}g(x)\Big]\,. \tag{3.10}$$

The functions $f(x)$ and $g(x)$ are defined by

$$f(x) = 8\int_0^x \frac{t^4 dt}{\sqrt{1+t^2}} = x(2x^2-3)\sqrt{x^2+1} + 3\ln\Big(x+\sqrt{x^2+1}\Big)\,, \tag{3.11}$$

$$g(x) = 24\int_0^x \Big(\sqrt{1+t^2}-1\Big)t^2 dt = 8x^3\Big(\sqrt{1+x^2}-1\Big) - f(x)\,. \tag{3.12}$$

In the limits $x \to 0$ and $x \to \infty$, Eqs.(3.11) and (3.12) take the form[5]

$$f(x) \sim \frac{8}{5}x^5 - \frac{4}{7}x^7 + \frac{1}{3}x^9 - \frac{5}{22}x^{11} + ... \qquad (x \to 0) \tag{3.15}$$

$$g(x) \sim \frac{12}{5}x^5 - \frac{8}{7}x^7 + \frac{1}{6}x^9 - \frac{15}{176}x^{11} + ... \qquad (x \to 0) \tag{3.16}$$

$$f(x) \sim 2x^4 - 2x^2 + ... \qquad (x \to +\infty) \tag{3.17}$$

$$g(x) \sim 6x^4 - 8x^3 + 6x^2 - ... \qquad (x \to +\infty) \tag{3.18}$$

The case $x \to 0$ corresponds to the nonrelativistic limit (i.e. the rest-mass dominates the internal energy $p_0 \ll mc$ or, equivalently, $u \ll \rho c^2$). The pressure and the energy density become

$$P \sim \frac{\pi m^4 c^5}{3h^3}x^5\,, \qquad \epsilon \sim \frac{8\pi m^4 c^5}{3h^3}x^3 = \rho c^2\,, \tag{3.19}$$

[in the last equality we have used Eq.(3.7)]. Combining the two preceding relations we can get the EOS

$$P \sim \frac{1}{20}\Big(\frac{3}{\pi}\Big)^{2/3}\frac{h^2}{m^{8/3}}\,\rho^{5/3}\,, \qquad P \sim \frac{1}{20}\Big(\frac{3}{\pi}\Big)^{2/3}\frac{h^2}{m^{8/3}c^{10/3}}\,\epsilon^{5/3}\,, \tag{3.20}$$

which is a polytrope of index $\gamma = 5/3$ (or $n = 3/2$). The case $x \to \infty$, by contrast, corresponds to the ultrarelativistic limit (i.e. the internal energy dominates the rest-mass $p_0 \gg mc$ or, equivalently, $u \gg \rho c^2$). So

$$P \sim \frac{2\pi m^4 c^5}{3h^3}x^4\,, \qquad \epsilon \sim \frac{2\pi m^4 c^5}{h^3}x^4\,, \tag{3.21}$$

[5]The asymptotic expansions (3.17) and (3.18) differ from those given by Chandrasekhar [41]:

$$f(x) \sim 2x^4 - 3x^2 + ... \tag{3.13}$$

$$g(x) \sim 6x^4 - 8x^3 + 7x^2 - ... \tag{3.14}$$

These expressions contain mistakes (see also Ref.[80]).

leading to

$$\epsilon \simeq u \sim \frac{3}{8}\Big(\frac{3}{\pi}\Big)^{1/3}\frac{hc}{m^{4/3}}\,\rho^{4/3}\,, \qquad P \sim \frac{1}{8}\Big(\frac{3}{\pi}\Big)^{1/3}\frac{hc}{m^{4/3}}\,\rho^{4/3}\,, \qquad P \sim \frac{\epsilon}{3}\,. \tag{3.22}$$

In this case the EOS is that of a polytrope of index $\gamma = 4/3$ (or $n = 3$). The system is formed by two gases at the equilibrium. The particles number densities for the two gases are written, respectively, as

$$n_1 = \frac{8\pi m_1^3 c^3}{3h^3}x_1^3\,, \qquad n_2 = \frac{8\pi m_2^3 c^3}{3h^3}x_2^3\,, \tag{3.23}$$

where n_1 refers to the gas exerting the pressure and n_2 to the gas providing the gravitational attraction that holds the entire system together. Charge neutrality[6] implies $n_1 = n_2$: from the foregoing expression we have

$$m_1 x_1 = m_2 x_2\,. \tag{3.24}$$

Thanks to the previous equality we can express the mass density ρ_2 in terms of ρ_1:

$$\rho_2 = m_2 n_2 = m_2 n_1 = \frac{m_2}{m_1}\rho_1 = \frac{\rho_1}{q}\,, \tag{3.25}$$

where we have defined the parameter q as follows

$$q = \frac{m_1}{m_2}\,. \tag{3.26}$$

When $m_1 = m_2$ we have that $q = 1$: this is the case of a star where the pressure and the gravity are created by the same kind of particle. A similar configuration corresponds to a NS. By contrast, when $m_1 \ll m_2$, we have that $q \sim 0$. This is the case of a star made by two different gases, one being formed by heavy particles, the other by light particles. So the range of values of q corresponds to the interval $[0, 1]$. Following Chandrasekhar we write[7] m for m_1, $\mu_e H$ for m_2, ρ_{grav} for ρ_2 and ρ for ρ_1. With this choice, Eqs.(3.25) and (3.26) become

$$\rho_{grav} = \frac{\mu_e H}{m}\rho = \frac{\rho}{q}\,, \tag{3.27}$$

$$q = \frac{m}{\mu_e H}\,. \tag{3.28}$$

Moreover, the energy density becomes

[6] In this model the stars are neutrally charged.

[7] H is the hydrogen atomic mass (i.e. the proton mass), which value is $H = 1.6674 \times 10^{-24}$ g. Differently from original Chandrasekhar's formalism, we indicate the mean molecular weight as μ_e instead of μ [see Eq.(1.24)].

$$\epsilon_{grav} = \rho_{grav} c^2 + u \,. \tag{3.29}$$

If we now define

$$A = \frac{\pi m^4 c^5}{3h^3} \,, \tag{3.30}$$

we have

$$\rho_{grav} = \frac{8A}{qc^2} x^3 = Bx^3 \,, \qquad P = Af(x) \,, \qquad \epsilon_{grav} = A\Big[\frac{8}{q} x^3 + g(x)\Big] \,. \tag{3.31}$$

In the following, we note ρ for ρ_{grav} and ϵ for ϵ_{grav}.

3.2. The Newtonian Regime: Chandrasekhar Limiting Mass

3.2.1. Gravitational Equilibrium

In Newtonian gravity, the equations determining the condition of hydrostatic equilibrium of a self-gravitating spherically symmetric distribution of matter are given by [see Eqs.(2.14) and (2.15)]

$$\begin{aligned} \frac{dP}{dr} &= -\frac{GM_r \rho}{r^2} \,, \\ \frac{dM_r}{dr} &= 4\pi \rho r^2 \,, \end{aligned} \tag{3.32}$$

with the conditions $P(0) = P_0$ and $M_r(0) = 0$. These equations can be combined to give the fundamental equation of hydrostatic equilibrium

$$\frac{1}{r^2} \frac{d}{dr}\Big(\frac{r^2}{\rho} \frac{dP}{dr}\Big) = -4\pi G \rho \,. \tag{3.33}$$

This equation can be solved if there exists an EOS of the form $P = P(\rho)$, i.e. a relation linking the pressure and the rest mass density. In our case, this corresponds to Eq.(3.31). Substituting that relation, we find

$$\frac{1}{r^2} \frac{d}{dr}\left[\frac{r^2}{x^3} \frac{df(x)}{dr}\right] = -\frac{4\pi G B^2}{A} x^3 \,. \tag{3.34}$$

From Eq.(3.11) we find that

$$\frac{1}{x^3} \frac{df(x)}{dr} = \frac{8x}{\sqrt{1+x^2}} \frac{dx}{dr} = 8 \frac{d\sqrt{1+x^2}}{dr} \,. \tag{3.35}$$

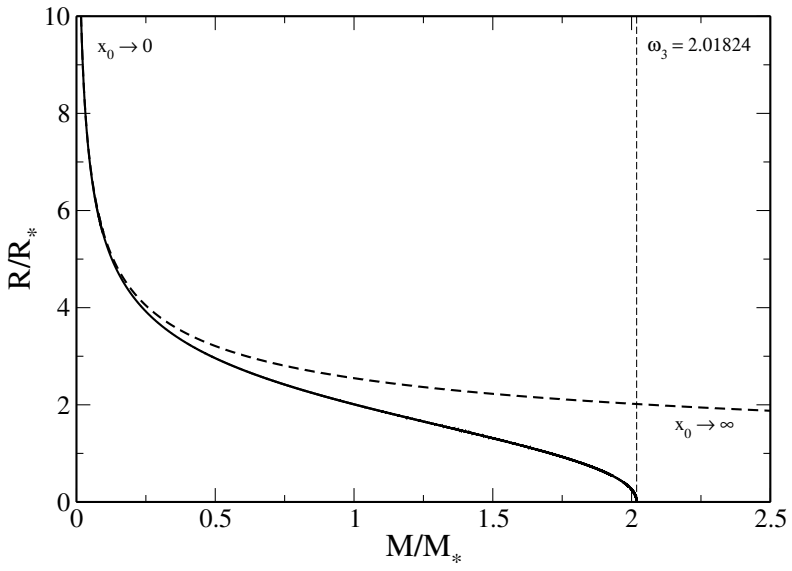

Figure 3.1: *Mass-radius relation of relativistic fermionic stars in Newtonian gravity. The radius R decreases as the mass M increases and tends to zero at the limiting mass $M_{max}/M_* = \omega_3$ (Chandrasekhar mass), obtained in the ultrarelativistic regime. The nonrelativistic regime (dashed line) is valid for $M \ll M_{\rm max}$ and the mass-radius relation reduces to Eq.*(3.55)*. We note that relativistic effects become important for $M \geq 0.2M_{max}$.*

Defining $y = \sqrt{1+x^2}$, we can rewrite Eq.(3.34) as

$$\frac{1}{r^2}\frac{d}{dr}\left(r^2\frac{dy}{dr}\right) = -\frac{\pi G B^2}{2A}(y^2-1)^{3/2}\,. \tag{3.36}$$

If we introduce the new variables[8] η and ϕ

$$r = a\eta\,, \qquad y = y_0\phi\,, \qquad a = \sqrt{\frac{2A}{\pi G}}\frac{1}{By_0}\,, \tag{3.37}$$

the differential equation (3.36) takes the form

$$\frac{1}{\eta^2}\frac{d}{d\eta}\Big(\eta^2\frac{d\phi}{d\eta}\Big) = -\Big(\phi^2 - \frac{1}{y_0^2}\Big)^{3/2} \tag{3.38}$$

with the conditions $\phi(0) = 1$ and $\phi'(0) = 0$. This is the Chandrasekhar equation [41]. Using Eqs.(3.31) and (3.37), the density can be expressed as

$$\rho = By_0^3\Big(\phi^2 - \frac{1}{y_0^2}\Big)^{3/2}. \tag{3.39}$$

[8] x_0 and $y_0 = \sqrt{1+x_0^2}$ correspond, respectively, to the values of x and y at the center of the configuration.

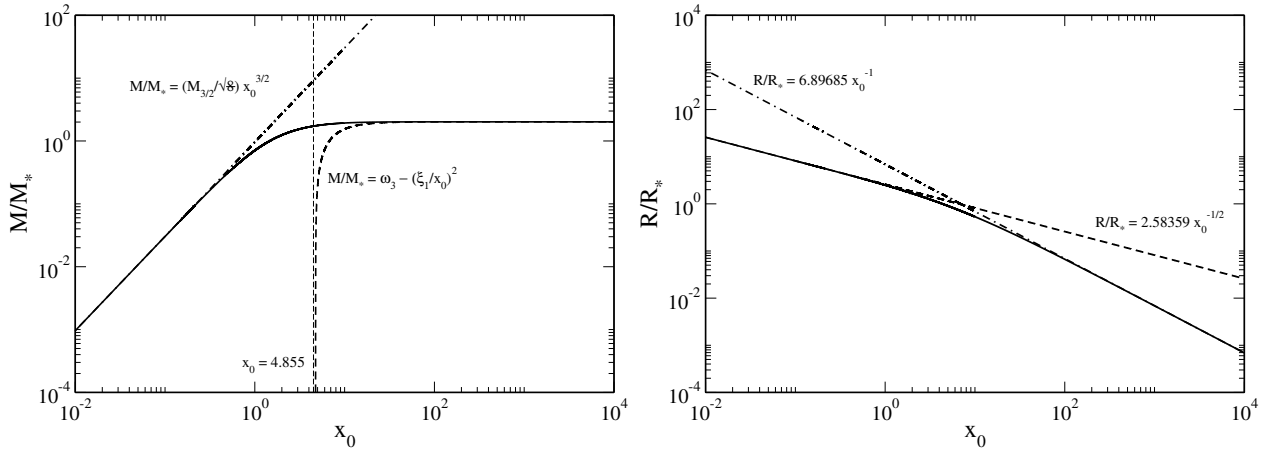

Figure 3.2: ***Left Panel****: Total mass as a function of* x_0 *for fermionic Newtonian configurations. The asymptotic expressions* (3.56) *(dash dotted line) and* (3.61) *(dashed line) are represented for comparison. The value of* x_0 *for which* $M/M_* = 0$ *(according to Eq.*(3.61)*) is also indicated.* ***Right Panel****: Total radius versus* x_0*. The asymptotic expressions obtained in the nonrelativistic [Eq.*(3.56)*, dashed line] and ultrarelativistic [Eq.*(3.59)*, dash dotted line] regime are also indicated.*

The mass M_r contained within the sphere of radius r is obtained by substituting Eqs.(3.37) and (3.39) into the second of Eqs.(3.32), using the Chandrasekhar equation (3.38) and performing the integration. This yields

$$M_r = \int_0^r 4\pi\rho(r')r'^2 dr' = -4\pi a^3 B y_0^3 \eta^2 \frac{d\phi}{d\eta}\,. \tag{3.40}$$

The radius R of the star is determined by the condition $\rho(R) = 0$, corresponding to a normalized radius η_1 such that [see Eq.(3.39)]

$$\phi(\eta_1) = \frac{1}{y_0}\,. \tag{3.41}$$

Consequently, the radius of the star is then given by

$$R = a\eta_1\,. \tag{3.42}$$

The foregoing expression shows that the radius of a degenerate star is obtained *a posteriori*. In this case, indeed, we do not need to spatially bind the gas within a box because the Fermi energy provides a natural self-confinement of the gas. To see it, suppose that the fermionic system is confined within a box of radius $R_b > R$ [where R is obtained from Eq.(3.42)]. Since the density profile (3.39) vanishes at the point $r = R$, the space between R and R_b is empty, making useless the utilization of an external

box. Vice-versa, if $R_b < R$, the density profile does not vanish. Consequently the distribution of matter is modified and confined within an "artificial" box (see Appendix E for more details).
The mass M of the star is obtained by integrating Eq.(3.40) at $r = R$ (or $\eta = \eta_1$). This yields

$$M = M_R = -4\pi a^3 B y_0^3 \Big(\eta^2 \frac{d\phi}{d\eta}\Big)_{\eta_1} . \tag{3.43}$$

If we introduce the characteristic radius, mass, particles number and density

$$R_* = \Big(\frac{2A}{\pi G}\Big)^{1/2} \frac{1}{B} = \Big(\frac{3}{32\pi^2}\Big)^{1/2} \frac{qh^{3/2}}{G^{1/2} m^2 c^{1/2}} = \Big(\frac{3}{32\pi^2}\Big)^{1/2} \Big(\frac{h^3}{Gc}\Big)^{1/2} \frac{1}{m\mu_e H} , \tag{3.44}$$

$$M_* = \frac{4\pi}{B^2}\Big(\frac{2A}{\pi G}\Big)^{3/2} = \Big(\frac{3}{32\pi^2}\Big)^{1/2} \frac{q^2 h^{3/2} c^{3/2}}{G^{3/2} m^2} = \Big(\frac{3}{32\pi^2}\Big)^{1/2} \Big(\frac{hc}{G}\Big)^{3/2} \frac{1}{(\mu_e H)^2} , \tag{3.45}$$

$$N_* = \frac{4\pi}{\mu H B^2}\Big(\frac{2A}{\pi G}\Big)^{3/2} = \Big(\frac{3}{32\pi^2}\Big)^{1/2} \frac{q^2 h^{3/2} c^{3/2}}{G^{3/2} m^2 \mu_e H} = \Big(\frac{3}{32\pi^2}\Big)^{1/2} \Big(\frac{hc}{G}\Big)^{3/2} \frac{1}{(\mu_e H)^3} , \tag{3.46}$$

$$\rho_* = B = \frac{8\pi m^4 c^3}{3qh^3} = \frac{8\pi m^3 c^3 \mu_e H}{3h^3} , \tag{3.47}$$

we can write the mass-radius relation in parametric form as

$$\frac{R}{R_*} = \frac{\eta_1}{y_0} , \qquad \frac{M}{M_*} = \Omega(y_0) = -\Big(\eta^2 \frac{d\phi}{d\eta}\Big)_{\eta_1} . \tag{3.48}$$

For a given value of $y_0 \geq 1$, we can solve the Chandrasekhar equation (3.38) until the normalized radius η_1, determined by the condition (3.41). We can then compute the dimensionless radius R/R_* and the dimensionless mass M/M_* according to Eq.(3.48). By varying y_0 from 1 to $+\infty$, we obtain the complete mass-radius relation $M = M(R)$ parameterized by y_0. The mass-radius relation of relativistic fermionic stars in Newtonian gravity is plotted in Fig. 3.1 (full line). The nonrelativistic and ultrarelativistic limits (see below) are also indicated for comparison. In addition, we note that

$$\frac{GM_*}{R_* c^2} = q , \qquad \rho_* = \frac{M_*}{4\pi R_*^3} , \qquad n_* = \frac{N_*}{4\pi R_*^3} = \frac{\rho_*}{\mu_e H} , \qquad N_* = \frac{M_*}{\mu_e H} . \tag{3.49}$$

Thanks to the first equality, we can give a second interpretation to the physical meaning of q. According to Eq.(3.49), indeed, q gives a measure of the importance of GR in the model. Small values of q imply weak gravitational fields, that is the system has recovered the Newtonian gravity. Values of q close to the unity, by contrast, indicate that the GR cannot be neglected.

Nonrelativistic limit ($x_0 \to 0$)

In the nonrelativistic limit $x_0 \to 0$ (or, equivalently, $y_0 \to 1$) the system is equivalent to a polytrope of index $n = 3/2$ [see Eq.(3.20)]. We can thus write

$$y_0 = \sqrt{1 + x_0^2} \simeq 1 + \frac{x_0^2}{2}\,, \tag{3.50}$$

where we have neglected terms of higher order. On the other hand, defining

$$\Theta = \phi^2 - \frac{1}{y_0^2} \tag{3.51}$$

we obtain

$$\phi \simeq 1 - \frac{1}{2}(x_0^2 - \Theta)\,. \tag{3.52}$$

By combining Eqs.(3.38) and (3.52), we derive the following differential equation

$$\frac{1}{2}\frac{1}{\eta^2}\frac{d}{d\eta}\Big(\eta^2\frac{d\Theta}{d\eta}\Big) = -\Theta^{3/2} \tag{3.53}$$

with the initial conditions $\Theta(0) = x_0^2$ and $\Theta'(0) = 0$. Now, introducing the variables $\theta = \Theta/x_0^2$ and $\xi = \sqrt{2x_0}\eta$, Eq.(3.53) reduces to

$$\frac{1}{\xi^2}\frac{d}{d\xi}\Big(\xi^2\frac{d\theta}{d\xi}\Big) = -\theta^{3/2} \tag{3.54}$$

with the conditions $\theta(0) = 1$, $\theta'(0) = 0$. This is the Lane-Emden equation for a polytrope of index $n = 3/2$. Using the results of Appendix B, we obtain the mass-radius relation

$$\frac{M}{M_*}\Big(\frac{R}{R_*}\Big)^3 = \frac{\omega_{3/2}}{8} \simeq 16.54804\,, \tag{3.55}$$

where we have used $\omega_{3/2} = 132.3843$. The radius R and the total mass M take the following asymptotic expressions[9]

$$\begin{aligned} \frac{R}{R_*} &\simeq \frac{\xi_1}{\sqrt{2x_0}}\,, \\ \frac{M}{M_*} &\simeq \frac{M_{3/2}}{\sqrt{8}}x_0^{3/2}\,. \end{aligned} \tag{3.56}$$

Ultrarelativistic limit ($x_0 \to +\infty$)

Analogous to the nonrelativistic limit, a simplified treatment can be obtained in the ultrarelativistic limit too. Defining $\theta = \phi$ and $\xi = \eta$, the Chandrasekhar equation (3.38), for $y_0 \to +\infty$, reduces to

[9] To obtain the equation for the mass we have substituted Eq.(3.52) in the second of Eqs.(3.48) and used the relation between ξ and η. $M_{3/2}$ is the total mass associated with the polytrope $n = 3/2$, which value is $M_{3/2} = 2.71406$.

$$\frac{1}{\xi^2}\frac{d}{d\xi}\Big(\xi^2\frac{d\theta}{d\xi}\Big) = -\theta^3 \tag{3.57}$$

with the conditions $\theta(0) = 1$, $\theta'(0) = 0$. This is the Lane-Emden equation for a polytrope of index $n = 3$. Using the results of Appendix B, we find that the radius vanishes ($R = 0$) and the mass is given by

$$\frac{M}{M_*} = \omega_3 \simeq 2.01824\,. \tag{3.58}$$

This is the Chandrasekhar limiting mass[10]. Thanks to the preceding results, the radius of the star (3.48) can be expressed as

$$\frac{R}{R_*} = \frac{6.89685}{y_0}\,, \tag{3.59}$$

where $\xi_1 = 6.89685$ is the radius of the polytrope $n = 3$. Eq.(3.59) shows that the radius vanishes in limit $y_0 \to \infty$. For what concerns the mass, numerically we find that, for $M/M_* \to \omega_3$

$$\frac{R}{R_*} \sim \Big(\omega_3 - \frac{M}{M_*}\Big)^{1/2}\,. \tag{3.60}$$

Thanks to Eq.(3.59), the foregoing expression can be rewritten as

$$\frac{M}{M_*} \sim \omega_3 - \frac{\xi_1^2}{y_0^2}\,. \tag{3.61}$$

which is represented in Fig. 3.2.

3.2.2. Dynamical Stability

We consider a self-gravitating gas with a barotropic equation of state $P = P(\rho)$, in Newtonian gravity, described by the Euler-Poisson equations [171]

$$\frac{\partial\rho}{\partial t} + \nabla\cdot(\rho\vec{u}) = 0\,, \tag{3.62}$$

$$\frac{\partial\vec{u}}{\partial t} + (\vec{u}\cdot\nabla)\vec{u} = -\frac{1}{\rho}\nabla P - \nabla\Phi\,, \tag{3.63}$$

$$\Delta\Phi = 4\pi G\rho\,. \tag{3.64}$$

The steady state of these equations satisfies the condition of hydrostatic equilibrium $\nabla P + \rho\nabla\Phi = \vec{0}$ which, for a spherically symmetric distribution, reduces to Eqs.(3.32). To determine the dynamical

[10]The existence of a limiting mass for WDs was originally argued by Anderson & Stoner [2, 177, 192, 31].

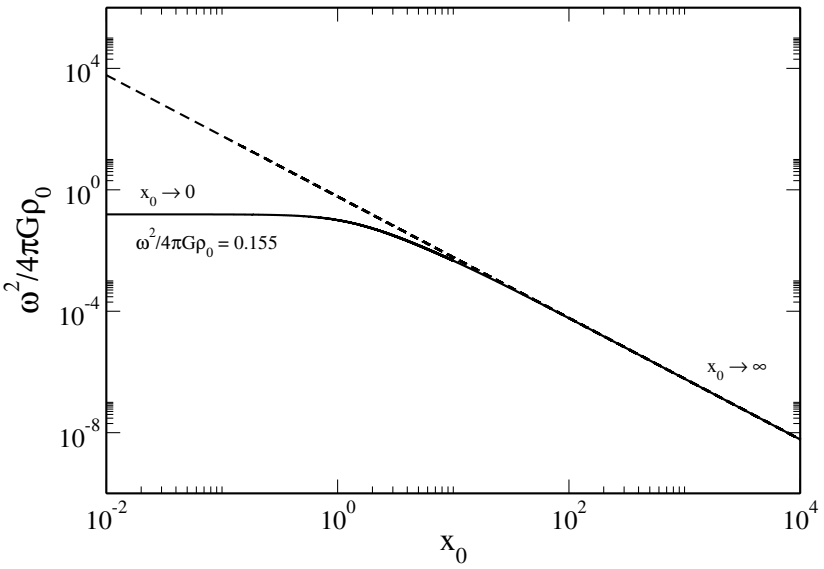

Figure 3.3: *Pulsation (expressed in terms of the dynamical time t_D) as a function x_0, for several degenerate self-gravitating fermionic configurations in Newtonian gravity, obtained from Eq.*(3.84). *The asymptotic expression* (3.90) *is represented by the dashed line.*

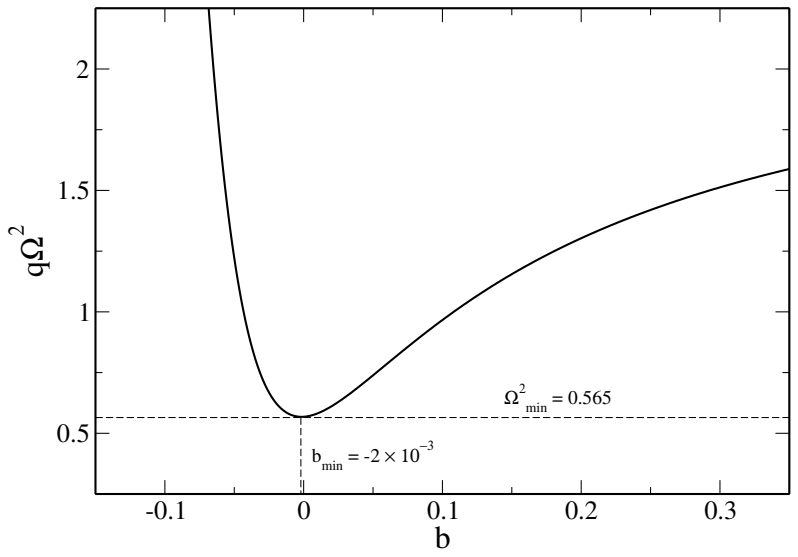

Figure 3.4: *An example of the minimization procedure, for $x_0 = 5$. The value $b = b_{min}$ is determined by the minimum value of Ω^2.*

stability of the system, we consider a small perturbation about equilibrium, linearize the equations of motion and write the temporal evolution of the perturbation as $e^{-i\omega t}$, where ω is the complex pulsation. Considering radial perturbations[11] and introducing the ratio $\xi \propto \delta r/r$ of the radial Lagrangian displacement to the radius, we can obtain the eigenvalue equation

$$\frac{d}{dr}\Big(P\gamma r^4\frac{d\xi}{dr}\Big) + r^3\xi\frac{d}{dr}\Big[(3\gamma-4)P\Big] = -\omega^2\rho r^4\xi\,, \tag{3.65}$$

where

$$\gamma(r) = \frac{d\ln P}{d\ln\rho} = \frac{\rho}{P}\frac{dP}{d\rho}\,, \tag{3.66}$$

is adiabatic local index[12] governing the perturbation [42, 171]. Eq.(3.65) is supplemented by the boundary conditions

$$\delta r = \xi r = 0 \qquad \text{at} \quad r = 0\,, \tag{3.67}$$

$$\delta P = -\gamma P\Big(3\xi + r\frac{d\xi}{dr}\Big) = 0 \qquad \text{at} \quad r = R\,, \tag{3.68}$$

where δP is the Lagrangian derivative of the pressure. Eq.(3.65) is the Eddington equation of radial adiabatic pulsations of a gaseous star [74]. This equation is self-adjoint and forms a Sturm-Liouville problem, which general form is [157, 97]

$$\frac{d}{dx}\Big[p(x)\frac{dy(x)}{dx}\Big] + q(x)y(x) = -\lambda w(x)y(x)\,, \tag{3.69}$$

with boundary conditions in a generic interval $[a, b]$. The functions $p(x)$, $q(x)$ and $w(x)$ are positive and specific for each model. Further, λ represents the eigenvalues (when they exist) of this equation. A direct comparison between Eq.(3.65) and Eq.(3.69) shows that the two expressions are equivalent if

$$\begin{aligned} &x = r\,, \qquad y(x) = \xi\,, \qquad p(x) = P\gamma r^4\,, \\ &q(x) = r^3\frac{d}{dr}\Big[(3\gamma-4)P\Big]\,, \qquad w(x) = \rho r^4\,, \qquad \lambda = \omega^2\,. \end{aligned} \tag{3.70}$$

From the theory of Sturm-Liouville problems, the system has a countably infinite number of eigenvalues ω_n^2 labeled by an integer n. All these eigenvalues are real and can be ordered as $\omega_0^2 < \omega_1^2 < ... < \omega_n^2 < ...$ with $\omega_n^2 \to +\infty$ as $n \to +\infty$. The eigenfunction $\xi_n(r)$ corresponding to the eigenvalue ω_n^2 has n nodes

[11] For a nonrotating barotropic star, only radial perturbations can induce dynamical instability (Antonov-Lebovitz theorem), see Ref.[7, 127, 26].

[12] Some authors refer to γ as the "ratio of the specific heat" because $\gamma = C_P/C_V$ [see also Eq.(B.22)]. C_P and C_P represent the specific heats of a fluid at constant pressure and volume, respectively.

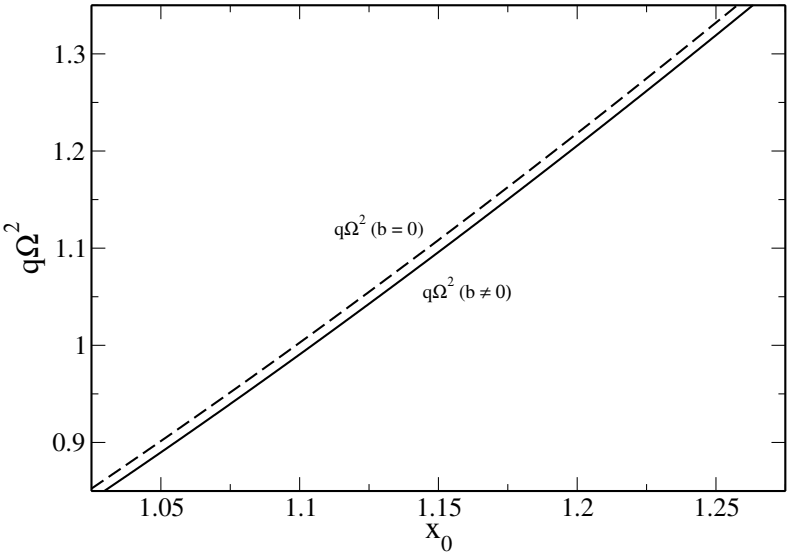

Figure 3.5: *Comparison between the minimization procedure and the application of Eq.*(3.72).

in the interval $[0, R]$, and the normalized eigenfunctions ξ_n form a complete set and can be taken to be orthonormal with the weighting function ρr^4 in the interval $[0, R]$.

The star is linearly dynamically stable if $\omega_0^2 > 0$ (the perturbed star oscillates, being $e^{-i\omega t}$) and unstable otherwise (a small disturbance grows exponentially with time, being $e^{\omega t}$). In the stable case, ω_0 represents the smallest pulsation (largest period). In the unstable case $\sqrt{-\omega_0^2}$ represents the largest growth rate.

It is possible to obtain an approximate analytical expression of the fundamental eigenvalue ω_0^2, valid for an arbitrary EOS $P = P(\rho)$, by using the method developed by Ledoux & Walraven in their investigation of stellar pulsations [129, 128, 92, 38]. Multiplying Eq.(3.65) by ξ and integrating between 0 and R, we obtain[13]

$$\omega^2 = \frac{\int_0^R P\gamma r^4 (\xi')^2 dr - \int_0^R r^3 [(3\gamma - 4)P]' \xi^2 dr}{\int_0^R \rho r^4 \xi^2 dr} \,. \tag{3.71}$$

From the theory of Sturm-Liouville problems, it is known that the above expression forms the basis of a variational principle. The function $\xi(r)$ minimizing the r.h.s. of Eq.(3.71) is the fundamental eigenfunction $\xi_0(r)$, and the minimum value of this expression gives the fundamental eigenvalue ω_0^2. Furthermore, any trial function overestimates the value of ω_0^2, so this variational principle may prove the existence of instability but can only give approximate information concerning stability. As shown by Ledoux & Walraven, we can get a good approximation of the fundamental eigenvalue by taking $\xi(r)$ to be a constant. For the trial function $\xi = \text{const}$ (homologous displacement), we get[14]

[13]Hereafter, when present, primes $'$ indicate the derivative with respect to the radial coordinate r.

[14]Note that $\xi = \text{const}$, i.e. $\delta r \propto r$, is the *exact* solution of the Sturm-Liouville equation (3.65) at the point of marginal

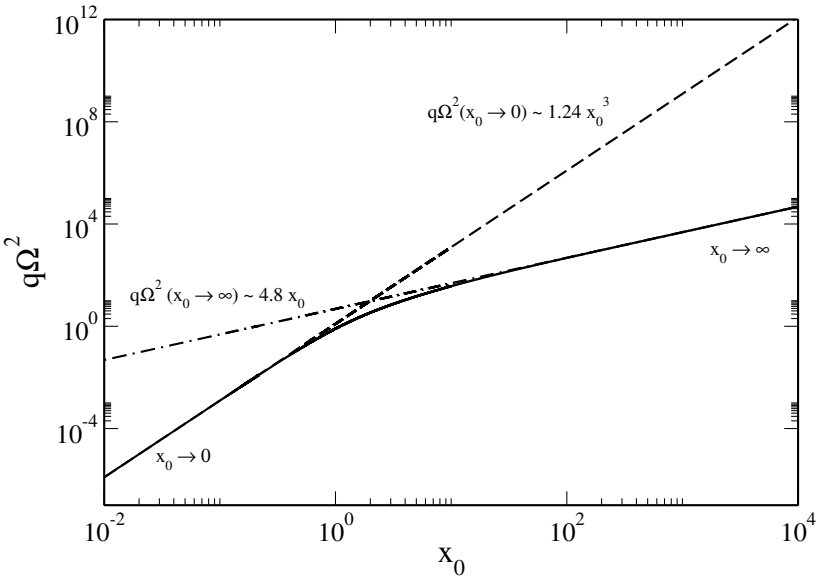

Figure 3.6: *Comparison among the rigourous solution* (3.80) *(full line) and the asymptotic expressions in nonrelativistic* (3.87) *(dashed line) and ultrarelativistic* (3.89) *(dash-dotted line) limits.*

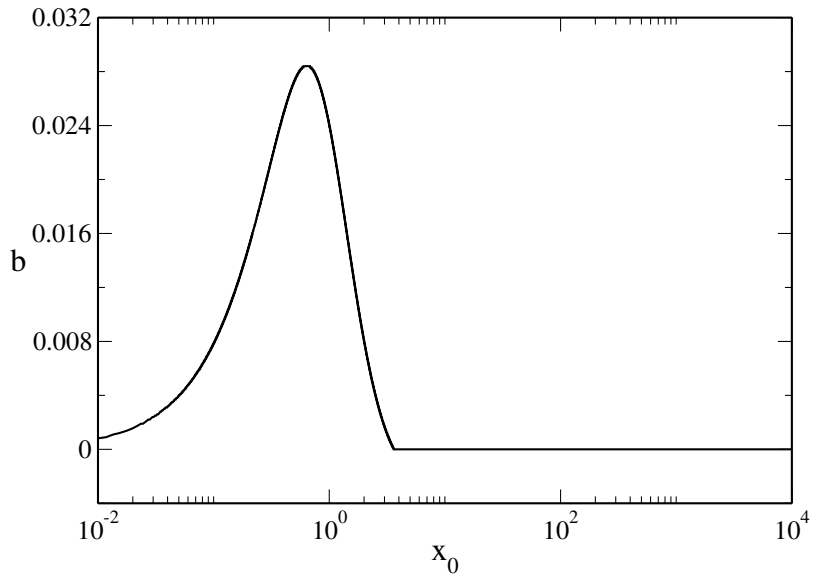

Figure 3.7: *Values of b obtained by means of the minimization procedure. As it can be noticed, the values are very small, by indicating that, in the Newtonian regime, the hypothesis of homologous displacement works quite well. The appearant discontinuity for $b = 0$ comes from the parametrization used in the generation of the values of b.*

$$\omega^2 = 9\frac{\int_0^R(\gamma - \frac{4}{3})Pr^2\,dr}{\int_0^R \rho r^4\,dr}\,, \tag{3.72}$$

where we have integrated by parts in the numerator. If we define the pressure averaged value of γ by

$$<\gamma>= \frac{\int_0^R \gamma P r^2\,dr}{\int_0^R Pr^2\,dr}\,, \tag{3.73}$$

the foregoing expression can be rewritten as

$$\omega^2 = 9\Big(<\gamma> - \frac{4}{3}\Big)\frac{\int_0^R Pr^2\,dr}{\int_0^R \rho r^4\,dr}\,. \tag{3.74}$$

Using the equilibrium virial theorem

$$W + 3\int P\,d^3\vec{r} = 0\,, \tag{3.75}$$

which can be derived from the condition of hydrostatic equilibrium, we can rewrite Eq.(3.74) as

$$\omega^2 = -(3<\gamma> - 4)\frac{W}{I}\,, \tag{3.76}$$

where

$$W = \frac{1}{2}\int \rho\Phi\,d^3\vec{r}, \qquad I = \int \rho r^2\,d^3\vec{r}, \tag{3.77}$$

are, respectively, the potential energy and the moment of inertia. Eq.(3.76) is the Ledoux formula [129]. As previously explained, the value ω^2 given by Eq.(3.76) is either equal or greater than the true value. It shows that the system is unstable if

$$<\gamma> < \gamma_{cr} = 4/3\,. \tag{3.78}$$

For a polytropic equation of state ($\gamma = \text{const}$), we see from Eq.(3.74) that the star is stable if $\gamma > 4/3$ since $dP/dr < 0$. Therefore, in this case, $\gamma < 4/3$ is a necessary and sufficient condition of instability. The previous equations are valid for an arbitrary equation of state $P = P(\rho)$. If we now specialize on the EOS (3.31) and introduce the normalized pulsation

$$\Omega = \frac{\omega}{\omega_*}\,, \qquad \omega_*^2 = \frac{4\pi^2}{3}\frac{Gm^4c^3}{h^3}\,, \tag{3.79}$$

we find that Eq.(3.72) can be written as

stability $\omega = 0$, for a polytropic equation of state ($\gamma = \text{const}$); see also Ref.[171].

$$\Omega^2 = 9\frac{y_0^2}{q}\frac{\int_0^{\eta_1}[\gamma(x) - \frac{4}{3}]f(x)\eta^2\,d\eta}{\int_0^{\eta_1} x^3\eta^4\,d\eta} \tag{3.80}$$

with

$$\gamma(x) = \frac{8x^5}{3f(x)\sqrt{1+x^2}}\,. \tag{3.81}$$

This can also be written as

$$\Omega^2 = \frac{9y_0^2}{q}\Big(< \gamma > -\frac{4}{3}\Big)\frac{\int_0^{\eta_1} f(x)\eta^2\,d\eta}{\int_0^{\eta_1} x^3\eta^4\,d\eta} \tag{3.82}$$

with

$$< \gamma >= \frac{\int_0^{\eta_1}\gamma(x)f(x)\eta^2\,d\eta}{\int_0^{\eta_1} f(x)\eta^2\,d\eta}\,. \tag{3.83}$$

We note that $\Omega^2 \propto 1/q$. If we measure the pulsation in terms of the dynamical time $t_D = (4\pi G\rho_0)^{-1/2}$, using the identity

$$\frac{\omega_*^2}{4\pi G\rho_0} = \frac{q}{8x_0^3}\,, \tag{3.84}$$

we obtain

$$\frac{\omega^2}{4\pi G\rho_0} = \frac{q\Omega^2}{8x_0^3} = \frac{9}{8}\frac{y_0^2}{x_0^3}\frac{\int_0^{\eta_1}[\gamma(x) - \frac{4}{3}]f(x)\eta^2\,d\eta}{\int_0^{\eta_1} x^3\eta^4\,d\eta}. \tag{3.85}$$

We note that $\omega^2/4\pi G\rho_0$ is independent of q. At the same time we have performed a second stability analysis, by means of a different choice of the function $\xi(r)$. We have used $\xi(r) = 1 + br^2$ [43], where b is a coefficient to be minimized (see also Fig. 3.4). In Fig. 3.5 we have represented a comparison between the application of Eq.(3.80) and the minimization procedure. As above explained, for $b = 0$ it is evident a (small) overestimation of the pulsation frequency.

Nonrelativistic limit ($x_0 \to 0$)

The star is equivalent to a polytrope of index $\gamma = 5/3$ and, since $\gamma > 4/3$, the configuration is stable. Using Eq.(B.11) (see Appendix B), the fundamental pulsation is given by

$$\frac{\omega^2}{4\pi G\rho_0} = \frac{6}{7}\frac{\omega_{3/2}^2}{\xi_1^7\int_0^{\xi_1}\theta^{3/2}\xi^4\,d\xi} = \frac{6}{5}\frac{\int_0^{\xi_1}\theta^{5/2}\xi^2\,d\xi}{\int_0^{\xi_1}\theta^{3/2}\xi^4\,d\xi} \simeq 0.155 \tag{3.86}$$

Using the identity (B.11), we have

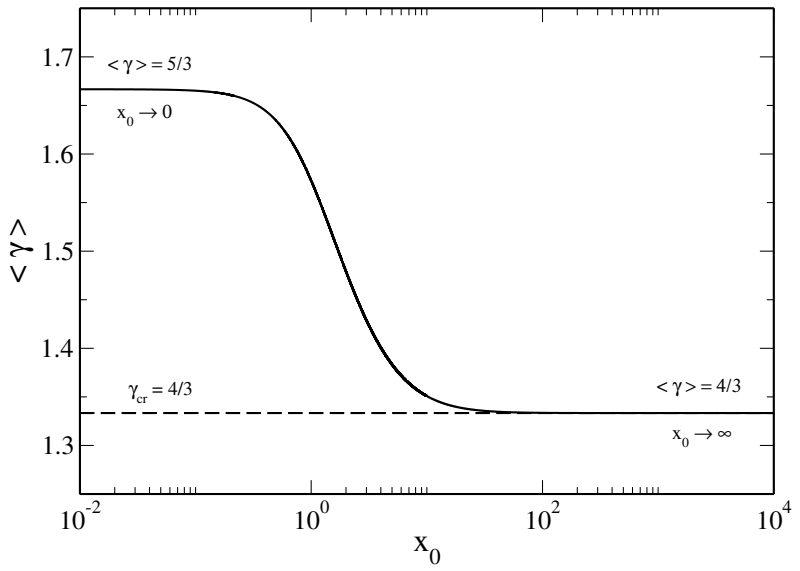

Figure 3.8: $< \gamma >$, *as a function of* x_0, *compared with* $\gamma_{cr} = 4/3$ *[see Eq.*(3.78)*]. As discussed in the text, being* $< \gamma >> \gamma_{cr}$, *Newtonian configurations are dynamically stable. This is not anymore true in the ultrarelativistic limit, being* $< \gamma >< \gamma_{cr}$. *In this case the system is marginally stable.*

$$\Omega^2 = \frac{48}{7}\frac{x_0^3}{q}\frac{\omega_{3/2}^2}{\xi_1^7 \int_0^{\xi_1} \theta^{3/2}\xi^4\, d\xi} = \frac{48 x_0^3}{5q}\frac{\int_0^{\xi_1} \theta^{5/2}\xi^2\, d\xi}{\int_0^{\xi_1} \theta^{3/2}\xi^4\, d\xi} \simeq \frac{1.24 x_0^3}{q} \tag{3.87}$$

The last relation can also be obtained from Eq.(3.82), by using $\gamma \to 5/3$, $f(x) \sim 8x^5/5$ and the variables define in Sec. 3.2.1.

Ultrarelativistic limit ($x_0 \to +\infty$)

The star is equivalent to a polytrope of index $\gamma = 4/3$ implying that the configuration is marginally stable ($\omega = 0$). Since the central density $\rho_0 \to +\infty$ as $M \to M_{max}$, Eq.(3.85) yields $\omega^2/4\pi G\rho_0 = 0$. To raise this indetermination, let us consider Eq.(3.82) in the limit $x \to +\infty$. We have

$$f(x) \sim 2x^4\,, \qquad \gamma(x) - \frac{4}{3} \sim \frac{2}{3x^2}\,. \tag{3.88}$$

Substituting the approximated expressions (3.88) into Eq.(3.82) and introducing the variables of Sec. 3.2.1, we obtain

$$\Omega^2 \sim \frac{12 y_0}{q}\frac{\int_0^{\xi_1} \theta^2\xi^2\, d\xi}{\int_0^{\xi_1} \theta^3\xi^4\, d\xi} = \frac{24}{5q} y_0\,. \tag{3.89}$$

Using the identity (3.84), we get

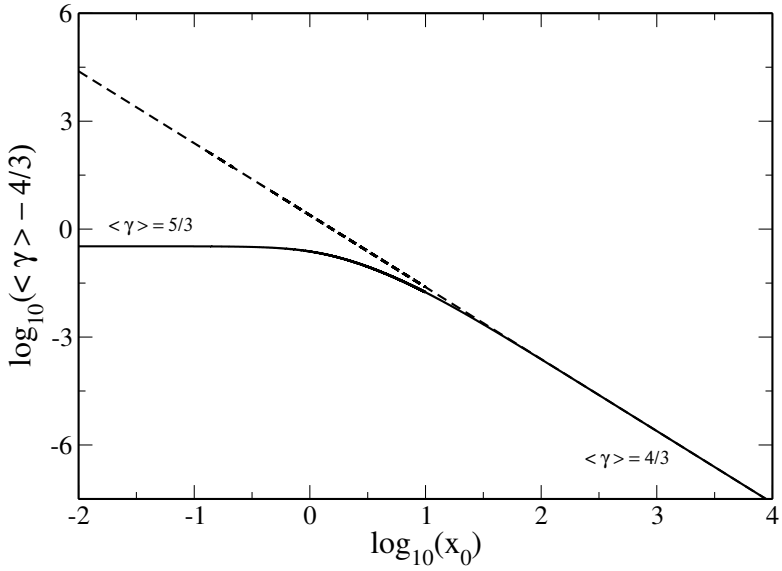

Figure 3.9: *Comparison between the exact solution* (3.83) *(full line) and the approximate expression* (3.91) *(dashed line) obtained in the ultrarelativistic regime.*

$$\frac{\omega^2}{4\pi G\rho_0} \sim \frac{3}{2y_0^2}\frac{\int_0^{\xi_1}\theta^2\xi^2\,d\xi}{\int_0^{\xi_1}\theta^3\xi^4\,d\xi} = \frac{3}{5y_0^2}\,. \tag{3.90}$$

Eq.(3.90) shows that the pulsation measured in terms of the dynamical time is infinitesimal as $M \to M_{\rm max}$. By contrast, Eq.(3.89) shows that the pulsation measured in terms of an intrinsic time[15] [defined in terms of fundamental constants, see Eq.(3.79)], $t_* = 2\pi/\omega_* \sim 840$ s, diverges as $M \to M_{\rm max}$. Moreover, by means of the relations (3.88), $<\gamma>$ takes the asymptotic expression

$$<\gamma> \simeq \frac{4}{3} + \frac{2}{3y_0^2}\frac{\int_0^{\xi_1}\theta^2\xi^2\,d\xi}{\int_0^{\xi_1}\theta^4\xi^2\,d\xi} = \frac{4}{3} + \frac{2.442}{y_0^2} = \frac{4}{3}\Big(1 + \frac{1.832}{y_0^2}\Big) \tag{3.91}$$

3.2.3. Series of Equilibria and Poincaré Theorem

We introduce the free energy

$$F = U + W\,, \tag{3.92}$$

where U and W are the internal and gravitational (potential) energies, respectively, of the star [190]

$$U = \int u\,d^3\vec{r}, \qquad \text{with} \qquad u = \rho\int_0^{\rho}\frac{P(\rho')}{\rho'^2}\,d\rho'\,, \tag{3.93}$$

[15] To evaluate this intrinsic time, we have considered the electron mass $m_e = 9.109 \times 10^{-28}$ g.

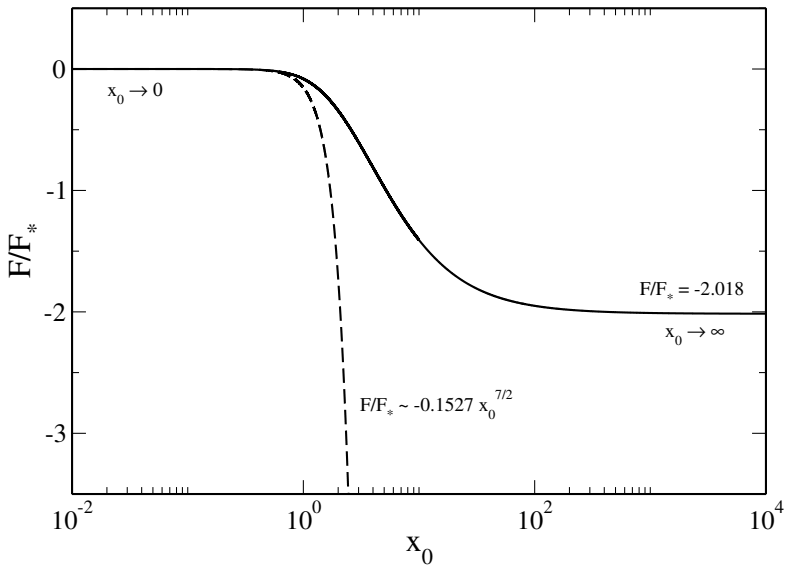

Figure 3.10: *Free energy as a function of* x_0*. The dosh-datted line represents the approximate solution* (3.102) *obtained in the nonrelativistic regime. The asymptotic value obtained in the ultrarelativistic regime [see Eq.*(3.107)*] is also indicated.*

$$W = \frac{1}{2}\int \rho\Phi\, d^3\vec{r} = -2\pi G \int_0^R M_r \rho r dr\,. \tag{3.94}$$

The free energy (3.92) is a conserved quantity by the Euler-Poisson equations (3.62)-(3.64), such as the mass. As a result, a minimum of free energy at fixed mass (or particle number N, since $M = Nm$) determines a steady state of the Euler-Poisson equations that is dynamically stable. By means of Lagrange multipliers, the first variations are given by $\delta F - \alpha\delta M = 0$, which returns the condition of hydrostatic equilibrium $\nabla P + \rho\nabla\Phi = \vec{0}$. Then, we have to make sure that the critical point is a true minimum of free energy at fixed mass. This is the case if $\delta^2 F > 0$ for all variations $\delta\rho$ that conserve the mass, i.e. $\delta M = 0$.

Using the Poincaré theorem, a change of stability can occur only at a turning point of mass along the series of equilibria $M = M(R)$. Since the series of equilibria of Newtonian fermion stars does not present turning point, and since the configurations with small mass and large radii are stable (they are polytropes of index $\gamma = 5/3 > \gamma_c$), we conclude that the whole series of equilibria is stable. Actually, the point $(R = 0, M = M_{\rm max})$ corresponding to the maximum mass can be seen as a singular turning point (see the general relativistic treatment in Sec. 3.3.4). This is why it is marginally stable. We introduce the characteristic free energy

$$F_* = \frac{GM_*^2}{R_*} = \frac{32\pi A}{B^3}\Big(\frac{2A}{\pi G}\Big)^{3/2} = \Big(\frac{3}{32\pi^2}\Big)^{1/2}\Big(\frac{hc}{G}\Big)^{3/2}\frac{mc^2}{(\mu H)^3}. \tag{3.95}$$

Using Eq.(3.9), we obtain

$$\frac{U}{F_*} = \frac{1}{8y_0^3}\int_0^{\eta_1} g(x)\eta^2\, d\eta\,. \tag{3.96}$$

To compute the potential energy, we can use Eq.(3.39) together with the relation (3.40). This yields

$$\frac{W}{F_*} = y_0\int_0^{\eta_1} \eta^3 \frac{d\phi}{d\eta}\Big(\phi^2 - \frac{1}{y_0^2}\Big)^{3/2}\, d\eta\,. \tag{3.97}$$

Actually, there exists the following relation between the internal energy and the potential energy (recalling that the internal energy reduces here to the kinetic energy of microscopic motion, this can be viewed as the virial theorem for a relativistic system of degenerate fermions)

$$U = -\frac{5}{3}W - \frac{GM^2}{R}\,. \tag{3.98}$$

Using Eq.(3.48), we obtain

$$\frac{U}{F_*} = -\frac{5}{3}\frac{W}{F_*} - \Omega^2(y_0)\frac{y_0}{\eta_1}\,. \tag{3.99}$$

From these relations, we can compute the free energy

$$\frac{F}{F_*} = \frac{U}{F_*} + \frac{W}{F_*} = -\frac{1}{12y_0^3}\int_0^{\eta_1} g(x)\eta^2 d\eta - \frac{y_0}{\eta_1}\Omega^2(y_0)\,, \tag{3.100}$$

which is represented in Fig. 3.10.

Nonrelativistic limit ($x_0 \to 0$)

In this case, using Eqs.(B.8) and (B.20), we obtain

$$W = -\frac{6}{7}\frac{GM^2}{R}\,, \qquad U = -\frac{W}{2} = \frac{3}{7}\frac{GM^2}{R}\,, \qquad F = \frac{W}{2} = -\frac{3}{7}\frac{GM^2}{R}\,. \tag{3.101}$$

The relation $2U + W = 0$ corresponds to the nonrelativistic virial theorem. Introducing normalized quantities and using the mass-radius relation (3.55), we obtain

$$\frac{F}{F_*} = -\frac{3\Omega^2}{7\eta_1} \simeq \frac{3\sqrt{2}M_{3/2}^2}{56\xi}x_0^{7/2} = 0.1527\, x_0^{7/2}\,, \tag{3.102}$$

where we used Eq.(3.56).

Ultrarelativistic limit ($x_0 \to +\infty$)

In this case, using Eqs.(B.8) and (B.20), we obtain

$$W = -\frac{3}{2}\frac{GM^2}{R}\,, \qquad U = -W = \frac{3}{2}\frac{GM^2}{R}\,, \qquad F = 0\,. \tag{3.103}$$

The relation $U + W = 0$ corresponds to the ultrarelativistic virial theorem. To have an expression of free energy, let us start from its definition (3.100). Substituting the asymptotic expression (3.18) of $g(x)$ (obtained in the limit $x \to +\infty$) and using the variables defined in Sec. 3.2.1, we have

$$\frac{U}{F_*} \sim \frac{3}{4}y_0\int_0^{\xi_1}\theta^4\xi^2 d\xi - \int_0^{\xi_1}\theta^3\xi^2 d\xi + \frac{3}{4y_0}\int_0^{\xi_1}\theta^2\xi^2 d\xi\,. \tag{3.104}$$

On the other hand, the potential energy is

$$\frac{W}{F_*} \sim y_0\int_0^{\xi_1}\xi^3\theta'\theta^3 d\xi = -\frac{3}{4}y_0\int_0^{\xi_1}\theta^4\xi^2 d\xi\,, \tag{3.105}$$

where in the last passage we have integrated by parts. Substituting Eqs.(3.104) and (3.105) in (3.100), we obtain

$$\frac{F}{F_*} = -\int_0^{\xi_1}\theta^3\xi^2 d\xi + \frac{3}{4y_0}\int_0^{\xi_1}\theta^2\xi^2 d\xi\,, \tag{3.106}$$

In the limit $y_0 \to \infty$, finally, we have

$$\frac{F}{F_*} = -\int_0^{\xi_1}\theta^3\xi^2 d\xi = -2.018\,. \tag{3.107}$$

The preceding result can be seen as a correction to the ultrarelativistic virial theorem. In Fig. 3.10 we have shown the free energy as a function of x_0. As the reader can notice the free energy is always negative.

3.3. The General Relativistic Regime: Oppenheimer - Volkoff Limit

3.3.1. Gravitational Equilibrium

As we have seen in Sec. 2.1, the equations determining the condition of hydrostatic equilibrium of a self-gravitating spherically symmetric distribution of matter are the TOV equations (2.17)

$$\begin{aligned}\frac{dP}{dr} &= -\frac{G}{c^4}\frac{(M_r c^2 + 4\pi P r^3)(P+\epsilon)}{r^2}\Big(1 - \frac{2GM_r}{rc^2}\Big)^{-1}\,,\\ \frac{dM_r}{dr} &= \frac{4\pi\epsilon r^2}{c^2}\,,\end{aligned} \tag{3.108}$$

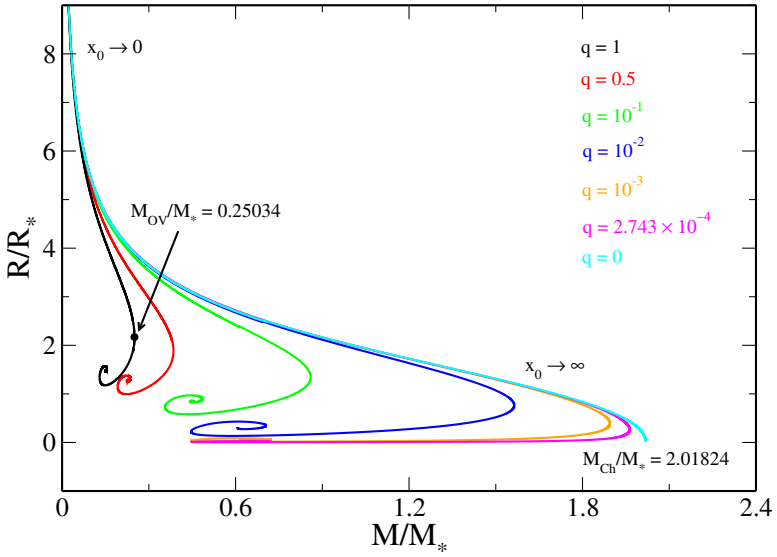

Figure 3.11: *Mass-radius relation for different values of q. In the limits $x_0 \to 0$ and $x_0 \to +\infty$ the curves recover the limiting cases studied in Sec. 3.2.1. The relativistic corrections have the effect of changing the nature of the mass-radius relation, which becomes a spiral. Differently from the Newtonian gravity, if $q \neq 0$ the curves are characterized by a limiting configuration, where the mass (radius) takes its highest (smallest) value. The Chandrasekhar (M_{Ch}) and the Oppenheimer-Volkoff (M_{OV}) limits are also indicated.*

with the following boundary conditions[16]

$$P(0) = P_0\,, \qquad M_r(0) = 0\,, \qquad e^{\nu(R)} = 1 - \frac{2GM}{Rc^2}\,. \tag{3.109}$$

The last boundary condition (3.109) is chosen so that e^{ν} is continuous with the exterior solution. Analogous to the hydrostatic equilibrium in Newtonian gravity, the TOV system can be solved if there exists a functional relation of the form $P = P(\epsilon)$, i.e. an EOS. For a relativistic degenerate Fermi gas, the EOS is determined by Eqs.(3.31)

$$\rho c^2 = \frac{8A}{q}x^3\,, \qquad P = Af(x)\,, \qquad \epsilon = \rho c^2 + u = \frac{8A}{q}\left[x^3 + \frac{1}{8}qg(x)\right], \tag{3.110}$$

where A and q are defined by Eqs.(3.30) and (3.28), respectively. Introducing the variables

$$r = a_{rel}\eta\,, \qquad a_{rel} = \frac{qc^2}{(32\pi GA)^{1/2}} = ay_0\,, \qquad v = \frac{GM(r)}{qc^2 a_{rel}}\,, \qquad y = \sqrt{x^2+1}\,, \tag{3.111}$$

[16]Here M_r indicates the mass-energy of the system at distance r from the centre of the configuration and M the total mass energy of the system. The rest mass of the system corresponds to $N\mu_e H$, where N is the baryon number [see Eq.(2.21)]. However, in the following, we refer to M_r or M simply as the mass.

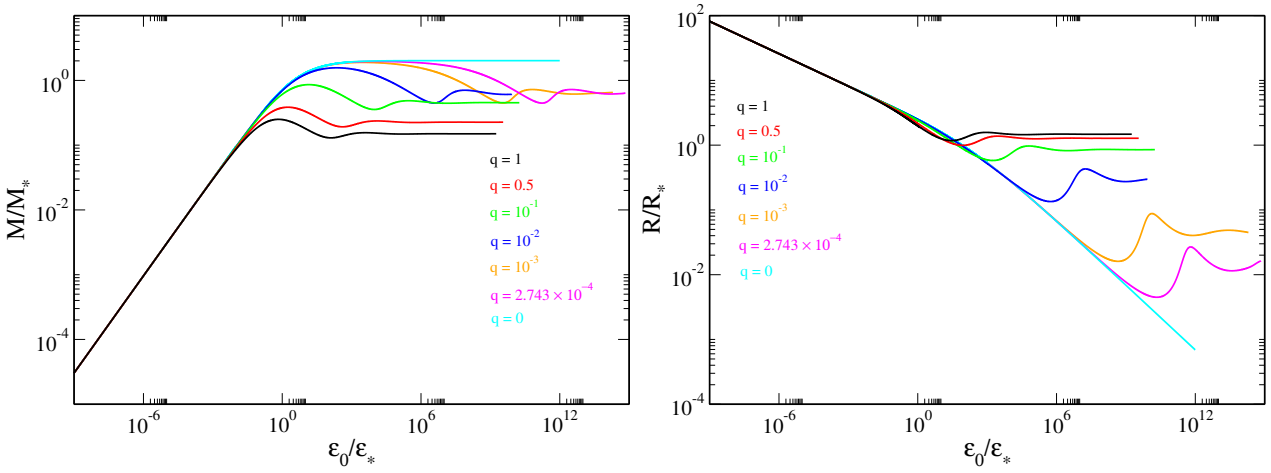

Figure 3.12: ***Left Panel***: *Total mass versus the central energy density, for several values of q. The curves present several oscillations, more and more damped in the limit* $\epsilon_0/\epsilon_* \to +\infty$. *As we have seen in the preceding figure, the GR has the effect to decrease the value of the limiting mass. For small values of q the peak related to the maximal mass is less and less pronounced (the system recovers the Newtonian behaviour, and the maximal mass is replaced by the asymptotic Chandrasekhar limit* $M/M_* = \omega_3$, *see Sec. 3.2.1).* ***Right Panel***: *Total radius versus the central energy density, for several values of* q. *Analogous to the case of the maximal mass, the curves present several oscillations, related to the turning points of the spirals represented in Fig. 3.11.*

[a is defined by Eq.(3.37)] the TOV system (3.108) can be reduced to the pair of equations

$$\begin{aligned} \frac{dy}{d\eta} &= -\frac{1+q(y-1)}{\eta^2}\left[v+\frac{q\eta^3 f(x)}{8}\right]\left(1-\frac{2qv}{\eta}\right)^{-1}, \\ \frac{dv}{d\eta} &= \eta^2\left[x^3+\frac{qg(x)}{8}\right]. \end{aligned} \tag{3.112}$$

with the conditions $y(0) = y_0 > 1$ (or equivalently $x_0 > 0$) and $v(0) = 0$. The coefficients of the metric are given by

$$e^{\lambda} = \left(1-\frac{2qv}{\eta}\right)^{-1}, \qquad e^{\nu} = \frac{1-2qv_1/\eta_1}{[1+q(y-1)]^2}, \tag{3.113}$$

(for η_1 and v_1 see below). Eqs.(3.112) are the CT equations[17] [43], which depend on q. The solutions of this system will be studied at varying the values of this parameter within the interval $[0, 1]$. To obtain the mass-radius relation we can proceed as follows. For a given value of y_0, we can solve Eqs.(3.112) until the point η_1 at which the density vanishes [i.e. $y(\eta_1) = 1$]. The radius and the mass of the star

[17] To obtain these equations we have used the identities $f'(x) = 8x^4/(1+x^2)^{1/2}$ and $f(x)+g(x) = 8x^3[(1+x^2)^{1/2}-1]$.

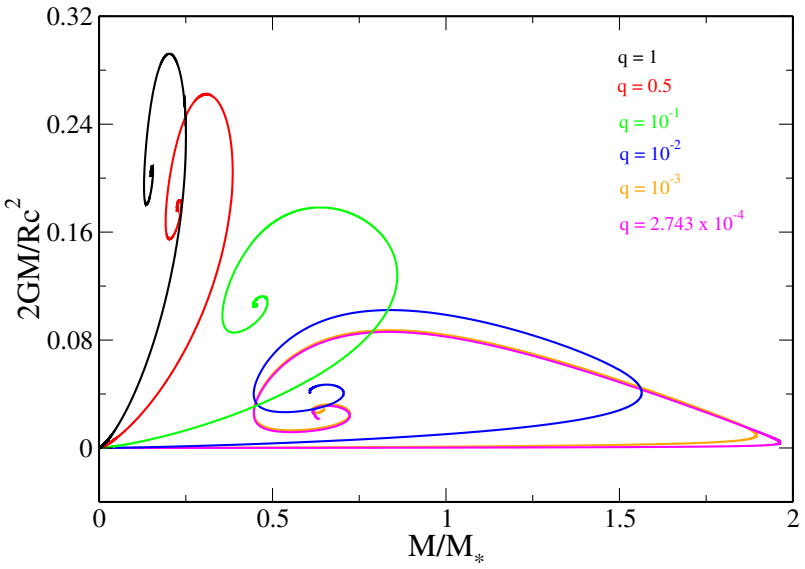

Figure 3.13: *Relativistic parameter as a function of the total mass, for several values of q. This figure displays the importance of the relativistic effects. It is interesting to note that, for $q = 1$ we reach $2GM/Rc^2 \simeq 0.29$, which is lower than Buchdahl limit $2GM/Rc^2 = 8/9$ [34]. In the Newtonian limit the relativistic parameter vanishes [see Eq.(3.49)].*

are then given by $R/a_{rel} = \eta_1$ and $GM/qc^2 a_{rel} = v_1$, where $v_1 = v(\eta_1)$. Introducing the characteristic values of the radius and the mass given in Sec. 3.2.1, we get

$$\frac{R}{R_*} = \eta_1 \,, \qquad \frac{M}{M_*} = v_1 \,. \tag{3.114}$$

These identities imply

$$R_* = a_{rel} \,, \qquad M_* = \frac{qc^2 a_{rel}}{G} \,, \qquad N_* = \frac{M}{\mu_e H} = \frac{qc^2 a_{rel}}{G\mu_e H} \,. \tag{3.115}$$

By varying y_0 between 1 and $+\infty$, we can obtain the mass-radius relation $M = M(R)$. We note that [see also Eq.(3.49)]

$$\frac{2GM}{Rc^2} = \frac{2qv_1}{\eta_1} \,. \tag{3.116}$$

The maximum mass is

$$\frac{GM_{max}}{qc^2 a_{rel}} = v_1^{\rm crit}(q) \equiv v[\eta_1(y_0^{\rm crit})] \tag{3.117}$$

The Newtonian treatment is recovered for $q \to 0$ [remember Eq.(3.49)]. In fact, in this case, Eqs.(3.112) reduce to

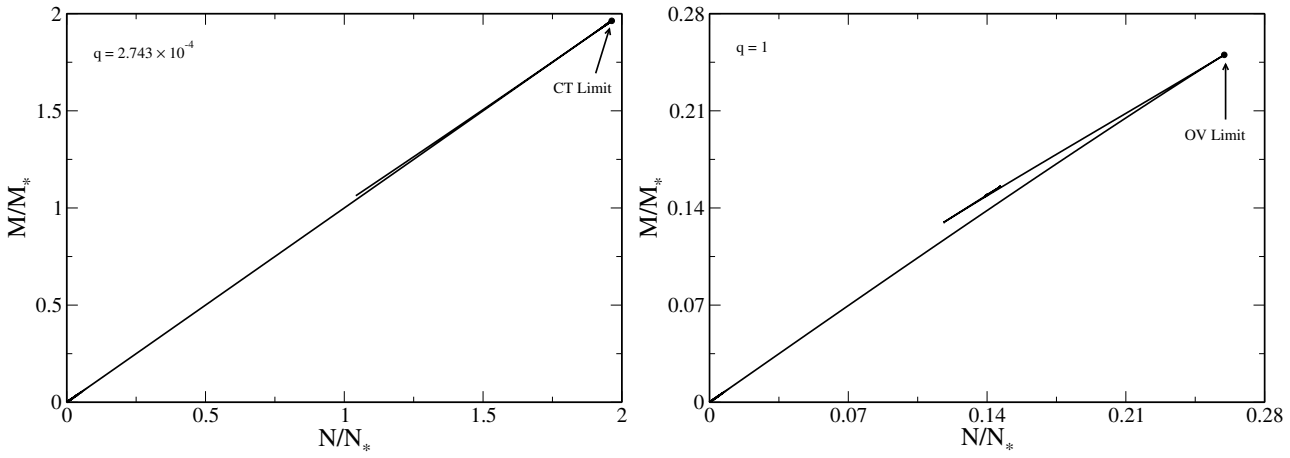

Figure 3.14: *Total mass versus the baryon number, for* $q = 2.743 \times 10^{-4}$ *(left panel) and* $q = 1$ *(right panel). The figures give a representation of the binding energy* E_b *of the system, defined as* $E_b = (N\mu H - M)c^2$ *[see Eq.*(3.143)*]. For small values of* M/M_* *and* N/N_**, we have that* $E_b \to 0$ *(not surprising, because in the Newtonian limit* $M = Nm$*). Once reached the limiting configuration, the curves decrease until a minimum value of* N/N_* *and then they begin to oscillate (in left panel this is less evident). This part of the curve corresponds to the winding of the spiral in the mass-radius relation (see Fig. 3.11).*

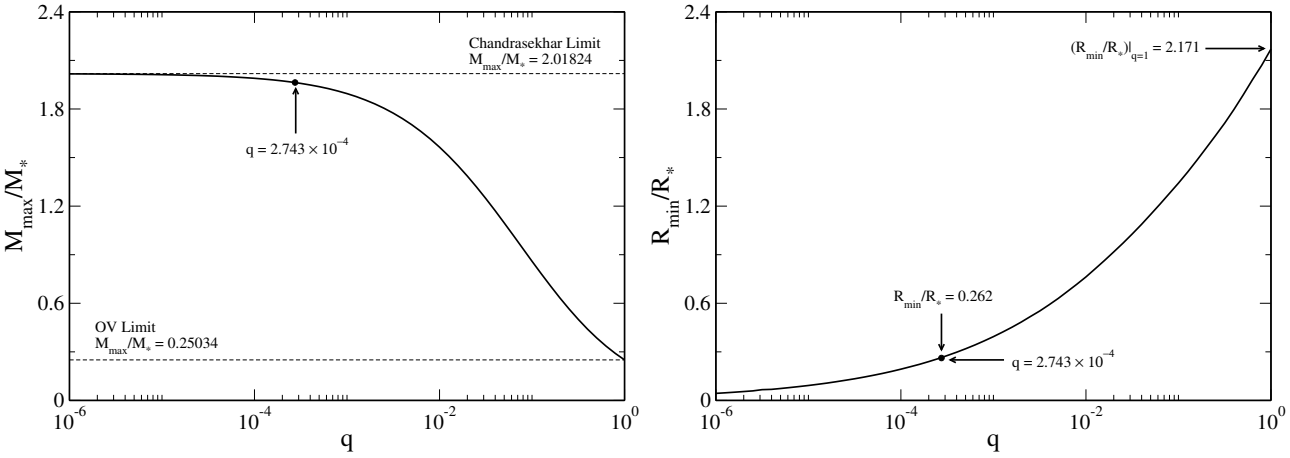

Figure 3.15: ***Left Panel****: Maximum mass (evaluated at the critical point) versus* q*. When the system recovers the Newtonian behaviour, the limiting mass (which is a critical value) becomes an asymptotic value (Chandrasekhar limit). This corresponds to the disappearance of the turning point for* $q \to 0$*.* ***Right Panel****: Minimal radius (evaluated at the critical point) versus* q*. In the Newtonian limit* $q \to 0$ *the values of* R_{min} *is infinitesimal, in accordance with Eq.*(3.59)*.*

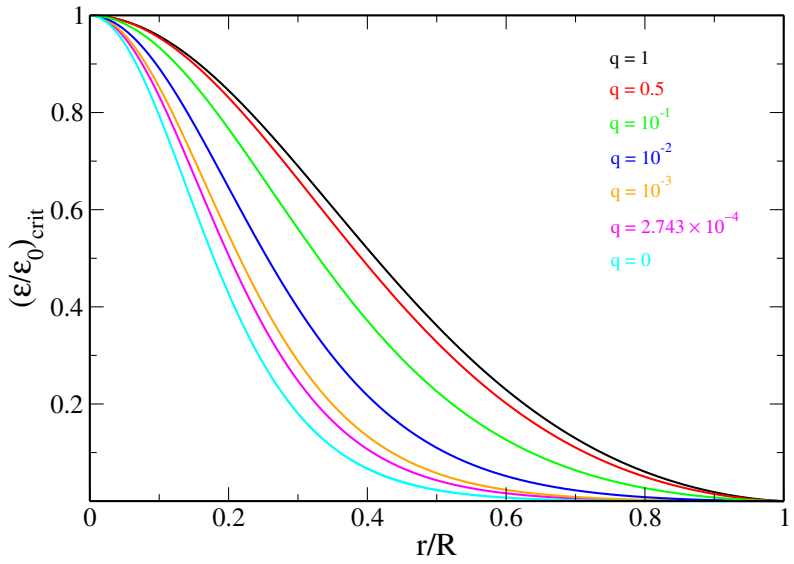

Figure 3.16: *Density profiles (evaluated at the critical point) as a function of the normalized radial coordinate $r/R = \eta/\eta_1$. The trend of the curve shows that, for increasing value of q, the distribution of the matter is more "homogeneous" than the case $q = 0$ (cyan line). Newtonian configurations (small values of q) present density profiles more peaked towards the center.*

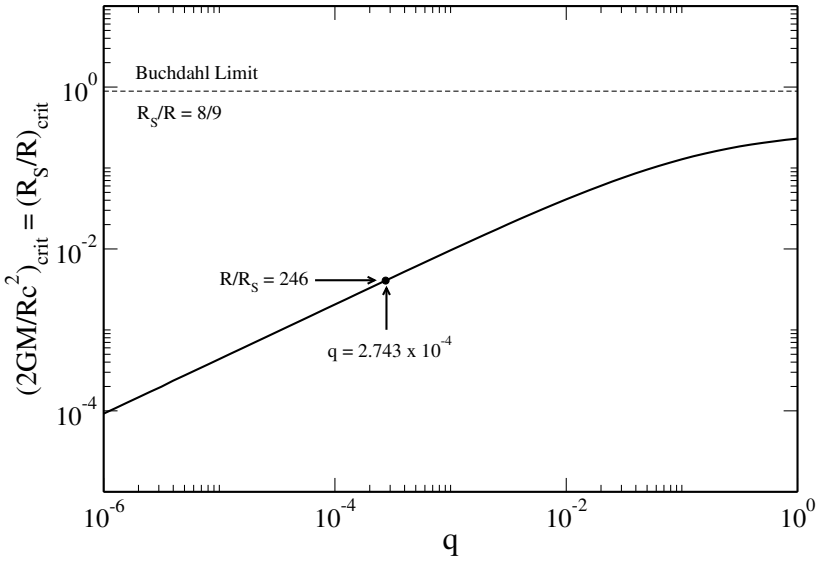

Figure 3.17: *Relativistic parameter (corresponding to the inverse of the ratio R_S/R, being R_S the Schwarzschild radius), evaluated at the turning point, as a function of* q. *The value obtained by Chandrasekhar & Tooper and the Buchdahl limit (dashed line) are also indicated. In the Newtonian limit we see that $R_S/R \propto q^\gamma$, where $\gamma = 2/3$ (see Sec. 3.4.1).*

$$\frac{dy}{d\eta} = -\frac{v}{\eta^2}\,, \qquad \frac{dv}{d\eta} = \eta^2 x^3\,, \tag{3.118}$$

and these equations can be combined to give

$$\frac{1}{\eta^2}\frac{d}{d\eta}\Big(\eta^2\frac{dy}{d\eta}\Big) = -(y^2-1)^{3/2} \tag{3.119}$$

with $y(0) = y_0$ and $y'(0) = 0$. Defining $y = y_0\phi$, we obtain

$$\frac{1}{\eta^2}\frac{d}{d\eta}\left(\eta^2\frac{d\phi}{d\eta}\right) = -y_0^2\left(\phi^2 - \frac{1}{y_0^2}\right)^{3/2} \tag{3.120}$$

with the conditions $\phi(0) = 1$ and $\phi'(0) = 0$. Apart from the presence of the factor y_0 [consequence of the different definition of η, see Eq.(3.111)], Eq.(3.120) corresponds to Eq.(3.38).

In Fig. 3.11 we have represented the mass-radius relation for several values of q. Differently from the Newtonian gravity (represented for comparison, see the cyan line in the figure), for any $q \neq 0$, the mass-radius relation shows the presence of a limiting configuration, where the mass (radius) achieves its maximum (minimum) value. This limiting configuration, as we shall see in the following, corresponds to the loss of the dynamical stability.

For increasing values of the central density, the spiral winds towards its center, where energy density ϵ_0 becomes infinite. For small values of x_0 all the curves recover the Newtonian behaviour. In particular, we mention two cases: one corresponding to $q = 2.743 \times 10^{-4}$ (that studied by Chandrasekhar & Tooper) which represents a helium WD; the other corresponds to $q = 1$ and represents a NS. The limiting configuration in this last case corresponds to the OV limit.

If, analogous to Fig. 3.11, we plot the baryon number as a function of radius for several values of q, we obtain a succession of spirals similar to those represented in Fig. 3.11. However, the spirals associated with the baryon number do not coincide with those associated with the mass-energy, because of the mass deficit of the body (see Sec. 2.1). In particular, let us discuss the $N = N(R)$ associated with $q = 1$. If we consider a line level (i.e. a particular value of N smaller than that of the OV limit) in the $N = N(R)$ diagram, we identify two solutions, one before and one after the turning point. Each solution represents, for the value of N considered, the limiting configuration of the ground state.

Consequently, a fermionic gas at $T \neq 0$ (for the same value of N), cannot never reach a value of the energy smaller than that of the ground state (for more details see Appendix D). This implies that the series of equlibria for $N < N_{OV}$ (see Chap. 5) will present an asymptote representing this limiting configuration. As we will see in the following (see Sec. 3.3.3), the solution before the OV limit is (dynamically) stable whereas that after unstable.

Fig. 3.12 shows the behaviour of the total mass and the total radius as a function of the central value of the energy density ϵ_0, for the same values of q listed in Fig. 3.11. The curves present a symmetrical trend. As the mass increases and achieves a maximum the radius, accordingly, decreases and reaches a minimum. After the critical point, both of types of curves present several oscillations, more and more damped when the value of the central density increases. This kind of diagram, as we shall see in Sec. 3.3.4, it is important to determine the stability by means of Poincaré Theorem.

In Fig. 3.13 we have represented the relativistic parameter $2GM/Rc^2$ (corresponding to the double of the compactness, see Sec. 4.2) as a function of the total mass of the system. As we see, relativistic configurations are placed on the left of the figure, where the relativistic parameter takes its highest values. The "degree of relativity" is high for configurations characterized by a large value of q whereas, for small values of q, the values of the relativistic parameter decrease. In the Newtonian limit $q \to 0$ we have $2GM/Rc^2 \to 0$ [remember Eq.(3.49)].

Fig. 3.14 represents the total mass as a function of the baryon number, for $q = 2.743 \times 10^{-4}$ and $q = 1$. As we will see in Appendix D, this kind of diagram is useful because allowing us to determine some characteristic values of the baryon number in the caloric curves (see Chap. 5).

Fig. 3.15 shows the behaviour of the mass and radius, evaluated at the critical point, as a function of q. As we see, the value of the mass for relativistic configurations is smaller than that achieved by Newtonian configurations. In the limit $q \to 0$ the system converges to the (asymptotic) Chandrasekhar mass and the mass-radius relation is that of a polytrope of index $n = 3$ [see Eq.3.61]. The minimal radius has an opposite behaviour compared to the limiting mass. It reaches its highest value for $q = 1$ and tends to zero according to Eq.(3.59) for small values of q.

The density profiles at the critical point are represented in Fig. 3.16. As we see, Newtonian configurations present a density profile more peaked at the center. The matter is not uniformingly distributed because largely concentrated within the sphere of radius $r \simeq R/2$. For increasing values of q, by contrast, the density profiles are smoother. Finally, in Fig. 3.17, we have represented the relativistic parameter evaluated at the critical point. As the reader can notice, for small values of q the relativistic parameter behaves as a power law of q whereas, for relativistic configurations, the curve reaches a "plateau". Moreover, all the values achieved by the relativistic parameter are lower than the Buchdahl limit [34].

3.3.2. Dynamical Stability

The equation of radial adiabatic pulsations in GR that replaces the Eddington equation of radial adiabatic pulsations in Newtonian gravity is the Chandrasekhar equation [42]

$$\sigma^2 e^{\lambda-\nu}(P+\epsilon)\zeta = \frac{4}{r}\frac{dP}{dr}\zeta - e^{-(\lambda+2\nu)/2}\frac{d}{dr}\Big[e^{(\lambda+3\nu)/2}\frac{\gamma P}{r^2}\frac{d}{dr}\Big(r^2 e^{-\nu/2}\zeta\Big)\Big] + \\ + \frac{8\pi G}{c^4}e^{\lambda}P(P+\epsilon)\zeta - \frac{1}{P+\epsilon}\Big(\frac{dP}{dr}\Big)^2\zeta\,, \tag{3.121}$$

where $\zeta = r\xi \propto \delta r$ is the radial Lagrangian displacement, $\sigma = \omega/c$ the pulsation, and

$$\gamma(r) = \frac{\rho}{P}\frac{dP/dr}{d\rho/dr} = \frac{d\ln P/dr}{d\ln\rho/dr} = \frac{P+\epsilon}{P}\frac{dP/dr}{d\epsilon/dr} \tag{3.122}$$

the "ratio of the specific heat" (or local adiabatic index) [18] Eq.(3.121) must be supplemented by the boundary conditions

$$\delta r = \zeta = 0 \qquad \text{at} \quad r = 0\,, \tag{3.123}$$

$$\delta P = -\gamma P\frac{e^{\nu/2}}{r^2}\frac{d}{dr}(r^2 e^{-\nu/2}\zeta) = 0 \qquad \text{at} \quad r = R\,, \tag{3.124}$$

where δP is the Lagrangian derivative of the pressure. In the Newtonian limit $q \to 0$, we have $\lambda = 0$, $\nu = 0$, and $\epsilon = \rho c^2$. Recalling that $\omega = \sigma c$, the Chandrasekhar equation (3.121) reduces to the form

$$\omega^2\rho\zeta = \frac{4}{r}\frac{dP}{dr}\zeta - \frac{d}{dr}\Big[\frac{\gamma P}{r^2}\frac{d}{dr}(r^2\zeta)\Big]\,. \tag{3.125}$$

Recalling that $\xi = r\zeta$, we can easily check that Eq.(3.125) is equivalent to the Eddington equation (3.65). Similarly, we can check that the boundary conditions (3.123)-(3.124) reduce to the boundary conditions (3.67)-(3.68). The Chandrasekhar equation (3.121), together with the boundary conditions (3.123) and (3.124), forms an eigenvalue problem for σ^2. This problem is self-adjoint and a variational base for determining σ^2 is provided by multiplying Eq.(3.121) by $r^2\zeta e^{(\lambda+\nu)/2}$ and integrating between 0 and R. This yields

$$\sigma^2\int_0^R e^{(3\lambda+\nu)/2}(P+\epsilon)r^2\psi^2\,dr = 4\int_0^R e^{(\lambda+3\nu)/2}P'\psi^2 r\,dr + \int_0^R e^{(\lambda+3\nu)/2}\frac{\gamma P[(r^2\psi)']^2}{r^2}dr + \\ + \frac{8\pi G}{c^4}\int_0^R e^{3(\lambda+\nu)/2}P(P+\epsilon)r^2\psi^2\,dr - \int_0^R e^{(\lambda+3\nu)/2}\frac{(P')^2r^2\psi^2}{P+\epsilon}\,dr\,, \tag{3.126}$$

where we have introduced the new function

$$\psi = e^{-\nu/2}\zeta\,. \tag{3.127}$$

[18] To get the last equality, we have used the first law of thermodynamics $d\epsilon/(P+\epsilon) = d\rho/\rho$ that is valid for a fluid at $T = 0$ or for an adiabatic fluid (see Ref.[139] and references therein).

The mathematical problem is similar to that described in Sec. 3.2.2. In particular, a sufficient condition of dynamical instability is that the right-hand side of Eq.(3.126) vanishes for some chosen trial function ψ which satisfies the boundary conditions. Before going further, it is convenient to rewrite Eq.(3.126) in a slightly different form. To that purpose, we need the identities (see Ref.[42])

$$\frac{dP}{dr} = -\frac{P+\epsilon}{2r}\Big(e^{\lambda} - 1 + \frac{8\pi G P r^2}{c^4} e^{\lambda}\Big)\,, \tag{3.128}$$

$$\frac{e^{-\lambda}}{r}\frac{d(\lambda+\nu)}{dr} = \frac{8\pi G}{c^4}(P+\epsilon)\,. \tag{3.129}$$

The first identity is obtained substituting Eq.(2.8) into Eq.(2.9). The second identity is obtained combining Eqs.(2.7) and (2.8) (see Sec. 2.1). Now, we substitute identity (3.128) in the last integral of Eq.(3.126). We integrate by parts the first integral on the right-hand side of Eq.(3.126) and use identities (3.129) and (2.8) to simplify the resulting expression. Finally, rearranging the terms, we find that Eq.(3.126) is equivalent to

$$\begin{aligned}
&\sigma^2 \int_0^R e^{(3\lambda+\nu)/2}(P+\epsilon)\psi^2 r^2\, dr = \int_0^R e^{(\lambda+3\nu)/2}\Big[\gamma(2\psi + r\psi')^2 - 4\psi(2r\psi' + \psi)\Big] P\, dr + \\
&-\frac{1}{4}\int_0^R e^{(\lambda+3\nu)/2}\Big[16P + (e^{\lambda}-1)(P+\epsilon)\Big](e^{\lambda}-1)\psi^2\, dr + \\
&-\frac{4\pi G}{c^4}\int_0^R e^{3(\lambda+\nu)/2}\Big[8P + (e^{\lambda}+1)(P+\epsilon)\Big] P\psi^2 r^2\, dr + \\
&-\frac{16\pi^2 G^2}{c^8}\int_0^R e^{(5\lambda+3\nu)/2}(P+\epsilon)P^2\psi^2 r^4\, dr\,.
\end{aligned} \tag{3.130}$$

We can obtain a simple approximate expression of the pulsation σ by choosing the trial function $\psi = Cr$ (C is a constant), which can be seen as the general relativistic equivalent of the trial function $\xi = \text{const}$ (see Sec. 3.2.2). With this trial function, we obtain

$$\begin{aligned}
&\frac{\sigma^2}{9}\int_0^R e^{(3\lambda+\nu)/2}(P+\epsilon) r^4\, dr = \int_0^R e^{(\lambda+3\nu)/2}\Big(\gamma - \frac{4}{3}\Big) P r^2\, dr + \\
&-\frac{1}{36}\int_0^R e^{(\lambda+3\nu)/2}\Big[16P + (e^{\lambda}-1)(P+\epsilon)\Big](e^{\lambda}-1) r^2\, dr + \\
&-\frac{4\pi G}{9c^4}\int_0^R e^{3(\lambda+\nu)/2}\Big[8P + (e^{\lambda}+1)(P+\epsilon)\Big] P r^4\, dr - \frac{16\pi^2 G^2}{9c^8}\int_0^R e^{(5\lambda+3\nu)/2}(P+\epsilon)P^2 r^6\, dr\,.
\end{aligned} \tag{3.131}$$

If we define the effective polytropic exponent [139]

$$<\gamma> = \frac{\int_0^R e^{(\lambda+3\nu)/2}\gamma P r^2\, dr}{\int_0^R e^{(\lambda+3\nu)/2} P r^2\, dr}\,, \tag{3.132}$$

the foregoing expression can be rewritten as

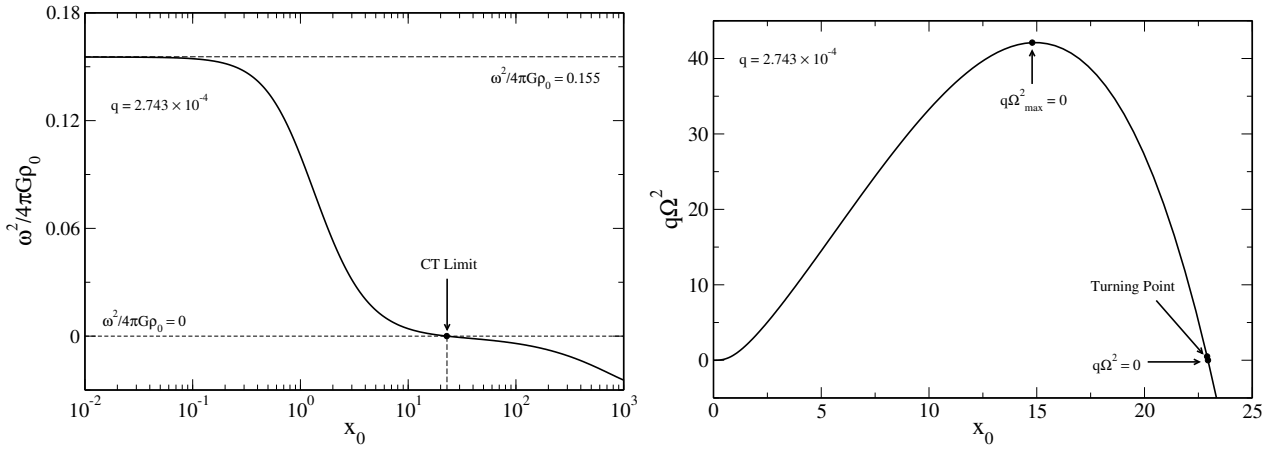

Figure 3.18: ***Left Panel****: Pulsation (expressed in terms of the dynamical time t_D) versus x_0, for $q = 2.743 \times 10^{-4}$ and $b = 0$. In the nonrelativistic limit, the curve reaches the asymptotic value* (3.86)*. At the turning point we have $x_0 = 22.803$ whereas $\omega^2/4\pi G\rho_0 = 0$ for $x_0 = 22.909$.* ***Right Panel****: Normalized pulsation $q\Omega^2$ versus x_0. The curve displays the presence of a maximum value $q\Omega^2_{max}$, diverging quantity in the Newtonian limit $q \to 0$ [see Eq.*(3.82)*].*

$$\sigma^2 = 9(<\gamma> - \gamma_{cr}) \frac{\int_0^R e^{(\lambda+3\nu)/2} P r^2 \, dr}{\int_0^R e^{(3\lambda+\nu)/2}(P+\epsilon) r^4 \, dr} \tag{3.133}$$

with [139]

$$\begin{aligned} \gamma_{cr} = \frac{4}{3} + \frac{1}{36} \frac{\int_0^R e^{(\lambda+3\nu)/2} \Big[16P + (e^\lambda - 1)(P+\epsilon)\Big](e^\lambda - 1) r^2 \, dr}{\int_0^R e^{(\lambda+3\nu)/2} P r^2 \, dr} + \\ + \frac{4\pi G}{9c^4} \frac{\int_0^R e^{3(\lambda+\nu)/2} \Big[8P + (e^\lambda + 1)(P+\epsilon)\Big] P r^4 \, dr}{\int_0^R e^{(\lambda+3\nu)/2} P r^2 \, dr} + \frac{16\pi^2 G^2}{9c^8} \frac{\int_0^R e^{(5\lambda+3\nu)/2}(P+\epsilon) P^2 r^6 \, dr}{\int_0^R e^{(\lambda+3\nu)/2} P r^2 \, dr} \, . \end{aligned} \tag{3.134}$$

If $<\gamma><\gamma_{cr}$, equivalent to $\sigma^2 < 0$, we can conclude that the system is dynamically unstable. However, if $<\gamma>>\gamma_{cr}$, we cannot conclude that the system is stable since $\psi = r$ is not in general the fundamental eigenfunction.

3.3.3. Stability: the case of the CT equation

The previous equations are valid for an arbitrary equation of state $P = P(\epsilon)$. If we now specialize on the EOS (3.110) of a relativistic degenerate Fermi gas and introduce the normalized pulsation

$$\Sigma^2 = \frac{8\sigma^2 a_{rel}^2}{q} \Big(1 - \frac{2q v_1}{\eta_1}\Big)^{-1} , \tag{3.135}$$

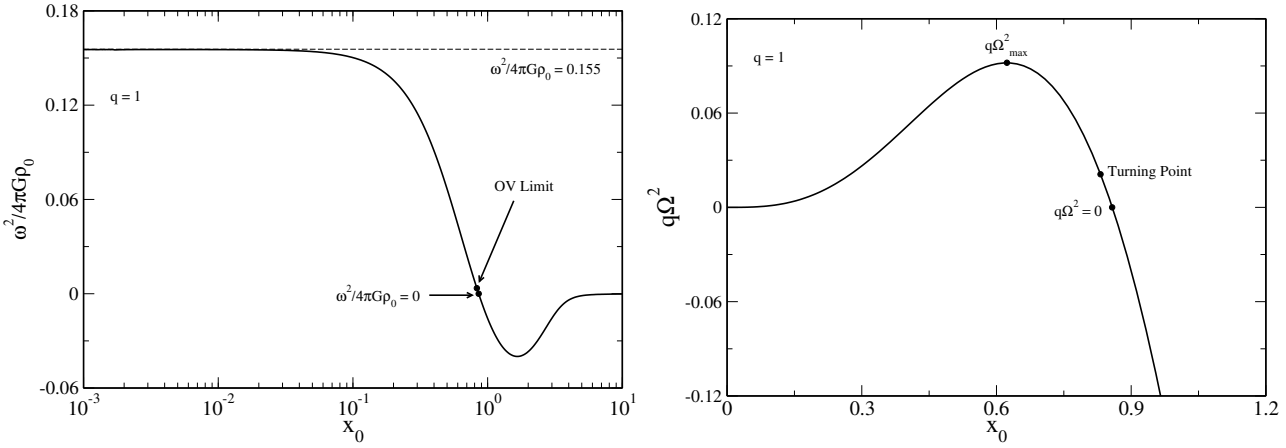

Figure 3.19: *The same as in Fig. 3.18, for $q = 1$. Compared to the case $q = 2.743 \times 10^{-4}$, the difference between the value of x_0, evaluated by means of the turning point method, and the value of x_0, evaluated at the point $\omega^2/4\pi G\rho_0 = 0$, is more evident. Numerically we find: $x_0 = 0.832$ (turning point) and $x_0 = 0.851$ ($\omega^2/4\pi G\rho_0 = 0$). We note also that the value of $q\Omega^2_{max}$ is lower than the one obtained for $q = 2.743 \times 10^{-4}$.*

we find that Eq.(3.130) can be written as

$$\begin{aligned}
&\Sigma^2 \int_0^{\eta_1} \frac{x^3\psi^2\eta^2}{(1-2qv/\eta)^{3/2}}\,d\eta = \int_0^{\eta_1} \frac{\gamma(2\psi+\eta\psi')^2 - 4\psi(2\eta\psi'+\psi)}{(1-2qv/\eta)^{1/2}[1+q(y-1)]^3} f(x)\,d\eta + \\
&- 8q\int_0^{\eta_1} \frac{\psi^2 v}{\eta(1-2qv/\eta)^{3/2}[1+q(y-1)]^3}\left[f(x) + \frac{x^3 v[1+q(y-1)]}{\eta(1-2qv/\eta)}\right] d\eta + \\
&- q^2\int_0^{\eta_1} \frac{f(x)\psi^2\eta^2}{(1-2qv/\eta)^{3/2}[1+q(y-1)]^3}\left[f(x) + \frac{2x^3(1-qv/\eta)[1+q(y-1)]}{q(1-2qv/\eta)}\right] d\eta + \\
&- \frac{q^3}{8}\int_0^{\eta_1} \frac{x^3 f(x)^2\psi^2\eta^4}{(1-2qv/\eta)^{5/2}[1+q(y-1)]^2}\,d\eta\,.
\end{aligned} \tag{3.136}$$

With the test function $\psi = \eta$, we obtain

$$\begin{aligned}
&\frac{\Sigma^2}{9}\int_0^{\eta_1} \frac{x^3\eta^4}{(1-2qv/\eta)^{3/2}}\,d\eta = \int_0^{\eta_1} \frac{(\gamma-4/3)\eta^2 f(x)}{(1-2qv/\eta)^{1/2}[1+q(y-1)]^3}\,d\eta + \\
&- \frac{8q}{9}\int_0^{\eta_1} \frac{\eta v}{(1-2qv/\eta)^{3/2}[1+q(y-1)]^3}\left\{f(x) + \frac{x^3 v[1+q(y-1)]}{\eta(1-2qv/\eta)}\right\} d\eta + \\
&- \frac{q^2}{9}\int_0^{\eta_1} \frac{f(x)\eta^4}{(1-2qv/\eta)^{3/2}[1+q(y-1)]^3}\left\{f(x) + \frac{2x^3(1-qv/\eta)[1+q(y-1)]}{q(1-2qv/\eta)}\right\} d\eta + \\
&- \frac{q^3}{72}\int_0^{\eta_1} \frac{x^3 f(x)^2\eta^6}{(1-2qv/\eta)^{5/2}[1+q(y-1)]^2}\,d\eta.
\end{aligned} \tag{3.137}$$

If we define

$$< \gamma >= \frac{\int_0^{\eta_1} \frac{\gamma\eta^2 f(x)}{(1-2qv/\eta)^{1/2}[1+q(y-1)]^3}\, d\eta}{\int_0^{\eta_1} \frac{\eta^2 f(x)}{(1-2qv/\eta)^{1/2}[1+q(y-1)]^3}\, d\eta}\,, \tag{3.138}$$

the foregoing equation can be rewritten as

$$\Sigma^2 = 9\,(< \gamma > -\gamma_c)\,\frac{\int_0^{\eta_1} \frac{\eta^2 f(x)}{(1-2qv/\eta)^{1/2}[1+q(y-1)]^3}\, d\eta}{\int_0^{\eta_1} \frac{x^3\eta^4}{(1-2qv/\eta)^{3/2}}\, d\eta} \tag{3.139}$$

with

$$\begin{aligned}\gamma_{cr} = \frac{4}{3} + \frac{8}{9}q\frac{\int_0^{\eta_1} \frac{\eta v}{(1-2qv/\eta)^{3/2}[1+q(y-1)]^3}\left\{f(x) + \frac{x^3 v[1+q(y-1)]}{\eta(1-2qv/\eta)}\right\} d\eta}{\int_0^{\eta_1} \frac{\eta^2 f(x)}{(1-2qv/\eta)^{1/2}[1+q(y-1)]^3}\, d\eta} + \\ + \frac{q^2}{9}\frac{\int_0^{\eta_1} \frac{f(x)\eta^4}{(1-2qv/\eta)^{3/2}[1+q(y-1)]^3}\left\{f(x) + \frac{2x^3(1-qv/\eta)[1+q(y-1)]}{q(1-2qv/\eta)}\right\} d\eta}{\int_0^{\eta_1} \frac{\eta^2 f(x)}{(1-2qv/\eta)^{1/2}[1+q(y-1)]^3}\, d\eta} + \\ + \frac{q^3}{72}\frac{\int_0^{\eta_1} \frac{x^3 f(x)^2\eta^6}{(1-2qv/\eta)^{5/2}[1+q(y-1)]^2}\, d\eta}{\int_0^{\eta_1} \frac{\eta^2 f(x)}{(1-2qv/\eta)^{1/2}[1+q(y-1)]^3}\, d\eta}\,.\end{aligned} \tag{3.140}$$

We note that the normalized pulsation defined in Sec. 3.2.2 is given by

$$\Omega^2 = \frac{\omega^2}{\omega_*^2} = \frac{\Sigma^2}{q}\Big(1 - \frac{2qv_1}{\eta_1}\Big)\,. \tag{3.141}$$

Using the identity (3.84), we also have

$$\frac{\omega^2}{4\pi G\rho_0} = \frac{q\Omega^2}{8x_0^3} = \frac{\Sigma^2}{8x_0^3}\Big(1 - \frac{2qv_1}{\eta_1}\Big)\,. \tag{3.142}$$

In Figs. 3.18 and 3.19 we have represented the pulsation frequency, evaluated by means of the test function $\psi = \eta$. It is evident that in the limit $x_0 \to 0$ we recover the same results already obtained in the Newtonian regime. When the intensity of the gravity increases, we see that there exists a critical point enabling us to separate stable from unstable configurations. This implies that, differently from Newtonian gravity, not all the equilibrium configurations are dynamically stable. This is related to the shape of the mass-radius relation (see Fig. 3.11), which presents a turning point (corresponding to the last stable configuration).

Figs. 3.18 and 3.19 show a second interesting feature: the normalized pulsation Ω^2 presents a maximum value, which value diverges in the Newtonian limit $q \to 0$[19]. In particular, for $q = 1$ (see Fig. 3.19),

[19]This is not surprising because $\Omega^2 \propto 1/q$, see Eq.(3.79).

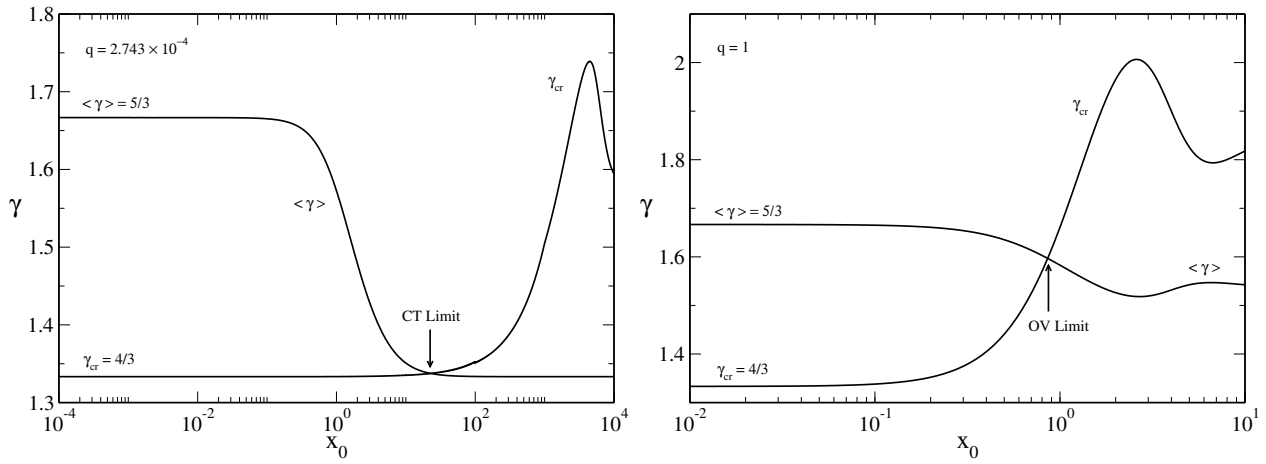

Figure 3.20: *The effective polytropic exponent $< \gamma >$ and the critical value γ_{cr} are plotted as a function of x_0 for $q = 2.743 \times 10^{-4}$ (left panel) and $q = 1$ (right panel). Only configurations with $< \gamma >> \gamma_{cr}$ are stable. The turning point corresponds to $< \gamma >= \gamma_{cr}$ and the system is marginally stable. It is remarkable that, for large values of x_0, the critical value of the effective polytropic exponent γ_{cr} achieves a maximum (see also Ref.[139]).*

we observe that for increasing values of x_0, the normalized pulsation $\omega^2/4\pi G\rho_0$ (always negative after the point of maginal stability) tends to zero. This is not suprising, because the density of the system reaches its largest values (remember that, in the mass radius relation, these points are placed in the spiralic part).

In Fig. 3.20 we have represented the effective polytropic exponent $< \gamma >$ (see also Ref.[139]) and its critical value (γ_{cr}) as functions of x_0, for $q = 2.743 \times 10^{-4}$ and $q = 1$. For small values of x_0 the system recovers the Newtonian behaviour and the configurations are stable (we are in the part of the mass-radius relation characterized by small values of the mass and large values of the radii). Conversely, when the density increases and the general relativistic effects become more and more present, $< \gamma >$ decreases and γ_{cr} increases. There exists a limiting configuration, corresponding to the turning point in the mass-radius relation, where $< \gamma >= \gamma_{cr}$. After this point, the system is not dynamically stable, anymore. For $q = 2.743 \times 10^{-4}$, we see that $< \gamma > \to 4/3$ for $x_0 >> 1$. For $q = 1$, by contrast, $< \gamma >$ converges to $4/3$ more slowly. In the end, both of figures display a non monotonic behaviour of γ_{cr}, which reaches a maximum and then oscillates (see also Ref.[139]).

3.3.4. Series of Equilibria and Poincaré Theorem

We define the free energy F (or binding energy) of the star by the relation

$$F = -E_b = (M - N\mu H)c^2\,. \tag{3.143}$$

where E_b represents the binding energy and N is the baryon number [see Eq.(2.21) in Sec. 2.1]. At the same time, similarly to the Newtonian regime (see Sec. 3.2.3), we can write the free energy as

$$F = U + W\,, \tag{3.144}$$

where U and W are, respectively, the internal and gravitational energies, defined as follows [190]

$$U = \int_0^R u(r)\Big[1 - \frac{2GM(r)}{rc^2}\Big]^{-1/2} 4\pi r^2\, dr\,, \tag{3.145}$$

$$W = \int_0^R \epsilon(r)\Big\{1 - \Big[1 - \frac{2GM(r)}{rc^2}\Big]^{-1/2}\Big\} 4\pi r^2\, dr\,. \tag{3.146}$$

In the limit $2GM_r/rc^2 \to 0$, the foregoing expressions converge to the expressions (3.93) and (3.94) of internal and gravitational energy, respectively. Let us introduce the characteristic relativistic free energy

$$F_*^{Rel} = M_* c^2 = \frac{32\pi A a_{rel}^3}{q} = \frac{32\pi A a^3 y_0^3}{q} = \frac{1}{q}\Big(\frac{3}{32\pi^2}\Big)^{1/2}\Big(\frac{hc}{G}\Big)^{3/2}\frac{mc^2}{(\mu H)^3} = \frac{F_*}{q}\,, \tag{3.147}$$

where F_* is defined by Eq.(3.95). In this way, the dimensionless expression of the free energy (3.144) is

$$\begin{aligned}\frac{F}{F_*^{Rel}} = \frac{qF}{F_*} = \frac{q}{8}\int_0^{\eta_1} g(x)\eta^2 d\eta + \int_0^{\eta_1} x^3\left[1 - \Big(1 - \frac{2qv}{\eta}\Big)^{-1/2}\right]\eta^2 d\eta = \\ = \int_0^{\eta_1}\left[x^3 + \frac{qg(x)}{8}\right]\eta^2 d\eta - \int_0^{\eta_1}\frac{x^3\eta^2 d\eta}{\sqrt{1 - \frac{2qv}{\eta}}} = v_1 - N_{B1}\,,\end{aligned} \tag{3.148}$$

where N_{B1} is the dimensionless baryon number. To recover the Newtonian expression of free energy (3.106), let us expand the square root for $q \to 0$: by taking only the terms of first order, we have

$$\frac{qF}{F_*} \sim \frac{q}{8}\int_0^{\eta_1} g(x)\eta^2 d\eta - \int_0^{\eta_1} x^3\Big(\frac{qv}{\eta} + \frac{3q^2v^2}{2\eta^2} + ...\Big)\eta^2 d\eta = \frac{q}{8}\int_0^{\eta_1} g(x)\eta^2 d\eta - q\int_0^{\eta_1} x^3 v\eta d\eta\,. \tag{3.149}$$

Simplifying q, using the first of Eqs.(3.118) and the second of Eqs.(3.37), we get

$$\frac{F}{F_*} = y_0^3\left[\frac{1}{8y_0^3}\int_0^{\eta_1} g(x)\eta^2 d\eta + y_0\int_0^{\eta_1}\Big(\phi^2 - \frac{1}{y_0^2}\Big)^{3/2}\eta^3\frac{d\phi}{d\eta}d\eta\right]. \tag{3.150}$$

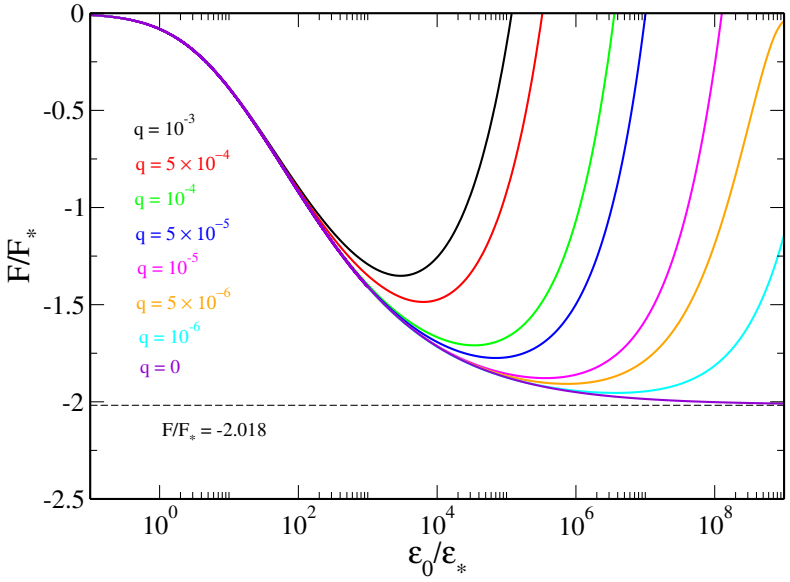

Figure 3.21: *Free energy F/F_* versus ϵ_0/ϵ_* for small values of q. The Newtonian curve (violet line) is shown for comparison. For high values of the central density, the minimum of the free energy reaches the asymptotic value* (3.107) *obtained in the ultrarelativistic regime for Newtonian configurations.*

that, apart from the presence of the term y_0^3 [because of Eq.(3.111)], corresponds to Eq.(3.106) and to the definitions (3.97) and (3.104) of the internal and gravitatinal energies, respectively. One can show that the mass M and the baryon number N are conserved by the Einstein equations. As a result, a minimum of mass at fixed baryon number determines a steady state of the Einstein equations that is dynamically stable. We thus have to consider the minimization problem

$$\min_{\epsilon,n}\Big\{M[\epsilon] \quad | \quad N[n,\epsilon] \quad \text{fixed}\Big\}\,. \tag{3.151}$$

This is obviously equivalent to

$$\min_{\epsilon,n}\Big\{F[n,\epsilon] \quad | \quad N[n,\epsilon] \quad \text{fixed}\Big\}\,. \tag{3.152}$$

Using the method of Lagrange multipliers, the first variations are given by $\delta M - \lambda\delta N = 0$ or, equivalently, by $\delta F - \alpha\delta N = 0$. It can be shown that this condition returns the TOV equations. Then, we have to make sure that the critical point is a true minimum of mass (or free energy) at fixed baryon number. This is the case if $\delta^2 M > 0$ (or $\delta^2 F > 0$) for all variations $\delta\epsilon$ and δn that conserve the baryon number, i.e. $\delta N = 0$. Using the Poincaré theorem, a change of stability can occur only at a turning point of baryon number, or equivalently at a turning point of mass (or free energy) along the series of equilibria $N(R)$, $M(R)$, or $F(R)$. In general, the series of equilibria becomes unstable at the first

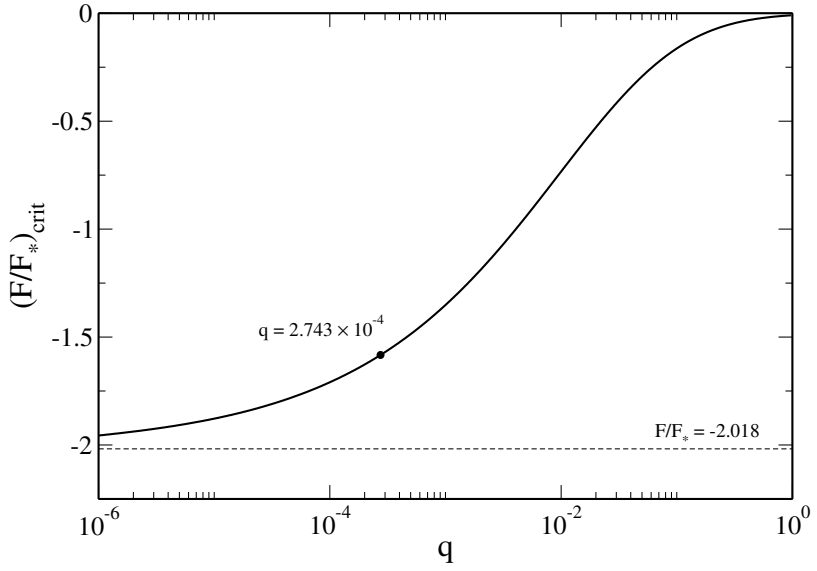

Figure 3.22: *Free energy (evaluated at the critical point) for several values of q. In Newtonian gravity, the value of the free energy reaches the asymptotic value* (3.107) *whereas, in the limit* $q \to 1$*, the critical free energy is infinitesimal. This appearent paradoxal behaviour [remember that the free energy corresponds to the binding energy, see Eq.*(3.143)*] is explained because* $(F/F_*)_{Newtonian} = (F/F_*)_{Rel}/q$.

turning point (corresponding to the maximum mass $M_{\max}$) and loses new modes of stability at the next turning points. Furthermore, since $\delta N = \delta M = \delta F = 0$ at a turning point, the curves $M(N)$ and $F(N)$ present angular points.

In Fig. 3.21 we have represented the free energy along the series of equilibria (for small values of q). We see that the free energy takes a minimum occurring at $\epsilon_0 = \epsilon_0^c$ (and corresponding to the maximum of the functions M and N). For decreasing values of q, the minimum will converge to the asymptotic value $F/F_* = -2.018$ obtained for Newtonian configurations in the ultrarelativistic regime (see also Fig. 3.22). Moreover, looking at Fig. 3.22, we see that the value of the free energy at the critical point of $q = 2.743 \times 10^{-4}$ is quite dissimilar from the asymptotic value $F/F_* = -2.018$. This means that, although small, this value of q still displays general relativistic effects.

3.4. Applications

3.4.1. Analytical Estimate of the Point of Instability of White Dwarfs Stars

In this Section, we obtain an analytical estimate of the point of instability of WDs in GR. Our approach is similar to that of Faulkner [79]. We obtain analytical expressions that can be used for WDs with arbitrary composition as long as $q \to 0$, which is the case in practice. Chandrasekhar [42] has shown

that, when $<\gamma>\to 4/3$, the condition of dynamical instability of a gaseous star in GR can be written in the form

$$R = \frac{K}{<\gamma> -4/3}\frac{2GM}{c^2}\,, \tag{3.153}$$

where K is a constant that depends on the configuration. We shall use this equation to estimate the point of instability of WDs. Since instability occurs when the WDs are highly relativistic (i.e. close to the polytrope of index $n = 3$), we can replace $<\gamma>(x_0)$ in Eq.(3.153) by its asymptotic expression (3.91) valid for $x_0 \gg 1$. In this way, we obtain

$$\frac{2.442}{3x_0^2} \sim K\frac{2GM}{Rc^2}\,. \tag{3.154}$$

In the limit $x_0 \to +\infty$ the mass and the radius are expressed by Eqs.(3.58) and (3.59). Moreover, $K = 1.1245$ [42]. Recalling Eq.(3.49), we note that[20]

$$\frac{GM}{Rc^2} \simeq q\frac{\omega_3}{\xi_1}x_0\,. \tag{3.155}$$

Substituting these estimates in Eq.(3.154), we obtain

$$x_0^c \simeq \Big(\frac{1.221\xi_1}{K\omega_3}\Big)^{1/3}\frac{1}{q^{1/3}} = \frac{1.548}{q^{1/3}}\,. \tag{3.156}$$

Therefore

$$\frac{R}{R_*} \simeq \frac{\xi_1}{x_0^c} = \Big(0.819K\xi_1^2\omega_3\Big)^{1/3}q^{1/3} = 4.455\,q^{1/3}\,, \tag{3.157}$$

$$\frac{2GM}{Rc^2} \simeq \frac{2q\omega_3}{\xi_1}x_0^c = \Big(\frac{9.768\omega_3^2}{\xi_1^2K}\Big)^{1/3}q^{2/3} = 0.906\,q^{2/3}\,, \tag{3.158}$$

$$\frac{R}{R_S} \simeq \Big(\frac{\xi_1^2K}{9.768\omega_3^2}\Big)^{1/3}\frac{1}{q^{2/3}} = \frac{1.104}{q^{2/3}}\,. \tag{3.159}$$

For $q = 2.743\times 10^{-4}$, we obtain $x_0^c = 23.825$, $R/R_* = 0.289$, $2GM/Rc^2 = 3.83\times 10^{-3}$ and $R/R_S = 261.4$, in good agreement with the numerical values. However, there is an alternative to the estimates above obtained. In fact, we can use a "proper" value of K and not that used by Chandrasekhar. Isolating K in Eq.(3.154) and evaluating x_0, R and M at the critical point, we get

$$K \simeq \frac{1.221Rc^2}{GM}\frac{1}{x_0^2} = \frac{1.221\eta_1(x_{oc})}{qv_1(x_{oc})}\frac{1}{x_{0c}^2}\,. \tag{3.160}$$

[20] In Eq.(3.155), ω_3 and ξ_1 are, respectively, the total mass and the total radius of the polytrope of index $n = 3$. The numerical values are $\omega_3 = 2.01824$ and $\xi_1 = 6.89685$.

For $q = 2.743 \times 10^{-4}$ Eq.(3.160) yields[21] $K = 1.1518$. Substituting this value in Eqs.(3.157)-(3.159), we have

$$\begin{aligned} x_0^c &\simeq \frac{1.536}{q^{1/3}}\,, \\ \frac{R}{R_*} &\simeq 4.491\, q^{1/3}\,, \\ \frac{2GM}{Rc^2} &\simeq 0.899\, q^{2/3}\,, \\ \frac{R}{R_S} &\simeq \frac{1.113}{q^{2/3}}\,. \end{aligned} \tag{3.161}$$

For $q = 2.743 \times 10^{-4}$, we get $x_0^c = 23.640$, $R/R_* = 0.292$, $2GM/Rc^2 = 3.79 \times 10^{-3}$ and $R/R_S = 263.5$ in good agreement with the numerical values and very close to the evaluations above given. Eq.(3.161), more generally, gives the value of x_0^c in the limit $q \to 0$.

3.4.2. Different Equations of State

In this Section we consider the case of WDs of different chemical composition (implying different values of μ_e and q, listed in Tab. 3.1). As we have seen in Sec. 1.1, WDs present a varied structure and the model of Chandrasekhar & Tooper is inaccurate to well describe the properties of these objects. Nevertheless we can obtain an (approximated) idea of the structural parameters of WDs (at the critical point). The chemical composition refer to cases known in literature and, as we see from Tab. 3.1, the values of μ_e (except for the hydrogen) are of the order of 2. The corresponding values of q are of the order of that used by Chandrasekhar & Tooper. In particular, μ_e is obtained by using the following formula:

$$\mu_e = \frac{A}{Z} \tag{3.162}$$

where A and Z represent, respectively, the mass and the atomic number of a given chemical element. In Tab. 3.2 we have recorded the central values of rest mass and energy density and, also, the values of radius and mass of the WD. By virtue of the smallness of the values of q, we see that the discard between ρ_0 and ϵ_0/c^2 is generally small. This can be interpreted as a confirmation, *a posteriori*, of the Newtonian nature of WDs. It is interesting to observe that the central density ρ_0 evaluated at the critical point is larger than the mean density of the $\rho_{mean} = 3M_{max}/4\pi R_{min}^3$. For example, if we consider the case $q = 2.743 \times 10^{-4}$ we obtain $\rho_{mean} = 6.179 \times 10^8$ g cm^{-3} whereas, for the central density is $\rho_0 = 2.321 \times 10^{10}$ g cm^{-3}.

[21] The values of x_0^c, $\eta_1(x_{oc})$ and $qv_1(x_{oc})$ used in this evaluation are those obtained from the numerical resolution of the Chandrasekhar-Tooper equations (3.112).

Table 3.1: *Chemical elements used, with the corresponding values of μ_e and* q. *With "CT" we indicate the value used by Chandrasekhar & Tooper (not corresponding to a real situation). Here the elements are listed according to the atomic number Z. The other values of μ_e are taken from Ref.[94] (by considering the most recent evaluations of A and Z).*

Element	μ_e	q
${}^{1}_{1}\mathrm{H}$	1.0079	5.4035×10^{-4}
${}^{4}_{2}\mathrm{He}$	2.0013	2.7213×10^{-4}
CT	1.9850	2.7430×10^{-4}
${}^{12}_{6}\mathrm{C}$	2.0018	2.7206×10^{-4}
${}^{16}_{8}\mathrm{O}$	1.9999	2.7232×10^{-4}
${}^{24}_{12}\mathrm{Mg}$	2.0254	2.6889×10^{-4}
${}^{28}_{14}\mathrm{Si}$	2.0061	2.7148×10^{-4}
${}^{32}_{16}\mathrm{S}$	2.0038	2.7180×10^{-4}
${}^{56}_{28}\mathrm{Fe}$	2.1479	2.5355×10^{-4}

The small difference between ρ_0 and ϵ_0/c^2 is reflected in the difference between $N\mu_e H$ and M. If we look at the values (expressed in solar masses) we that, typically (except for the WD of hydrogen), we have $|N\mu_e H - M| \sim 3\times 10^{-4} M_\odot$. Although small, this value corresponds to an energy $|N\mu_e H - M|c^2 \sim 5.36 \times 10^{50}$ erg (see fourth column in Tab. 3.3). Energies of this order of magnitude are typical in events as *gamma ray bursts* [85]. The values of q listed in Tab. 3.1 show also that values of $q \geq 10^{-3}$ do not represent any physical situation (except for $q = 1$, corresponding to NSs).

3.5. Summary of the Previous Results

In this Chapter we have considered degenerate fermionic configurations, by extending the original model advanced by Chandrasekhar & Tooper. In the Newtonian regime, we have obtained the mass-radius relation, leading to the Chandrasekhar limiting mass in the ultrarelativistic limit. The dynamical study has shown that the Newtonian configurations are always dynamically stable although, in the ultrarelativistic limit, the system is marginally stable. Besides, in the ultrarelativistic regime, we have found a modification to the virial theorem [see Eq.(3.107)]. As we have seen, the free energy reaches a negative value when, rather, we would have expected $F = 0$. We can interpret this modification as a first order correction to the ultrarelativistic virial theorem.

Table 3.2: *Physical parameters for WDs at the critical point. The densities are expressed in g cm^{-3}, the radii in km and the masses in solar masses $M_\odot$.*

q	ρ_0	ϵ_0/c^2	R	M
2.5335×10^{-4}	2.718×10^{10}	2.730×10^{10}	927.63	1.2122
2.6889×10^{-4}	2.409×10^{10}	2.419×10^{10}	1002.0	1.3620
2.7148×10^{-4}	2.361×10^{10}	2.372×10^{10}	1014.8	1.3881
2.7180×10^{-4}	2.357×10^{10}	2.367×10^{10}	1016.3	1.3913
2.7206×10^{-4}	2.351×10^{10}	2.362×10^{10}	1017.7	1.3940
2.7213×10^{-4}	2.351×10^{10}	2.361×10^{10}	1018.0	1.3947
2.7232×10^{-4}	2.346×10^{10}	2.356×10^{10}	1019.0	1.3966
2.7430×10^{-4}	2.310×10^{10}	2.321×10^{10}	1028.8	1.4168
5.4035×10^{-4}	5.696×10^{9}	5.735×10^{9}	2498.9	5.4160

Table 3.3: *Physical parameters for WDs at the critical point. The particle number $N\mu_e H$ is expressed in solar masses $M_\odot$, the binding energy in erg.*

q	$N\mu_e H$	N	E_b	R/R_S
2.5335×10^{-4}	1.2125	6.713×10^{56}	4.457×10^{50}	259
2.6889×10^{-4}	1.3623	7.998×10^{56}	5.287×10^{50}	249
2.7148×10^{-4}	1.3884	8.230×10^{56}	5.436×10^{50}	248
2.7180×10^{-4}	1.3917	8.259×10^{56}	5.455×10^{50}	247
2.7206×10^{-4}	1.3943	8.283×10^{56}	5.470×10^{50}	247
2.7213×10^{-4}	1.3950	8.289×10^{56}	5.473×10^{50}	247
2.7232×10^{-4}	1.3969	8.306×10^{56}	5.485×10^{50}	247
2.7430×10^{-4}	1.4168	8.488×10^{56}	5.602×10^{50}	246
5.4035×10^{-4}	5.4182	6.393×10^{57}	3.984×10^{51}	156

The general relativistic configurations present a different mass-radius relation, which is characterized by the presence of a turning point. According to our stability analysis, the presence of the turning point is related to a change of stability. For any $q \neq 0$, the general relativistic configurations become dynamically unstable after the turning point (moreover, new modes of stability are lost when the function $M = M(R)$ reaches the next turning points).

To carry out our stability analysis, we have used two methods, *i.e.* (i) the turning point and (ii) the point where the pulsation vanishes (i.e. $\omega^2/4\pi G\rho_0 = 0$). As we have seen, the two methods become equivalent in the Newtonian limit $q \to 0$ (remember that in Newtonian gravity the mass-radius relation does not present any turning point) but give different results when general relativistic effects are taken into account. Generally, we have obtained that the method (ii) overestimates the value of x_0. In addition, differently from the Newtonian gravity, there exists a point that maximizes the pulsation $q\Omega^2$ (see Figs. 3.18 and 3.19, right panels). It is interesting to note that we do not get this point if we consider only the pulsation normalized by the dynamical time (see Figs. 3.18 and 3.19, left panels).

In the limit $q \to 0$ we have obtained an analytical estimate of the point of instability of WDs in GR. The results obtained show that these estimates can be considered correct, as a first approximation (if compared with the numerical results). These estimates can be used, in particular, to study the stability of a specific class of WDs, i.e. the Helium WDs. For WDs of different chemical composition (e.g. the CNO WDs) the model should be improved because of the coexistence of more than one chemical species.

We have also to stress that the typical values of q for the numerical applications are of the order of 10^{-4}. This is a further evidence of the fact that the model is inadequate to describe real systems if the value of q is of the order of 10^{-1}. However, the case $q = 1$ (which recovers the results of Oppenheimer & Volkoff) can be useful to give an idea concerning the inner cores of NSs.

4

Non-quantum Limit: the Case of Boltzmann Statistics

As we have seen in Sec. 1.2, in the framework of Newtonian gravity, thermodynamical instabilities set in when the reverse temperature η [see Eq.(1.27)] exceeds the critical value $\eta_c = 2.525$ (canonical instabilities) and the energy Λ [see Eq.(1.27)] exceeds the critical value $\Lambda_c = 0.335$ (see also Refs.[5, 133, 6, 8, 7, 131, 53]). In the canonical ensemble, the system undergoes a collapse forming a small and compact core (Dirac peak). In the microcanonical ensemble, vice-versa, the system collapses and takes a core-halo structure.

When general relativistic effects are included (see Sec. 1.4), a second kind of instability appears. As Chavanis [46, 55] has shown, if the system gets hotter or more energetic than a critical threshold, it will collapse. This kind of instability is conceptually different from that obtained in Newtonian gravity, where the system undergoes a collapse if it is colder or less energetic than a critical threshold.

In this Chapter we complete the previous investigations, by extending to GR the works of Antonov and Lynden-Bell & Wood and making the link with the results of Chavanis. As we shall see, when general relativistic effects are included, the critical values of energy and temperature for the onset of the microcanonical and canonical instabilities change and depend on the strength of the gravity.

The measure of the intensity of the gravitational fields is controlled by a parameter defined by the ratio of the gravitational to the rest mass energies (i.e. $\mathcal{N}$, see Sec. 4.2). Moreover, there exists a second control parameter, corresponding to Λ [see Eq.(A.2)], which gives a measure of the importance of the binding energy with respect to the gravitational energy.

In Sec. 4.1 we introduce the main relations describing the system and we show the existence of a semi-

analytical set of equations. In Sec. 4.2 we show existence of a scaling, related to the control parameter $\mathcal{N}$. This scaling is a direct consequence of the symmetries of the problem (it comes naturally out from Schwarzschild's metric). In addition, we analyze the limits of strong and gravitational fields.
With Sec. 4.3 the discussion of the results takes place. Specifically, this section is dedicated to the study of the particle number function, by virtue of its importance concerning the construction of the caloric curves (see Appendix A). Thanks to this analysis the existence of a limiting configuration (that we indicate as $\mathcal{N}_{max}$) is shown.
Successively, Sec. 4.4 analyzes the nature of the series of equilibria and, also, of entropy and free energy. In Sec. 4.5, finally, the phases diagrams are discussed.

4.1. Main Equations

In the limit $T \to \infty$ the Fermi - Dirac statistics (2.29) recovers the Boltzmann statistics

$$f = \frac{g}{h^3} e^{(\mu_r - E)/k_B T_r} \,. \tag{4.1}$$

The thermodynamic quantities (2.54)-(2.56) are therefore

$$\tilde{n} = \frac{e^\alpha}{\pi^2} \int_0^\infty e^{-|\alpha| \frac{\sqrt{y^2+1}}{\sqrt{\Phi+1}}} y^2 dy \,, \tag{4.2}$$

$$\tilde{\epsilon} = \frac{e^\alpha}{\pi^2} \int_0^\infty e^{-|\alpha| \frac{\sqrt{y^2+1}}{\sqrt{\Phi+1}}} y^2 \sqrt{y^2+1} dy \,, \tag{4.3}$$

$$\tilde{P} = \frac{e^\alpha}{3\pi^2} \int_0^\infty e^{-|\alpha| \frac{\sqrt{y^2+1}}{\sqrt{\Phi+1}}} \frac{y^4 dy}{\sqrt{y^2+1}} \,. \tag{4.4}$$

By defining $y = \sinh\theta$ (Juettner transformation), the foregoing expressions become

$$\tilde{n} = \frac{e^\alpha}{\pi^2} \int_0^\infty \sinh^2\theta \cosh\theta \, e^{-\frac{|\alpha|}{\sqrt{\Phi+1}} \cosh\theta} d\theta \,, \tag{4.5}$$

$$\tilde{\epsilon} = \frac{e^\alpha}{\pi^2} \int_0^\infty \sinh^2\theta \cosh^2\theta \, e^{-\frac{|\alpha|}{\sqrt{\Phi+1}} \cosh\theta} d\theta \,, \tag{4.6}$$

$$\tilde{P} = \frac{e^\alpha}{3\pi^2} \int_0^\infty \sinh^4\theta \, e^{-\frac{|\alpha|}{\sqrt{\Phi+1}} \cosh\theta} d\theta = \frac{\sqrt{\Phi+1}}{|\alpha|} \tilde{n} \tag{4.7}$$

(the last equality corresponds to the perfect gas law). The integrals can be evaluated by means of Bessel functions, defined by

$$K_u\Big(\frac{|\alpha|}{\sqrt{\Phi+1}}\Big) = \int_0^\infty e^{-\frac{|\alpha|}{\sqrt{\Phi+1}} \cosh\theta} \cosh(u\theta) d\theta \,. \tag{4.8}$$

The functions $K_u(|\alpha|/\sqrt{\Phi+1})$ are related to the Hankel function with imaginary argument [1, 41]

$$K_u\Big(\frac{|\alpha|}{\sqrt{\Phi+1}}\Big) = \frac{\pi i}{2} e^{\frac{u\pi i}{2}} H_u\Big(\frac{|\alpha|}{\sqrt{\Phi+1}}\Big)\,. \tag{4.9}$$

Substituting Eq.(4.8) into Eqs.(4.5)-(4.7), we have

$$\tilde{n} = \frac{e^{\alpha}}{4\pi^2}\left[K_3\Big(\frac{|\alpha|}{\sqrt{\Phi+1}}\Big) - K_1\Big(\frac{|\alpha|}{\sqrt{\Phi+1}}\Big)\right], \tag{4.10}$$

$$\tilde{\epsilon} = \frac{e^{\alpha}}{8\pi^2}\left[K_4\Big(\frac{|\alpha|}{\sqrt{\Phi+1}}\Big) - K_0\Big(\frac{|\alpha|}{\sqrt{\Phi+1}}\Big)\right], \tag{4.11}$$

$$\tilde{P} = \frac{e^{\alpha}\sqrt{\Phi+1}}{4\pi^2|\alpha|}\left[K_3\Big(\frac{|\alpha|}{\sqrt{\Phi+1}}\Big) - K_1\Big(\frac{|\alpha|}{\sqrt{\Phi+1}}\Big)\right]. \tag{4.12}$$

From the previous expressions, we see that the thermodynamic quantities are functions of the ratio $|\alpha|/\sqrt{\Phi+1}$. For this reason, let us define the new parameter[1]

$$b = \frac{|\alpha|}{\sqrt{\Phi+1}}\,. \tag{4.13}$$

Combining Eqs.(2.34) and (4.13), the local temperature (2.28) can be written as

$$\frac{k_B T_r}{mc^2} = \frac{k_B T}{mc^2}\frac{1}{\xi} = \frac{k_B T}{|\mu|}\sqrt{\Phi+1} = \frac{\sqrt{\Phi+1}}{|\alpha|} = \frac{1}{b} \qquad \Longleftrightarrow \qquad b = \frac{mc^2}{k_B T_r}\,. \tag{4.14}$$

Eq.(4.14) shows the meaning of b: this parameter corresponds to the reverse local temperature[2]. Small values of b imply $k_B T_r \gg mc^2$, corresponding to the ultrarelativistic limit. Further, according to Eq.(4.13), we have $\Phi \to +\infty$, indicating that the gravity is very strong (see Sec. 4.2.1). High values of b, by contrast, imply $k_B T_r \ll mc^2$ that corresponds to the nonrelativistic limit. According to Eq.(4.13), we have $\Phi \to 0$, corresponding to the Newtonian gravity (see Sec. 4.2.2). Thanks to Eq.(4.13), the dependency on α in the thermodynamic quantities (4.10)-(4.12) is restricted only to the term e^{α}, being $K_u = K_u(b)$. Therefore

$$\tilde{n} = \frac{e^{\alpha}}{4\pi^2}\Big[K_3(b) - K_1(b)\Big], \tag{4.15}$$

$$\tilde{\epsilon} = \frac{e^{\alpha}}{8\pi^2}\Big[K_4(b) - K_0(b)\Big], \tag{4.16}$$

$$\tilde{P} = \frac{e^{\alpha}}{4\pi^2 b}\Big[K_3(b) - K_1(b)\Big]. \tag{4.17}$$

[1] The definition of b is equivalent to the parameter x defined in Ref.[46]. We have:

$$x = \frac{mc^2}{k_B T}$$

.

[2] At the edge we have $\tilde{T}_R = \tilde{T} = 1/b_R$, where b_R indicates $b(R)$.

By now using the recursive formula [1]

$$K_{u+1}(b) = K_{u-1}(b) + \frac{2u}{b}K_u(b)\,, \tag{4.18}$$

Eqs.(4.15)-(4.17) can be written as [41, 159]

$$\tilde{n} = \frac{e^{\alpha}}{\pi^2 b}K_2(b)\,, \tag{4.19}$$

$$\tilde{\epsilon} = \frac{e^{\alpha}}{4\pi^2 b}\Big[3K_3(b) + K_1(b)\Big]\,, \tag{4.20}$$

$$\tilde{P} = \frac{e^{\alpha}}{4\pi^2 b}\Big[K_3(b) - K_1(b)\Big] = \frac{\tilde{n}}{b}\,. \tag{4.21}$$

Furthermore, the expressions of entropy $\tilde{S}$ (2.61) and free energy $\tilde{F}$ (2.65) become

$$\tilde{S} = |\alpha|\int_0^{\tilde{R}} \frac{4\pi(\tilde{P}+\tilde{\epsilon})\tilde{r}^2 d\tilde{r}}{\sqrt{\Phi+1}\sqrt{1-\frac{2\tilde{M}_r}{\tilde{r}}}} - \alpha\tilde{N} = \int_0^{\tilde{R}} \frac{4\pi b(\tilde{P}+\tilde{\epsilon})\tilde{r}^2 d\tilde{r}}{\sqrt{1-\frac{2\tilde{M}_r}{\tilde{r}}}} - \alpha\tilde{N} = I_S - \alpha\tilde{N}\,, \tag{4.22}$$

$$\tilde{F} = \tilde{M} - \sqrt{1-\frac{2\tilde{M}}{\tilde{R}}}\,\frac{\tilde{S}}{b_R}\,, \tag{4.23}$$

The relations (4.19)-(4.23) suggest that the system is parameterized only by α and b. Since b is linked to the gravitational field Φ via Eq.(4.13), we can also express the field equations in terms of b. Inverting the relation between Φ and b, we get

$$\Phi = \frac{\alpha^2}{b^2} - 1\,. \tag{4.24}$$

Deriving both members of the preceding relation with respect to b, we have

$$\frac{d\Phi}{d\tilde{r}} = \frac{d\Phi}{db}\frac{db}{d\tilde{r}} = -\frac{2\alpha^2}{b^3}\frac{db}{d\tilde{r}}\,. \tag{4.25}$$

Substituting Eq.(4.25) in the TOV system (2.59), we obtain

$$\begin{aligned} \frac{db}{d\tilde{r}} &= \frac{b(\tilde{M}_r + 4\pi\tilde{P}\tilde{r}^3)}{\tilde{r}^2}\Big(1-\frac{2\tilde{M}_r}{\tilde{r}}\Big)^{-1}\,, \\ \frac{d\tilde{M}_r}{d\tilde{r}} &= 4\pi\tilde{\epsilon}\,\tilde{r}^2\,. \end{aligned} \tag{4.26}$$

with the conditions $b(0) = b_0$ and $\tilde{M}_r(0) = 0$. Recalling the definition of the density contrast $\mathcal{R}$ [see Eq.(1.20)], we have

$$\mathcal{R} = \frac{\epsilon_0}{\epsilon_R} = \frac{\tilde{\epsilon}_0}{\tilde{\epsilon}_R} = \frac{b_R}{b_0}\,\frac{3K_3(b_0)+K_1(b_0)}{3K_3(b_R)+K_1(b_R)}\,. \tag{4.27}$$

From the foregoing expression we note that the density contrast depends only on b_0 and b_R.

4.2. Scaling GNm/Rc^2 and Universality

Let us consider a nonrotating and spherical body of mass-energy M/c^2 and radius R: in the framework of Schwarzschild's metric, the compactness $\mathcal{C}$ of this body is given by

$$\mathcal{C} = \frac{GM}{Rc^2} = \frac{1}{2}\Big(\frac{V_{esc}}{c}\Big)^2 , \tag{4.28}$$

where V_{esc} indicates the escape velocity defined as $V_{esc} = \sqrt{2GM/R}$. This new parameter gives a measure of the strength[3] of the gravity produced by the body and it is independent of its dimensions. The ratio (4.28) can be seen as a "geometrized mass-energy" and enables us to reduce the description of the physics to the evaluation of one parameter, that is $\mathcal{C}$. In the framework of the Thomas-Fermi model, for a given value of the box radius R, the thermodynamics is analyzed for a specific value of the baryon number N. This last argument suggests that the study of the thermodyanmical properties can be carried out by means of a new parameter, related to the compactness (4.28). Let us therefore define the "modified compactness" as follows

$$\mathcal{C}_N = \frac{GNm}{Rc^2} , \tag{4.29}$$

where, differently from Eq.(4.28), we have used the rest mass Nm of the body instead of its mass-energy[4] M. For one value of $N = N_1$ and one value of $R = R_1$, there exists a specific value of the modified compactness $\mathcal{C}_{N1}$. However, for a second pair (N_2, R_2) we could have $\mathcal{C}_{N2} = \mathcal{C}_{N1}$, suggesting that the pairs (N_1, R_1) and (N_2, R_2) might represent the same system. This implies the existence of a coordinate changement, a scaling, such that it becomes possible to work within a sphere of arbitrary radius, that can be used as a landmark. In addition, from the numerical point of view, the treatment would be considerably simplified. In order to find analytically this scaling, let us define the normalized radial coordinate

$$\lambda = \frac{r}{R} = \frac{\tilde{r}}{\tilde{R}} . \tag{4.30}$$

[3]From Eq.(4.28) we easily see that, for a BH, $\mathcal{C}_{BH} = 0.5$. For NSs and WDs we have, respectively, $\mathcal{C}_{NS} \simeq 0.2$ and $\mathcal{C}_{WD} \simeq 10^{-3}$. For comparison, the Earth and the Sun have $\mathcal{C}_{\oplus} \simeq 10^{-10}$ and $\mathcal{C}_{\odot} = 10^{-6}$, respectively.

[4]We can rewrite Eq.(4.29) as the ratio of the gravitational energy $G(Nm)^2/R$ to the rest mass energy Nmc^2, that is

$$\mathcal{C}_N = \frac{E_{grav}}{E_{rest}} = \frac{\frac{G(Nm)^2}{R}}{Nmc^2}$$

When the rest mass E_{rest} is prevalent we have $\mathcal{C}_N \to 0$ and the system recovers the Newtonian gravity. Conversely, when $E_{grav} \gg E_{rest}$, we have $\mathcal{C}_N \to \infty$ and the system is highly relativistic.

According to the previous equation we have that $0 \leq \lambda \leq 1$. Substituting Eq.(4.30) in Eqs.(4.26) and (2.60), we find that

$$\begin{aligned} \frac{db}{d\lambda} &= b\frac{\tilde{M}_\lambda(\lambda\tilde{R}) + 4\pi\tilde{R}^3\tilde{P}(\lambda\tilde{R})\lambda^3}{\tilde{R}\lambda^2}\left[1 - \frac{2\tilde{M}_\lambda(\lambda\tilde{R})}{\tilde{R}\lambda}\right]^{-1}, \\ \frac{d\tilde{M}_\lambda}{d\lambda} &= 4\pi\tilde{R}^3\,\tilde{\epsilon}(\lambda\tilde{R})\,\lambda^2\,, \end{aligned} \tag{4.31}$$

$$\tilde{N} = 4\pi\tilde{R}^3\int_0^1 \tilde{n}(\lambda\tilde{R})\lambda^2\left[1 - \frac{2\tilde{M}_r(\lambda\tilde{R})}{\tilde{R}\lambda}\right]^{-1/2} d\lambda\,, \tag{4.32}$$

where, thanks to Eq.(4.30), we have $\tilde{M}_r = \tilde{M}_\lambda$. Writing $\tilde{M}_\lambda = \tilde{R}\mathcal{M}_\lambda$ and $\tilde{N} = \tilde{R}\mathcal{N}$, where $\mathcal{M}_\lambda = \mathcal{M}(\lambda)$, Eqs.(4.31) and (4.32) become[5] (we do not write anymore the dependence on the product $\lambda\tilde{R}$)

$$\begin{aligned} \frac{db}{d\lambda} &= b\frac{\mathcal{M}_\lambda + 4\pi\tilde{R}^2\tilde{P}\lambda^3}{\lambda^2}\Big(1 - \frac{2\mathcal{M}_\lambda}{\lambda}\Big)^{-1}, \\ \frac{d\mathcal{M}_\lambda}{d\lambda} &= 4\pi\tilde{R}^2\,\tilde{\epsilon}\,\lambda^2\,, \end{aligned} \tag{4.34}$$

$$\mathcal{N} = 4\pi\tilde{R}^2\int_0^1 \tilde{n}\lambda^2\Big(1 - \frac{2\mathcal{M}_\lambda}{\lambda}\Big)^{-1/2} d\lambda\,, \tag{4.35}$$

To drop the presence of $\tilde{R}$ in the previous relations, we define a new class of thermodynamic quantities being only functions of λ, such that

$$\nu(\lambda) = \tilde{R}^2\,\tilde{n}(\lambda R)\,, \qquad \Theta(\lambda) = \tilde{R}^2\,\tilde{\epsilon}(\lambda\tilde{R})\,, \qquad \Pi(\lambda) = \tilde{R}^2\tilde{P}(\lambda R)\,. \tag{4.36}$$

Substituting the definitions (4.36) in Eqs.(4.34) and (4.35), we get

$$\begin{aligned} \frac{db}{d\lambda} &= b\frac{\mathcal{M}_\lambda + 4\pi\Pi\lambda^3}{\lambda^2}\Big(1 - \frac{2\mathcal{M}_\lambda}{\lambda}\Big)^{-1}, \\ \frac{d\mathcal{M}_\lambda}{d\lambda} &= 4\pi\Theta\lambda^2\,, \end{aligned} \tag{4.37}$$

$$\mathcal{N} = 4\pi\int_0^1 \nu\lambda^2\Big(1 - \frac{2\mathcal{M}_\lambda}{\lambda}\Big)^{-1/2} d\lambda\,. \tag{4.38}$$

The total mass energy of the system is given by

[5] We note that

$$\mathcal{N} = \frac{\tilde{N}}{\tilde{R}} = \frac{N}{R}\frac{r_*}{N_*} = \frac{GNm}{Rc^2}\frac{r_*c^2}{GN_*m} = \mathcal{C}_N \tag{4.33}$$

[because $r_*c^2/GN_*m = 1$, see Eq.(2.58)]. In addition, Roupas [159] studied the gravitational instabilities in GR for classical systems defining $\xi = 2\mathcal{N}$. In the following, however, we refer to $\mathcal{N}$ as the "particle number".

$$\mathcal{M} = \mathcal{M}_1 = \mathcal{M}(\lambda = 1) = 4\pi \int_0^1 \Theta \lambda^2 d\lambda \,. \tag{4.39}$$

Eqs.(4.37)-(4.39) are formally independent of $\tilde{R}$. Let us now consider the three functions ν, Θ and Π. According to the definitions (4.36) we have

$$\nu = \frac{\tilde{R}^2 e^{\alpha}}{\pi^2 b} K_2(b) \,, \tag{4.40}$$

$$\Theta = \frac{\tilde{R}^2 e^{\alpha}}{4\pi^2 b} \Big[3K_3(b) + K_1(b) \Big] \,, \tag{4.41}$$

$$\Pi = \frac{\tilde{R}^2 e^{\alpha}}{4\pi^2 b} \Big[K_3(b) - K_1(b) \Big] \,. \tag{4.42}$$

From the previous expressions we see that the thermodynamical functions still depend on $\tilde{R}$. To get around this problem, we define a new chemical potential $\tilde{\alpha}$ such that

$$e^{\tilde{\alpha}} = \tilde{R}^2 e^{\alpha} \qquad \Longleftrightarrow \qquad \tilde{\alpha} = \alpha + 2 \log \tilde{R} \,. \tag{4.43}$$

Eq.(4.43) shows an intriguing feature: the normalized chemical potential becomes a function of the box radius. Remplacing α by $\tilde{\alpha}$, Eqs.(4.40)-(4.42) become

$$\nu = \frac{e^{\tilde{\alpha}}}{\pi^2 b} K_2(b) \,, \tag{4.44}$$

$$\Theta = \frac{e^{\tilde{\alpha}}}{4\pi^2 b} \Big[3K_3(b) + K_1(b) \Big] \,, \tag{4.45}$$

$$\Pi = \frac{e^{\tilde{\alpha}}}{4\pi^2 b} \Big[K_3(b) - K_1(b) \Big] \,, \tag{4.46}$$

In order to complete this new set of equations independent of $\tilde{R}$, let us consider the temperature, the entropy and the free energy. The temperature (2.64) becomes

$$\tilde{T} = \frac{\sqrt{\Phi_R + 1}}{|\alpha|} \sqrt{1 - \frac{2\tilde{M}}{\tilde{R}}} = \frac{1}{b_R} \sqrt{1 - \frac{2\tilde{R}\mathcal{M}}{\tilde{R}}} = \frac{\sqrt{1 - 2\mathcal{M}}}{b_1} = \mathcal{T} \,, \tag{4.47}$$

where we have used Eqs.(4.13) and (4.39) [moreover, $b_1 = b(\lambda = 1)$]. According to the previous equation, we have $\tilde{T} = \mathcal{T}$: this is not surprising because $\tilde{T}$ (or $\mathcal{T}$) is the temperature measured by an infinitely remote observer, independent of the general relativistic effect. By now considering the entropy, we have

$$\tilde{S} = \tilde{R} \Bigg\{ \int_0^1 \frac{4\pi b (\Pi + \Theta) \lambda^2 d\lambda}{\sqrt{1 - \frac{2\mathcal{M}_\lambda}{\lambda}}} - (\tilde{\alpha} - 2 \log \tilde{R}) \mathcal{N} \Bigg\} = \tilde{R} \Big[\mathcal{I}_{\mathcal{S}} - (\tilde{\alpha} - 2 \log \tilde{R}) \mathcal{N} \Big] \,, \tag{4.48}$$

where

$$\mathcal{I}_{\mathcal{S}} = \int_0^1 \frac{4\pi b(\Pi + \Theta)\lambda^2 d\lambda}{\sqrt{1 - \frac{2\mathcal{M}_\lambda}{\lambda}}}\,. \tag{4.49}$$

Writing $\tilde{S} = \tilde{R}\mathcal{S}$, the foregoing expression becomes

$$\mathcal{S} = \mathcal{I}_{\mathcal{S}} - (\tilde{\alpha} - 2\log\tilde{R})\mathcal{N}\,. \tag{4.50}$$

Substituting Eqs.(4.39), (4.47) and (4.50) into the free energy (4.23), we have

$$\tilde{F} = \tilde{R}(\mathcal{M} - \mathcal{T}\mathcal{S}) \qquad \Longleftrightarrow \qquad \mathcal{F} = \frac{\tilde{F}}{\tilde{R}} = \mathcal{M} - \mathcal{T}\mathcal{S}\,. \tag{4.51}$$

Let us now go back to the entropy (4.50). If we now compute the entropy per particle $\mathcal{S}/\mathcal{N}$, we note that

$$\frac{\mathcal{S}}{\mathcal{N}} = \frac{\mathcal{I}_{\mathcal{S}}}{\mathcal{N}} - \tilde{\alpha} - 2\log\tilde{R} = \frac{\sigma}{\mathcal{N}} + 2\log\tilde{R} \qquad \text{where} \qquad \sigma = \mathcal{I}_{\mathcal{S}} - \tilde{\alpha}\mathcal{N}\,. \tag{4.52}$$

We see that the entropy per particle (4.52) is the sum of two terms: a "universal" (σ) and an "effective" ($\log\tilde{R}$) entropy, which takes into account the effects of the box[6]. Similarly, the free energy per particles can be expressed as

$$\frac{\mathcal{F}}{\mathcal{N}} = \frac{\mathcal{M} - \mathcal{T}(\sigma + 2\mathcal{N}\log\tilde{R})}{\mathcal{N}} = \frac{\mathcal{M} - \mathcal{T}\sigma}{\mathcal{N}} - 2\mathcal{T}\log\tilde{R} = \frac{f_H}{\mathcal{N}} - 2\mathcal{T}\log\tilde{R}\,. \tag{4.53}$$

where the terms f_H and $-2\mathcal{T}\log\tilde{R}$ represent a "universal" and an "effective" free energy, respectively. Differently from the entropy, this additive term includes also the temperature $\mathcal{T}$.

As we have previously seen, the integration of the TOV system is arrested at $\lambda = 1$, i.e. $\tilde{r} = \tilde{R}$. This implies that the workspace has been reduced to the sphere of unitary radius $\tilde{R} = 1$. Thus, in order to get the description of the thermodynamical properties of the isothermal spheres in GR, we need only to study this particular case. Consequently, Eqs.(4.52) and (4.53) yield $\mathcal{S} = \sigma$ and $\mathcal{F} = f_H$. In addition, from Eq.(4.43) we find $\tilde{\alpha} = \alpha$. For this reason, in the following, we shall drop the notation with $\sim$ and write α instead of $\tilde{\alpha}$.

4.2.1. The Nonrelativistic Limit $b \to \infty$

In this Section we consider the nonrelativistic limit $b \to \infty$. For large values of b, the Bessel functons (4.8) (see Ref.[1]) take the asymptotic form

[6] Similar results have been obtained by Banks *et al.* [15] and Pesci [154].

$$K_u(b) \simeq \sqrt{\frac{\pi}{2b}}e^{-b}\Big[1+\frac{4u^2-1}{8b}+\frac{(4u^2-1)(4u^2-9)}{2!(8b)^2}+\frac{(4u^2-1)(4u^2-9)(4u^2-25)}{3!(8b)^3}+...\Big]. \quad (4.54)$$

The thermodynamic quantities (4.44)-(4.46) become

$$\nu \simeq \frac{e^{\alpha-b}}{\sqrt{2\pi^3 b^3}}\Big(1+\frac{15}{8b}+\frac{105}{128b^2}-\frac{315}{1024b^3}+...\Big), \quad (4.55)$$

$$\Theta \simeq \frac{e^{\alpha-b}}{\sqrt{2\pi^3 b^3}}\Big(1+\frac{27}{8b}+\frac{705}{128b^2}+\frac{2625}{1024b^3}+...\Big) = \nu+\frac{3e^{\alpha-b}}{\sqrt{8\pi^3 b^5}}\Big(1+\frac{25}{8b}+\frac{245}{128b^2}+...\Big), \quad (4.56)$$

$$\Pi \simeq \frac{e^{\alpha-b}}{\sqrt{2\pi^3 b^5}}\Big(1+\frac{15}{8b}+\frac{105}{128b^2}+...\Big) = \frac{\nu}{b}. \quad (4.57)$$

From Eq.(4.56) we have that $\Theta \sim \nu$, implying $\mathcal{M} \sim \mathcal{N}$. The other terms in Eq.(4.56) can be seen as corrections due to GR. This implies that the nonrelativistic limit corresponds, also, to the limit of Newtonian gravity. As we have seen in Sec. 2.4, the Newtonian gravity is recovered for $\Phi \to 0$. This means, according to Eq.(4.13), that $\alpha \to \infty$. Let us define the new variable Ψ in the following way

$$\Psi = b-\alpha \qquad \Longleftrightarrow \qquad b = \alpha+\Psi = \alpha\Big(1+\frac{\Psi}{\alpha}\Big). \quad (4.58)$$

From the foregoing expression we have $\Psi/\alpha \to 0$. Taking only the dominant terms of the asymptotic expansions, the thermodynamic quantities (4.55)-(4.57) become

$$\nu \simeq \frac{e^{-\Psi}}{\sqrt{2\pi^3\alpha^3}}\Big(1+\frac{\Psi}{\alpha}\Big)^{-3/2} \simeq \frac{e^{-\Psi}}{\sqrt{2\pi^3\alpha^3}}\Big(1-\frac{3\Psi}{2\alpha}+\frac{15\Psi^2}{8\alpha^2}+...\Big), \quad (4.59)$$

$$\Theta = \nu \simeq \frac{e^{-\Psi}}{\sqrt{2\pi^3\alpha^3}}\Big(1-\frac{3\Psi}{2\alpha}+\frac{15\Psi^2}{8\alpha^2}+...\Big), \quad (4.60)$$

$$\Pi \simeq \frac{e^{-\Psi}}{\sqrt{2\pi^3\alpha^5}}\Big(1+\frac{\Psi}{\alpha}\Big)^{-5/2} \simeq \frac{e^{-\Psi}}{\sqrt{2\pi^3\alpha^5}}\Big(1-\frac{5\Psi}{2\alpha}+\frac{35\Psi^2}{8\alpha^2}+...\Big). \quad (4.61)$$

By now expanding the denominator of the first of Eq.(4.37) in the limit $2\mathcal{M}_\lambda/\lambda \to 0$, we have

$$\frac{d\Psi}{d\lambda} \simeq \frac{\alpha}{\lambda^2}\Big(1+\frac{\Psi}{\alpha}\Big)\frac{\mathcal{N}_\lambda}{\lambda^2} \simeq \frac{\alpha\mathcal{N}_\lambda}{\lambda^2}. \quad (4.62)$$

Now, isolating $\mathcal{N}_\lambda$ on the r.h.s. of the preceding equation and deriving the expression obtained

$$\frac{1}{\lambda^2}\frac{d}{d\lambda}\Big(\lambda^2\frac{d\Psi}{d\lambda}\Big) = \sqrt{\frac{8}{\pi\alpha}}e^{-\Psi}. \quad (4.63)$$

Defining the new radial coordinate $\xi = (8/\pi\alpha)^{1/4}\lambda$, Eq.(4.63) recovers the Emden equation in Newtonian gravity

$$\frac{1}{\xi^2}\frac{d}{d\xi}\Big(\xi^2\frac{d\Psi}{d\xi}\Big)=e^{-\Psi} \tag{4.64}$$

which solution is the singular sphere

$$e^{-\Psi}=\frac{2}{\xi^2}\qquad\Longleftrightarrow\qquad e^{-\Psi}=\sqrt{\frac{\pi\alpha}{2}}\frac{1}{\lambda^2}\,. \tag{4.65}$$

4.2.2. The Ultrarelativistic Limit $b\to 0$

In the ultrarelativistic limit, according to Eq.(4.14), $k_BT\gg mc^2$ and the thermal energy dominates the rest mass energy. A high amount of thermal energy implies a high amount of gravitational energy and for this reason we talk about *high energy instabilities*. It has been shown (see Ref.[55]) that the behaviour of the matter, in these conditions, is similar to that of a self-gravitating photonic gas (for this reason, some authors talk about "photon stars", see Ref.[55] and references therein). In the following, when we write "radiation" we mean the matter in the ultrarelativistic limit. In the limit $b\to 0$, the Bessel functions (4.8) take the asymptotic form [1]

$$K_u(b)\sim\frac{2^{u-1}\Gamma(u)}{b^u}\,, \tag{4.66}$$

where $\Gamma(u)$ is the Euler function

$$\Gamma(u)=\int_0^\infty t^{u-1}e^{-t}dt\,. \tag{4.67}$$

Thanks to Eq.(4.66), the thermodynamic quantities (4.44)-(4.46) become

$$\nu\sim\frac{2e^\alpha}{\pi^2b^3}\,, \tag{4.68}$$

$$\Theta\sim\frac{e^\alpha}{4\pi^2b}\Big(\frac{24}{b^3}+\frac{1}{b}\Big)\sim\frac{6e^\alpha}{\pi^2b^4}=\frac{3\nu}{b}\,, \tag{4.69}$$

$$\Pi\sim\frac{e^\alpha}{4\pi^2b}\Big(\frac{8}{b^3}-\frac{1}{b}\Big)\sim\frac{2e^\alpha}{\pi^2b^4}=\frac{\nu}{b}\,, \tag{4.70}$$

By comparing Eq.(4.69) and Eq.(4.70), the reader can see $\Theta=3\Pi$, which corresponds to the EOS (3.22) $P=\epsilon/3$ (see Sec. 3.1). Isothermal gaseous spheres in GR, described by an EOS of the kind (3.22), have been analyzed by Chavanis [45, 46, 55] and, in the following, we refer to his results. In the ultrarelativistic regime, the density contrast (4.27) becomes

$$\mathcal{R}=\frac{b_1}{b_0}\,\frac{3K_3(b_0)+K_1(b_0)}{3K_3(b_1)+K_1(b_1)}\sim\Big(\frac{b_1}{b_0}\Big)^4\,. \tag{4.71}$$

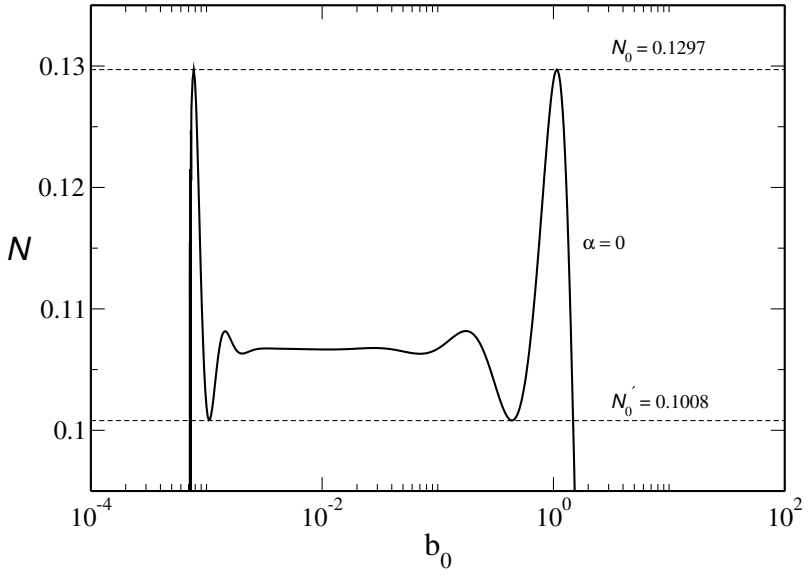

Figure 4.1: *Particle number $\mathcal{N}$ versus central value of the reverse temperature b_0, for $\alpha = 0$ (the curve goes from the right to the left). As the reader can see, the curve is spatially delimited by two maximal points (the descending part of the curve is not represented). As we will see in the following, only the points forming the "gaseous" phase (starting from large values of b_0 until the maximum $\mathcal{N}_0$) represent stable physical solutions. The values of $\mathcal{N}$ associated with the two first critical points are also listed.*

4.3. Particle number and Definition of $\mathcal{N}_{max}$

For a given value of α, the TOV system (4.37) can be integrated for several values of b_0 in the interval $(0, +\infty)$. As a result, we obtain the functions $\mathcal{M} = \mathcal{M}(b_0)$, $\mathcal{N} = \mathcal{N}(b_0)$ and $\mathcal{T} = \mathcal{T}(b_0)$ (remember that $\mathcal{T}_1 = 1/b_1$). In this Section we will focus our attention, in particular, on the particle number $\mathcal{N}$. The reason for a detailed study of $\mathcal{N}$ arises because, in the framework of the Thomas-Fermi model, the series of equilibria are obtained for fixed values of the baryon number (see Appendix A).

In Fig. 4.1 we give a first graphical representation of $\mathcal{N}(b_0)$, for $\alpha = 0$. Starting from large values of b_0, we see the achievement of a maximal point, representing the highest value that the baryon number can reach, for a given value of α. Then, the curve starts to decrease and presents a sequence of several oscillations, more and more damped (due to the lenght scales involved, the small oscillations are not evident). The damping starts being reduced for $b_0 \sim 5 \times 10^{-3}$. The amplitude of the oscillations become more and more considerable and the curve takes a symmetric structure respect to the right part. We observe the achievement of a second local minimum and a second local maximum which values, such as the maximum and minimum of the right part, are $\mathcal{N}_0$ and $\mathcal{N}_0'$, respectively. Then the curve begins decreasing, to be infinitesimal for $b_0 \to 0$ (not represented in the figure).

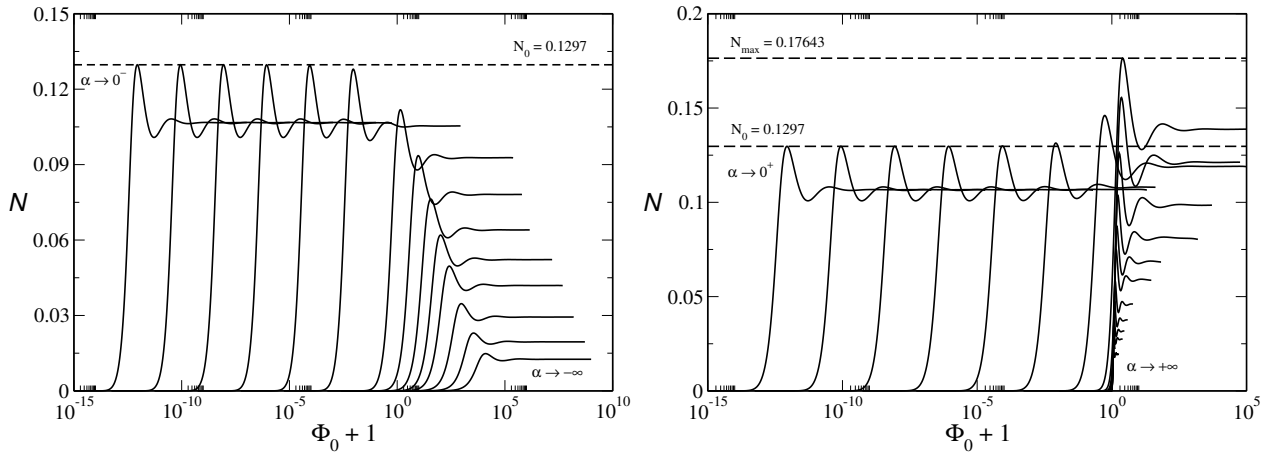

Figure 4.2: ***Left Panel****: Total particle number $\mathcal{N}$ versus the central value of the gravitational potential Φ_0, for several (negative) values of α. Starting from the small values of α and going on to large and negative ones, the curves move progressively from the left to the right of the figure, in the region of intense gravitational fields. In the limit $\Phi_0 \to -1$ the asymptotic configuration $\alpha = 0$ is achieved.* ***Right Panel****: From the left to the right (according to the values of α, from the smallest to the biggest), the curves leave the limiting configuration $\alpha = 0$ to achieve a limiting configuration, characterized by the critical value $\mathcal{N}_{max} = 0.1764$, obtained for $\alpha = 5.012$. For $\alpha > 5.012$, the curves start to decrease and to become more and more narrow.*

The right part of the curve, starting from $b_0 >> 1$ and ending in $\mathcal{N}_0$ forms the so called "gaseous" phase in the series of equilibria [24]. In the following we will better see that the maximum of the function $\mathcal{N}(b_0)$ corresponds to the collapsing point of the series of equilibria in the canonical ensemble.

Although the numerical integration has been performed by means of b, to be consistent with the results presented in Chap. 5, we use the representation in terms of Φ_0 [remember Eq.(4.13)]. This changement presents an unpleasant feature: the configuration $\alpha = 0$, well computed by the b-representation, cannot be reached when we consider the Φ-representation. According to Eq.(4.13), indeed, we have $\sqrt{\Phi + 1} = |\alpha|/b$, which implies $\sqrt{\Phi + 1} = 0$, being $b \neq 0$. So, in terms of the new representation, we can reach the configuration $\alpha = 0$ only *asymptotically.*

In Fig. 4.2 we distinguish, respectively, between the negative (left panel) and the positive (right panel) values of α. In both of figures, we have represented $\mathcal{N}(\Phi_0)$. According to Eq.(4.13), the curves appear inverted passing from the b-representation to the Φ-representation. More precisely, the "right" part in b-representation becomes the "left" part in Φ-representation. Consequently, the "gaseous" phase is placed on the left of Fig. 4.2.

Let us now start our discussion from the negative values of α, represented in the left panel of Fig. 4.2.

Differently from Fig. 4.1, we did not represent the second minimum and maximum (as we shall see in the following they refer to unstable configurations). The limiting situations $\alpha \to -\infty$ and $\alpha \to 0^-$ are placed in two different regions, far from each others. For large (in absolute value) and negative values of α, the curves are placed in the region of strong gravitational fields, corresponding to the ultrarelativistic limit. In this part, the EOS of the fluid is $\Pi = \Theta/3$ or, equivalently, $P = \epsilon/3$.

If we progressively increase the value of α, we see a constant increase of the maximum value of the curves $\mathcal{N}(\Phi_0)$ and a "left-shift" of the maximum position. By still increasing (reducing if we consider $|\alpha|$) the values of α, we see that the curves reach the asymptotic value $\mathcal{N}_0$ in a region where the importance of the general relativistic effects is considerable. In fact, we have $\Phi_0 \to -1$ which means, according to Eq.(2.39), $\xi \to +\infty$ (see Sec. 2.2).

Different behaviour is shown in the right panel of Fig. 4.2, where we have considered the case $\alpha > 0$. For $\alpha \to 0^+$, the trend of the curves reproduces the same behaviour found for $\alpha < 0$. This "equivalence" between the two situations is kept until $\Phi_0 + 1 \sim 10^{-5}$, when small modifications in the behaviour of the curves are more evident. As we see, for increasing values of α and Φ_0, the maximum of the function $\mathcal{N}(\Phi_0)$ converges to a critical point, a "maximum of maxima", indicated by $\mathcal{N}_{max}$ (see also Ref.[159]). Numerically[7], we find that $\mathcal{N}_{max} = 0.1764$, $\alpha(\mathcal{N}_{max}) = 5.012$, $b_0 = 3.149$ $\Phi_0(\mathcal{N}_{max}) = 1.533$.

From a physical point of view, $\mathcal{N}_{max}$ can be seen as the maximum number of particles that can fill up the sphere encapsulating the system without collapsing. In Sec. 4.4 we will see that the caloric curve associated with $\mathcal{N}_{max}$ consists of only one point. For $\alpha > 5.012$ the maximum value of the $\mathcal{N}(\Phi_0)$ decreases and its position converges to $\Phi_0 \sim 0$ (corresponding to the nonrelativistic limit). For increasing values of α the curves become more and more narrow and the typical values of the particle number are reduced respect to those reached for small and positive values of α.

In Fig. 4.3 we have represented, as a function of α, the maximum value $\mathcal{N}_{gm}$ of $\mathcal{N}(\Phi_0)$. This diagram is very important because it allows us to understand some features present in the series of equilibria (see Sec. 4.4). If we look at Fig. 4.3, we see that $\mathcal{N}_{gm} = \mathcal{N}_{gm}(\alpha)$ is infinitesimal in the ultrarelativistic limit $\alpha \to -\infty$ (due to the scale used in the figure, it seems $\mathcal{N}_{gm} = 0$). Subsequently, for $\alpha \sim -17$, the curve begins increasing and reaches the point $\mathcal{N}_{max}$. It is remarkable to note that $\alpha = 0$ does not represent a peculiar case in this diagram. Once reached $\mathcal{N}_{max}$, the curve regularly starts its decrease, which is less steep than the part $\alpha < 5.012$. We note also that the behaviour of $\mathcal{N}_{gm} = \mathcal{N}_{gm}(\alpha)$ is asymmetric with respect to $\mathcal{N}_{max}$.

[7]These values are in accordance with the results of Roupas [159]: $2\mathcal{N}_{max} = 0.35$, $b_0 = 3.18$. However, thanks to the scaling derived in Sec.4.2, our model does not provide a critical value of the radius associated with $\mathcal{N}_{max}$ as Roupas' model does.

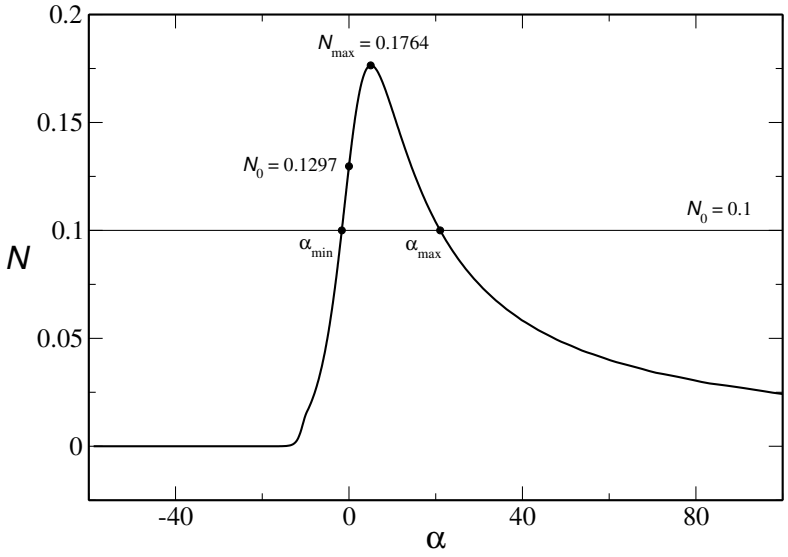

Figure 4.3: $\mathcal{N}_{gm}$ *versus* α*, for relativistic isothermal spheres. For a given line level (*$\mathcal{N} = 0.1$ *in the case here considered), there exist two solutions, corresponding to* α_{min} *and* α_{max}*. These points determine the lowest and the highest value of* α *providing physical solutions in the series of equilibria. The points* $\mathcal{N}_0$ *and* $\mathcal{N}_{max}$ *are also represented.*

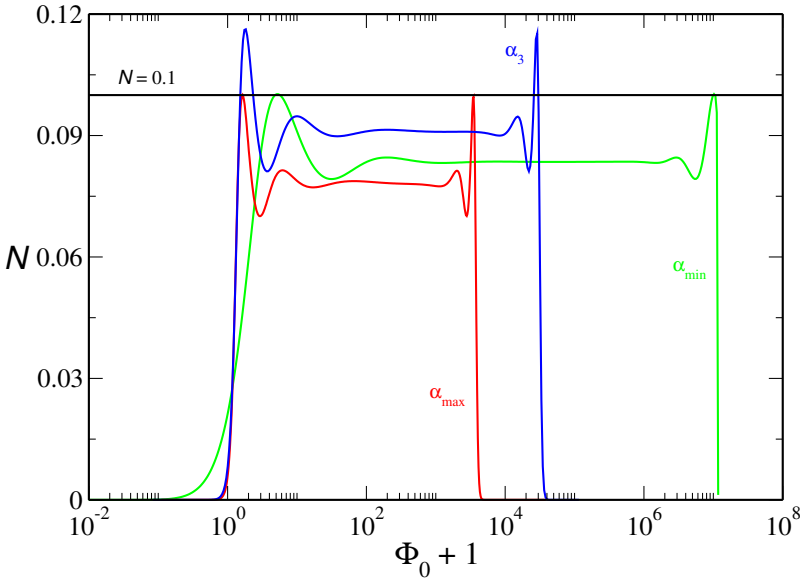

Figure 4.4: $\mathcal{N}$ *versus* Φ_0 *for several values of* α*. The line level* $\mathcal{N} = 0.1$ *identifies the maxima of the curves associated with* α_{min} *and* α_{max}*. In particular, the maxima delimiting the gaseous phase determine the points* Λ_{min} *and* η_c*. By contrast, for* $\alpha = \alpha_3$*, the line level identifies four intersection points that, in the series of equilibria, are placed between* Λ_{min} *and* η_c*.*

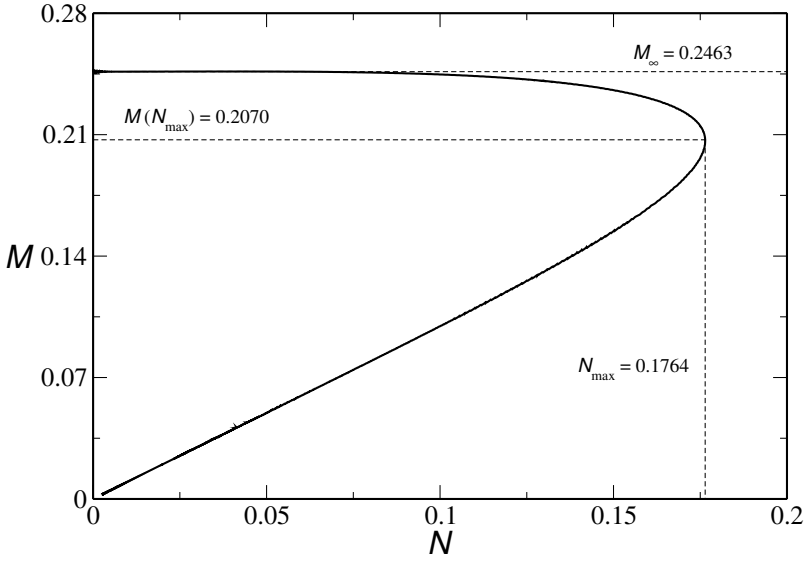

Figure 4.5: *Maximum mass $\mathcal{M}_{gm}$ as a function of the maximum particle number $\mathcal{N}_{gm}$. In the limit $\mathcal{N}_{gm} \to 0$ we can observe two different behaviours: for $\alpha < 0$, the function $\mathcal{M}_{gm} = \mathcal{M}_{gm}(\mathcal{N}_{gm})$ achieves the asymptotic value $\mathcal{M}_\infty$. Conveserly, for $\alpha > 0$, there exists linear proportionality $\mathcal{M}_{gm} \propto \mathcal{N}_{gm}$. Moreover, there exists a maximum value (not shown in the figure), which value is $\mathcal{M}_{max} =$* 0.2464.

To understand the link between this diagram and the caloric curves, let us consider, as an example, the line level $\mathcal{N} = 0.1$. As we see from the figure, there exist two intersection points between the line level and the curve, identified by the values α_1 (being the point before $\mathcal{N}_{max}$) and α_2 (being the point after $\mathcal{N}_{max}$). If we consider the corresponding curve $\mathcal{N}(\Phi_0)$ of α_1 (green line in Fig. 4.4), we see that the line level $\mathcal{N} = 0.1$ identifies the two maxima of the curve. If we now take a value of α in the interval $\alpha_1 < \alpha_3 < \alpha_2$ (blue line in Fig. 4.4), we see that the line level identifies more than two intersection points.

This happens because the value of $\mathcal{N}_{gm}(\alpha_3)$ is higher than that associated with α_1. This is true for *all* the values of α in the interval $[\alpha_1, \alpha_2]$. When the line level $\mathcal{N} = 0.1$ reaches α_2, we are in a situation similar to α_1: there are two intersection points, corresponding to the maxima of the function $\mathcal{N}(\Phi_0)$. This argument suggests that for $\alpha < \alpha_1$ and $\alpha > \alpha_2$ there are not intersections between the line level and the curve $\mathcal{N}_{gm}(\alpha)$. This implies that α_1 and α_2 are the minimum (α_{min}) and the maximum (α_{max}) value of α that can provide physical solutions for the caloric curve.

The existence of α_{min} and α_{max}, for *any* line level $\mathcal{N} = \mathcal{N}_{spec}$, implies that the caloric curve is spatially delimited. In Sec. 4.4 we shall see that this spatial limitation is manifested by the presence of two spirals [159].

Furthermore, in Fig. 4.5, we have represented the mass-energy corresponding to the points $\mathcal{N}_{gm}$, for a wide range of values of α. We distinguish two different regimes, separated by $\mathcal{N}_{max}$. At this point, the mass energy reaches the value $\mathcal{M}(\mathcal{N}_{max}) = 0.207$. For $\mathcal{M} \geq 0.207$ (corresponding to the case $\alpha < 5.012$ in Fig. 4.3), the mass reaches an asymptotic value[8] in the limit $\mathcal{N} \to 0$. Subsequently, for increasing values of $\mathcal{N}$, the mass-energy decreases by reaching the characteristic value 0.207 for $N_{gm} = \mathcal{N}_{max}$. By now considering the case $\mathcal{M}_{gm} < 0.207$, we see a decrease of the values of $\mathcal{M}_{gm}$ for decreasing values of $\mathcal{N}_{gm}$. Moreover, we observe that, for $\mathcal{N}_{gm} \leq 0.12$, there exists a direct proportionality between $\mathcal{M}_{gm}$ and $\mathcal{N}_{gm}$, that is $\mathcal{M}_{gm} \propto \mathcal{N}_{gm}$. This scaling property is more accentuated in the Newtonian limit $\mathcal{N}_{gm} \to 0$. Numerically, we find

$$\mathcal{M}_{gm} = 0.9878\,\mathcal{N}_{gm}\,. \tag{4.72}$$

4.4. Caloric Curves

In this Section we analyze the behaviour of the series of equilibria. The goal of this section is to see how much the general relativistic corrections influence the onset of the stability compared to Newtonian gravity (Refs.[53, 133] and references therein). In Fig. 4.6 we recall the procedure used to get the series of equilibria. For a given line level (in the case here considered $\mathcal{N} = 0.1$), we can determine the values of Φ_0 satisfying the condition (see Appendix A)

$$\mathcal{N}(\Phi_0) = \mathcal{N}_{spec}\,, \tag{4.73}$$

where $\mathcal{N}(\Phi_0)$ is computed by means of Eq.(4.38). As we have seen in Sec. 1.3 and Appendix A, the natural variables apt to describe the series of equilibria are the rescaled energy Λ and the rescaled reverse temperature η [see Eq.(A.2)] which definitions, because of the scaling $\mathcal{C}_N$ found in Sec. 4.2, are

$$\Lambda = \frac{\mathcal{N} - \mathcal{M}}{\mathcal{N}^2}\,, \qquad \eta = \frac{\mathcal{N}}{\mathcal{T}}\,. \tag{4.74}$$

For a given value of $\mathcal{N}$, the curve $\eta = \eta(\Lambda)$ is parameterized by the pair of values (α, Φ_0). This implies that the problem has three free parameters: $\mathcal{N}$, α and Φ_0. In the following, we study the series of equilibria for five values of $\mathcal{N}$ in the interval $(0, \mathcal{N}_{max}]$. Furthermore, we develop parallely the analysis in the microcanonical and canonical ensembles. In Fig. 4.7 we have represented the caloric curve for

[8] Although not shown in the figure, we note that, for $\alpha = -5.754$, the mass-energy achieves a (absolute) maximum value, being $\mathcal{M}_{max} = 0.2464$ (in accordance with Chavanis [55]).

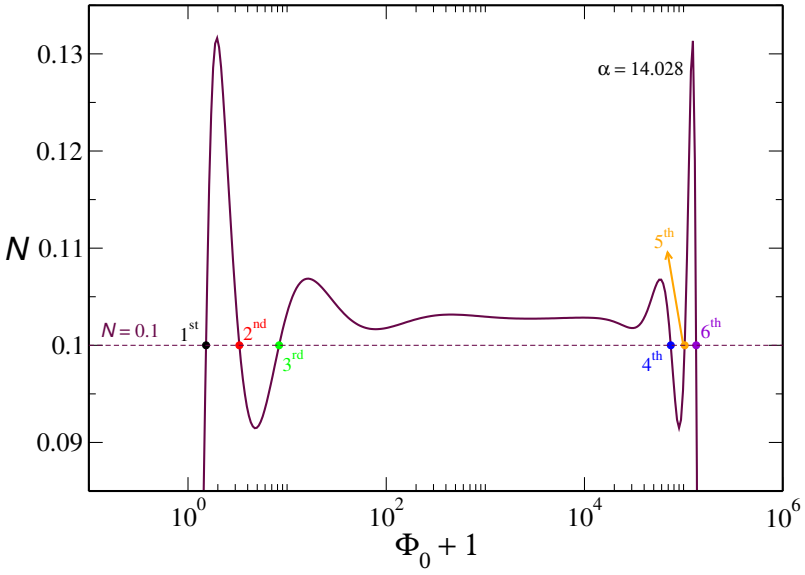

Figure 4.6: *Graphic construction of the caloric curve. Fixed the line level ($\mathcal{N} = 0.1$, the six points are identified by means of the constraint* (4.73)*. The intersection points are indicated by the full circles and are classified according to the sequence order. The first intersaction is related to the "gaseous" phase and represents the only stable physical state. The other points correspond to unstable states (see also Fig. 4.7). The value of α is also shown.*

$\mathcal{N} = 0.01$. In both of figures (such as the others, see below) we have emphasized the contribution of negative[9] (left panel) and positive (right panel) values of α, by means of different colors (red for $\alpha < 0$ and black for $\alpha \geq 0$).

Starting from the case $\alpha > 0$, the trend of the curve corresponds to that obtained in Newtonian gravity, suggesting that the conditions of the gravitational collapse in both microcanonical and canonical ensembles do not depend on the intensity of the gravity. However, the general relativistic corrections change the limiting values of the reverse critical temperature η_c and the critical energy Λ_c. In particular, we find that canonical instabilities set in for $\eta < 2.525$ (see Secs. 1.2 and 4.5) and microcanonical instabilities for a critical energy $\Lambda < 0.335$ (see Secs. 1.2 and 4.5). This implies that, in GR, the system undergoes a collapse *more easily* than in Newtonian gravity and that a higher level of gravity makes the system more unstable than a Newtonian one. This feature is more evident for large values of $\mathcal{N}$ (see below).

Apart from that, the thermodynamical interpretation of the right panel of Fig. 4.7 is the same as that discussed in Sec. 1.2, where we have considered Lynden-Bell & Wood's model [133]. In the canonical ensemble, the instability sets in for $\eta = \eta_c$ and, in the microcanonical one, for $\Lambda = \Lambda_c$. Also, GR

[9] More precisely, the high energy instabilities correspond to *all* $\alpha < 5.012$.

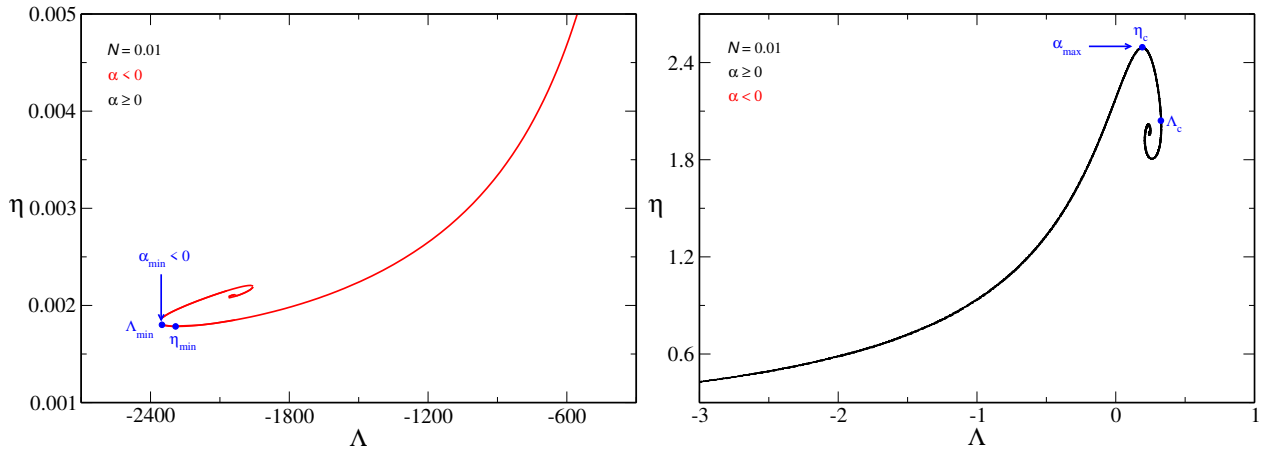

Figure 4.7: *Equilibrium phase diagram for* $\mathcal{N} = 0.01$. *Hereafter, the red part shows the contribution of* $\alpha < 0$ *whereas the black one the contribution of* $\alpha \geq 0$. *The left panel shows the case of the high energy instabilities. The values at the critical points are* $\Lambda_{min} = -2344.3$ *and* $\eta_{min} = 1.925 \times 10^{-3}$. *The right panel refers to the case of low energy instabilities. The values at the critical points are* $\Lambda_c = 0.325$ *and* $\eta_c = 2.495$, *relatively close to the Emden and Antonov limits. The shape of the curve, moreover, is very similar to the spiral of Lynden-Bell & Wood.*

did not modify the ensemble inequivalence. Let us indeed consider the part of the spiral between the points η_c and Λ_c. Analogous to Newtonian gravity (see Sec. 1.2), this part of the curve is unstable from a canonical point of view but stable in a microcanonical description. Furthermore, the specific heat is negative. Because the value of $\mathcal{N}$ is relatively small ($\mathcal{N} = 0.01$), the density profiles associated with the collapsing points have a trend very similar to those observed in Newtonian gravity. Therefore, we can say that Fig. 4.7 (right panel) offers the generalization of Antonov instability to GR. As we shall see in the following, the properties above described do not change for higher values of $\mathcal{N}$.

Let us now go back to Fig. 4.7 (left panel). We observe a specular behaviour compared to the situation precedingly analyzed. However, there are noticeable differences. Although not perfectly evident (see also Fig. 4.8), the left part of the caloric curve is delimited by a critical point, corresponding to a maximum of energy (corresponding to the minimum of Λ, identified by Λ_{min}). In addition, there exists a critical temperature (corresponding to a minimum of η) which plays the same role of η_c. After the point Λ_{min} the curve makes several rotation, becoming a spiral. The"shape" of the spiral is nonetheless slightly different from the right spiral. As the reader can appreciate, the spiral is narrow.

The thermodynamical interpretation of the points Λ_{min} and η_{min} is analogous to, respectively, Λ_c and η_c. In the microcanonical ensemble the stable solutions are represented by all the points between Λ_{min} and Λ_c whereas, in the canonical ensemble, the stable states are between η_{min} and η_c. Looking at the

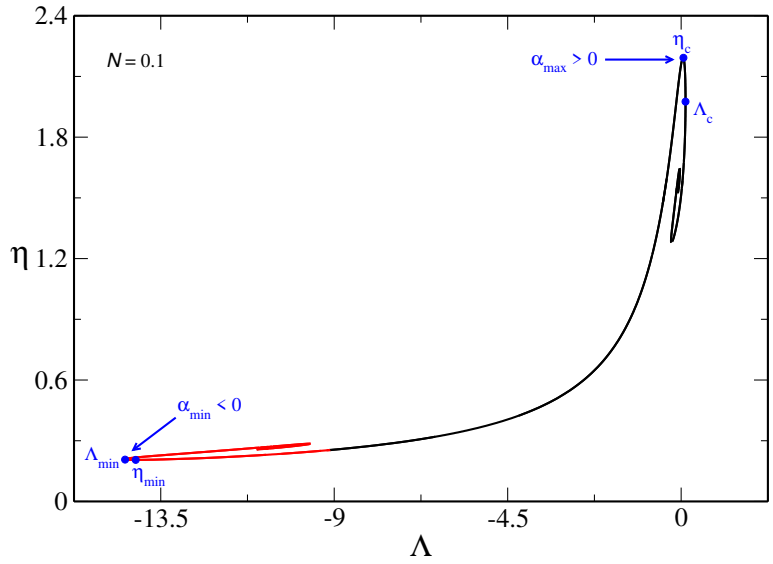

Figure 4.8: *Equilibrium phase diagram for* $N = 0.1$. *The values at the critical points are* $\Lambda_{min} = 14.43$, $\Lambda_c = 0.114$, $\eta_{min} = 0.205$ *and* $\eta_c = 2.192$. *Compared to the preceding figure, the reader can appreciate a substantial modification in the shape of the two spirals. This shows the manifestation of the relativistic effects. However, the thermodynamical interpretation of the curve is the same as those previously shown.*

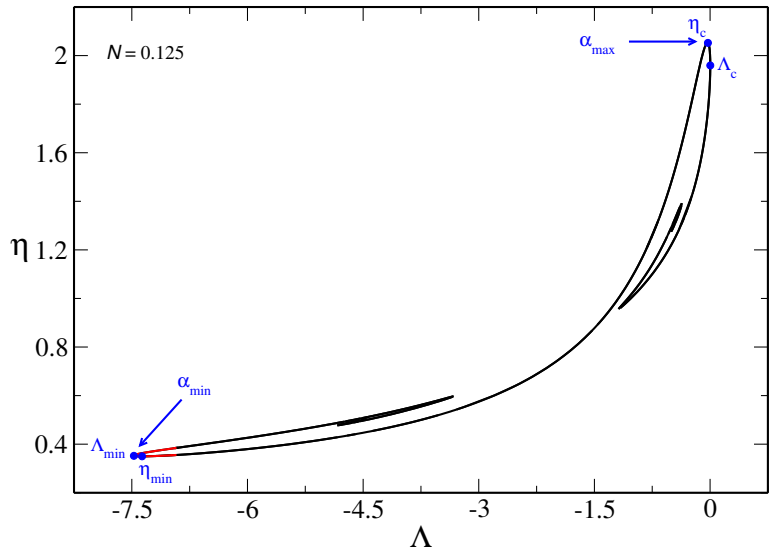

Figure 4.9: *Equilibrium phase diagram for* $\mathcal{N} = 0.125$. *The values of the critical points are* $\Lambda_{min} = -7.472$, $\Lambda_c = 0.018$, $\eta_{min} = 0.354$ *and* $\eta_c = 2.051$.

numerical values involved, we see that $|\Lambda_{min}| \gg \Lambda_c$ and that $\eta_{min} \ll \eta_c$, by implying that the left part of the caloric curve is formed by states having a high amount of gravitational energy and an elevated temperature [remember that $\eta \to 0$ implies $\mathcal{T} \to +\infty$, see Eq.(4.74)].

For this reason, in his work [159], Roupas distinguishes between "low" and "high" energy gravitational instabilities. Low energy instabilities correspond to the usual Antonov instabilities: in this case, indeed, the thermal energy is weak compared to the gravity and not able to halt the onset of the gravitational instability. Conversely, high energy instabilities are caused by the high amount of the thermal energy which produces an intense gravitational field. For this reason, high energy instabilities have a general relativistic origin.

Let us now consider the caloric curve obtained for $\mathcal{N} = 0.1$ (Fig. 4.8). The spatial extension of the curve is considerably reduced respect to the former case. This is explained by considering Fig. 4.3. In this case, indeed, the height of the line level is higher than $\mathcal{N} = 0.01$ and, consequently, the values of α_{min} and α_{max} are closer. This implies that the difference between the values of Λ_{min} and Λ_c, as η_{min} and η_c, is reduced. In other words, for increasing values of $\mathcal{N}$, we expect that the four critical points converge to the same limiting one, represented by $\mathcal{N}_{max}$.

We note a second difference compared to the case $\mathcal{N} = 0.01$. There is a strong asymmetry between the part of the curve formed by $\alpha < 0$ and that formed by $\alpha \geq 0$. This is not surprising, because the system is slowly approaching the value $\mathcal{N}_0$. From a thermodynamical point view, Figs. 4.7 and 4.8 describe the same physical situation[10]. This leads us to the conclusion that GR does not change the thermodynamical properties of the gas but, rather, it modifies the critical values of energy and temperature for the onset of the instabilities.

Figs. 4.9 and 4.10 represent the natural evolution of the diagram depicted in Fig. 4.8. In Fig. 4.9 we have represented the caloric curve associated with a value of $\mathcal{N}$ slightly below $\mathcal{N}_0$. We see that the red part is almost disappeared. The shape of the spiral is very different from that typical of the Newtonian gravity[11]. This is a clear manifestation of the general relativistic corrections when the intensity of the gravitational fields is higher. Another interesting feature comes out if we consider the point Λ_c. Compared to the preceding cases, indeed, its value is considerably reduced and it is now close to zero.

The case $\mathcal{N} = 0.13$ (Fig. 4.10) displays a new interesting feature. As we see, the two spirals are not anymore split but, rather, they are linked. This phenomenon can be explained by means of the

[10] The two figures show the same kind of gravitational collapse but, of course, they do not represent the *same* physical system.

[11] This comparison is missing for what concerns the left spiral, because the high energy instabilites are not present in the Newtonian regime (they can be reached only in the limits $\Lambda_{min} \to -\infty$ and $\eta_{min} \to 0$).

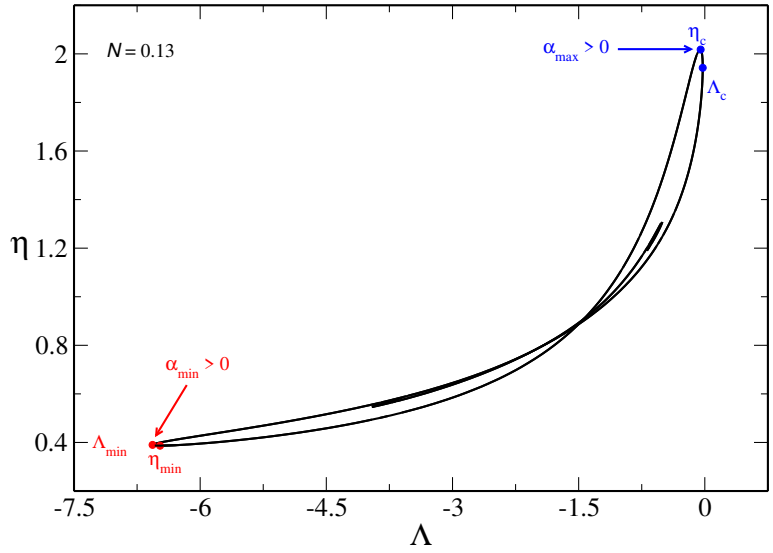

Figure 4.10: *Equilibrium phase diagram for* $\mathcal{N} = 0.13$. *The values at the critical points are* $\Lambda_{min} = -6.566$, $\Lambda_c = -0.025$, $\eta_{min} = 0.387$ *and* $\eta_c = 2.018$. *Differently from the preceding case, the values of* α *are all positive, by virtue of the fact that* $\mathcal{N} > \mathcal{N}_0$. *Moreover, we see a "junction" points between the two spirals. As discussed in the text, this is a consequence of the fact that* $\mathcal{N} > \mathcal{N}_S$.

diagram $\mathcal{N} = \mathcal{N}(\Phi_0)$ (Fig. 4.11). Here we have represented, for the line level $\mathcal{N} = 0.1$, the values of α related to the points η_c and η_{m2} (we did not have represented η_{m1} but the treatment is equivalent). In Fig. 4.8 the two spirals are not linked because η_{m1} and η_{m2} are determined by two different values of α. In Fig. 4.10, the spirals are linked because $\mathcal{N} = 0.13 > \mathcal{N}_S$, where $\mathcal{N}_S$ is defined as the first local minimum of the function $\mathcal{N}(\Phi_0)$ evaluated for $\alpha = 5.012$ (see Fig. 4.11). $\mathcal{N}_S$ represents the highest value achievable by the first local minimum, corresponding to the highest (lowest) position for η_{m1} (η_{m2}) in the caloric curve. In other words, $\mathcal{N}_S$ represents the value at which $\eta_{m1} = \eta_{m2}$. This happens for any α having $\mathcal{N}_{gm} \geq \mathcal{N}_S$ (numerically we find $\mathcal{N}_{gm} = \mathcal{N}_S$ for $\alpha = -0.102$ and $\alpha = 14.69$).

The reason is easily comprehensible if we consider again Fig. 4.11. A line level $\mathcal{N} \geq \mathcal{N}_S$ does not intersect any local minimum of the curve $\mathcal{N}(\Phi_0)$, that is the local minimum of $\mathcal{N}(\Phi_0)$ is always under $\mathcal{N}_S$. The only critical points identified by the line level correspond either to N_{gm} or to secondary critical points (placed in the oscillatory part of the curve). For this reason, if $\alpha > -0.102$ ($\alpha < 14.69$), the two spirals are linked.

If we increase the value of $\mathcal{N}$, we arrive to the situation depicted in Fig. 4.12, where we have considered the caloric curve for $\mathcal{N} = 0.15$. The two spirals are not anymore present and the caloric curve got a "8-shape". Looking at the series of equilibria, we also mention that its spatial extension is considerable reduced respect to the cases previously analyzed. The four critical points Λ_{min}, η_{min}, η_c and Λ_c are

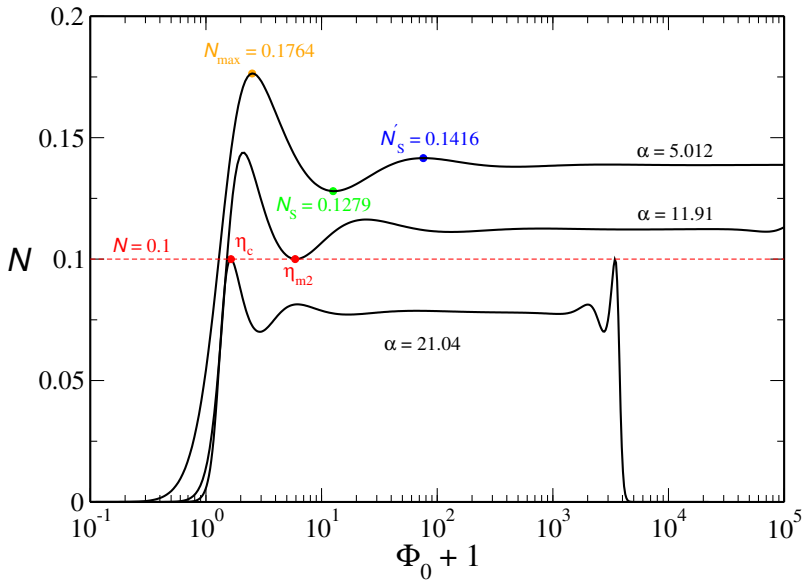

Figure 4.11: *Identification of the points η_c and η_{m2} in the $\mathcal{N}(\Phi_0)$ diagram (η_{min} and η_{m1} are missing). As discussed in the text, η_c and η_{m2} are determined by the critical points of the curve $\mathcal{N}(\Phi_0)$ that are placed on the line level $\mathcal{N} = 0.1$. In addition, the critical values $\mathcal{N}_S$ and $\mathcal{N}'_S$ are also indicated. These points are responsible of the "spiral junction" ($\mathcal{N}_S$, see Fig. 4.10) and of "8-shape" ($\mathcal{N}'_S$, see Fig. 4.12).*

closer and closer. At the same time, we notice that the position of this "junction" point of the spirals did not change. This is not surprising, because it is related to $\mathcal{N}_S$.

By means of the $\mathcal{N}(\Phi_0)$ diagram depicted in Fig. 4.11, we can easily understand the rising of this new feature in the caloric curve. The first intersection of a line level with the $\mathcal{N}(\Phi_0)$ curve is placed, in the caloric curve, on the stable branch, in both microcanonical and canonical ensemble (see Figs. 4.6 and 4.13). The second intersection belongs instead to the branch starting after the point η_c. The intersections of higher order are placed in the region of the winding of the spiral.

If we now consider again Fig. 4.11, we have identified a third critical point, namely $\mathcal{N}'_S$, corresponding to the first maximum (after $\mathcal{N}_{max}$) of the curve $\mathcal{N} = \mathcal{N}(\Phi_0)$. For a line level $\mathcal{N} \geq \mathcal{N}'_S$, we find *at the most* two solutions, corresponding to the gaseous and the condensed phase. The caloric curve in Fig. 4.12 is obtained for $\mathcal{N} = 0.15 > \mathcal{N}'_S$: for this reason there are not anymore evidences about the presence of the two spirals. The two branches are indeed formed only by points corresponding to the first or the second intersection.

If we now increase the value of $\mathcal{N}$, the caloric curves keep the "8-shape", becoming however more and more narrow (the four critical points move to the "junction" point). In the end, for $\mathcal{N} = \mathcal{N}_{max}$ the caloric curve is reduced to one point. Although the shape of the caloric curve changes according to

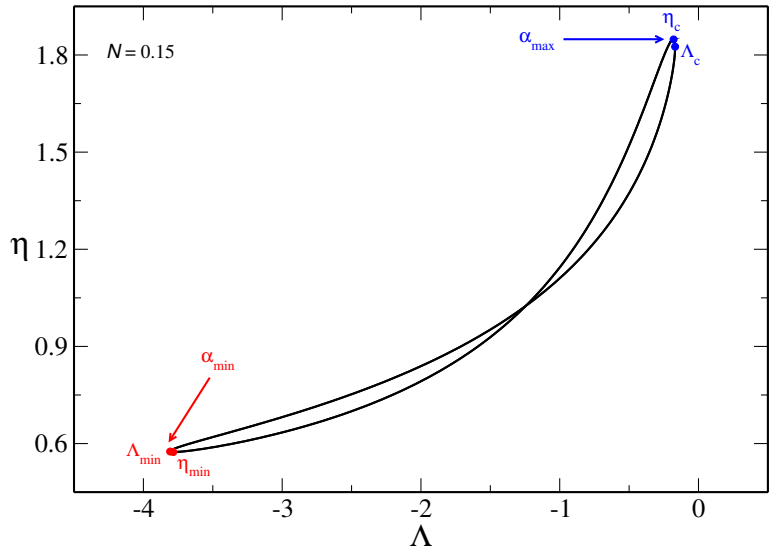

Figure 4.12: *Equilibrium phase diagram for* $\mathcal{N} = 0.15$. *The values at the critical points are* $\Lambda_{min} = -3.807$, $\Lambda_c = -0.168$, $\eta_{min} = 0.574$ *and* $\eta_c = 1.848$. *The trend of the curve displays a new behaviour, the "8-shape". From a thermodynamical point of view, however, the rising of this "8-shape" does not modify the onset of the thermodynamical instabilities. We stress that the origin of this feauture is purely general relativistic.*

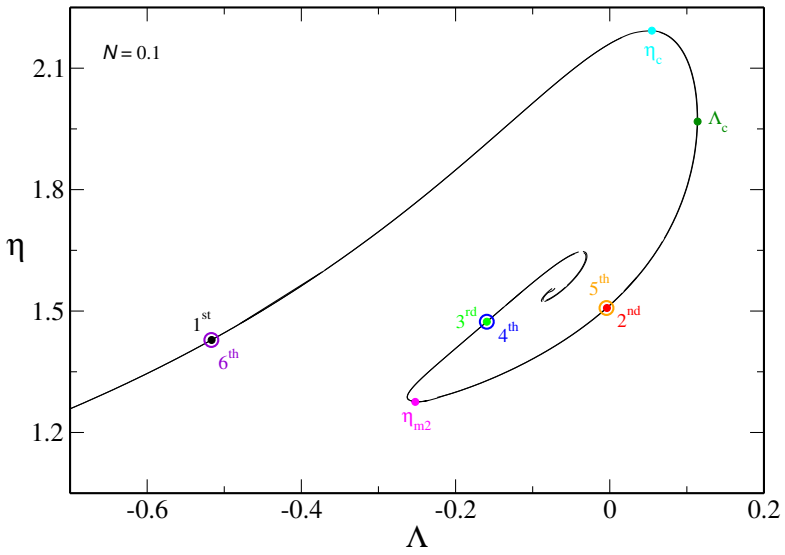

Figure 4.13: *Representation of the position in the series of equilibria of the intersection points defined in Fig. 4.6. The presence of a second spiral (not visible because of the scale used in the figure but represented by the three empty circles) is a pure relativistic effect. As discussed in the text, this second spiral originates in the right part of the* $\mathcal{N}(\Phi_0)$ *diagram.*

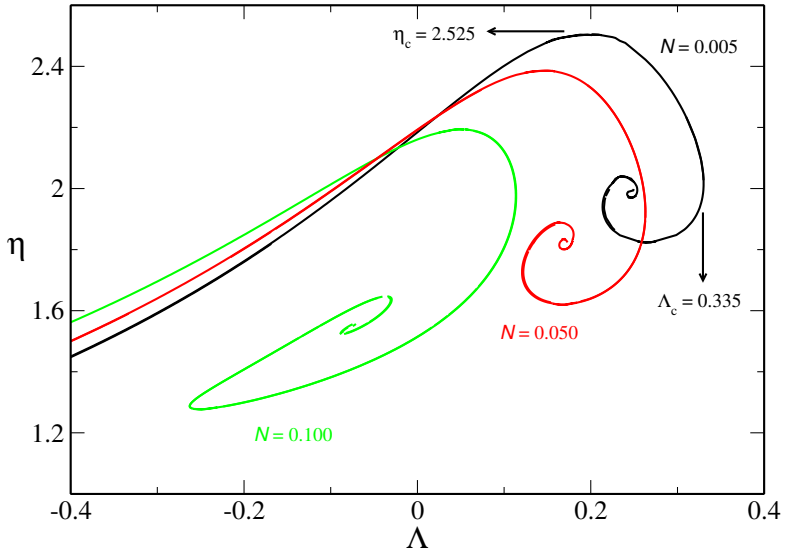

Figure 4.14: *Evolution of the series of equilibria according to the "degree of relativity" of the system, in the case of low energy instabilities. From the left to the right, the importance of the general relativistic effects is more and more reduced ($\mathcal{N}$ decreasing). For small values of the modified compactness $\mathcal{C}_N$ [see Eq.*(4.33)*], the curves converge to the spiral of Lynden-Bell & Wood (black line).*

the value of $\mathcal{N}$, from a thermodynamical point of view, the interpretation of the different series of equilibria is the same. Once exceeded the critical energies (reverse temperatures) Λ_{min} and Λ_c (η_{min} and η_c) the system will undergo a collapse, in both microcanonical and canonical ensembles.

However, Fig. 4.13 shows a second interesting feature. Let us consider the position of the points corresponding to the fourth, fifth and sixth intersection (represented by the empty circles). Apparently, these points seem to coincide with those corresponding to first, second and third intersection. If we look more carefully, we see that the empty points are slightly shifted respect to the full ones. By considering all the amount of the points making the series of equilibria, we conclude that these (unstable) points form a "second caloric curve", which goes on in opposite sens respect to that forming the main part of the diagram. This leads us to conclude that the series of equilibria are made by "two" curves, very close, one being the general relativistic extension of the usual Newtonian spiral and the other being completely unstable. We stress that this second curve is formed by the points placed in the region of intense gravitational fields within the $\mathcal{N}(\Phi_0)$ diagram (see Fig. 4.6).

Because of this specularity of the $\mathcal{N} = \mathcal{N}(\Phi_0)$ diagram we have that, for $\mathcal{N} = \mathcal{N}_{max}$, the caloric curve is made by *two* points and not one, as we have previously asserted. Only one point represents a stable state (that corresponding to the first maximum of the curve $\mathcal{N}(\Phi_0)$) and, only in this case, the system does not collapse (in both microcanonical and canonical ensemble).

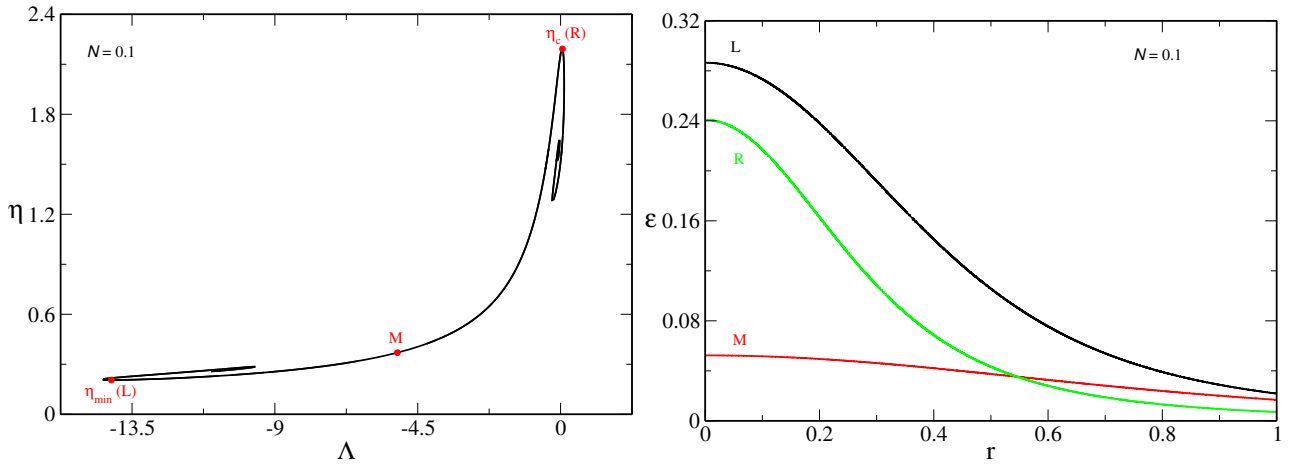

Figure 4.15: ***Left Panel**: Equilibrium phase diagram for $\mathcal{N} = 0.1$. Three distinct points are indicated, corresponding to three different physical situations. Points* L *and* R *correspond, respectively, to η_{min} and η_c. Point* M*, by contrast, refer to a generic point belonging to the gaseous phase.* ***Right Panel**: Density profiles of the three points* R*,* M *and* L*. The point* M *presents a "smooth" density profile whereas for points* R *and* L *the profile is more peaked.*

The Newtonian gravity is recovered for $\mathcal{N} \to 0$: in Fig. 4.14 we have represented three different caloric curves, for decreasing values of $\mathcal{N}$, in order to show the relativistic devations from the Newtonian behaviour. The series of equilibria obtained for $\mathcal{N} = 0.005$ (black line) practically coincides with the series of equilibria obtained by Lynden-Bell & Wood [133]. The red line in the figure represents the series of equilibria obtained for a value of $\mathcal{N}$ ten times larger than the previous one. As the reader can see, both the critical temperature and the critical energy increased (η_c and Λ_c decreased). We interpret this behaviour as a consequence of the presence of the relativistic corrections, which require a big amount of energy to let the instabilities manifest. On the other hand, because the values of η and Λ are smaller than the case $\mathcal{N} = 0.005$, we can affirm that relativistic effects make the systems more thermodynamically unstable.

The green line in Fig. 4.14 shows the series of equilibria for $\mathcal{N} = 0.1$. Here, the effects due to the "relativistic instabilities" are more evident than the preceding cases. In his analysis concerning isothermal spheres in GR, Chavanis [46] obtained similar results. His study is characterized by the following parameter

$$\mu_{gr} = \frac{2R}{R_S}\,, \tag{4.75}$$

where R is the box radius and R_S the Schwarzschild radius. Large values of μ_{gr} imply that $R \gg R_S$, indicating that the system is Newtonian. Chavanis obtained a diagram similar to that represented in

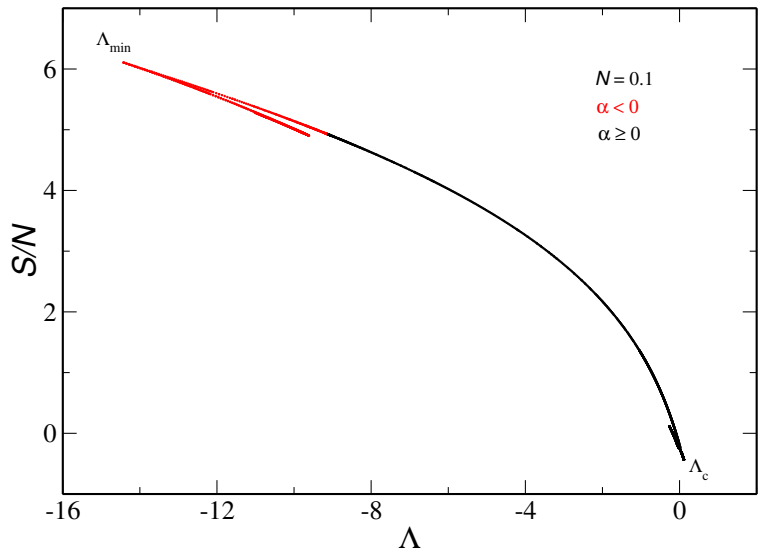

Figure 4.16: *Entropy per particle as a function of the normalized binding energy* Λ. *The critical points* Λ_{min} *and* Λ_c *are also indicated. As the figure shows, there is not phase transition for isothermal spheres in GR. This suggests that the collapses arise from the nature of the gas more than the level of gravity. We stress that the red part of the curve confirms the results of Chavanis (see Fig.19 in Ref.[46]).*

Fig. 4.14. Analogous to our result, the effect of relativity is to shift the spiral to the left. Differently, the value of the critical temperature is constant, corresponding to the Emden temperature $\eta_c = 2.52$. This difference is explained by virtue of the fact that the treatment of Chavanis is *semirelativistic*. Nevertheless, both our and his result (as Roupas too) show that the "general relativistic gravothermal catastrophe" occurs *sooner* than in the Newtonian case.

In Fig. 4.15 we have represented the density profiles of three distinct points in the series of equilibria. The points identified correspond to the critical points η_{min} and η_c and to a generic point belonging to the gaseous phase (left panel in Fig. 4.15). The profiles are quite distinct. Concerning the point M (red line in right panel of Fig. 4.15), we observe that the profile is smooth, indicating that the distribution of the matter inside the system is almost uniform. Conversely, the density profiles related to the reverse critical temperatures η_{min} and η_c show a more peaked trend.

We end this section by briefly discussing the entropy and the free energy, here represented for $\mathcal{N} = 0.1$ (Figs. 4.16, 4.17 and 4.18). The absence of the phase transitions (which has a quantum and not a relativistic origin, see Sec. 1.3) allows us to say that we expect a global behaviour very similar to that obtained in Newtonian gravity [47].

A phase transition is identified as the point where the entropy (in the microcanonical ensemble) or

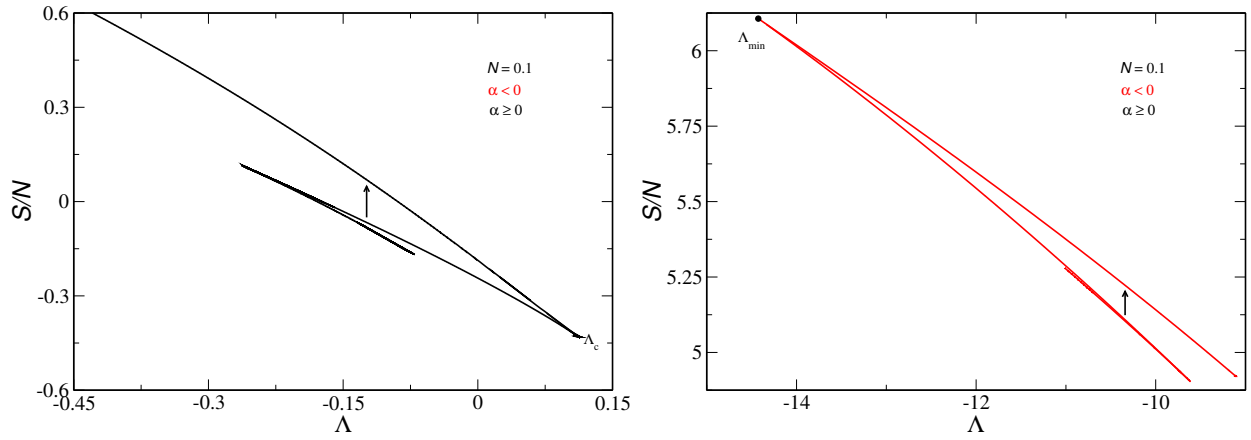

Figure 4.17: *Entropy per particle versus* Λ. *For low energy instabilities (left panel), when several solutions exist at the same temperature, the unstable saddle points can evolve towards metastable states with highest entropy (according to the arrow). For high energy instabilities (right panel) the interpretation is the same (see also Ref.[55]).*

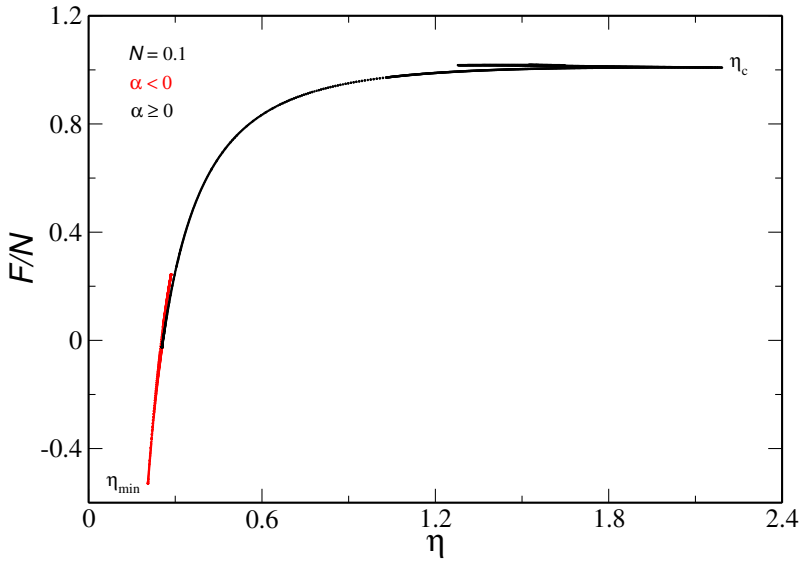

Figure 4.18: *Free energy per particle as a function of the (rescaled) global temperature. The critical points* η_{min} *and* η_c *are also indicated. The interpretation of the curve is the same as that given in Fig. 4.17.*

the free energy (in the canonical ensemble) of the gaseous and the condensed phases coincide. From a graphical point of view, we can get the phase transition as the crossing point between the two phases. Looking at Figs. 4.16 and 4.17, the reader can notice that this crossing point is missing (see Sec. 5.4 for a comparison with fermionic systems). For this reason, systems described by the DF (4.1) do not exhibit any phase transition, both at low and high energies.

Because of the presence of the two critical energies, we see that the entropy (Fig. 4.16) is a limited function. Concerning the case of low-energy instabilities, the interpretation of the curve is the same as that given in Ref. [47]. When several solutions exist for the same energy Λ, the states with lower entropy are unstable saddle points. The fate of these states presents two possible evolutions. A first possibility concerns the evolution towards metastable states with highest entropy (see the arrow in Fig. 4.17). A second possibility regards the evolution to states of ever-increasing entropy (Ref.[61]). Considering the high energy instabilities, we arrive to the same conclusions (see also Ref.[55]). Further, the peak of the entropy (corresponding to Λ_{min}) coincides with the mass (or baryon number) peak (see Fig. 4.2 for example). As pointed out by Chavanis [55], the angular points of the entropy versus energy curve correspond to the peak of the mass[12].

Similar interpretation can be given by considering the case of the free energy (Fig. 4.18). The two reverse critical temperature η_{min} and η_c are the canonical equivalent of Λ_{min} and Λ_c in the microcanonical ensemble. The unstable saddle points can evolve towards state with lowest free energy.

4.5. Phase Diagrams

The analysis of the caloric curves developed in the last Section has shown the existence of four critical points (two in energy and two in temperature). In this Section we focus our attention on the evolution of the critical points, according to the value of the particle number.

Let us start from the microcanonical ensemble. In Fig. 4.19 we have represented the behaviour of Λ_{min} and Λ_c, according to the value of the particle number $\mathcal{N}$. Differently from the Newtonian gravity, indeed, the critical points depend on the intensity of the gravitational fields (measured via $\mathcal{N}$) and, consequently, become functions of this parameter. Let us recall the definition of the particle number:

$$\mathcal{N} = \frac{GNm}{Rc^2}\,. \tag{4.76}$$

The previous equation can be seen as an estimate of the gravitational field[13]. The behaviour of the

[12]The same thing happens for the low energy instabilities (see left panel of Fig. 4.17).

[13]We remind the reader that, in Newtonian gravity, the gravitational potential at the boundary of a body is defined as $\phi \sim GM/R$. We may write Eq.(4.76) as ϕ/c^2.

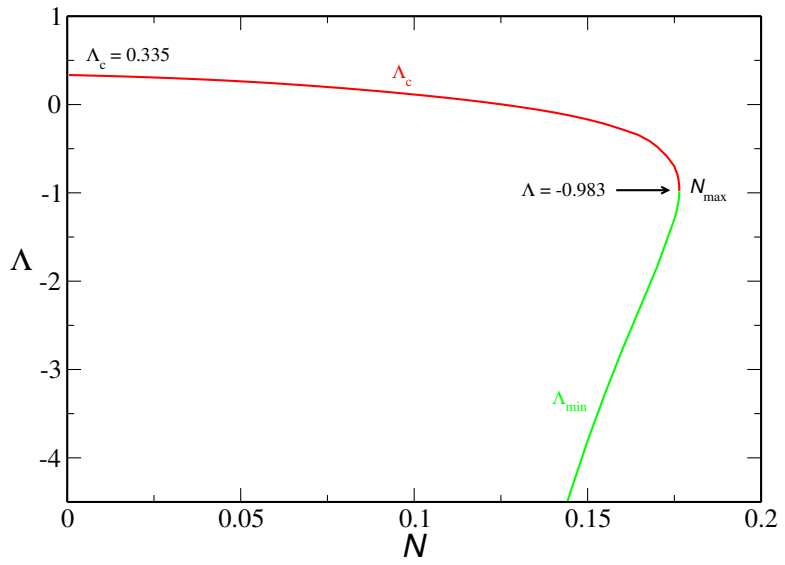

Figure 4.19: *Phase diagram in the microcanonical ensemble:* Λ_{min} *(quantity always negative, green line) and* Λ_c *(red line) are represented as a function of the particle number* $\mathcal{N}$*. Although not shown, for small values of* $\mathcal{N}$*,* Λ_{min} *is a diverging quantity. The diagram shows the existence of a unique critical point, corresponding to* $\mathcal{N}_{max}$*.*

curves displays a different evolution of Λ_{min} and Λ_c. For $\mathcal{N} = \mathcal{N}_{max}$ the two points coincide and reach (negative) limiting value $\Lambda(\mathcal{N}_{max}) = -0.983$. This implies that the binding energy of the system is positive, i.e. $E_b > 0$ (remember the definitions (4.74) and (A.2)), implying that $Mc^2 > Nmc^2$.

From the diagram, we observe that Λ_{min} is always negative and decreases as $\mathcal{N}$ decreases. Although not shown in the figure (see below for an analytical derivation of its behaviour in the limit of small values of $\mathcal{N}$) Λ_{min} diverges in the limit $\mathcal{N} \to 0$. Λ_c, by contrast, shows an opposite trend. As $\mathcal{N}$ decreaes, Λ_c increases its value and reaches the Antonov limit for $\mathcal{N} \to 0$. We note also that there is a point where Λ_c moves from negative to positive values. Moreover, the diagram shows that relativistic configurations get more unstable (than Newtonian configurations) because the value of the critical energy for the collapse is higher (Λ_c lower).

If we fix a line level $\mathcal{N} = \mathcal{N}_{spec} < \mathcal{N}_{max}$, we get *always* two intersection points, corresponding to the limiting configuration energies for the onset of high and low energy instabilities. As Roupas pointed out [159], for *any* value of $\mathcal{N}$, both types of instabilities are present. In the limit $\mathcal{N} \to 0$, by contrast, the energy required for the onset of high energy instabilities becomes infinite and the system is not anymore able to undergo a collapse.

In the Newtonian limit $\mathcal{N} \to 0$ we can obtain a theoretical evaluation of the asymptotic behaviour of Λ_{min}. For a fixed value of $\mathcal{N}$, in principle, it is possible to get a functional relation $\mathcal{M} = f(\mathcal{N})$, where

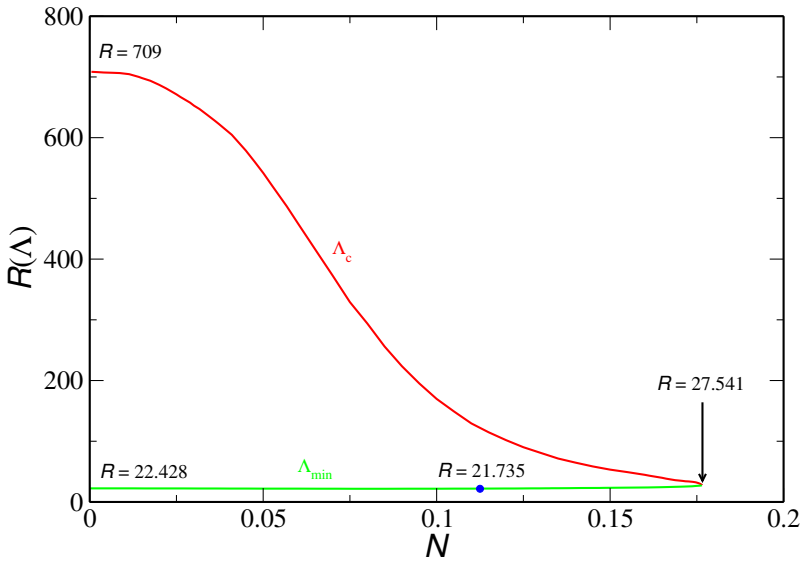

Figure 4.20: *Density contrast $\mathcal{R}$ versus the particle number $\mathcal{N}$. Low energy instabilities (red line) set in for higher values of $\mathcal{R}$ than the high energy instabilities (green line). For* any *line level $\mathcal{N} < \mathcal{N}_{max}$, the two collapses are always present.*

$f(\mathcal{N})$ is a function unknown *a priori*. In this way, the binding energy (4.74) can be expressed as a function of $\mathcal{N}$

$$\Lambda = \frac{\mathcal{N} - f(\mathcal{N})}{\mathcal{N}^2} = \frac{1}{\mathcal{N}} - \frac{f(\mathcal{N})}{\mathcal{N}^2}\,. \tag{4.77}$$

In the hypothesis that f is analytical, we can expand in Taylor series:

$$f(\mathcal{N}) = \sum_{j=0}^{\infty} \frac{f^{(j)}(0)}{j!}\mathcal{N}^j\,. \tag{4.78}$$

Substituting the previous result in Eq.(4.77), we get

$$\Lambda = \frac{1}{\mathcal{N}} - \sum_{k=0}^{\infty} \frac{f^{(k)}(0)}{k!}\mathcal{N}^{k-2} = \frac{1}{\mathcal{N}} - \left[\frac{f(0)}{\mathcal{N}^2} + \frac{f'(0)}{\mathcal{N}} + \sum_{j=2}^{\infty} \frac{f^{(j)}(0)}{j!}\mathcal{N}^{j-2}\right]. \tag{4.79}$$

Now, defining a new index $k = j - 2$ and rearranging the terms we have

$$\Lambda = -\frac{f(0)}{\mathcal{N}^2} + \frac{1 - f'(0)}{\mathcal{N}} - \sum_{k=0}^{\infty} \frac{f^{(k+2)}(0)}{(k+2)!}\mathcal{N}^k\,, \tag{4.80}$$

that has general validity. In the Newtonian gravity we know that Λ_{min} is a diverging quantity, so we can write

$$\Lambda_{min} \sim -\frac{\delta}{\mathcal{N}^\gamma}\,. \tag{4.81}$$

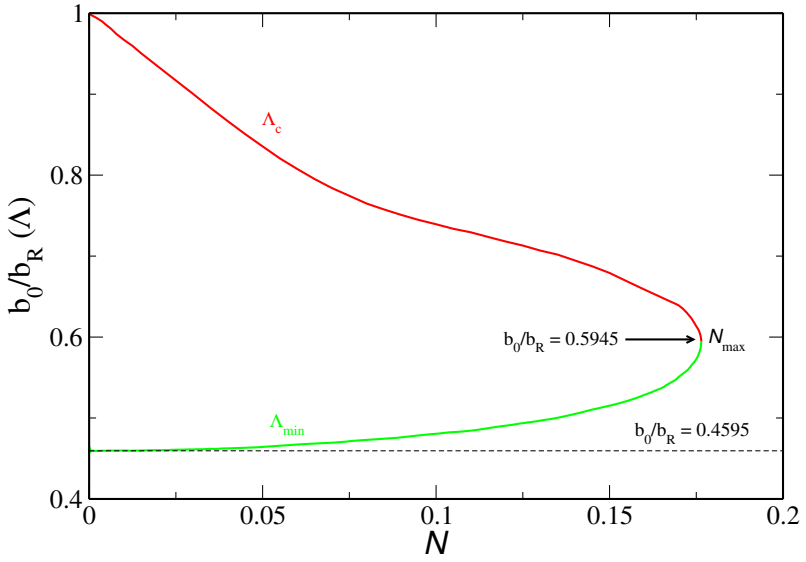

Figure 4.21: *Temperature contrast b_0/b_R as a function of the baryonic number $\mathcal{N}$. High energy instabilities (green line) reach an asymptotic value in the ultrarelativistic limit whereas, low energy instabilities recover the isothermality in the limit of Newtonian gravity (the ratio $b_0/b_R \to 1$). The behaviour of $b_0/b_R(\Lambda_c)$ is similar to that of $b_0/b_R(\eta_c)$ (see Fig. 4.24).*

where $\gamma > 0$ and $\delta > 0$ are constants to be determined. Substituting Eq.(4.80) in the foregoing expression, we have

$$-\frac{\delta}{\mathcal{N}^{\gamma}} = -\frac{f(0)}{\mathcal{N}^2} + \frac{1 - f'(0)}{\mathcal{N}} - \frac{f''(0)}{2} - \frac{f'''(0)}{6}\mathcal{N} + \dots . \tag{4.82}$$

Terms such as $\mathcal{N}^k$ with $k = 1, 2, ...$ are infinitesimal in the limit $\mathcal{N} \to 0$, so they can be neglected. Now, comparing the terms on l.h.s and r.h.s of Eq.(4.82), we get

$$\begin{cases} f(0) = \delta\,, \\ f'(0) = 1\,, \\ f''(0) = 0\,, \\ \gamma = 2\,. \end{cases} \tag{4.83}$$

This implies

$$f(\mathcal{N}) \sim f(0) + \mathcal{N} \tag{4.84}$$

and

$$\Lambda_{min} \sim \frac{\mathcal{N} - f(\mathcal{N})}{\mathcal{N}^2} = \frac{\mathcal{N} - [f(0) + \mathcal{N}]}{\mathcal{N}^2} = -\frac{f(0)}{\mathcal{N}^2}\,. \tag{4.85}$$

The term $f(0)$ can be easily evaluated by using the results of Sec. 4.3: we know indeed that, for $\alpha < 5.012$, $\mathcal{M} \to \mathcal{M}_\infty$ in the limit $\mathcal{N} \to 0$. Since $f(0) = \mathcal{M}$ (remember Eq.(4.77)), we get

$$\begin{aligned} f(\mathcal{N}) &\sim \mathcal{M}_\infty + \mathcal{N} = 0.2463 + \mathcal{N} \\ \Lambda_{min} &\sim -\frac{\mathcal{M}_\infty}{\mathcal{N}^2} = -\frac{0.2463}{\mathcal{N}^2}\,. \end{aligned} \tag{4.86}$$

The evaluation (4.86) is confirmed by the numerical data. For Λ_c we could get a similar evaluation but the result is not practical and not even useful for our purposes. However, numerically, we find

$$\Lambda_c \sim 0.335 - 1.057\mathcal{N} \tag{4.87}$$

showing that Λ_c reaches the Antonov limit linearly. Moreover, in the limit $\mathcal{N} \to \mathcal{N}_{max}$, numerically we find

$$\begin{aligned} \Lambda_{min} &\sim -0.9829 - 14.138\,(\mathcal{N}_{max} - \mathcal{N})^{1/2}\,, \\ \Lambda_c &\sim -0.9829 + 14.138\,(\mathcal{N}_{max} - \mathcal{N})^{1/2}\,. \end{aligned} \tag{4.88}$$

In Fig. 4.20 we have represented the evolution of the density contrast (4.27) evaluated at the critical points Λ_c and Λ_{min}. At each point of the curves, as in Fig. 4.19, a gravitational collapse occurs. Low-energy density contrast is in the interval $[27.541, 709]$ (this last value corresponds to the onset of the Antonov instability). For high-energy instabilities (green line) we observe the presence of a minimum value of the density contrast. Further, in the Newtonian limit $\mathcal{N} \to 0$, we recover the result already obtained by Chavanis [46].

A third diagram is depicted in Fig. 4.21. Here, we have considered the temperature contrast b_0/b_R. The evaluation of this ratio gives an idea about the degree of isothermality of the system. Thanks to Eq.(4.14) we obtain

$$\frac{\mathcal{T}_R}{\mathcal{T}_0} = \frac{b_0}{b_R}\,. \tag{4.89}$$

The behaviour of the temperature contrast associated with Λ_{min} and Λ_c is very different, in particular when we recover the limit $\mathcal{N} \to 0$. We observe that for the contrast b_0/b_R associated with Λ_c, the system recovers the isothermality typical of the Newtonian gravity. By contrast, Λ_{min} achieves a critical value.

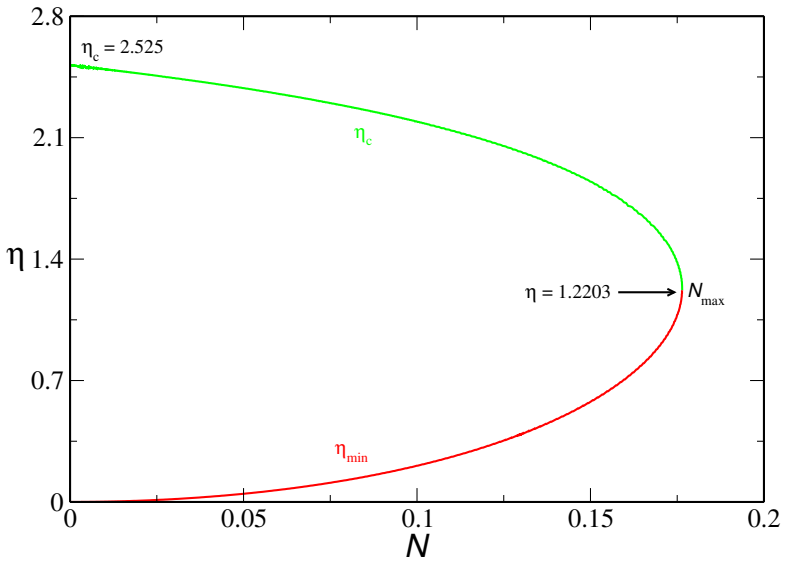

Figure 4.22: *Critical points η_{min} and η_c as a function of the particle number $\mathcal{N}$. The figure shows clearly that, in the limit $\mathcal{N} \to \mathcal{N}_{max}$, η_{min} and η_c tend to the same asymptotic value $\eta_* = 1.2203$ (which identifies one only critical value of $\mathcal{N}$). By contrast, the behaviour of the two functions in the Newtonian gravity is opposite: one converging to the reverse Emden temperature (η_c), the other infinitesimal (η_{min}).*

In his model, Roupas evaluated a critical radius for the occurrence of the gravitational instability. In our model, because of the scaling found in Sec. 4.2, this critical radius does not have a countpart.
Let us now consider the case of the canonical ensemble. In Fig. 4.22 we have represented the behaviour of the two critical points η_c and η_{min} according to $\mathcal{N}$. Similar to the microcanonical ensemble, the phase diagram shows a closed space solution. In fact, for a given line level, the collapses at low and high energy are always present. The functions η_c and η_{min} have a specular behaviour and this symmetry comes from the considerations given in Sec. 4.3.
Both curves converge to the same critical temperature when $\mathcal{N}$ approaches $\mathcal{N}_{max}$. From the diagram we see that $\eta_c \geq 1.22$ always whereas $\eta_{min} \leq 1.22$. The trend of the curves is regular, not presenting diverging points or oscillations (the diagram identifies indeed only one critical point). In the Newtonian limit, we note that η_c converges to the Emden temperature $\eta_c = 2.525$ whereas $\eta_{min} \to 0$ (implying $\mathcal{T} \to +\infty$). In the Newtonian limit, numerically, we find that

$$\begin{aligned} \eta_{min} &\sim 17.83\mathcal{N}^2\,, \\ \eta_c &\sim 2.525 - 3.316\mathcal{N}\,, \end{aligned} \tag{4.90}$$

where, analogous to the microcanonical ensemble for Λ_c, η_c tends linearly to the reverse Emden

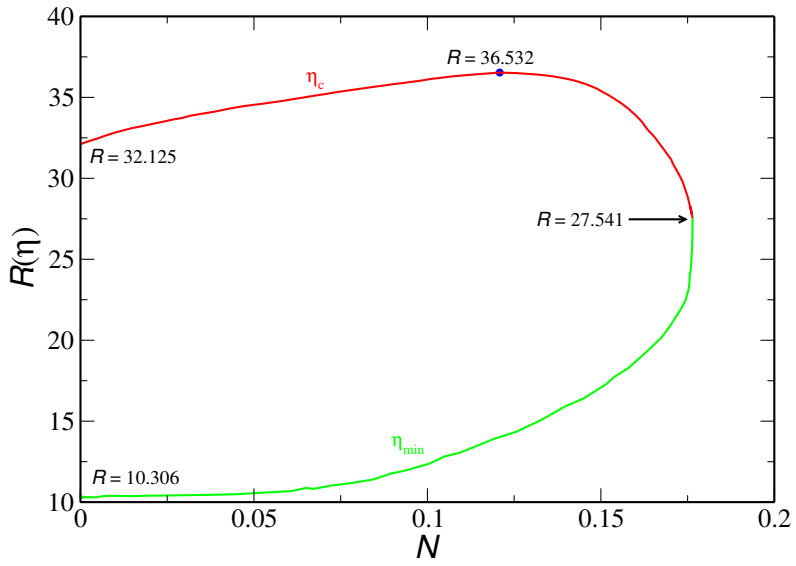

Figure 4.23: *Density contrast as a function of $\mathcal{N}$, in the canonical ensemble. As the analogous diagram obtained in the microcanonical ensemble (see Fig. 4.20), the evolution of $\mathcal{R}$ is different for low and high energy instabilities. The function $\mathcal{R}(\eta_c)$ displays a monotonic increasing behaviour (starting from the Newtonian value $\mathcal{R} = 32.125$) till a maximum value $\mathcal{R} = 36.5$. Then the curves decreases by reaching the limiting configuration for $\mathcal{N} = \mathcal{N}_{max}$. Opposite behaviour for what concerns the density contrast associated with η_{min}, which decreases until the limiting value $\mathcal{R} = 10.3$.*

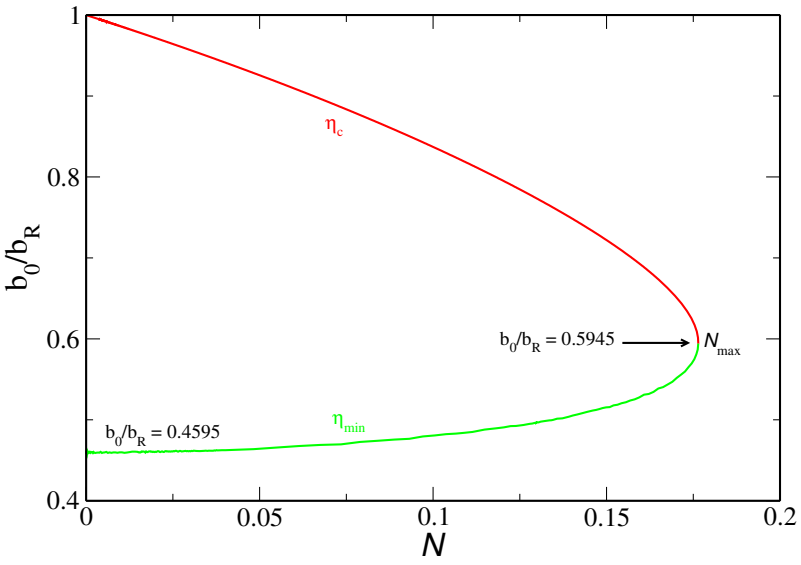

Figure 4.24: *Temperature contrast b_0/b_R, for η_c and η_{min}, as a function of the particle number $\mathcal{N}$. Such as Λ_{min}, the density contrast associated with η_{min} reaches an asymptotic value in the limit $\mathcal{N} \to 0$. Concerning low energy instabilities, we see that $b_0/b_R(\eta_c) \to 1$. Both curves approach the same critical value in the limit $\mathcal{N} \to \mathcal{N}_{max}$.*

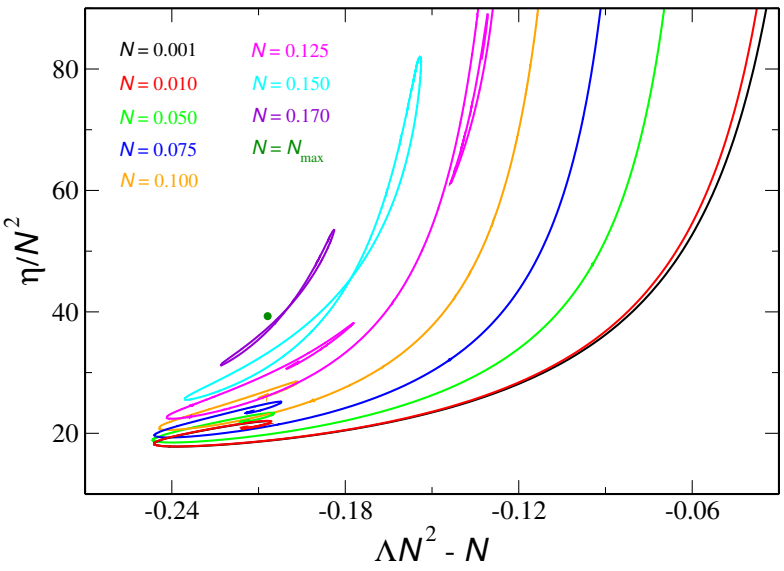

Figure 4.25: *Rescaled temperature $\eta/\mathcal{N}^2$ versus rescaled energy $\Lambda\mathcal{N}^2 - \mathcal{N}$, for several values of $\mathcal{N}$. The curve has been obtained applying the scalings* (4.86) *and* (4.90)*. In the Newtonian limit, as the reader can see, the black line represents a universal curve (we did not shown smaller values of $\mathcal{N}$ because the resulting curves are perfectly superimposed). The relativistic effects become more evident for increasing values of $\mathcal{N}$.*

temperature. This is not surprising because we work in the mean field approximation. At the same time it is remarkable that $\eta_{min} \propto \mathcal{N}^2$. Similarly, in the microcanonical ensemble we have seen that Λ_{min} has a quadratic dependence of $\mathcal{N}$. Anyway, in that case, Λ_{min} diverges. By contrast, in the limit $\mathcal{N} \to \mathcal{N}_{max}$, we have

$$\begin{aligned} \eta_{min} &\sim 1.2203 - 4.606\,(\mathcal{N}_{max} - \mathcal{N})^{1/2}\,, \\ \eta_c &\sim 1.2203 + 4.606\,(\mathcal{N}_{max} - \mathcal{N})^{1/2}\,. \end{aligned} \tag{4.91}$$

Similar to the microcanonical ensemble, in Fig. 4.23 we have represented the density contrast $\mathcal{R}$ associated with the critical points η_c and η_{min}. Here the distinction between the regimes of high and low energy is clear. Values of the density contrast $\mathcal{R} < 27.5$ refer to high energy canonical instabilities whereas, values of $\mathcal{R}$ above this critical value are related to the usual isothermal collapses generalizing the Emden instabilities. It is remarkable the presence of a maximum value for the density contrast in η_c, which value is $\mathcal{R} = 36.5$.

To better understand the difference of the two regimes, we have plotted, in Fig. 4.24, the contrast b_0/b_R. Considering the upper curve (i.e. η_c) and starting from $\mathcal{N}_{max}$, we see a continuous increase, until the achievement, in the limit of Newtonian gravity, of the value $b_0/b_R = 1$. This implies $b_R \to b_0$,

showing that system has recovered the isothermality. By considering η_{min}, we note that, starting from $\mathcal{N}_{max}$, the ratio b_0/b_R decreases until the achievement of an asymptotic value, in the limit $\mathcal{N} \to 0$. The value reached is the same found in the microcanonical ensemble. We could expect that, because for small values of $\mathcal{N}$, Λ_{min} and η_{min} converge to the same point.

Thanks to the scaling found in the limit $\mathcal{N} \to 0$ corcerning the high energy instabilities, we can define a new set of variables which enable us to plot a "rescaled" caloric curve (see Fig. 4.25). If we rescale the temperature as $\eta \to \eta/\mathcal{N}^2$ and the energy as $\Lambda \to \Lambda\mathcal{N}^2 - \mathcal{N}$, we find a universal curve (represented by the black line in Fig. 4.25). This curve represents the "proper" caloric curve associated with the "radiation", which also gives the "universal" critical values of the energy and the temperature for the onset of the instability. These values coincide with the coefficients given in Eqs.(4.86) and (4.90).

The critical temperature η_{min} (energy Λ_{min}) increases (decreases) as $\mathcal{N}$ increases. The right spiral moves towards the left spiral (e.g. magenta and cyan lines in Fig. 4.25). From the figure we also see that the relativistic effects are present for $\mathcal{N} > 0.01$. This can be seen as a confirmation, *a posteriori*, of the robustness of the semi-relativistic model advanced by Chavanis [46].

4.6. Summary of the Previous Results

In this Chapter we have studied the thermodynamical instabilities of general relativistic isothermal spheres. Differently from Newtonian gravity, the presence of GR induces the presence of a second instability in the series of equilibria, which is characterized by the presence of two spirals. Our analysis has shown that the origin of these two types of instability is different: the so-called low energy instabilities are produced by the ordinary matter whereas the so-called high energy instabilities are produced by ultrarelativistic particles (that behave such as photons) and have a relativistic origin.

The analysis has also shown that GR renders the system more unstable: indeed, the critical values of energy Λ and temperature η for the onset of the instabilities are lower than those obtained in Newtonian gravity. The shape of the series of equilibria changes according to the "degree of relativity" (i.e. the value of $\mathcal{N}$). As we have seen in Sec. 4.4, the spirals are closer and closer when $\mathcal{N}$ increases. In particular, we have identified the critical value $\mathcal{N}_S$ corresponding to the "junction point" of the spirals. Then, when $\mathcal{N}$ reaches the value $\mathcal{N}'_S$, the series of equilibria take an "8-shape".

In contrast with Newtonian gravity, general relativistic isothermal spheres show the existence of a limiting configuration, that is $\mathcal{N}_{max}$, corresponding to the maximum number of non-interacting particles that the sphere can hold without collapsing, under any conditions (in addition, the critical points Λ_{min}, η_{min}, Λ_c and η_c coincide). The nature of this point is very particular because, if we add a parti-

cle, the system becomes automatically unstable and collapses. So, we conclude that $\mathcal{N}_{max}$ represents a *metastable* configuration.

In the next Chapter we will consider the case of semidegenerate fermions. Since Boltzmann statistics can be obtained from Fermi - Dirac statistics in the limit of high temperatures, we can see the results obtained in this Chapter as the limiting situations where fermionic configurations tend when the temperature of the system increases.

5

The General Case

This Chapter is devoted to the description of the thermodynamics of a fermionic system in GR. Differently from the systems analyzed in Chap. 4, fermions exhibit the gravitational phase transition, in both microcanonical and canonical ensembles. As we have seen in Chap. 1, to describe the fermions we need to introduce a new parameter, corresponding to the degeneracy (via the chemical potential μ). The inclusion of the degeneracy in the series of equilibria has the effect of unwinding the spiral. Moreover, the occurrence of the two types of phase transition depends on the degeneracy level [47]. However, the phase transition can occur also by considering hard sphere models, by showing that this phenomenon is not necessarily related to the quantum nature of the gas. Although in Newtonian gravity the nature of the phase transitions for self-gravitating fermionic systems is well understood, the investigations about the same topic in GR are incomplete.

Bilić & Viollier [25] have firstly pioneered that a gravitational phase transition necessarily occurs also in GR. Nonetheless, in their work, they have considered only the case of the canonical phase transition for systems below the OV limit. In this Chapter we complete their investigation, by studying the phase transitions in the most general case.

As a consequence of the presence of the degeneracy, we expect that the scaling GNm/Rc^2 does not work for fermionic systems. This implies, as we will see, that also the value of the cavity radius[1] R. has a non-negligible effect on the thermodynamical properties (the occurrence of the phase transition is indeed strictly linked to the value of R).

In Sec. 5.1 we briefly recall the main relations (already derived in Secs. 2.1 - 2.2) describing the

[1] We remind the important the relation linking the chemical potential and the box radius, i.e. $\tilde{\alpha} = \alpha + 2\log\tilde{R}$ [see Eq.(4.43)].

model, by further showing that the scaling GNm/Rc^2 does not work for fermionic systems.
Similarly to Chap. 4, we dedicate Sec. 5.2 to the understanding of the properties of the baryonic number N, by showing the link between the critical points of the function $N = N(\Phi_0)$ and the critical points of the caloric curve. As we shall see in the following, the occurrence of the phase transition (in the canonical ensemble) is related to the presence of an inflection point in the $N = N(\Phi_0)$ diagram.
Because of the failure of the scaling GNm/Rc^2, we will study the nature of the phase transitions for three different values of the cavity radius[2], namely $R = 10\ r_*$, $50\ r_*$, $600\ r_*$. The first value (see Sec. 5.3) corresponds to the case of a fermionic system that does not exhibit any phase transition. The second value (see Sec. 5.4) corresponds to the occurrence of the canonical phase transition. The third value (see Sec. 5.5) corresponds to the occurrence of the microcanonical phase transition.
Finally, in Sec. 5.6, we discuss the variation of the critical points according to the value of the box radius, by obtaining the "phase diagram of phase diagrams".

5.1. Main Equations

Let us briefly recall the main relations[3] (already expressed in dimensionless form), starting from the thermodynamic quantities[4] [density state number, energy density and pressure, respectively, see Eqs.(2.54)-(2.56)]

$$\tilde{n} = \frac{1}{\pi^2}\int_0^\infty y^2\Big(ze^{b\sqrt{y^2+1}}+1\Big)^{-1}dy\,, \tag{5.1}$$

$$\tilde{\epsilon} = \frac{1}{\pi^2}\int_0^\infty y^2\sqrt{y^2+1}\Big(ze^{b\sqrt{y^2+1}}+1\Big)^{-1}dy\,, \tag{5.2}$$

$$\tilde{P} = \frac{1}{3\pi^2}\int_0^\infty \frac{y^4 dy}{\sqrt{y^2+1}}\Big(ze^{b\sqrt{y^2+1}}+1\Big)^{-1}dy\,. \tag{5.3}$$

The TOV system (2.59) is expressed as

$$\begin{aligned}\frac{d\Phi}{d\tilde{r}} &= -\frac{2(\Phi+1)(\tilde{M}_r+4\pi\tilde{P}\tilde{r}^3)}{\tilde{r}^2}\Big(1-\frac{2\tilde{M}_r}{\tilde{r}}\Big)^{-1}\,,\\ \frac{d\tilde{M}_r}{d\tilde{r}} &= 4\pi\tilde{\epsilon}\,\tilde{r}^2\,,\end{aligned} \tag{5.4}$$

[2]We recall that the characteristic length r_* is defined by [see Eq.(2.57)]

$$r_* = \sqrt{\frac{2\hbar^3}{gGm^4c}}\,.$$

[3]See Chap. 2 for more details.
[4]The variables z and b are defined by Eqs.(2.34) and (4.13).

with the initial conditions $\Phi(0) = \Phi_0 > -1$ and $\tilde{M}_r(0) = 0$. The following relations define the baryonic number, the entropy and the free energy

$$\tilde{N} = 4\pi \int_0^{\tilde{R}} \tilde{n}\tilde{r}^2 \Big(1 - \frac{2\tilde{M}_r}{\tilde{r}}\Big)^{-1/2} d\tilde{r}\,, \tag{5.5}$$

$$\tilde{S} = |\alpha| \Bigg[\int_0^{\tilde{R}} \frac{4\pi(\tilde{P} + \tilde{\epsilon})\tilde{r}^2}{\sqrt{\Phi + 1}} \Big(1 - \frac{2\tilde{M}_r}{\tilde{r}}\Big)^{-1/2} d\tilde{r} - \mathrm{sgn}(\alpha)\tilde{N} \Bigg] = |\alpha| \Big[I_S - \mathrm{sgn}(\alpha)\tilde{N} \Big]\,, \tag{5.6}$$

$$\tilde{F} = \tilde{M} - \tilde{T}\tilde{S}\,. \tag{5.7}$$

Further, the dimensionless temperature $\tilde{T}$ is defined by

$$\tilde{T} = \frac{\sqrt{\Phi_R + 1}}{|\alpha|} \sqrt{1 - \frac{2\tilde{M}}{\tilde{R}}}\,, \tag{5.8}$$

and the variables Λ and η are

$$\Lambda = \frac{(\tilde{N} - \tilde{M})\tilde{R}}{\tilde{N}^2}\,, \qquad \eta = \frac{\tilde{N}}{\tilde{T}\tilde{R}}\,. \tag{5.9}$$

Now, we end this section by showing that the scaling found in Sec. 4.2 is not applicable to the case of the self-gravitating Fermi gas. Let us define, analogous to Sec. 4.2, the normalized radial coordinate $\lambda = r/R = \tilde{r}/\tilde{R}$ and substitute this definition in the TOV system (5.4). We get[5]

$$\begin{aligned} \frac{d\Phi}{d\lambda} &= -\frac{2(\Phi + 1)(\mathcal{M}_\lambda + 4\pi\Pi\lambda^3)}{\lambda^2} \Big(1 - \frac{2\mathcal{M}_\lambda}{\lambda}\Big)^{-1}\,, \\ \frac{d\mathcal{M}_\lambda}{d\lambda} &= 4\pi\Theta\lambda^2\,, \\ \mathcal{N} &= 4\pi \int_0^1 \nu\lambda^2 \Big(1 - \frac{2\mathcal{M}_\lambda}{\lambda}\Big)^{-1/2} d\lambda\,. \end{aligned} \tag{5.10}$$

Here, the functions ν, Θ and Π are defined by the following relations

$$\nu = \frac{\tilde{R}^2}{\pi^2} \int_0^\infty y^2 \Big(z e^{|\alpha|\sqrt{\frac{y^2+1}{\Phi+1}}} + 1 \Big)^{-1} dy = \frac{1}{\pi^2} \int_0^\infty y^2 \Big(\tilde{z} e^{b\sqrt{y^2+1}} + \frac{1}{\tilde{R}^2} \Big)^{-1} dy\,, \tag{5.11}$$

$$\Theta = \frac{\tilde{R}^2}{\pi^2} \int_0^\infty y^2 \sqrt{y^2+1} \Big(z e^{|\alpha|\sqrt{\frac{y^2+1}{\Phi+1}}} + 1 \Big)^{-1} dy = \frac{1}{\pi^2} \int_0^\infty y^2 \sqrt{y^2+1} \Big(\tilde{z} e^{b\sqrt{y^2+1}} + \frac{1}{\tilde{R}^2} \Big)^{-1} dy\,, \tag{5.12}$$

$$\Pi = \frac{\tilde{R}^2}{3\pi^2} \int_0^\infty \frac{y^4 dy}{\sqrt{y^2+1}} \Big(z e^{|\alpha|\sqrt{\frac{y^2+1}{\Phi+1}}} + 1 \Big)^{-1} dy = \frac{1}{3\pi^2} \int_0^\infty \frac{y^4 dy}{\sqrt{y^2+1}} \Big(\tilde{z} e^{b\sqrt{y^2+1}} + \frac{1}{\tilde{R}^2} \Big)^{-1} dy\,, \tag{5.13}$$

where we have used Eq.(4.13). Moreover, $\tilde{z}$ is defined by

[5] We keep the same formalism outilined in Sec. 4.2.

$$\tilde{z} = ze^{-2\ln\tilde{R}} = e^{-(\alpha+2\ln\tilde{R})} = e^{-\tilde{\alpha}}\,. \tag{5.14}$$

In the foregoing expression, we have applied the scaling (4.43). As we see, the presence of the radius cannot be dropped in Eqs.(5.11)-(5.13). In the following, we will get a confirmation of this feature, because the occurrence of the phase transition is related to some specific values of the box radius. Nevertheless, the non-quantum limit is recovered for $\tilde{R} \to \infty$ [i.e. $\hbar \to 0$, see Eqs.(2.47) and (2.57)], corresponding to a gas encapsulated in a box which walls fill the hole space. In this regime, the expressions of the thermodynamic quantities (5.11)-(5.13) become

$$\nu(\tilde{R}\to\infty) \sim \frac{1}{\pi^2\tilde{z}}\int_0^\infty y^2 e^{-b\sqrt{y^2+1}}dy = \frac{e^{\tilde{\alpha}}}{\pi^2}\int_0^\infty y^2 e^{-b\sqrt{y^2+1}}dy\,, \tag{5.15}$$

$$\Theta(\tilde{R}\to\infty) \sim \frac{1}{\pi^2\tilde{z}}\int_0^\infty y^2\sqrt{y^2+1}e^{-b\sqrt{y^2+1}}dy = \frac{e^{\tilde{\alpha}}}{\pi^2}\int_0^\infty y^2\sqrt{y^2+1}e^{-b\sqrt{y^2+1}}dy\,, \tag{5.16}$$

$$\Pi(\tilde{R}\to\infty) \sim \frac{1}{3\pi^2\tilde{z}}\int_0^\infty \frac{y^4}{\sqrt{y^2+1}}e^{-b\sqrt{y^2+1}}dy = \frac{e^{\tilde{\alpha}}}{3\pi^2}\int_0^\infty \frac{y^4}{\sqrt{y^2+1}}e^{-b\sqrt{y^2+1}}dy \tag{5.17}$$

which correspond to the expressions (4.40)-(4.42) of ν, Θ and Π obtained in Sec. 4.2. In the rest of the Chapter, to not make heavier the writing, we note N for $\tilde{N}$, R for $\tilde{R}$ and similarly for the other dimensionless quantities.

5.2. Particle Number and Definition of N_{max}

In last Chapter (see Sec. 4.3), we have seen that there exists a link between the critical points of the $\mathcal{N}(\Phi_0)$ function and the critical points of the caloric curve, in the canonical ensemble. In particular, we have seen that the values of η_c and η_{min} could be determined by taking the maximum of $\mathcal{N}(\Phi_0)$. In addition, the other critical points of the curve (i.e. local minima and maxima) were related to the shrinking of the spiral. This link is preserved for fermionic systems too. For this reason, in this Section[6], we focus on the study of the properties of the function $N(\Phi_0)$.

As already mentioned in Sec. 2.2 [see Eq.(2.38)], according to the value of α, there exist two limiting situations. Large and negative values of α correspond to the case of the Boltzmann statistics while large and positive values of α enable us to recover the full degeneracy limit. Thanks to the results presented in the previous two Chapters, we know what happens in these limiting situations. Therefore, in this Section, we restrict the analysis to the semidegenerate case.

To make sure that we go the right way, we start our discussion by considering Fig. 5.1, where we have represented both negative and positive values of α. In particular, we have separated the two types

[6] In particular we discuss the case $R = 50$.

of α, by identifying the positive ones by a full line and the negative ones by a dashed line. Starting from these last ones, we see that the trend of the curves corresponds to those discussed in Sec. 4.3. Because of the big values acheived by the gravitational potential, the right part is not represented. The figure illustrates the existence of a critical value of α, related to the limiting configuration N_{max} (red line in Fig. 5.1). The value of $\alpha(N_{max})$ can be obtained by applying Eq.(4.43) (using $\tilde{\alpha} = -5.012$): we get[7] $\alpha(N_{max}) = -2.812$. Nonetheless, we see some differences compared to the results presented in Chap. 4. As a matter of fact, we have obtained the sequence $N_S < N_0 < N'_S < N_{max}$. As the reader can easily check, Fig. 5.1 shows $N_S < N'_S < N_0 < N_{max}$, that is an inversion between N'_S and N_0. The reason of this changement arises from the different nature of the points. While N_{max}, N_S and N'_S depend on one specific value of α, which is universal [and the scaling (4.43) can be applied], N_0 is an "absolute". As a matter of fact, every radius has its "own" configuration $\alpha = 0$, leading to a different value of N_0 that cannot be related to that of another radius. This is due to the presence of a new degree of freedom, i.e. the degeneracy in the DF (2.29). If in Eq.(4.43) we put $\tilde{\alpha} = 0$, we obtain

$$\alpha(N_0) = -2 \ln R \,. \tag{5.18}$$

From the foregoing expression, if $R \neq 1$, we get the absurd case $\alpha(N_0) \neq 0$ when, rather, $\alpha(N_0) = 0$ *strictly*.

If we now specialize on the case $\alpha > 0$, we see that the general trend of the curves is different from that above analyzed. Obviously, in the limit $\alpha \to 0^+$ (top left in Fig. 5.1), the distinction between negative and positive α is very subtle. The dissimilarities come out around $\alpha \sim 0.1$, when the curves start to move towards the bottom part of the figure (α increasing). The global values of the function $N(\Phi_0)$ progressively reduce (we can appreciate a substantial decrease of the value of the maximum N_{gm} associated with α) and, surprisingly, the position of the maximum tends to $\Phi_0 \sim 0$.

By recalling the results obtained in Sec. 2.2, $\Phi_0 \to 0$ implies that the system is recovering the Newtonian gravity. Thus, the results obtained for small values of Φ_0 recover those of Chavanis [47] (see Secs. 5.4 and 5.5). Anyway, large values of α, not only imply that the gravity inside the fermionic system is weaker and weaker, but also it allows us to reach the OV limiting curve (green line in Fig. 5.1). As already noticed by Bilić & Viollier [24], all curves with finite α present a first peak around the position $\Phi_0 = 0$, in contrast to the case $T = 0$ (see Appendix D). In addition, we see that the curves present the sequence maximum-minimum before reaching the OV limit (see, e.g., also Figs. 5.2 and 5.3). Analogous to Chap. 4, this sequence enables us to distinguish between a "gaseous" and a "condensed" phase. Following Bilić & Viollier, we can define an order parameter as

[7] This result is confirmed by the numerical data.

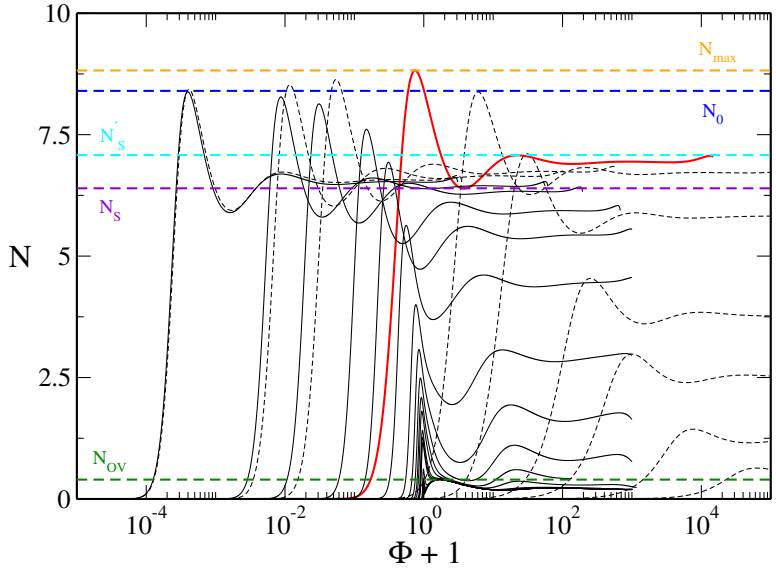

Figure 5.1: *Total particle number versus the central value of the gravitational potential* $\Phi_0 + 1$*, for several values of* α *and for* $R = 50$*. The positive values of* α *are represented by full lines whereas the dashed lines refer to* $\alpha < 0$*. The points* N_{max}*,* N_0*,* N_S *and* N'_S *are also represented. The reader can note that, differently from what we have seen in Sec. 4.4 (see also Fig. 4.11), the value corresponding to* N_0 *is higher than those corresponding to* N_S *and* N'_S*. Finally,* N_{OV} *represents the OV limit.*

$$\delta = \Phi_0 + |\Phi_0| \,, \tag{5.19}$$

which is stricly positive in the condensed (ordered) phase and equal to zero in the gaseous (disordered) phase[8]. From Fig. 5.1, moreover, we deduce that the Thomas-Fermi model may provide more than one solution, similar to the case of Boltzmann statistics. In order to explain this feature more quantitatively, let us consider Fig. 5.2. Here, we have represented an enlargement of the preceding figure.

As earlier mentioned, the green line represents the OV limiting curve. As the reader can see, the curve is "linear", in the sens that it increases regularly its value (it does not present local maxima or minima, for example). Now, if we relax the condition $T = 0$ (or, equivalently, $\alpha = +\infty$), we see a deviation from this behaviour (see the dashed line closest to the OV curve in Fig. 5.2). The increase of the curve slightly "deviates" and, for a smaller value of α, there is evidence of a progressive rising of an inflection point (orange line). For a value of $\alpha < \alpha_{orange}$ we see the presence of a maximum and a minimum in the curve. As we shall see in the following, the presence of this inflection point is related to the occurrence of the canonical phase transition (see Sec. 5.4). For this reason, we call the value of

[8]Using the representation given in the figures of this Section, $\Phi_0 + 1 \leq 1$ for the gas and $\Phi_0 + 1 > 1$ for the condensate.

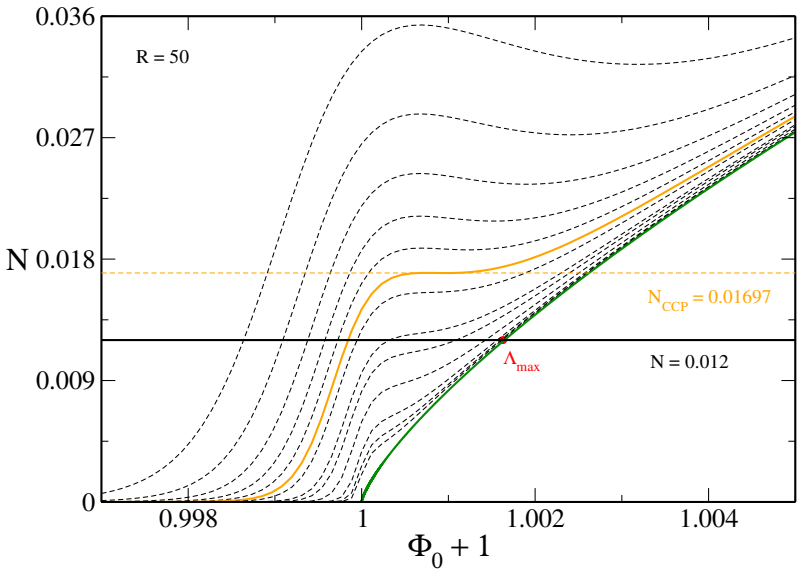

Figure 5.2: *Total particle number versus the central value of the gravitational potential* $\Phi_0 + 1$*, for the line level* $N = 0.012$ *and for* $R = 50$ *(the values of* α *decrease going to the top of the figure). The presence of the inflection point* N_{CCP} *gives rising to the phase transition. For* $N > N_{CCP}$*, indeed, the caloric curve presents a maximum* (η_c) *and a minimum* (η_*) *in temperature, determining the sequence gaseous-condensed phase. The intersection with the OV curve (green line) allows us to get the value of the accessible minimal energy* (Λ_{max})*. At this point, the nucleus is completely degenerate and contains all the mass of the system [47]. The figure shows the case* $N < N_{CCP}$*.*

N associated with this inflection point as "canonical critical point", namely N_{CCP}. Numerically, for $R = 50$, we get $N = 0.017$.

Further, in Fig. 5.2, we have represented a line level below N_{CCP}, specifically at the height $N = 0.012$. The line level crosses all the $N = N(\Phi_0)$ curves in, *at the most*, one point. Since we are below N_{CCP}, we expect that the corresponding series of equilibria is characterized by the absence of the canonical phase transition (see Sec. 5.4). This means that, to have the phase transition, the Thomas-Fermi model has to provide, *at least*, more than one solution. Bilić & Viollier interpret this behaviour as the indication of an instability (which can exist even below the OV limit as we see), implying the occurrence of a first-order phase transition.

For $N < N_{OV}$ any line level identifies, at least (see below) an intersection point with the OV curve. In this case, since $T = 0$, we do not find a critical value of temperature but, rather, of energy. As we know [47], for low energies the system takes a "core-halo" structure. The intersection with the OV curve allows us to find the minimum energy (maximum Λ) at which the core contains all the mass. In Newtonian gravity the system has the same structure of a WD. In GR, by contrast, the system is

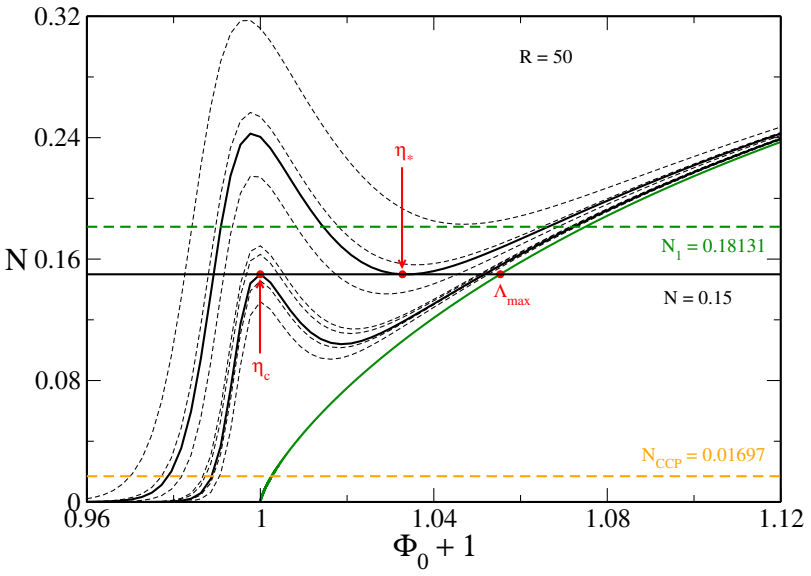

Figure 5.3: *The same as the preceding figure, by showing the case $N_{CCP} < N < N_1$ (the point N_1 is defined in Appendix D). The OV Limit is represented by the green line. Here, the occurrence of the phase transition is more evident than in Fig. 5.2. The physical interpretation, however, is the same.*

rather similar to a NS.

In Fig. 5.3, we have represented the case corresponding to the line level $N = 0.15$. As the reader can see, there exists a critical value of α (identified by the point η_c), above which no solutions are obtainable. This is similar to what we have observed in Sec. 4.3. By analogy we deduce that α_{min} is reached in the limit $\alpha \to -\infty$. However, differently from the case of Boltzmann statistics, we can identify a second range of values of α, delimited by the points η_c and η_* in the figure.

The nature of these two points is different. As we know, η_c is associated with the critical temperature leading the system to collapse. In the series of equilibria, points placed at $\eta > \eta_c$ are unstable saddle points [47]. Then, when $\eta = \eta_*$ the condensed phase emerges and the stability is gained back. Consequently, we conclude that each turning point of the curve $N(\Phi_0)$ is associated with a gain or a loss of the stability[9].

If we now increase the value of N, we arrive to the situation depicted in Fig. 5.4, where we have taken into consideration the line level $N = 0.29$. Compared to the previous case, a new critical point (associated with a critical value of the energy) appeares. This new critical energy corresponds to the presence, in the series of equilibria, of a second (unstable) branch (see Sec. 5.4). The rising of this unstable branch is related to a specific value of N that, differently from N_{CCP}, does not depend on

[9]This is true in a first approximation. As we shall see in the following, the intersections of higher orders are related to unstables branches in the series of equilibria.

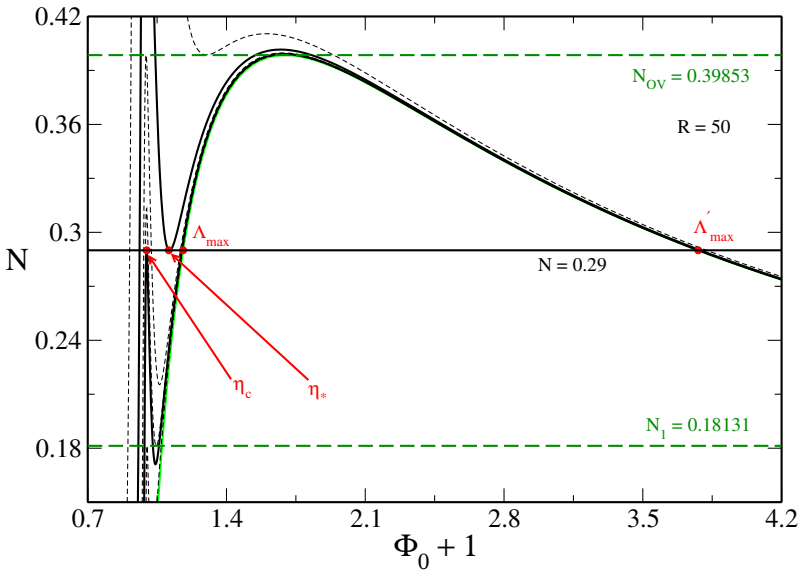

Figure 5.4: *Total particle number versus the central value of the gravitational potential* $\Phi_0 + 1$*, for the case* $N_1 < N < N_{OV}$ *(line level* $N = 0.29$*) and for* $R = 50$*. Compared to the case represented in Fig. 5.3, the line level identifies a second intersection point with the OV curve (green line), indicated by* Λ'_{max}*. The origin of this point is purely general relativistic.*

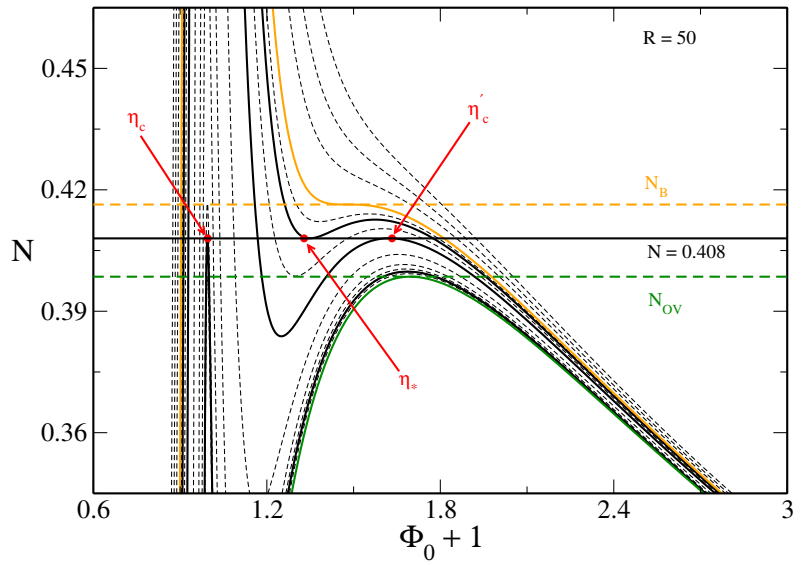

Figure 5.5: *Total particle number versus the central value of the gravitational potential* $\Phi_0 + 1$*, for the case* $N = 0.408$ *and for* $R = 50$*. The point* η'_c *represents the maximum value of the reverse temperature that can be reached by the second gaseous phase. However, this diagram does not let us to establish if this second gaseous phase is formed by stable or metastable physical solutions.* N_B *correspond to an inflection point in the* $N = N(\Phi_0)$ *curve and corresponds to the merging of* η_* *and* η'_c*.*

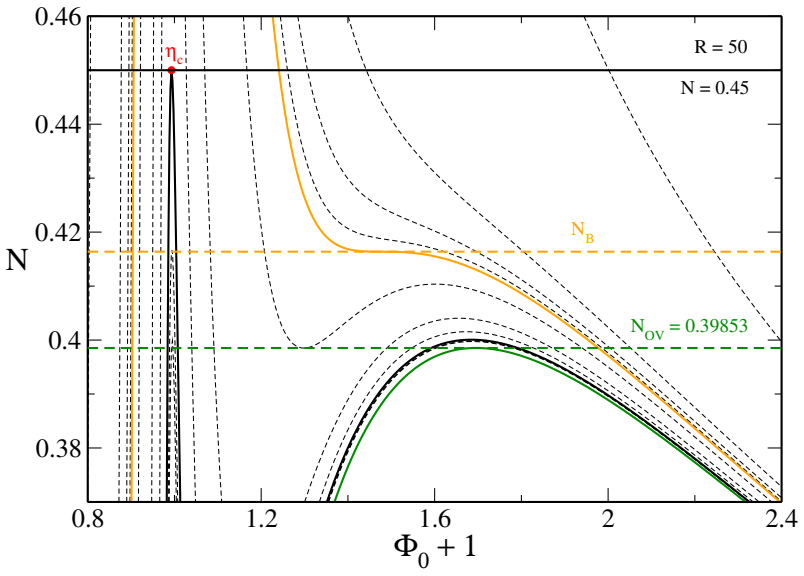

Figure 5.6: *Total particle number versus the central value of the gravitational potential* $\Phi_0 + 1$*, for the case* $N = 0.45$ *and for* $R = 50$*. From a thermodynamical point of view, indeed, the system is equivalent to the isothermal gas sphere, in spite of the different shape of the curve (see Fig. 5.16).*

the value of the box size and corresponds[10] to $N_1 = 0.18131$.

From Fig. 5.4 we can also deduce that, if we move the line level towards N_{OV}, the critical points Λ_{max} and Λ'_{max} get closer. This means that the unstable branch delimited by Λ'_{max} approaches that delimited by Λ_{max}. In the limit $N \to N_{OV}$ we argue that they should merge "merge".

The preceding discussion allows us to conclude that, for $N_{CCP} < N < N_{OV}$, the occurrence of the phase transition and the global thermodynamical behaviour of the fermionic system is not particularly affected by GR[11]. We expect general relativistic corrections when we consider the case $N > N_{OV}$. About that, let us consider Fig. 5.5, where we have illustrated the case corresponding to $N = 0.408$. As we observe, the line level identifies three critical points, namely η_c, η_* and η'_c.

This last point corresponds to the second local maximum of the $N(\Phi_0)$ curve and can be seen as the fermionic version of the point N'_S (see Sec. 4.4 and Fig. 5.1). Due to its quantum nature, we expect that this point is associated with a second collapse of the system. In fact, because placed after η_*, we can argue that in the interval $\eta_* < \eta < \eta'_c$ the system gains a second time the stability. Since between η_* and η'_c the function $N(\Phi_0)$ is monotonic increasing, we expect that the gaseous phase emerges. Therefore, the points $\eta > \eta'_c$ represent unstable configurations. We stress that this feature

[10] In Appendix E we show that, in the limit $R \to 0$, the value of N_1 (and also of N_{OV}) changes according to the radius.

[11] The presence of the branch Λ'_{max} does not alter the thermodynamical interpretation, because this branch is made by unstable physical solutions.

has a general relativistic origin[12].

In addition, Fig. 5.5 shows another feature. By increasing the value of N associated with the line level, we see that the points η_* and η_c' get closer, analogous to Λ_{max} and Λ'_{max}. There exists a critical value of α (orange line in the figure) where $\eta_* = \eta_c'$. In contrast with N_{CCP}, this point (N_B) is related to the disappearance of the second collapse associated with η_c'. We thus expect that the system exhibits only the collapse in η_c. From a thermodynamical point of view, this situation is equivalent to what we have seen in the context of Boltzmann statistics. So, the point $N = N_B$ represents the critical value of N above which the system is thermodynamically equivalent to the isothermal sphere.

By still looking at Fig. 5.5, we note the absence of intersection points between the line level and the OV curve. As a consequence, we do not expect to get a theoretical evaluation of the limiting values of the energy (see Sec. 5.4 and Appendix D). In Fig. 5.6 we can appreciate that our former assertion is confirmed. For a line level $N > N_B$, we can get only the point of the isothermal collapse η_c.

The mathematical properties of the $N(\Phi_0)$ function allowed us to understand the nature of the critical points of the series of equilibria in the canonical ensemble. In the microcanonical ensemble this link cannot be made: indeed, the critical points in energy are not related to the critical points of the $N(\Phi_0)$ function (see Sec. 5.5).

5.3. The Case $R = 10$: Absence of Phase Transition

As previously mentioned, we have carried out the thermodynamical analysis for three values of the box radius, namely $R = 10$, 50, 600. As we shall see, these different values are related to the occurrence or the suppression of the phase transitions, both canonical and microcanonical. Before going further, we want to introduce a new parameter, useful to compare the results here obtained with those existing in literature. Let be

$$\chi = \frac{N}{N_*}\Big(\frac{R}{r_*}\Big)^3 = \tilde{N}\tilde{R}^3\,. \tag{5.20}$$

From the foregoing expression, for $N/N_* \to 0$ and $R/r_* \to \infty$, we have that $\chi \to const.$ Moreover, substituting Eqs.(2.57) and (2.58) in Eq.(5.20), we have

$$\chi = NR^3\Big(\frac{2\hbar^3c^3}{gG^3m^6}\Big)^{-1/2}\Big(\frac{8\hbar^9}{g^3G^3m^{12}c^3}\Big)^{-1/2} = \frac{NR^3g^2G^3m^9}{4\hbar^6} = \frac{G^3NmR^3g^2m^8}{4\hbar^6}\,. \tag{5.21}$$

Reintroducing the Planck constant h and defining $\eta_0 = gm/h^3$ [47], Eq.(5.21) becomes

[12] In Ref.[24], the existence of η_c' has not been brought to the light. The reason is due to the fact that, in their work, Bilić & Viollier have only studied the general relativistic Thomas-Fermi model for $N < N_{OV}$.

Table 5.1: *Values of N_{CCP} and N_{MCP}, evaluated by means of Eqs.* (5.20) *and* (5.23)*, for the three radii $R = 10,\ 50,\ 600$. The values of N_{max} are also listed for comparison.*

R	N_{CCP}	N_{MCP}	N_{max}
10	2.099×10^{1}	2.084×10^{3}	1.762×10^{0}
50	1.679×10^{-2}	1.668×10^{1}	8.821×10^{0}
600	9.719×10^{-6}	9.653×10^{-3}	1.061×10^{2}

$$\chi = \frac{\pi^2\,\eta_0^2 m^6 512\pi^4 G^3 N m R^3}{32} = \frac{\pi^2\mu_d^2}{32} \qquad \Longleftrightarrow \qquad \tilde{N}\tilde{R}^3 = \frac{\pi^2\mu_d^2}{32} \tag{5.22}$$

where μ_d is the "degeneracy parameter" defined by Eq.(1.28). The occurrence of the phase transitions is related to precise values of μ_d. For the canonical phase transition we have $\mu_{CCP} = 82.5$ whereas, for the microcanonical phase transition, we have $\mu_{MCP} = 2600$ [47].

These estimates imply that canonical instabilities set in before the microcanonical ones and this behaviour, as we shall see, is maintained in GR. Although coming from a Newtonian framework, we can use the values of μ_{CCP} and μ_{MCP} to have a preliminar rough idea about the values of N linked to the occurrence of the phase transitions[13]. If we apply Eq.(5.22) to the cases above mentioned we get

$$\begin{aligned} \chi_{CCP} &= \frac{\pi^2\mu_{CCP}^2}{32} \simeq 2.099 \times 10^3 \\ \chi_{MCP} &= \frac{\pi^2\mu_{MCP}^2}{32} \simeq 2.085 \times 10^6\,. \end{aligned} \tag{5.23}$$

If we now apply the results (5.23) to the three values of the box radius $R = 10, 50, 600$ [via Eq.(5.20)], we get the critical values of N related to the occurrence of the canonical and microcanonical phase transitions (Tab. 5.1). To have a precise about the accuracy of the evaluation, in Tab.5.1 we have compared the values of N_{CCP} and N_{MCP} with N_{max}. For the case $R = 10$, we see that Newtonian estimate fails: the values of N_{CCP} and N_{MCP} are bigger than N_{max} and, as we know, this is not possible. However, the fact that these values are so big can suggest that a box of this size is too small to let the phase transitions occur.

[13] In Sec. 5.6 we will show, by means of the "phase diagram of phase diagrams", that relativistic instabilities set in for values of μ_d smaller than those found in Newtonian gravity. However, these relativistic deviations from the Newtonian theory are more evident in the canonical ensemble than in the microcanonical one.

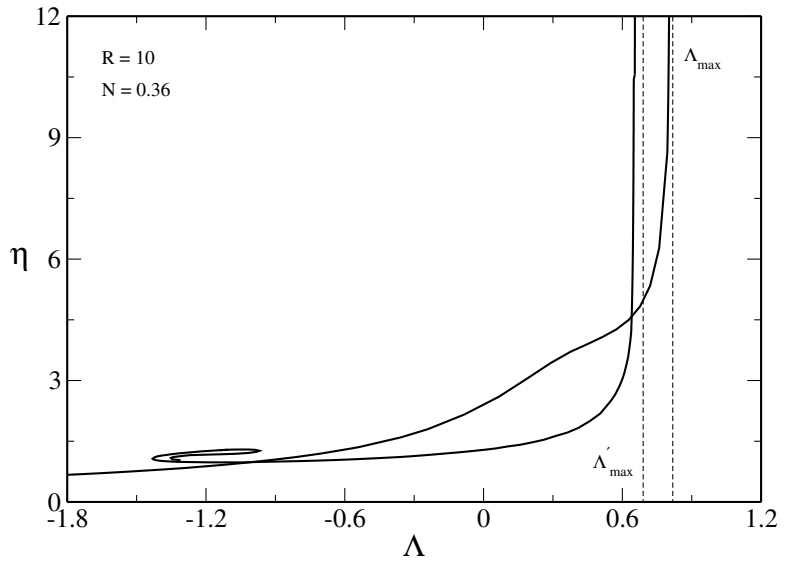

Figure 5.7: *Equilibrium phase diagram of self-gravitating fermions, for $N = 0.36$ and $R = 10$. This corresponds to $\chi = 360 < \chi_{CCP}$. In spite of the presence of a plateau, the system does not exhibit any transition phase, in neither canonical nor microcanonical ensemble. The spiral represented in the curve comes from the unstable branch of minimal energy Λ'_{max} and should not be confused with the left spiral representing the high energy instabilities studied in Chap. 4 (not here represented).*

The evaluations obtained for the other two values of the box radius show that the microcanonical transition is suppressed for $R = 50$. Surprisingly, we find that the value of N_{CCP} obtained for this radius matches with that obtained numerically (see Fig. 5.2). The small difference (of the order of 1.07%) is due to GR. This result shows that a sphere with $R = 50 \sim 15\ R_{OV}$ ($R_{OV} = 3.3569$ is the radius at the OV limit) can be considered *almost* Newtonian. Consequently, we can deduce that $R = 600$ represents a Newtonian fermionic system. The values obtained for N_{CCP} and N_{MCP} are consistent with those provided by the numerical analysis.

5.3.1. Caloric Curves

In this section we discuss the nature of the phase transitions (if present) for $R = 10 \sim 3R_{OV}$. Hereafter, we do not show the part referring to $\alpha < 0$. The treatment will be focused only on the part corresponding to $\alpha > 0$ related, as we have seen, to the occurrence of the phase transition.

In Fig. 5.7 we have considered the caloric curve associated with $N = 0.36$, value in the interval $[N_1, N_{OV}]$. According to the analysis carried out in Sec. 5.2, we should expect a phase transition for a value of N in this range but, as we note from the figure, the transition phase is missing (compare with Fig. 1.6). This confirms what we were above supposing, i.e. that $R = 10$ is too small to allow

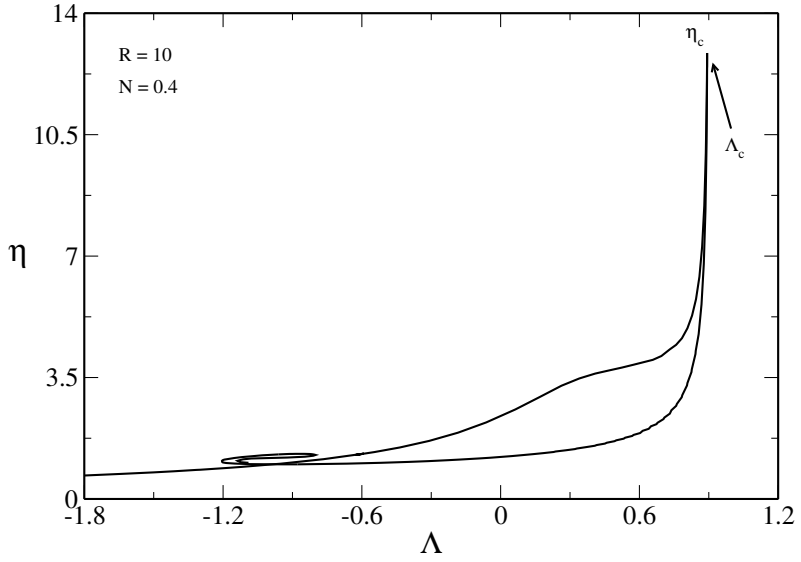

Figure 5.8: *Equilibrium phase diagram of self-gravitating fermions, for* $N = 0.4$ *and* $R = 10$ *(moreover* $\chi = 400 < \chi_{CCP}$*). There exists an isothermal collapse in the canonical ensemble (*η_c*) and a gravitational collapse in the microcanonical ensemble (*Λ_c*). The region of negative specific heat is very thin and not visible. From a thermodynamical point of view (although the shape of the curve is dissimilar) the system represented in the figure is equivalent to the isothermal sphere.*

the system to collapse. However, looking at the figure, we deduce that the value of the radius chosen is not so far from that allowing the occurrence of the phase transition, i.e. the "canonical critical radius" R_{CCP}. As we will see in Sec. 5.6), we find $R_{CCP} = 13$.

The series of equilibria consists of two parts, both delimited by a minimal value of energy (maximal in Λ). These two critical values of the energy correspond to the intersections between the line level $N = 0.36$ and the OV curve. As we have seen in Sec. 3.3, the OV limit allows us to separate between the (dynamically) stable and (dynamically) unstable configurations. By analyzing the behaviour of the mass radius relation (see Fig. 3.11), the stable states are placed before the turning point (i.e. the OV limit) whereas the unstable ones after that.

If we consider a line level $N = N_{spec} \geq N_1$, we get two intersection points having a different dynamical nature, the former being stable, the latter unstable. The energies corresponding to these points, which represent the two solutions of the ground state associated with N_{spec}, can be easily evaluated by using the results of Chap. 3. As matter of fact, once solved the CT equations (3.112) for several values of the central density, we get the total values of the radius, of the mass-energy and of the baryonic number N. The line level $N = N_{spec} \geq N_1$ identifies two solutions among those obtained and these solutions are characterized by two different values of the binding energy E_b, that correspond to Λ_{max}

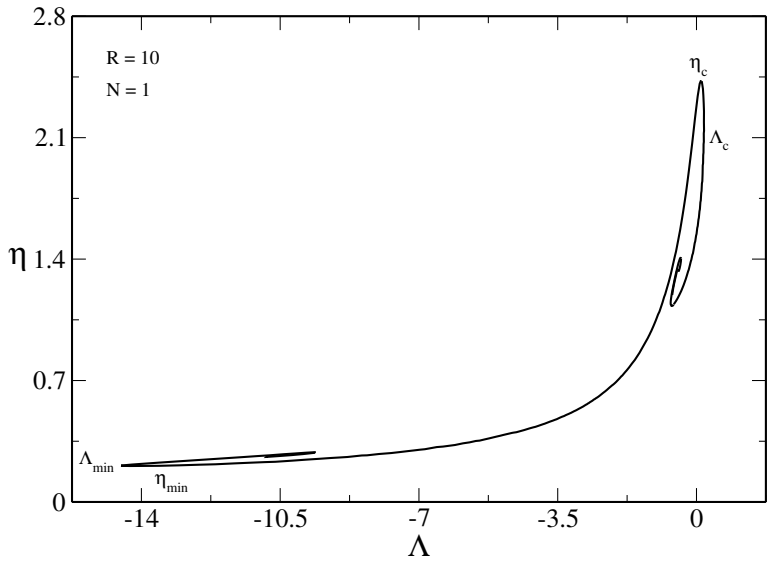

Figure 5.9: *Equilibrium phase diagram of self-gravitating fermions for $N = 1$ and $R = 10$ ($\chi = 10^3 < \chi_{CCP}$). The trend of the curve reproduces the behaviour already analyzed in Sec. 4.4, by indicating that the self-gravitating Fermi gas became equivalent to the non-quantum gas.*

and Λ'_{max} (see also Appendix D).

For this reason and, also, because of the absence of the phase transition, the main branch of the caloric curve (corresponding to the gaseous phase) is made by stable points. Conversely, the secondary branch is formed by (dynamically) unstable physical solutions. It is remarkable to note that this secondary branch ends with a spiral. Since the system does not exhibit a phase transition for $N = 0.36$, we can conclude that the phase transition does not occur for $N < 0.36$. We could also conclude that by analyzing the $N(\Phi_0)$ diagrams (not here represented for $R = 10$). In fact, for finite (but large) values of α, the particle number does not exhibit local maxima or minima that could lead to a collapse.

In Fig. 5.8 we have represented the caloric curve for N slightly above N_{OV} (specifically $N = 0.4$): the absence of the phase transition is confirmed. The shape of the caloric curve changed: the asymptotic energy Λ_{max} has been replaced by the critical energy Λ_c, leading the system to undergo a gravitational collapse in the microcanonical ensemble. At the same time, this critical point is characterized by the reverse critical temperature η_c, which guarantees the existence of an isothermal collapse also in the canonical ensemble. Because η_c and Λ_c are the temperature and the energy of the same critical point, the region characterized by the presence of the negative specific heat is missing. Moreover, the spiral placed on the bottom left of the diagram will recover, for increasing values of N, the spiral of classical systems (see Fig. 5.9).

For increasing values of N there is a decrease of the values of η, by implying a reheating of the system.

A confirmation comes by considering Fig. 5.9. In this case, we see that both the values of energy and temperature are increased (Λ and η reduced). As we could expect, far from the OV limit, the points η_c and Λ_c do not anymore coincide, by allowing the formation of the region with negative specific heat (in the middle of the two points). The trend of the curve shows that the fermionic system has recovered the behaviour of the classical gas.

5.3.2. Phase Diagrams

The former analysis has shown the presence of several critical points in the series of equilibria. In this Section we want to study the variation of these points according to the value of the particle number N. Let us firstly consider the microcanonical phase diagram, depicted in Fig. 5.10. We can consider the diagram as divided in two parts where the OV limit plays the role of the point where there is a changement of regime.

For $N < N_{OV}$, the diagram is formed only by Λ_{max} and Λ'_{max}. As we have seen, these two points can be obtained by the intersection between the line level and the OV curve. In Appendix D we have shown that the evaluation of Λ_{max} and Λ'_{max}, in the fully degenerate limit, is independent of the cavity radius. This means that the part of the phase diagram for $N < N_{OV}$ can be obtained "theoretically"[14]. Considering Λ_{max}, we see that the curve (always positive) starts from small values in the limit $N \to 0$ and reaches regularly the OV limit. The asymptotic behaviours in these limiting regions are

$$\begin{aligned} &\Lambda_{max} \simeq 0.9498\, N^{1/3} && N \to 0\,, \\ &\Lambda_{max} \simeq 0.898 - 2.739\,(N_{OV} - N) && N \to N_{OV}\,. \end{aligned} \tag{5.24}$$

Λ'_{max}, by contrast, rises suddenly for $N = N_1$ and reaches Λ_{max} at the OV limit. We stress that both Λ_{max} and Λ'_{max} represent, in the caloric curve, asymptotic values. In particular, if we look at the red dashed line in Fig. 5.10 (representing the Newtonian evaluation of Λ_{max}), we see that there is an important discrepancy between the relativistic and the Newtonian solution. For Λ'_{max} we find the asymptotic relations

$$\begin{aligned} &\Lambda'_{max} \simeq -5.362 + 90.46\,(N - N_1) && N \to N_1\,, \\ &\Lambda'_{max} \simeq 0.898 - 3.708\,(N_{OV} - N) && N \to N_{OV}\,. \end{aligned} \tag{5.25}$$

[14] This theoretical estimate has been numerically checked for all the radii considered.

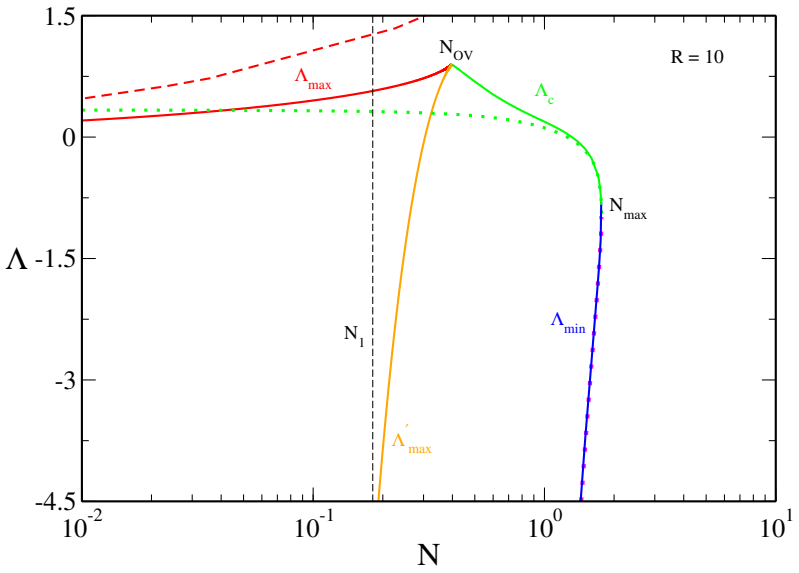

Figure 5.10: *Phase diagram in the microcanonical ensemble, for $R = 10$. The red dashed line represents the Newtonian evaluation of Λ_{max}. As the figure shows, the Newtonian prediction is far from the relativistic results. This is not surprising, because $R = 10$ is a value quite close to R_{OV}. The dotted lines reproduce the behaviour of Λ_c and Λ_{min} obtained in the nonquantum limit.*

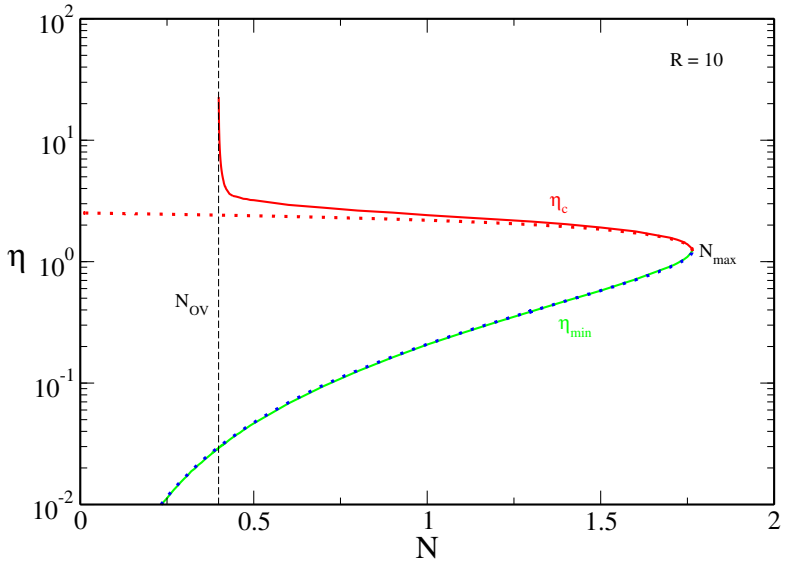

Figure 5.11: *Phase diagram in the canonical ensemble, for $R = 10$. The dotted lines are the results obtained in the nonquantum limit. The behaviour of the fermionic η_{min} (green line) is equivalent to the classical one (blue line). By contrast, the difference between the two η_c are important, especially when we approach the OV limit.*

If we consider the case $N > N_{OV}$, we see that the diagram is formed by Λ_c and Λ_{min}. Λ_c can be considered as the prolongation of Λ_{max} above the OV limit. However, differently from Λ_{max}, Λ_c is not an asymptotic value but, rather, a critical value. In Fig. 5.10 we have compared the fermionic Λ_c with that evaluated for classical systems (dotted green line in the figure). The two curves present the same behaviour only in the limit $N \to N_{max}$. As the reader can see, for $N < 10$ the trend of the curves is dissimilar. The fermionic Λ_c converges to the OV limit whereas the classical Λ_c reaches the Antonov limit. In the limit $N \to N_{OV}$, we find

$$\Lambda_c \simeq 0.898 + 1.078\,(N - N_{OV}) \qquad\qquad N \to N_{OV}\,. \tag{5.26}$$

Concerning Λ_{min}, we observe that the classical and fermionic curve coincide. This is a further evidence that, in the limit $\alpha \to -\infty$, Fermi-Dirac statistics recovers Boltzmann statistics.

In Fig. 5.11 we have illustrated the canonical phase diagram. The dotted lines represent the evaluations of η_c and η_{min} obtained in the nonquantum limit. Analogous to Λ_{min}, we note that the fermionic η_{min} matches very well with the classical one (as Λ_{min}, we do not report the scaling laws in the limits $N \to 0$ and $N \to N_{max}$). By contrast, if we analyze the behaviour of η_c, we observe two dissimilar behaviours. In the limit $N \to N_{max}$ the two curves practically coincide.

If we start to reduce the value of N, we see that for $N \sim 1$, the fermionic curve reaches values which are higher than the classical ones. The differences become more and more pronounced when we approach the OV limit. The classical η_c, as we know, tends to the reverse Emden temperature $\eta_c = 2.525$ whereas, the fermionic η_c diverges. In this limit, we have

$$\eta_c \simeq \frac{0.589}{(N - N_{OV})^{1/2}}\,. \tag{5.27}$$

5.4. The Case $R = 50$: Canonical Phase Transition

5.4.1. Caloric Curves

Let us now consider a fermionic gas encapsulated in a box of size $R = 50$. As we have previously seen, the general relativistic effects reduce their importance when the dimensions of the cavity are enlarged and the system can be considered approximately Newtonian. This means that, for $N < N_{OV}$ we expect to deduce a thermodynamics of the Fermi gas quite similar to that studied in Newtonian gravity. To show in detail the steps leading the system to exhibit the phase transition, in the following, we will show the series of equilibria for several value of N, in the interval $(0, N_{max}]$.

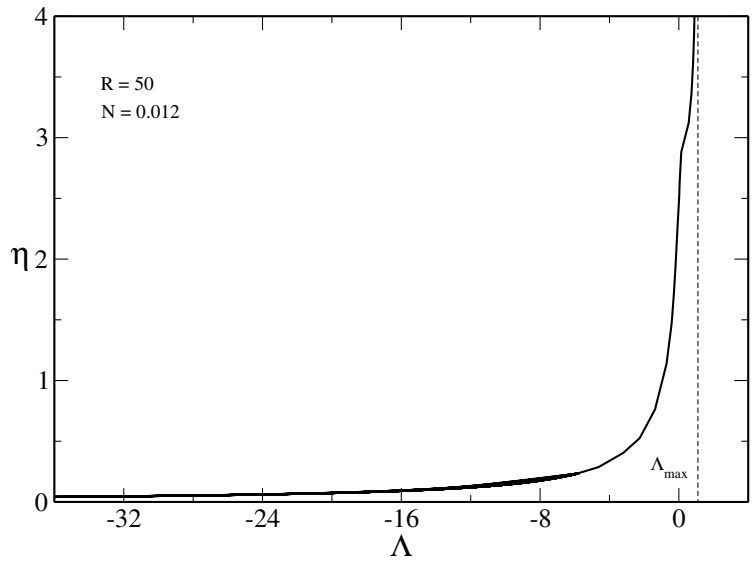

Figure 5.12: *Equilibrium phase diagram for self-gravitating fermions, for* $N = 0.012$ *and* $R = 50$ *(*$\chi = 1.5 \times 10^3 < \chi_{CCP}$*). The behaviour of the curve is similar to that obtained in Newtonian gravity [47] for* $\mu_d = 10$*. As the case previously analyzed, there exists a "plateau-like" region for* $\eta \sim 3$*. In this region of the space* $[\Lambda, \eta]$*, as we shall see in the following, the phase transition takes place.*

Let us start our analysis by considering the case $N < N_{CCP}$ (Fig. 5.12). The curve does not present peculiar properties. As we see, it comes from the region of big energies (Λ large and negative) and high temperature (η small) and reaches the asymptotic minimal energy Λ_{max} for increasing values of the reverse normalized temperature (the system is approaching the OV limit $T \to 0$). The solution can be considered similar to the isothermal sphere until the "plateau-like" region (for $\eta \sim 3$), where there is a changement in the shape of the curve. However, though the achievement of the limiting energy Λ_{max} is faster and faster for increasing values of η, the collapses are suppressed in both canonical and microcanonical ensemble. We note that the behaviour of the curve is also similar to that shown in last section for $N < N_{OV}$ (see Fig. 5.7).

As emphasized in Sec. 5.2, the presence of an inflection point in the $N(\Phi_0)$ diagram implies the existence of an inflection point in the caloric curve, corresponding to the occurrence of the canonical phase transition. This occurrence is represented, analogous to the $N(\Phi_0)$ diagram, by the sequence maximum-minimum in the temperature diagram. Consequently, we can define two critical temperatures, one being related to the isothermal collapse (η_c), the other linked to the appearance of the condensed phase (η_*). To better clarify this idea, let us consider Fig. 5.13, which illustrates the case $N_{CCP} < N < N_1$.

The series of equilibria is formed by three parts, the first one corresponding to the gaseous phase,

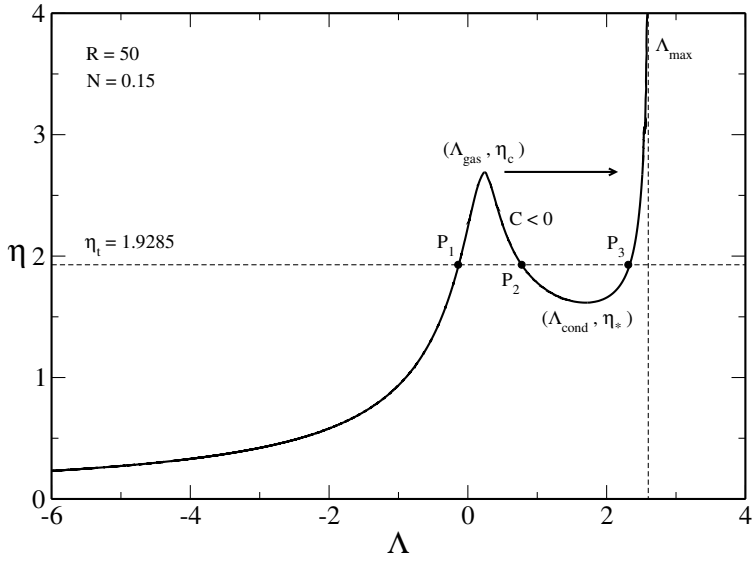

Figure 5.13: *Equilibrium phase diagram for self-gravitating fermions, for* $N = 0.15$ *and* $R = 50$ *(*$\chi_{CCP} < \chi = 1.88 \times 10^4 < \chi_{MCP}$*). The three points identified by the transition temperature* η_t *are also indicated. Points placed on the first branch (e.g.* P_1*) form the gaseous phase and are GFEm if* $\eta < \eta_t$ *and LFEm vice-versa. Points forming the condensed phase (points* P_2*) are unstable saddle points. Points* P_3*, finally, are LFEm if* $\eta < \eta_t$ *and GFEm vice-versa. In the microcanonical ensemble, the specific heat is negative in the region between* η_c *and* η_**. The diagram represents the case* $N_{CCP} < N < N_1$*.*

the second one to the unstable physical states and the third one to the condensed phase. Fixing a value of the temperature, the diagram shows the existence of more than one solution, of different nature (points P_1, P_2 and P_3). The temperature transition η_t enables us to separate the gaseous phase from the condensed one. This value of the temperature manifests the occurrence of the phase transition, which corresponds to a discontinuity in the free energy [24]. The gaseous phase (points P_1) is thus distinguished in a stable and a metastable part, according to the value of the temperature. The solutions having $\eta < \eta_t$ are global free energy minima[15] (GFEm) while, those characterized by a temperature bigger than η_t, are local free energy minima (LFEm) and represent metastable states.
For decreasing values of the temperature (η increasing), the curve approaches a critical temperature (η_c), responsible of the isothermal collapse of the system. The system collapses on a new equilibrium solution (according to the direction of the arrow) and takes a "core-halo" structure, forming a fermions ball (see Sec. 1.3). If we now increase the temperature (η decreasing), the series of equilibria is formed

[15] Chavanis [47] classifies the points forming the gaseous phase as global ($\eta < \eta_t$) or local ($\eta > \eta_t$) *maxima* of free energy (GFEM or LFEM respectively). This (appearent) inconsistency with the results of the present work arises because the free energy defined by Chavanis differs for a negative proportionality factor from that here used [see Eq.(5.7)].

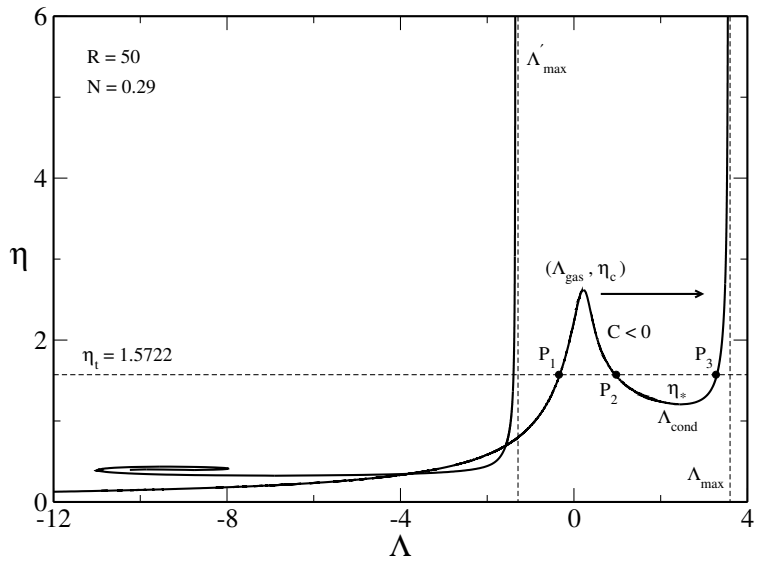

Figure 5.14: *Equilibrium phase diagram for self-gravitating fermions, for $N = 0.29$ and $R = 50$ ($\chi_{CCP} < \chi = 3.63 \times 10^4 < \chi_{MCP}$). Because $N > N_1$, the presence of the branch delimited by the minimal energy Λ'_{max} is manifest. However, due to its (dynamical) unstable nature (remember the mass radius relation obtained in Sec. 3.3.1, the presence of this secondary branch does not influence the thermodynamical properties of the system and the interpretation of the curve is the same as that given in the preceding figure.*

by a region (delimited by the critical temperatures η_c and η_*) which points (P_2) do not represent any physical solution, because unstable saddle points.

The condensed phase emerges at the critical temperature η_*. The physical solutions belonging to this part of the series of equilibria (points P_3) have opposite nature compared to the points of the gaseous phase. They are indeed LFEm if $\eta < \eta_t$ and GFEm $\eta > \eta_t$. In addition, Fig. 5.13 shows that the microcanonical instabilities are suppressed.

As pointed out by Chavanis [47], there exists one critical point of entropy for each value of the energy. However, the critical temperatures η_c and η_* enable us to the definition of two critical points in energy, representing the maximal (Λ_{gas}) and the minimal (Λ_{cond}) accessible energies at which the system can be a gas or a condensate. Fig. 5.14 displays the same physical situation above described. Being $N > N_1$, we see the appearance of the branch delimited by the minimal energy Λ'_{max}. In the canonical ensemble the presence of this branch does not influence the occurrence of the phase transition. Equivalent interpretation can be done in the microcanonical ensemble, because this branch is not related to the occurrence of a phase transition that, as we know, is suppressed for $R = 50$.

If we now take into consideration a value of N bigger than N_{OV}, we arrive to the situation plotted in

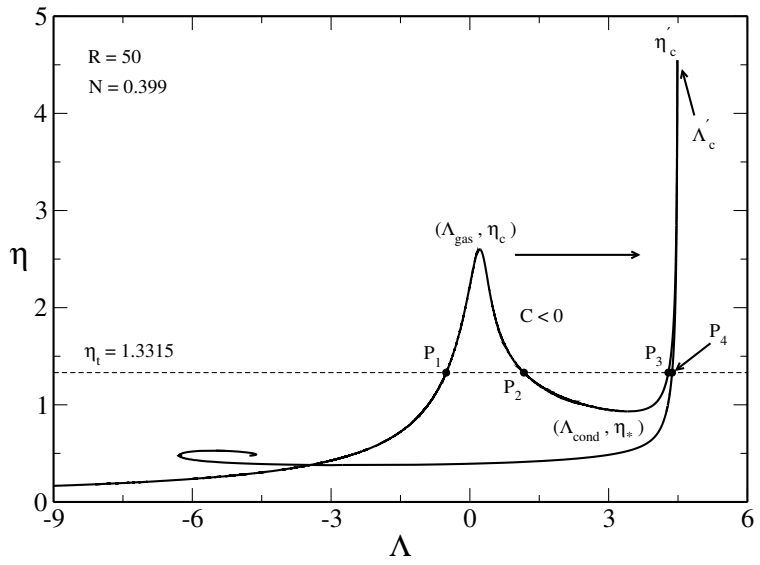

Figure 5.15: *Equilibrium phase diagram for self-gravitating fermions, for* $N = 0.399$ *and* $R = 50$ *(*$\chi_{CCP} < \chi = 4.99 \times 10^4 < \chi_{MCP}$*). Being* $N > N_{OV}$*, the condensed phase is delimited by the critical temperature* η_c'*. The figure displays the existence of two collapses, associated with the temperatures* η_c *and* η_c'*. Points* P_4*, anyway, represent unstable physical solutions. In the microcanonical ensemble, the asymptotic energy* Λ_{max} *is replaced by a critical value* Λ_c'*. Moreover, in the (very thin) region between* η_c' *and* Λ_c' *the specific heat is negative.*

Fig. 5.15. Here, the line level has been fixed at the height $N = 0.399$, slightly above the OV limit. The presence of GR has changed the shape of the caloric curve. As we see, the condensed phase reaches a critical temperature (indicated by the point η_c'), which allows the system to undergo a second collapse. The nature of the points (P_4) placed after the critical temperature η_c' is unstable. We stress that the rising of this second collapsing temperature is a pure relativistic effect.

In the microcanonical ensemble, we observe that the asymptotical energy Λ_{max} has been replaced by the critical energy Λ_c'. This is not of course a phase transition but just an instability, analogous to the Antonov instability. Although not visible in the figure, there exists a (thin) region between η_c' and Λ_c' where the specific heat becomes negative (see also Fig. 5.16).

The existence of this new critical temperature has a dramatic consequence for what concerns the occurrence of the phase transition. For $N \leq N_{OV}$ we have that the reverse normalized temperature of the condensed phase diverges ($\eta = +\infty$). The diagram in Fig. 5.15 lets us to suppose that, for $N = N_{OV} + \epsilon$ ($\epsilon \to 0$), we have $\eta = \eta_c' < \infty$. Therefore, if we increase the value of N, we expect that the value of η_c' decreases, becoming also smaller than η_c. There will be a point where the phase transition cannot occur anymore, because the free energies of the two phases are not anymore

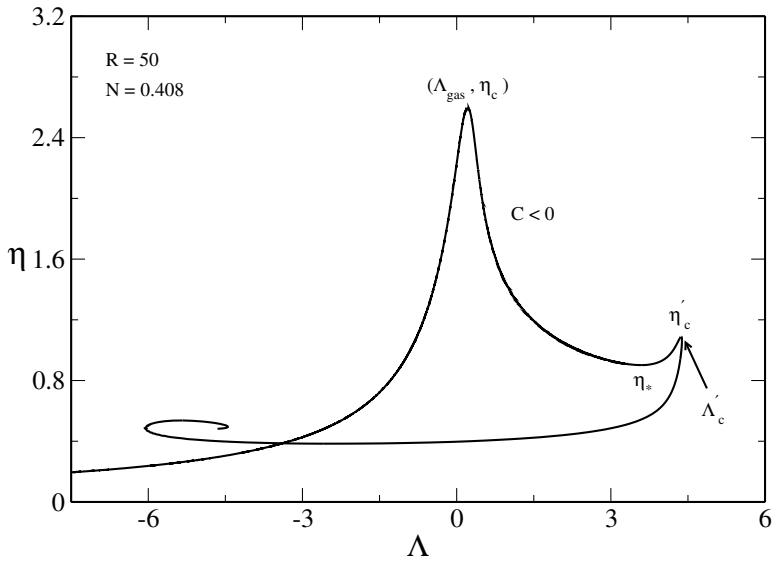

Figure 5.16: *Equilibrium phase diagram for self-gravitating fermions, for* $N = 0.408$ *and* $R = 50$ *(*$\chi_{CCP} < \chi = 5.1 \times 10^4 < \chi_{MCP}$*). Although the two isothermal collapses keep existing, the phase transition does not occur anymore. There is not anymore equivalence between the free energy of the gas and the condensate. In the microcanonical ensemble we observe the presence of two regions with negative specific heat and the exhibition of a "secondary" gravitational collapse associated with the point* Λ_c'.

equivalent. Speaking in terms of the Maxwell construction [105], this implies the inequivalence of the areas delimited by the transition temperature and the plateau, that is

$$\int_{P_1}^{P_3} (\eta - \eta_t)\, d\Lambda \neq 0\,. \tag{5.28}$$

In Fig. 5.16 we have represented the physical situation above described. Although the value of N is relatively close to N_{OV}, we note that the value of η_c' is considerably reduced compared to the case $N = 0.399$. The caloric curve looks like that illustrated in Fig. 5.15. Nevertheless, we see that the gaseous phase almost coincides with the gaseous phase of the isothermal sphere. In the microcanonical ensemble, we see that the two regions with negative specific heat still exist. If we increase the value of the temperature η, we see that the condensed phase has noticeably reduced its extension (the value of η_c' is close to η_*). Consequently, it seems difficult that the free energies of the two phases (gas and condensate) can be equivalent.

To make sure, in Figs. 5.17 and 5.18 we have represented the free energies corresponding to the series of equilibria obtained for $N = 0.399$ and $N = 0.408$. Considering Fig. 5.17, we see that the system exhibits the phase transition. The point η_t, indeed, is identified by the intersection between

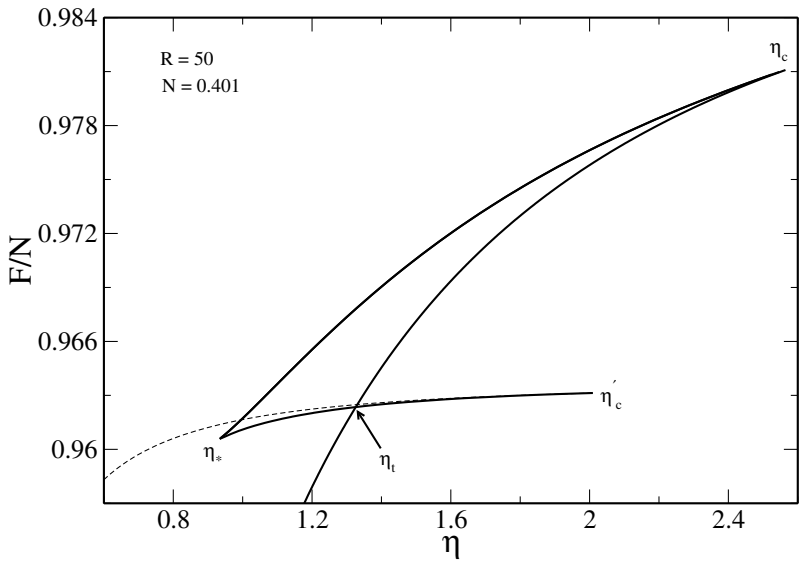

Figure 5.17: *Free energy per fermion as a function of the temperature, for* $N = 0.399$ *and* $R = 50$. *The phase transition occurs at the temperature* η_t, *when the two stable branches intersect. The dashed line represent unstable configurations, of general relativistic origin.*

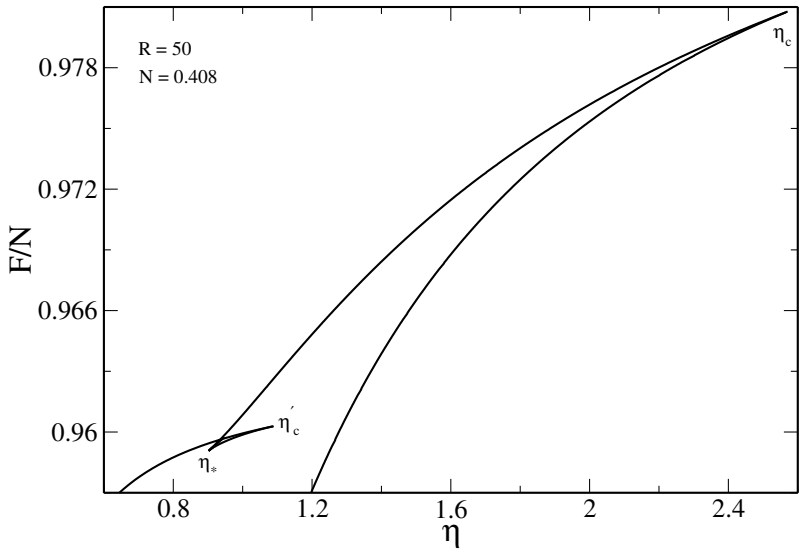

Figure 5.18: *Free energy per fermion as a function of the temperature, for* $N = 0.408$ *and* $R = 50$. *Differently from the preceding situation, the phase transition does not occur. The diagram shows that the branches of the gaseous and the condensed phase are far from each others and do not intersect. However, the systems exhibits a phase transition, but it is related to unstable states and it is not taken into account.*

the gaseous and the condensed phase, showing that the two free energies are equal. In Fig. 5.18, by contrast, this equivalence is missing. The gaseous and the condensed phase do not cross in any point, showing the suppression of the phase transition. However, we see a transition temperature, but it is related to unstable states and does not have a physical meaning. These considerations imply that the series of equilibria obtained for $N = 0.408$ is an intermediate state between the "pure" fermionic systems and the classical ones.

Increasing the value of N implies a continuous decrease of the values of η'_c, which are closer and closer to those of η_*. There exists a critical value of N where $\eta_* = \eta'_c$. At this point, that we call N_B, the fermionic system has recovered the properties typical of the isothermal gas sphere. Because of the equality $\eta_* = \eta'_c$, the condensed phase disappeared and, in the canonical ensemble, the stability is lost for $\eta > \eta_c$. In Fig. 5.19 we have represented the caloric curve describing this physical situation (we have taken $N = 0.45 > N_B = 0.418$).

As the reader can see, there exist two critical points (Λ_{min} and η_{min}, as we have said, are not represented), leading the system to the isothermal (canonical) and the gravitational (microcanonical) collapse. On the left of the curve we see the presence of a spiral, which originates from the spiral of the branch Λ'_{max}. As we know, for $N < N_{OV}$, Λ_{max} and Λ'_{max} converge to the same point in the limit $N \to N_{OV}$. This implies that also the spiral "moves", going to merge with the condensed phase. When $N > N_{OV}$ (see Fig. 5.15), the spiral (which is not disappeared) comes from the unstable branch delimited by Λ'_c (corresponding to Λ'_{max} when the particle number is bigger than N_{OV}).

If we keep increasing the value of N, the caloric curve evolves as represented in Figs. 5.19 and 5.20. As the reader can note, the shape of the curves is more and more similar to those studied in Chap. 4.

5.4.2. Phase Diagrams

The preceding analysis has shown the existence of a (tri)critical point, i.e. N_{CCP}. This implies that the phase diagrams, compared to the case $R = 10$, present some differences, in both microcanonical (in spite of the absence of the phase transition) and canonical ensembles. In Fig. 5.22 we have represented the phase diagram in the microcanonical ensemble which looks quite different from that plotted in Fig. 5.10.

The diagram can be read in two different ways, according to the nature of the gas or to the intensity of the gravity. From the left to the right, the system is quantum (according to the species of the particles filling up the sphere) and Newtonian (according to the strength of the gravity). For increasing values of N, the intensity of the gravity increases and, accordingly, the classical behaviour of the gas is more and more manifest. The full lines in Fig. 5.22 represent the solutions obtained by means of the general

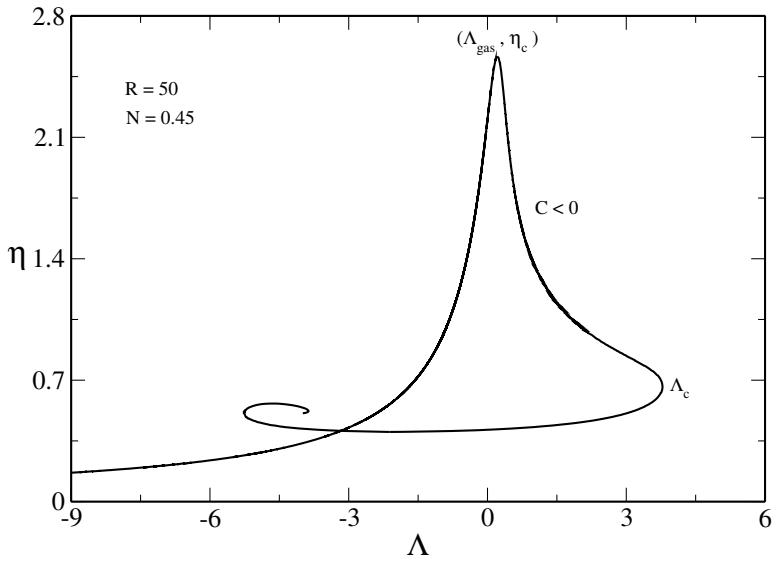

Figure 5.19: *Caloric curve for* $N = 0.45$ *and* $R = 50$ *(*$\chi = 5.63 \times 10^4$*). In the canonical ensemble, after the isothermal collapse, the system cannot gain the stability a second time. In the microcanonical ensemble, the critical energy* Λ_c *is the fermionic generalization of the Antonov instability. From a thermodynamical point of view, this diagram is equivalent to those obtained in the context of the classical gas.*

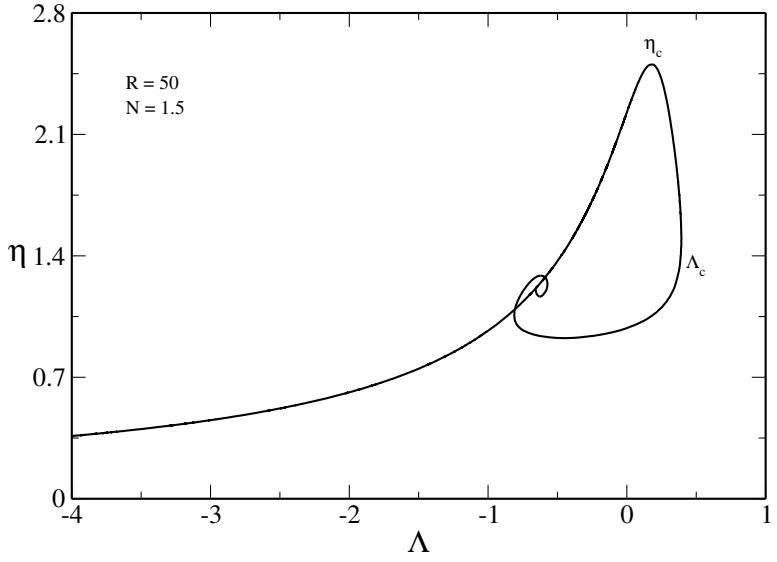

Figure 5.20: *Caloric curve for* $N = 1.5$ *and* $R = 50$ *(*$\chi = 1.88 \times 10^5$*). Compared to the previous case, the trend of the curve is more similar to that of a typical classical system.*

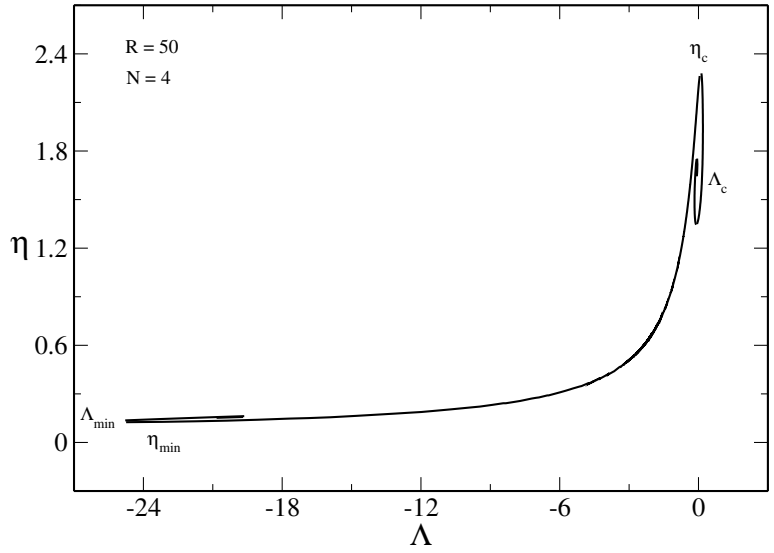

Figure 5.21: *Caloric curve for $N = 4$ and $R = 50$ ($\chi = 5.63 \times 10^7$). The diagrams shows the presence of four collapses, two in the canonical and two in the microcanonical ensemble. Under these conditions, the original fermionic system becomes a classical system.*

relativistic Thomas - Fermi model. The dashed and the dotted lines refer to the case of Newtonian fermionic configurations and to the general relativistic isothermal spheres.

In the limit $N \to 0$, as we know, there are not collapses and the system reaches its limiting energy Λ_{max}. As we know, for small values of N, Λ_{max} behaves as (see Appendix D)

$$\Lambda_{max} \simeq 4.749\, N^{1/3} \qquad\qquad N \to 0\,. \tag{5.29}$$

If we keep increasing the value of N, we find the critical point N_{CCP}. In spite of its canonical origin, it plays a role in the microcanonical ensemble too, because of the energies associated with the temperatures η_c and η_*. As we have previously seen (see Tab. 5.1), the value of N_{CCP} obtained thanks to the Newtonian model is slightly smaller than the value obtained by means of the numerical resolution of the TOV system. Anyway, due to the small value of this difference (1.07 %), which is caused by the general relativistic corrections, we can use the Newtonian scaling laws for Λ_{gas} and Λ_{cond} obtained in Ref.[47] (here not reported).

Looking at the diagram, we see that the Newtonian theory deviates from the relativistic one for $N \sim 0.1$. This is not suprising, because we are approaching the OV limiting curve (indeed $N_1 = 0.18131$) and we find a new branch, identified by Λ'_{max}. In this limiting situation, We have

$$\Lambda'_{max} \simeq -26.81 + 452.325\,(N - N_1) \qquad\qquad N \to N_1\,. \tag{5.30}$$

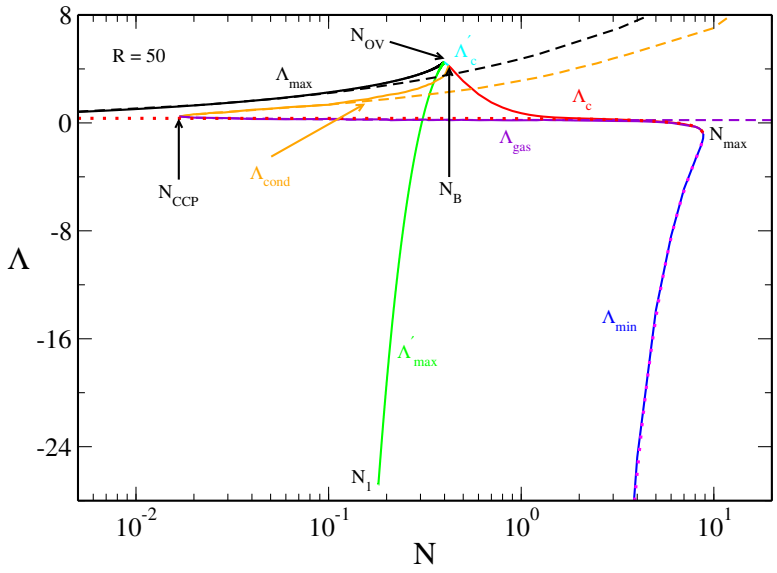

Figure 5.22: *Phase diagram in the microcanonical ensemble, for* $R = 50$*. The dashed lines represents the Newtonian evaluations while the dotted lines represent the evaluations of* Λ_c *and* Λ_{min} *obtained in Chap. 4. In spite of the absence of the microcanonical phase transition, we can identify five critical values of* N*. Compared to the phase diagram obtained for* $R = 10$*, the novelty is represented by the energies of the gas and the condensate, which are equal at the canonical critical point* N_{CCP}*.*

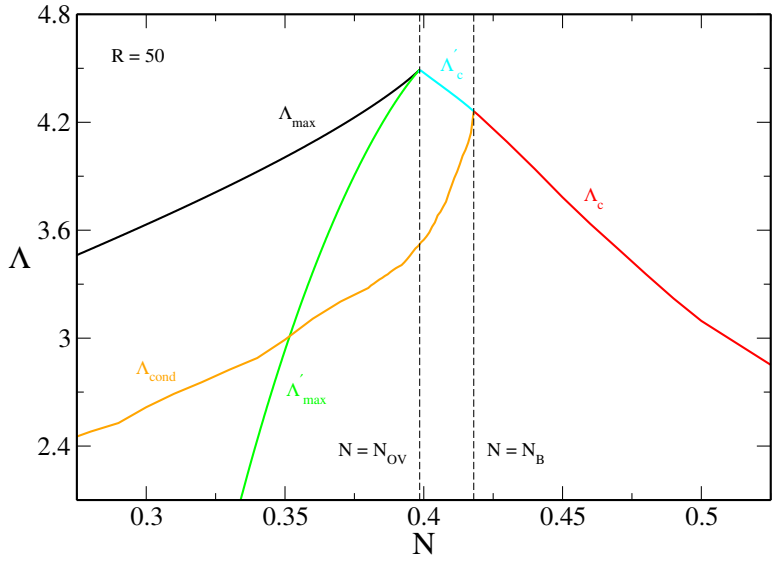

Figure 5.23: *Enlargement of the phase diagram near the critical point* N_B*, determined by the equivalence of* Λ_{cond} *(orange line),* Λ'_c *(cyan line) and* Λ_c *(red line).*

The general relativistic effects increase their importance and are not anymore negligible. From the diagram we see that the deviations from the Newtonian behaviour of Λ_{max} and Λ_{cond} are more important. In particular, Λ_{max} reaches the OV limit (in contrast with the Newtonian curve that diverges for large values of N) while Λ_{cond} reaches the curves Λ_c' and Λ_c in the new (and relativistic) critical point N_B (in Fig. 5.23 we have enlarged the phase diagram to better show this part). For $N \to N_{OV}$ we find

$$\begin{aligned} \Lambda_{max} &\simeq 4.49 - 13.70\,(N_{OV} - N)\,, \\ \Lambda'_{max} &\simeq 4.49 - 18.54\,(N_{OV} - N)\,, \\ \Lambda'_c &\simeq 4.49 + 16.48\,(N - N_{OV})\,. \end{aligned} \tag{5.31}$$

In the limit $N \to N_B$ we obtain

$$\begin{aligned} \Lambda'_c &\simeq 4.249 + 5.707\,(N_B - N)\,, \\ \Lambda_{cond} &\simeq 4.249 - 3.487\,(N_B - N)\,, \\ \Lambda_c &\simeq 4.249 - 8.005\,(N - N_B)\,. \end{aligned} \tag{5.32}$$

For $N = N_B$, as we have previously seen, the system has recovered the Boltzmannian behaviour. We can see that by looking the trend of the curves in the diagram. The red dotted line (Boltzmannian Λ_c) coincides with the fermionic one for large values of N and, in the limit $N \to N_{max}$, the behaviour of the two curve are superimposed. Moreover, by looking at Λ_{min}, we see that the classical curve (magenta dotted line) matches perfectly with the fermionic one. We can intepret to these features as a confirmation, *a posteriori* that, the nonquantum limit is recovered for $\alpha \to -\infty$.

In Fig. 5.24 we have represented the canonical phase diagram. The interpretation is the same as that given for the microcanonical case. The quantum and the relativistic nature of the system evolve moving from the left to the right of the figure. Differently from the microcanonical ensemble, four critical points are "pertinent" for the comprehension of the global properties.

For $N = N_{CCP}$ the system exhibits the phase transition and there is equivalence among the three temperatures η_c, η_* and η_t. Similar to Λ_{cond} and Λ_{gas}, the scaling laws are given by the Newtonian theory [47]. If we increase the value of N, we see that the deviations from the Newtonian behaviour arise for $N \sim 0.1$ and become especially noticeable for η_* and η_t. In fact, as we know, the GR suppresses the occurrence of the phase transition (when $\eta_t = \eta_c'$). In such conditions, the system becomes classical ($N = N_B$). In this limit we have

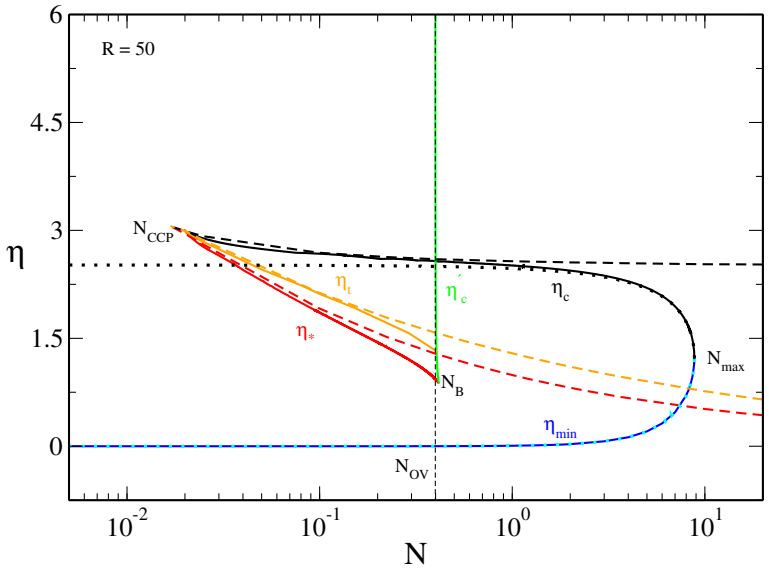

Figure 5.24: *Phase diagram in the canonical ensemble, for $R = 50$. The full lines represent the numerical results whereas the dashed ones the Newtonian predictions. The dotted lines are the estimates obtained in Chap. 4. It is remarkable that the fermionic and the classical η_{min} are practically the same.*

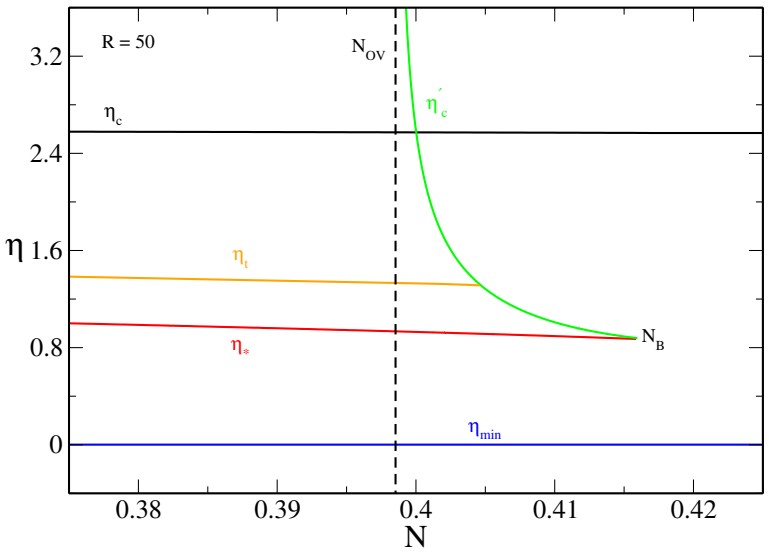

Figure 5.25: *Enlargement of the phase diagram in the interval $N_{OV} < N < N_B$. The point N_B is defined by the intersection of the temperatures η'_c and η_*. We note also that the transition temperature η_t intersects η'_c for $N < N_B$.*

$$\begin{aligned} \eta_c' &\simeq 0.849 + 1.647\,(N_B - N)^{4/3}\,, \\ \eta_* &\simeq 0.849 + 1.656\,(N_B - N)\,. \end{aligned} \tag{5.33}$$

As a confirmation of the relativistic origin of the second collapse, the temperature η_c' has a diverging behaviour in the limit $N - N_{OV}$, behaving as

$$\eta_c' \simeq \frac{0.103}{(N - N_{OV})^{1/2}}\,. \tag{5.34}$$

Eq.(5.34) displays the same power dependence obtained in Eq.(5.27). We can thus say that $\eta_c' \propto (N - N_{OV})^{-1/2}$ independently of the cavity radius.

5.5. The Case $R = 600$: Microcanonical Phase Transition

The preceding discussion indicates that the occurrence of the phase transition depends on two parameters, that is R and N. Actually, to find evidences about the onset of the microcanonical instabilities, we argue that we have to extend the dimensions of the box[16]. A first attempt is depicted in Fig. 5.26. We have indeed represented the series of equilibria for $R = 100 \sim 30\ R_{OV}$ (case studied by Bilić & Viollier [25]), for a range of values of N of the order of unity[17]. If look carefully at the diagram, in the microcanonical ensemble we see that, compared to Fig. 5.20, the system exhibits a changement of regime. In fact, in the region evidenced by the red circle, the reader can observe the presence of an inflection point for $N \simeq N_{MCP} = 1.15$.

For a value of $N < N_{MCP}$, the interpretation of the curve is the same as that given in Sec. 5.4.1. We indeed see that, after the point η_c, the curve comes down until Λ_c, where the gravitational collapse is allowed. As precedingly remarked, in this case, the system is thermodynamically equivalent to a classical gas. For a value of $N > N_{MCP}$, although not well visible in Fig. 5.26, there exist two critical values of the energy, interpretable as the microcanonical version of the points η_c and η_{min} in the canonical ensemble. The presence of these two critical points, which enable us to distinguish between a gaseous and a condensed phase in the microcanonical ensemble, shows the occurrence of the phase transition[18] in the box of size $R = 100$.

[16] By virtue of Eq.(5.20), we expect a decrease of the value of N, accordingly.

[17] The related values of χ (or μ_d) are close to those discussed by Chavanis in his study on the microcanonical phase transition.

[18] We stress that Bilić & Viollier did not discuss the case of the microcanonical instabilities. In their model they have studied the occurrence of the canonical phase transition for $N = 0.38 < N_{OV}$.

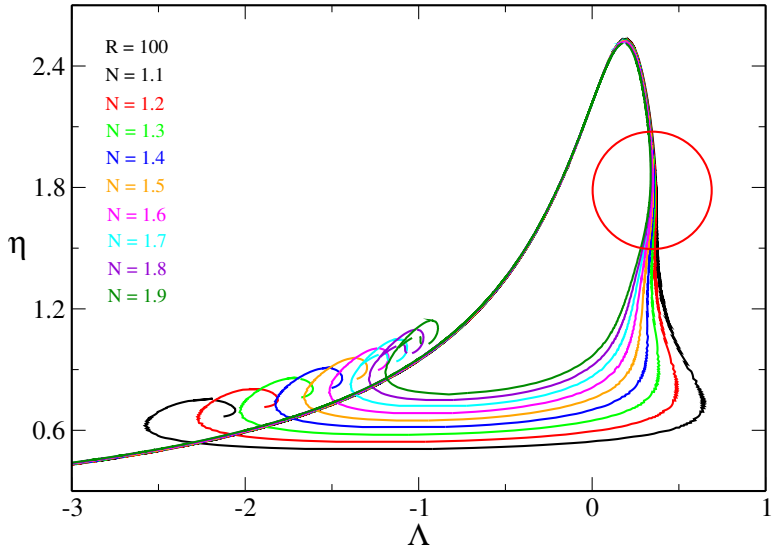

Figure 5.26: *Equilibrium phase diagram of self-gravitating fermions, for* $R = 100$ *and several values of* N. *It is possible to appreciate the presence of a small concavity (evidenced by the circle) before reaching* Λ_c. *This effect is due to the bigger spatial extension of the box.*

By recalling the previous evaluations of the critical values of χ_{MCP} [Eq.(5.23)], if we apply it to $R = 100$, we obtain $N_{MCP} \simeq 20.878 > N_{max} = 17.601$, in contrast with Fig. 5.26 illustrates. This shows that the Newtonian theory does not work for values of the box sizes of this order of magnitude. In Sec. 5.6, by analyzing Fig. 5.37, we will better appreciate the general relativistic corrections to the Newtonian theory. However, to emphasize the idea as regards the occurrence of the microcanonical phase transition, in the following we work within the sphere $R = 600$.

5.5.1. Caloric Curves

According to the results listed in Tab. 5.1, we expect that the fermionic system exhibits the microcanonical phase transition for $N < N_{OV}$. For that reason, in Fig. 5.27 we have plotted the curve $\eta = \eta(\Lambda)$ for $N = 0.29$. From a canonical point of view, the phase diagram is equivalent to that depicted in Fig. 5.14 for $R = 50$ (we did not represent in the plot because we want to focus on the microcanonical instabilities). Due to the smallness of the instability region (delimited by the energies Λ_c and Λ_*), the energy transition Λ_t is very close to the energy Λ_{gas} associated with the isothermal collapse. As in the canonical ensemble, we can distinguish a gaseous (points $\Lambda < \Lambda_c$) from a condensed (points $\Lambda > \Lambda_*$) phase.

As we have recalled in Sec.1.3, the phase transition occurs when the entropy of the gas is equal to that of the condensate (see also Fig. 5.30). This implies that the nature of the points forming the

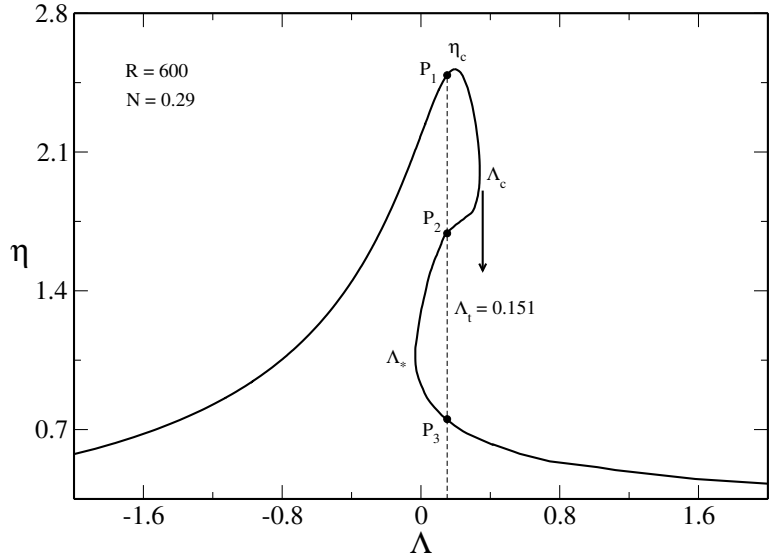

Figure 5.27: *Equilibrium phase diagram of self-gravitating fermions, for* $N = 0.29$ *and* $R = 600$ *(*$\chi = 6.26 \times 10^7 > \chi_{MCP}$*). In the canonical ensemble (not shown in the figure), the caloric curve has the same behaviour of that represented in Fig. 5.14. By contrast, a larger value of the box size guarantees the occurrence of the microcanonical phase transition for* $N < N_{OV}$*.*

gaseous and the condensed phase is different, according to their position with respect to the transition energy Λ_t. For what concerns the gaseous phase (points P_1), we find that points placed before the transition energy are global entropy maxima (GEM) whereas points placed after are local entropy maxima (LEM). By analogy with the canonical ensemble, the points forming the condensed phase have opposite nature of the points forming the gaseous one. Further, the solutions placed between the critical energies Λ_c and Λ_* are unstable saddle points and do not represent any physical real system.

The critical energy Λ_c represents the minimal accessible energy beyond which the system cannot anymore substain the gravity and undergoes a collapse (according to the arrow direction). The results of this process consists in the formation of a compact object (a "relativistic" fermions ball, as in the canonical ensemble). The energy Λ_*, by contrast, is the maximal energy leading the system to the formation of the condensate.

As in Newtonian gravity, the dissimilar nature of the points P_1, P_2 and P_3 is reflected in the density profiles. Points forming the gaseous phase have a "diluted" (smooth) profile whereas, points in the unstable branch, show the existence of a small nucleus, a "germ" [47]. The points forming the condensed phase, as we know, they have a core-halo structure by looking like a NS.

The preceding discussion can be summarized by saying that the phase transitions (both of types) are exhibited by the system because of the quantum nature of the gas. The presence of GR, compared

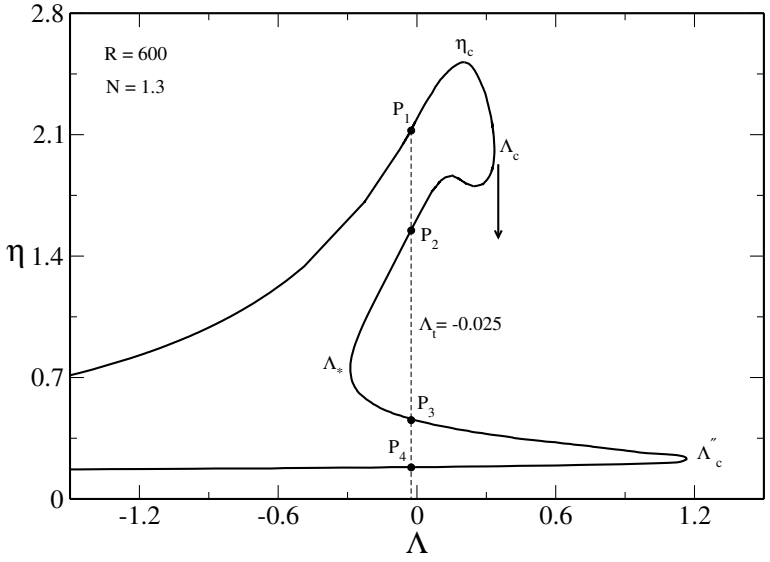

Figure 5.28: *Equilibrium phase diagram of self-gravitating fermions, for* $N = 1.3$ *and* $R = 600$ *(*$\chi = 2.81 \times 10^8 > \chi_{MCP}$*). The transition energy* Λ_t *is also indicated. Points forming the gaseous phase before* Λ_t *are global entropy maxima (GEM) while points after* Λ_t *are local entropy maxima (LEM). Points forming the condensed phase are LEM for* $\Lambda < \Lambda_t$ *and GEM for* $\Lambda > \Lambda_t$*. The solutions* P_2 *and* P_4 *are unstable.*

to Newtonian gravity, has the effect of "accelerating" the appearance of the transition phase. As we have also seen in Chap. 4, relativistic configurations are more unstable than the Newtonian ones and this fact is independent of the nature of the fluid.

When the value of N exceeds the OV limit, as we have seen in Sec. 5.4.1, a second isothermal collapse appears in the canonical ensemble. The unstable states forming the second descending branch (where the system reaches its minimal energy Λ_c') go to form a spiral (see, e.g., Figs. 5.16, 5.19 and 5.20) and the critical energy Λ_c' reduces progressively its value. This feature has consequences also in the microcanonical ensemble.

When the secondary isothermal collapse in η_c' extinguishes, the system reaches a new critical value of the energy, that we have called Λ_c'' (see Figs. 5.28 and 5.29). Analogous to the canonical ensemble with η_c', this critical value will decrease for increasing values of N. In other words, the energy Λ_c'' is the microcanonical equivalent of the temperature[19] η_c'.

In Figs. 5.28 and 5.29 we have represented the series of equilibria for $N = 1.3$ and $N = 1.6$. The figures display two different situations. In the first case, we have $\Lambda_c'' > \Lambda_c$ and, as indicated by the

[19]There is however a difference between the nature of the two points. η_c' is the temperature that comes from the infinity (because related to the OV limit). Λ_c'' originates from Λ_c' and Λ_{max}, which are finite values of the energy.

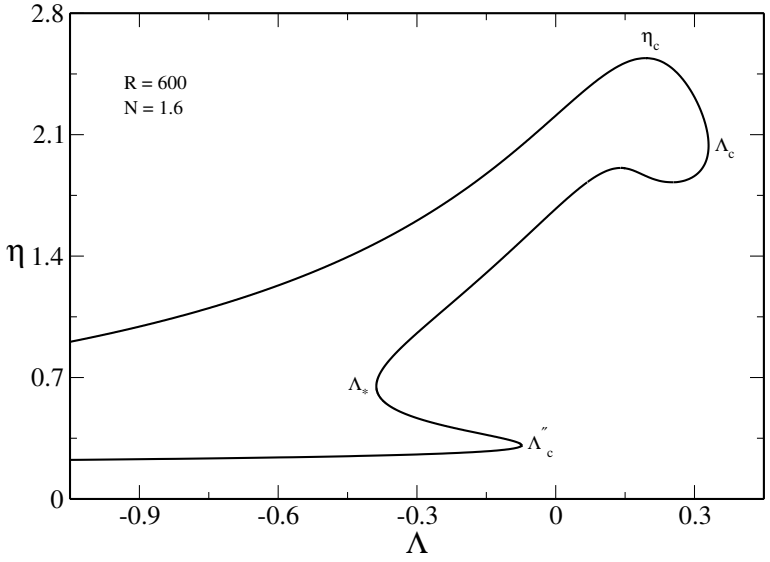

Figure 5.29: *Equilibrium phase diagram of self-gravitating fermions, for $N = 1.6$ and $R = 600$ ($\chi = 3.46 \times 10^8$). Differently from the preceding figure, the system does not exhibit the phase transition. Once collapsed in $\Lambda = \Lambda_c$, it is not anymore possible to form a new structure.*

vertical dashed line, a phase transition occurs at the transition energy $\Lambda_t = -0.025$. There exist two collapses, identified by the critical points Λ_c and Λ_c''. However, differently from the case $N < N_{OV}$, the condensed phase is delimited by the point Λ_c''.

If we now consider Fig. 5.29, we see that $\Lambda_c'' < \Lambda_c$: once undergone the gravitational collapse, the system cannot become a condensate (there still exists a reduced condensed region). Further, similar to the canonical ensemble, we observe the suppression of the phase transition. In fact, the entropies of the gas and the condensate are not anymore equal and the system *must* collapse (at the point Λ_c). By analogy with the analysis carried out in Sec. 5.4.1, we can claim that also in the microcanonical ensemble we observe the disparition of the Maxwell plateau in presence of the gravitational collapse[20]. In Figs. 5.30 and 5.31 we illustrate the entropies as a function of the binding energy Λ for the situations above discussed. For $N = 1.3$, we note the intersection point between the two phases (gas and condensate) and the transition can take place. We stress that the dashed line in Fig. 5.30 is related to unstable states of relativistic origin. Conversely, for $N = 1.6$, there exists a phase transition, but it concerns unstable states (points P_2 in the caloric curve).

If we now increase the value of N, we expect that the system achieves a critical value of N where

[20]The reader could not find surprising this feature, because also in Newtonian gravity the Maxwell plateau disappears. In that case, however, the disappearance of the plateau is linked to the inflection points (in both of ensembles) which enable the system to exhibit the transition phase. In GR the situation is different because the plateau disappears when the system *has already suffered* the collapse.

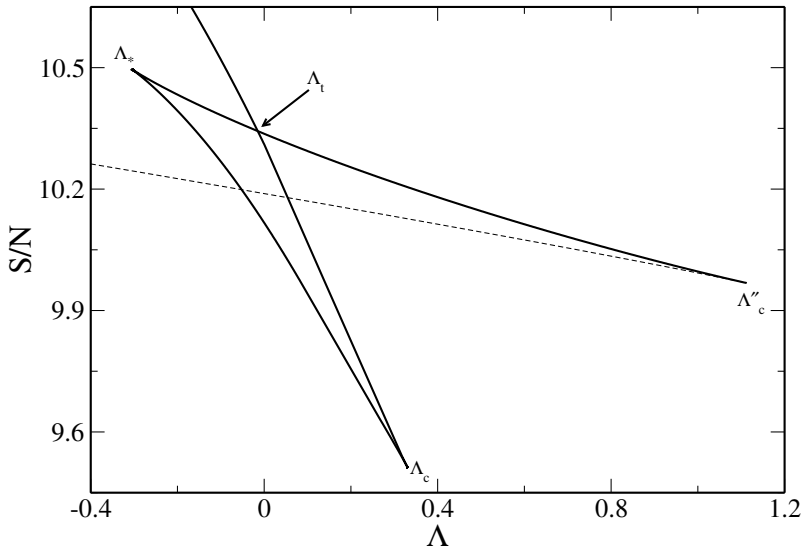

Figure 5.30: *Entropy per fermion as a function of the normalized binding energy, for* $N = 1.3$ *and* $R = 600$*. The transition phase occurs when the gaseous and the condensed branch intersect at the point* Λ_t*. The dashed line represents unstable physical solutions of general relativistic origin.*

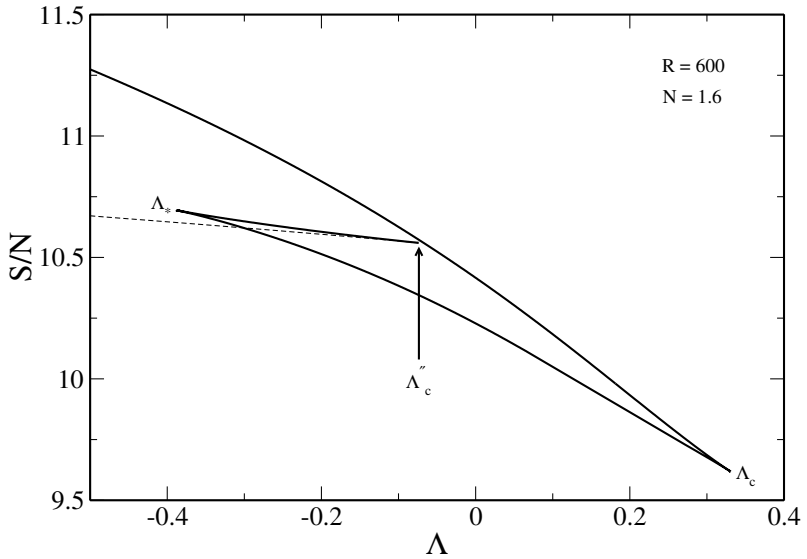

Figure 5.31: *Entropy per fermion as a function of the normalized binding energy, for* $N = 1.6$ *and* $R = 600$*. The dashed line represents unstable physical solutions of general relativistic origin. Differently from the case* $N = 1.3$*, the system does not exhibit any transition phase because of the non-vanishing difference between the entropies of the gaseous and the condensed phases.*

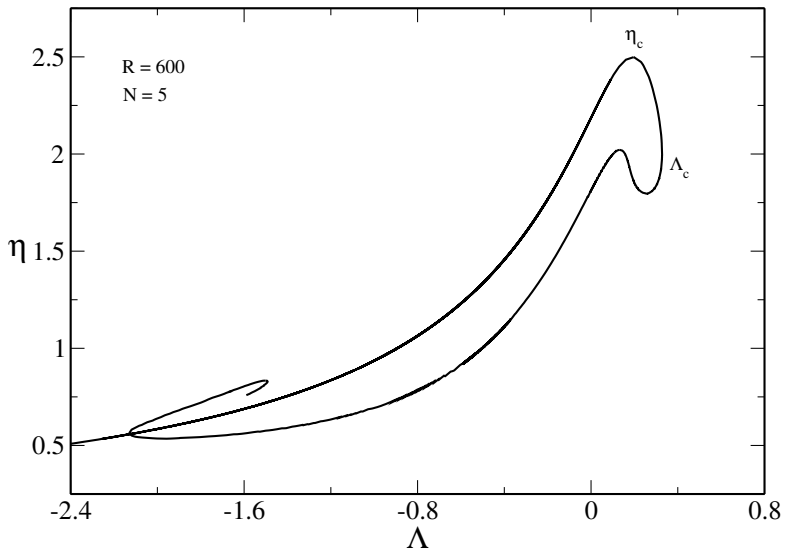

Figure 5.32: *Equilibrium phase diagram of self-gravitating fermions, for $N = 5$ and $R = 600$ ($\chi = 1.08 \times 10^9$). The figure represents an intermediate situation between the "dinosaur" and spiral shape. Although the system is still fermionic, its thermodynamical properties are equivalent to those of the non-quantum gas.*

$\Lambda_* = \Lambda_c''$. This point, called N_B', represents the points at which the fermionic system has recovered, in the microcanonical ensemble, the classical behaviour. Naturally, we expect a gradual passage from the "dinosaur-like" to the "spiral-like" configurations, and this happens for increasing values of N. In Fig. 5.32 we have represented an intermediate step of this process. The spiral on the bottom left of the curve (which should not be confused with that provided by $\alpha < 0$, not represented in the figure) moves, for increasing values of N, towards the collapsing points η_c and Λ_c. We stress, again, that this spiral originates from the unstable branch Λ_{max}' (see Fig. 5.14).

We want to end this section showing that the critical points in the microcanonical ensemble cannot be determined by means of the graphic construction discussed in Sec. 5.2. In Fig. 5.33 we have represented the positioning of the critical points Λ_c, Λ_* and Λ_c'' of Fig. 5.29 in the $N(\Phi_0)$ diagram. The line level $N = 1.6$ (orange line) identifies three intersection points (for three different values of α, see black full lines in the figure) which are placed in the descending part of the $N(\Phi_0)$ curve.

More in detail, Λ_c is placed between the first local minimum and the second local maximum whereas, Λ_* and Λ_c'' are placed after the second local maximum of the curve. Differently from the canonical points (we have also represented η_c by the blue line), the microcanonical points are placed in a part of the $N(\Phi_0)$ where there is not evidence of critical points. Thus, we can conclude, as previously anticipated, that the graphic construction is not appliable to the determination of the critical points

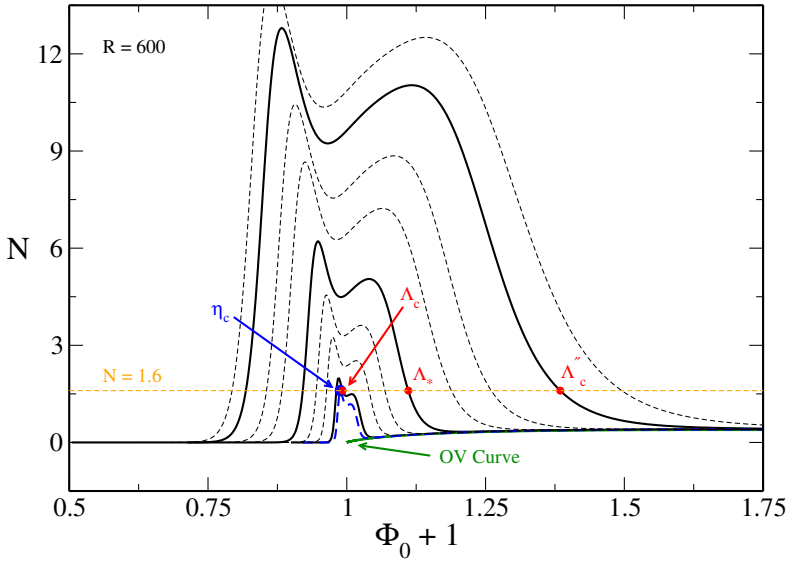

Figure 5.33: *Total particle number versus the central value of the gravitational potential* $\Phi_0 + 1$*, for the line level* $N = 1.6$ *and for* $R = 600$*. The OV curve is represented by the green line. The blue line represents the curve obtained for* $\alpha = \alpha(\eta_c)$*. As we expected, the point* η_c *corresponds to maximum of the curve. By constrast, the position of the points* Λ_c*,* Λ_* *and* Λ_c'' *cannot be* a priori *determined, because not related to any critical point of the* $N(\Phi_0)$ *functions (see the full black lines).*

in the microcanonical ensemble.

5.5.2. Phase Diagrams

The microcanonical phase diagram (Fig. 5.34) is more complex than that analyzed in Sec. 5.4.2 (see Fig. 5.22). Anyway the interpretation of the diagram above given, in terms of the combination of quantum and general relativistic effects, still holds. For $N < N_{MCP}$ the diagram displays the same features already analyzed for $R = 50$ and the scaling laws are *exactly* the same as those obtained in the Newtonian theory.

The most interesting part, which makes the diagram dissimilar from that obtained in Sec. 5.4.2, is placed in the region close to N_{MCP} (Fig. 5.35). The three energies Λ_c, Λ_t and Λ_* appear simultaneously in $N = N_{MCP}$ but their behaviour, for $N > N_{MCP}$, is very different. The collapsing energy (red line) can be considered almost constant (the dinosaur does not change its position in the caloric curves) and, for $N \to N_{max}$, coincides with the Λ_c evaluated in the context of Boltzmann statistics. We see the existence of a point where $\Lambda_c = \Lambda_c''$.

The transition energy Λ_t can be considered basically Newtonian. As we see, the numerical and the Newtonian solutions split up for $N \sim 1$. Since $N > N_{OV}$, the system can be considered relativistic:

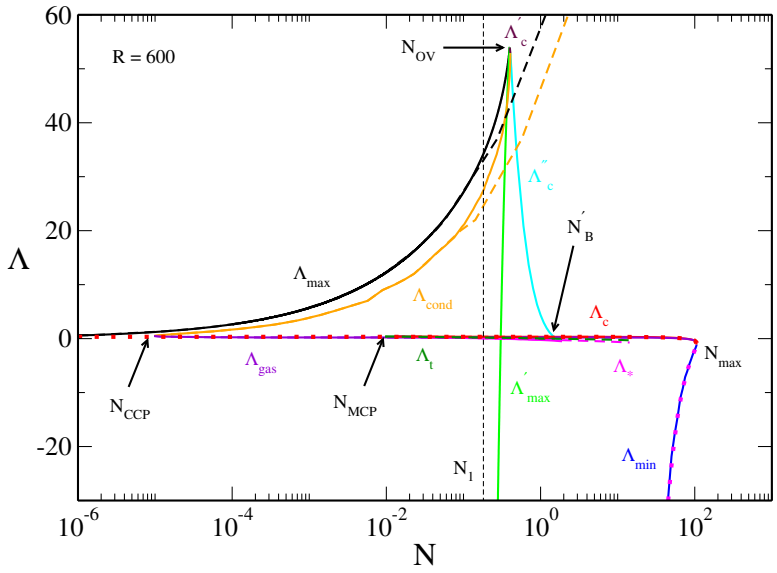

Figure 5.34: *Phase diagram in the microcanonical ensemble, for $R = 600$. The full lines represent the numerical results whereas the dashed line are the results obtained by the Newtonian theory. The dotted lines are the evaluations of Λ_c and Λ_{min} in the context of the Boltzmann statistics. Compared to the Newtonian phase diagram, GR "added" four critical points, as discussed in the text.*

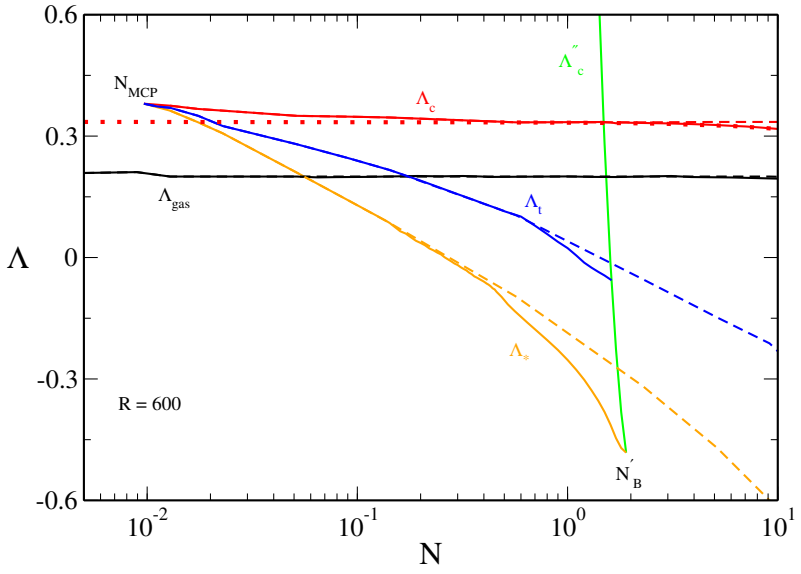

Figure 5.35: *Enlargement of the phase diagram in the region near the critical point N'_B. It is remarkable that the relativistic corrections, in spite of their small numerical entity, change the behaviour of the critical points Λ_* and Λ_t.*

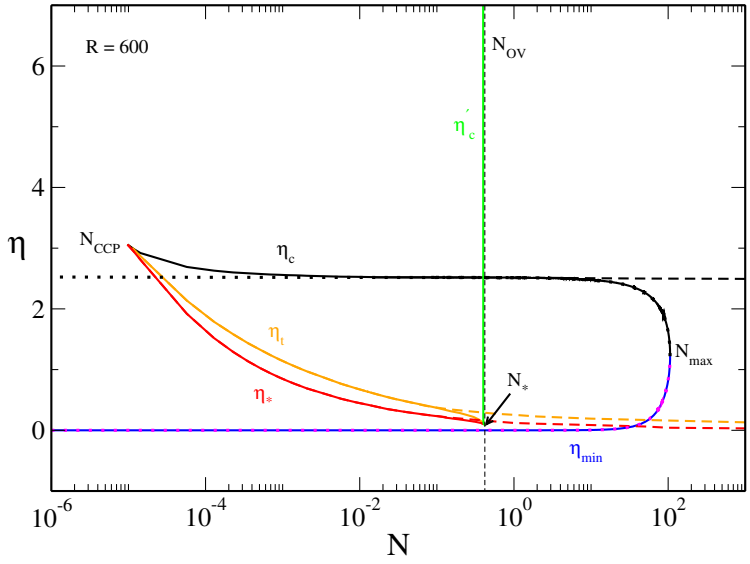

Figure 5.36: *Phase diagram in the canonical ensemble, for* $R = 600$. *The interpretation of the curve is the same as that given in Sec. 5.4.2. Large values of* R *do not alter the occurrence of the canonical phase transition neither the behaviour of the critical points. On the contrary, the figure shows that a sphere with radius* $R = 600$ *can be considered Newtonian more than relativistic.*

nevertheless, in the microcanonical ensemble, the influence of the gravity is less important than in the canonical ensemble. The Newtonian curve continues whereas the relativistic intersects the collapsing energy Λ_c'' that, we remind, has a "canonical" origin. At this point, the phase transition is suppressed and the system can only undergo the generalized Antonov collapse.

For what concerns the condensing energy Λ_*, we see that the relativistic solution differs from the Newtonian one for $N \sim N_{OV}$. The decrease of the curve becomes more and more important when we approach the critical point N_B', where the two energies Λ_* and Λ_c'' become equal. In this region of the phase diagram we have

$$\begin{aligned} \Lambda_c'' &\simeq 0.334 - 0.296\,(N_B' - N)\,, \\ \Lambda_* &\simeq 0.334 + 0.253\,(N_B' - N)\,. \end{aligned} \tag{5.35}$$

The scaling laws in the limits $N \to N_{CCP}$ and $N \to N_{MCP}$ are determined by the Newtonian theory. Moreover, in the limit $N \to N_{OV}$, the asymptotic beheaviour of the energies Λ_{max}, Λ_{max}' and Λ_c' is practically the same obtained for $R = 50$. For large values of N, as we know, the system has recovered the classical behaviour and the scalings found in Sec. 4.5.

Due to the dimensions of the box, the importance of the presence of GR is restricted only to a small region of the phase diagram. Analyzing the caloric curves, we have seen that GR has the effect

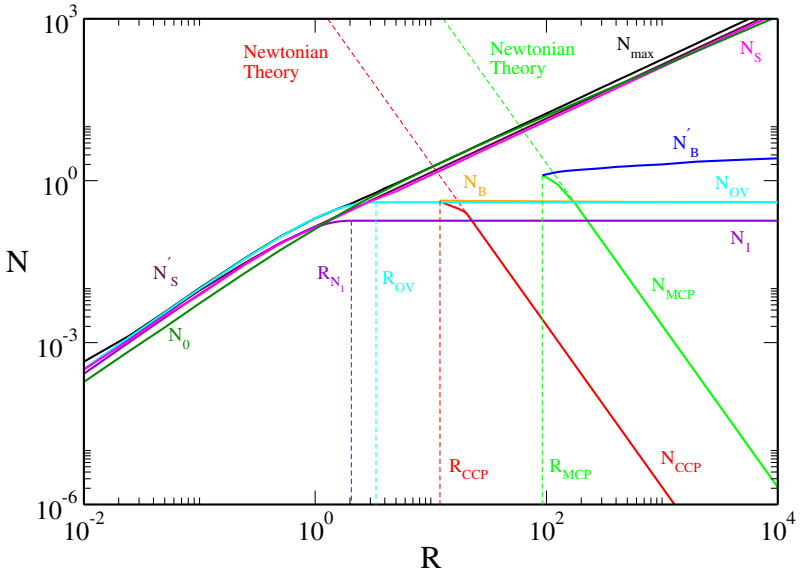

Figure 5.37: *"Phase diagram of the phase diagrams". The figure represents the critical points as a function of the box radius. R_1 is the value of R related to the point N_1 while R_{OV} is the radius at the OV limit. R_{CCP} and R_{MCP}, finally, are the values of R where, respectively, the canonical and the microcanonical phase transitions occur. The dashed lines represent the Newtonian prediction.*

of "anticipating" and suppressing the occurrence of the phase transition. If we increase the sphere radius, the entity of the general relativistic effects is reduced and a post-Newtonian treatment can be used. For the sake of completeness, we have plotted in Fig. 5.36 the phase diagram in the canonical ensemble. As the reader can see, it presents the same properties already analyzed in Sec. 5.4.2.

5.6. Critical Points Variation according to the Box Size

The analysis developed during the Chapter has shown the nature of the phase transition for fermionic system in a general relativistic framework. We have specifically studied the case of three radii, related to the suppression and the occurrence of the phase transitions. However, the study can be generalized to the case of box of different dimensions. For this reason in this section, by means of a further diagram, we will show how the global properties of the system vary according to the value of the cavity radius.

In Fig. 5.37 we have represented the critical points as a function of the cavity radius. As the reader can see, we can distinct three different regions: small values of N and R (bottom left), small values of N and large values of R (bottom right), large values of N and R (top right). We remark the presence of an empty region, corresponding to the case of large values of N and small values of R.

Let us start by considering the case $N >> 1$ and $R >> 1$. Here we are in the part of the diagram corresponding to isothermal gas spheres. As the reader can see, there are four lines, related to the points N_{max}, N_0, N_S and N'_S. The line related to N_{max} marks the diagram and define the empty region above mentioned. As we know, for $N > N_{max}$, no physical solutions can exist. The dependance on the radius confirms the scaling found in Sec. 4.2. The functions N_{max}, N_S and N'_S are linear functions of the cavity radius although, when $R \to R_{OV}$, a small deviation from the linearity arises (not visible in the figure).

This deviation from the linearity is due to the application of the Thomas-Fermi model to the degenerate configurations (see Appendix E), which provides some important modifications in the behaviour of these systems (as we see from the diagram, N_1 and N_{OV} are not anymore constant). The function N_0 does not follow the scaling valid for N_{max}, N_S and N'_S for the reason explained in Sec. 5.2.

Still remaining in the region of large radii, let us decrease a bit the value of N. In this region, we find the three functions N'_B, N_{OV} and N_1. Here we are in a part of the diagram indicating that the quantum nature of the gas begins to be more present. If we still decrease the value of N, we find the curves related to N_{MCP} (green line) and N_{CCP} (red line). This part of the diagram represents the Newtonian fermionic configurations. From the figure we see that $N_{MCP} \propto R^{-3}$ and $N_{CCP} \propto R^{-3}$ [remember Eq.(5.20)].

If we now follow the trend of the two curves, we restart increasing N and decreasing R. Following the green line, we arrive to the microcanonical radius $R_{MCP} \simeq 92$, a different value from that obtainable by the application of Eq.(5.23) ($R_{MCP} \simeq 126$). It is also possible to observe how the presence of GR modifies the Newtonian behaviour of the fermionic gas. Moving on the left of the curve, we arrive to the canonical critical radius $R_{CCP} \simeq 13$ (Newtonian evaluation $R_{CCP} \sim 17.8$). Here, because of the more reduced dimensions of the box, the general relativistic effects are dominant. We are thus in the regime of a full relativistic fermionic gas, which degree of degeneracy starts to increase more and more. We note that the curve N_B is very close to the OV limit (in the figures they look superimposed but they are not).

By still reducing the value of R, we arrive to the OV limit (R_{OV}) and here the fermionic system can be considered completely degenerate, behaving as a NS. However, the dimension of the box can be also smaller than R_{OV} and we observe that the functions N_{OV} and N_1 are not anymore constant, becoming functions of the radius. In this part of the diagram, the "Boltzmannian" functions N_{max}, N_0, N_S and N'_S link with the functions N_{OV} and N_1 and, in the limit $R \to 0$, they are infinitesimal.

In Fig. 5.38 we have represented several caloric curves at different radii for $\chi = \chi_{CCP}$. In this way we can better appreciate what Fig. 5.37 displays in the region near R_{CCP}. By firstly taking into

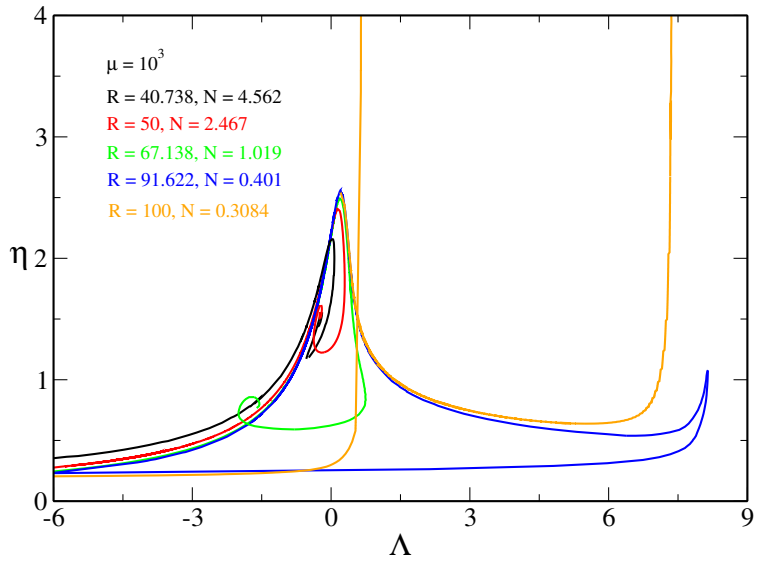

Figure 5.38: *Equilibrium phase diagram of self-gravitating fermions, for* $\mu_d = 10^3$ *and five different values of the radius, in the canonical ensemble. We aim at showing how, for increasing values of the radius, the results obtained in Newtonian gravity are recovered.*

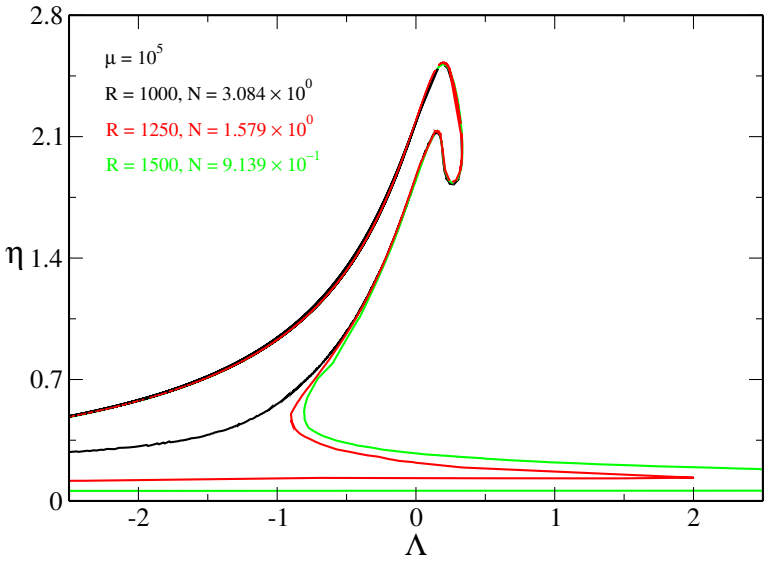

Figure 5.39: *Equilibrium phase diagram of self-gravitating fermions, for* $\mu_d = 10^5$ *and three different values of the radius, in the microcanonical ensemble. We aim at showing how, for increasing values of the radius, the results obtained in Newtonian gravity are recovered.*

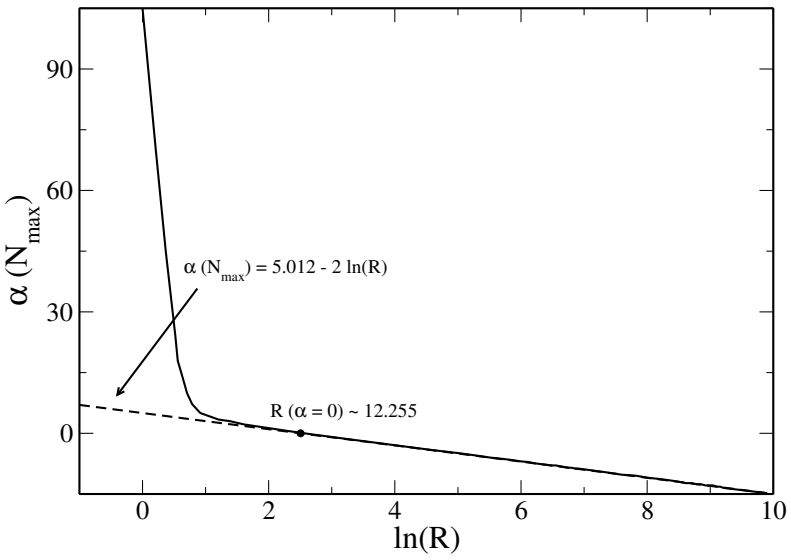

Figure 5.40: $\alpha(N_{max})$ *as a function of the radius. The dashed line represents the scaling law found in the context of Boltzmann statistics.*

consideration the case $R = 40.74$, $N = 4.562$ (black line in Fig. 5.38, the reader can recognize the typical behaviour of the classical gas, being[21] $N_B << N < N_{max}$.. By increasing the size of the box, (red line, corresponding to $R = 50$ and $N = 2.562$), we start to see the first modifications from the spiralic behaviour (from a thermodynamically point of view the system is classical).

By still increasing the value of R ($R = 67.14$ and $N = 1.019$, green line), we see that the first quantum effects begin to influence the thermodynamics of the system. We stress that, even in this case, $N > N_B$. However we are closer to the critical point compared to the previous situations. The blue line ($R = 92.622$, $N = 0.401$) exhibits the two isothermal collapses, at the points η_c and η_c'. Finally, the orange line ($R = 100$ and $N = 0.3084$) recovers the Newtonian curve. The difference is only due to the presence of the secondary branch in Λ'_{max} that, as we know, has relativistic origin.

The same kind of analysis can be made for what concerns the microcanonical ensemble. In Fig. 5.39 we have represented three caloric curves showing how the system recovers the Newtonian behaviour. We observe a gradual evolution, starting from the case $\Lambda_c'' < \Lambda_c$ (black line) and reaching the usual Newtonian behaviour (green line). Both Figs. 5.38 and 5.39 show that the Newtonian gravity and the nonquantum limit are recovered for $R \to +\infty$.

In Fig. 5.40, we have represented the deviations, from the scaling (4.43), for small radii. The full black represents the values of $\alpha(N_{max})$ evaluated numerically, while the dashed line the values of $\alpha(N_{max})$ obtained by the following equation

[21] For $R = 40.74$ we have $N_{max} = 7.187$.

$$\alpha = 5.012 - 2\log\tilde{R}\,. \tag{5.36}$$

where the numerical value corresponds to $\alpha(N_{max})$ esteemed in Chap. 4. From the figure, we see clearly that the scaling (5.36) works properly until $R \sim R_{CCP}$, where the degenerate nature of the fermionic gas begins to become more and more present. For small values of R, $\alpha(N_{max})$ has a divergent behaviour. This feature is explained because, for small radii, the function N_{OV} is not anymore constant, obeying to the constraint $N_{OV} \leq N_{max}$.

5.7. Summary of the Previous Results

In this Chapter we have analyzed the thermodynamics of a self-gravitating (and static) fermionic configuration in GR. Differently from the case of Boltzmann statistics, where there was one control parameter (i.e. $\mathcal{N}$), here the different features are determined by the combined values of N and R [remember Eq.(5.20)]. In particular, the occurrence of the gravitational phase transition is strictly related to the value of R.

The diagram represented in Fig. 5.37 summarizes all the different physical situations brought to the light by our study. The systems placed in the region where $R < R_{CCP}$ can be considered fully degenerate if $N \leq N_{OV}$: in this case, indeed, the degeneracy pressure can balance the gravity of the system, which is stable (both dynamically and thermodynamically). Things change when we choose a value of N larger than N_{OV}: in this situation the system undergoes a gravitational collapse (in both canonical and microcanonical ensemble) because the pressure is not enough to balance the gravity. From a thermodynamical point of view, these systems are equivalent to those analyzed in Chap. 4. This fact displays well the influence of the dimensions of the box: apparently, if $R < R_{CCP}$, it seems that the fermionic gas suddenly leaves the full degeneracy to directly "jump" on the non-quantum behaviour.

Things change when $R > R_{CCP}$, because the fermionic system exhibits the canonical phase transition for $N < N_{OV}$. In this case, we recover the results of the Newtonian theory for $N < N_{OV}$: the general relativistic effects play their role when we consider the case $N_{OV} < N < N_B$. As we have seen, when N exceeds a bit the OV limit, the fermionic system exhibits a second isothermal collapse, because of the existence of a second critical temperature.

However, this coexistence is kept until $N < N_B$ because when $N = N_B$ the fermionic system has recovered the typical behaviour of the classical gas. During this gradual evolution towards the non-quantum behaviour, for a specific value of N, GR suppresses the occurrence of the phase transition

(at this point the free energy of the gaseous and condensed phases are not anymore equivalent).
If we now increase the size of the system and we have $R > R_{MCP}$, we see that a phase transition occurs even in the microcanonical ensemble. Analogous to the canonical ensemble, GR introduces a second gravitational collapse (there exists indeed a second critical energy). Increasing the value of N, the fermionic gas recovers the behaviour of non-quantum systems by showing, even in the microcanonical ensemble, the suppression of the phase transition for a specific value of N (in this case the entropies of the gas and the condensed are not anymore equivalent). In the limit $R \to +\infty$, the effects of GR are more and more reduced and we recover the Newtonian theory.

6

Conclusions and Perspectives

In this work we have described the nature of the phase transitions by considering self-gravitating systems of fermions in a general relativistic framework. Two physical parameters characterize the models studied, that is the level of degeneracy and the intensity of the gravitational fields (the "degree of relativity"). In particular, the General Relativity provides new features that induce some modifications in the nature of the series of equilibria such that the occurrence of the phase transitions can be dissimilar from the phase transitions obtained in the Newtonian framework (see Secs. 5.4 - 5.5).

In Chap. 3 we have considered the case of degenerate fermionic configurations, by extending the validity of Chandrasekhar & Tooper's model. Similar to Narain *et al.* [144], we have provided a unified description of White Dwarfs and Neutron Stars, by means of the parameter q, defined by the ratio m_1/m_2 [where m_1 and m_2 are the particle masses of the two gases at the equilibrium, see Eq.(3.26)]. However, the model is too simplistic to properly describe White Dwarfs and Neutron Stars because it does not take into account, for example, electromagnetic interactions. In the case of Neutron Stars, moreover, the equation of state is more complicated than that used in the present work, because effects due to strong interactions, for example, cannot be neglected.

Although incomplete, the model can provide an estimate of the point of instability of White Dwarfs that can be observationally tested if we consider White Dwarfs in binary systems and, in particular, binary systems where the mass transfer dominates the evolution. In this case, indeed, the inflowing gas from the donor star, that has filled up its Roche lobe, to the White Dwarf (i.e. the accretor) forms an accretion disk that can alter the achievement of the point of instability. Naturally the dynamics of this process is more complex because other physical phenomena are present.

Anyway, from a thermodynamical point of view, the degenerate fermionic configurations offer a sketch

regarding the nature of the condensed phase emerging in the series of equilibria analyzed in Chap. 5. As we have seen, indeed, the structure of the condensed phase is very similar to that of the systems obtained for high values of q. Moreover, we have found that (dynamically) unstable configurations cannot be thermodynamically stable (remember the secondary branch of the series of equilibria delimited by the energy Λ'_{max}).

In Chap. 4 we have considered the high temperature limit of Fermi-Dirac statistics, leading us to study the case of the non-quantum self-gravitating gas in General Relativity. We have identified two kinds of instability, at low and high energy. The first type corresponds to the general relativistic equivalent of Antonov instabilities. From a thermodynamical point of view, indeed, when the system reaches a temperature below the (generalized) Emden temperature or an energy above the (generalized) Antonov limit, it undergoes a collapse. The General Relativity does not change the nature of these instabilities but their occurrence because general relativistic isothermal spheres are more unstable than Newtonian isothermal spheres and the collapse occurs sooner.

The second kind of instabilities is produced by the "radiation" (i.e. ultrarelativistic particles) and they give rise to a second spiral in the series of equilibria. Analogous to the low energy instabilities, high energy instabilities are characterized by the presence of a critical temperature and a critical energy, leading the system to collapse if the values of the temperature and energy of the system exceed the critical ones. We stress that the high energy instabilities have a relativistic origin.

Analyzing the behaviour of the $N = N(\Phi_0)$ (N and Φ_0 are the particle number and the central value of the gravitational potential, respectively) diagrams we have discovered the existence of a limiting configuration, namely N_{max}. From a physical point of view, N_{max} represents the maximum number of particles that can fill up the sphere without collapsing. When $N = N_{max}$ the series of equilibria is reduced to only one point and does not display any collapse.

By virtue of the symmetries of the problem, we have shown the existence of a scaling which has the effect to reduce the workspace to the sphere of unitary radius. The existence of this scaling is also related to the nature of the gas because, as we have seen in Sec. 5.1, the fermionic configurations do not preserve this scaling (see below). We stress that this scaling originates from Schwarzschild's metric and its applicability is restricted to spherical systems. Other metrics could not preserve this scaling *a priori*.

In Chap. 5, finally, we have considered the semidegenerate fermionic configurations. We have analyzed three different cases, according to the value of the cavity radius R. The first case, $R = 10 \simeq 2.98\ R_{OV}$ (where R_{OV} is the radius at the Oppenheimer-Volkoff limit, see Appendix D), refers to the suppression of the phase transition, in both canonical and microcanonical ensembles. When $R < R_{CCP} \simeq 3.87$

R_{OV} (R_{CCP} corresponds to the canonical critical radius, see Sec. 5.6) the fermionic system does not exhibit any phase transition.

Conversely, for $R > R_{CCP}$ (in this work we have considered the case $R = 50 \simeq 14.9\ R_{OV}$, see Sec. 5.4), the system can *at least* exhibit the phase transition in the canonical ensemble. For $N \leq N_{OV}$ (N_{OV} is the value of N at the Oppenheimer-Volkoff limit) the nature of the phase transition is equivalent to that studied in Newtonian gravity [23, 47]. The differences between the Newtonian and the general relativistic treatise are evident when $N > N_{OV}$, because the fermionic system exhibits a second collapse, determined by the critical point η_c'.

Furthermore, the phase transition is suppressed when the reversal transition temperature η_t becomes equal to the reversal critical temperature η_c'. This happens because, differently from the Newtonian gravity, the General Relativity offers the disparition of the Maxwell plateau. More specifically, there exists a value of N for which the free energy associated with the gaseous phase is not anymore equal to the free energy associated with the condensed phase.

When $R > R_{MCP} \simeq 27.4\ R_{OV}$ the fermionic system exhibits the microcanonical phase transition. For sufficiently large values of R, the phase transition occurs also for $N < N_{OV}$ (the case considered, $R = 600 \simeq 179\ R_{OV}$, displays this occurrence). The disparition of the Maxwell plateau in the canonical ensemble causes the disparition of the Maxwell plateau also in the microcanonical ensemble (see Sec. 5.5). The presence of two critical values of the cavity radius related to the occurrence of the phase transition shows that the scaling GNm/Rc^2 found in the context of Boltzmann statistics cannot be applied to fermions. This is a direct consequence of the presence of the degeneracy.

The results obtained in this work call for further investigations. The fermionic system considered in this work is static: including the effect of the rotations (by extending to General Relativity the work of Chavanis & Rieutord [60]) may exhibit new features or alter the values of the critical parameters for the occurrence of the phase transition. More generally, the presence of anisotropies breaks some symmetries that can lead the system to reach different equilibrium configurations. In addition, deviations from the spherical symmetry, by means of different metric, could have consequences on the global behaviour of the fermionic systems.

A second kind of study can be developed by using the truncated models (see Sec. 1.3), i.e. the models that introduce a cut-off energy in the distribution function. In this last case, indeed, we do not need to confine the system in an artificial container. The comparison between the results of this thesis and those obtainable by means of this second method can give us not only a better comprehension of our model but also a check about its validity and applicability.

To check the robustness of the model, a comparison of our results with those obtainable from ob-

servational analysis and N-body simulations is fundamental. Thanks to the methods and techniques developed by the Numerical Relativity [88], it is now possible to perform N-body simulations in General Relativity. This could provide an "experimental" confirmation of the results obtained in this work. At the same time, the N-body simulations can stress the limits of the theory.

From an observational point of view, the model here advanced can refer to objects supposed to be formed in the early Universe. As a matter of fact, since the matter is very hot, we expect that a gravitational collapse might occur and form structures that can lead to the formation of galaxies. The presence of the second collapse in the canonical ensemble at the point η_c' could also explain, within a statistical-thermodynamical approach, the formation of Black Holes.

The formation of structure at cosmological scales [64] could be also explained in terms of the phase transitions obtained in the canonical ensembles for the fermionic gas, analogous to the fermions balls scenario [188, 189, 23]. A similar scenario might explain the formation of Dark Matter structures in the early Universe too. Beyond the fermionic paradigm, systems formed by other kinds of particles can be considered. For example, bosons systems far from the Bose-Einstein condensation could represent a good candidate for further investigations on the thermodynamics of self-gravitating systems in General Relativity.

7

Résumé

7.1. Introduction

La mécanique statistique des systèmes auto-gravitants présente des propriétés très particulières, comme l'existence de chaleurs spécifiques négatives dans l'ensemble micro-canonique, qui donne lieu au phénomène de la non-équivalence des ensembles[1]. Ces propriétés (au même titre qu'autres) ne sont pas une prérogative exclusive des systèmes gravitationnels mais, plutôt, elles appartiennent au cadre général des systèmes à longue portée (Campa *et al.*, [35]). Conceptuellement, à cause de phénomènes comme l'évaporation (Spitzer [176]), les systèmes auto-gravitants ne se trouvent pas en équilibre statistique, d'où le fait que leur description est un problème hors-équilibre. Cependant, comme l'évaporation est un processus lent, on peut modéliser ces objets à travers une succession d'états de quasi-équilibre.
Afin d'éviter l'évaporation ou, encore, le problème de la masse infinie, deux schématisations sont possibles. Une première possibilité consiste dans le confinement du gaz dans une boîte aux dimensions fixées. Bien que mathématiquement utile pour, surtout, récupérer la limite thermodynamique $N \to \infty$ (où N est le nombre des particules qui forment le système), il n'existe aucune motivation physique qui en justifie l'application[2].
En revanche, un modèle plus proche de la réalité peut être obtenu en considérant des modifications de la fonction de distribution décrivant la nature des particules qui peuplent le système (King [119],

[1] En mécanique statistique, un ensemble est défini comme une collection de plusieurs copies (virtuelles) d'un même système physique. Cette collection donne une mesure de la totalité des états accessibles par le système sous étude, en nous permettant de discerner ses propriétés macroscopiques d'un point de vue microscopique (cf. Huang [105]).

[2] On peut arriver à obtenir un système confiné par des parois externes en invoquant une relaxation violente (Lynden-Bell [132]). Un amas globulaire dans une galaxie peut être vu de la sorte.

Ruffini & Stella [165]). Dans ce cadre on défini, dans l'espace des phases des positions et vitesses des particules, une énergie maximale ϵ_c, liée à la vitesse d'échappée v_e du système. Une particule ayant une énergie plus grande que ϵ_c (et, par conséquent, $v > v_e$) n'est pas considérée faisant partie du système (la particule a effectivement abandonné le système) et donc ignorée. Par contre, une particule ayant une énergie inférieure à ϵ_c (et donc $v \leq v_e$) restera confinée à l'intérieur du système.

Ces considérations ont un caractère général, c'est-à-dire elles sont indépendantes par la nature des particules constituant l'objet. Historiquement, les systèmes auto-gravitants étaient modélisés comme des agglomérats de particules classiques, c'est-à-dire qu'ils étaient décrits comme un gaz parfait dans lequel les particules n'interagissent entre elles que par l'interaction gravitationnelle. En utilisant cette approche, Antonov [4], Lynden-Bell [132] et Lynden-Bell & Wood [133] furent les premiers à découvrir l'existence de ce que l'on appelle *effondrement gravitationnel*. Ce phénomène, dont l'origine réside dans les instabilités thermodynamiques micro-canoniques et canoniques[3], amène le système vers un changement de son état d'équilibre (cf. Sec. 7.4).

Si l'on considère les effets quantiques (autrement dit, si l'on change la nature des particules en considérant, par exemple, des fermions[4]), on observe la manifestation de ce que l'on appelle *transition de phase gravitationnelle*, qui a lieu dans l'ensemble canonique ainsi que dans l'ensemble micro-canonique (Chavanis [47]). Comme on verra dans la suite, les courbes caloriques[5] diffèrent beaucoup dans les deux cas: en effet, dans le cas des particules classiques la forme de la courbe rappelle une spirale (cf. Sec. 7.4) alors que les fermions montrent des solutions à "N" ou "Z", respectivement, dans les ensembles canoniques et micro-canoniques (cf. Sec. 7.5).

Les résultats mentionnés jusqu'à ce point ont été obtenus dans le cadre de la gravité newtonienne. Cependant, l'étude de certains systèmes astrophysiques exige une description dans le cadre de la Relativité Générale. Dans le cas non-quantique, il a été montré l'existence d'une double instabilité, aux basses énergies (correspondant à la généralisation de l'instabilité d'Antonov) et aux hautes énergies

[3]L'ensemble micro-canonique décrit un système isolé thermodynamiquement où le volume total V, l'énergie E et le nombre des particules N sont des paramètres fixés. L'ensemble canonique décrit un système en contact avec un autre système (réservoir), avec lequel il ne peut échanger que de l'énergie (volume et nombre des particules restent fixes). La température (imposée par le réservoir) est une contrainte extérieure (comme N et V) et elle est fixée.

[4]Les fermions sont les particules historiquement introduites par Enrico Fermi (1926) afin d'expliquer les propriétés électroniques des métaux. Elles diffèrent des particules classiques surtout aux basses températures, lorsque le principe d'exclusion de Pauli se manifeste (cf. Huang [105]).

[5]La courbe calorique (ou série d'équilibre) est le diagramme dans lequel on représente la température (souvent normalisée par d'autres variables) en fonction de l'énergie du système (souvent normalisée aussi). Cela permet d'étudier la stabilité thermodynamique, en montrant la présence de collapses (effondrements) ou de transitions de phase (cf. Secs. 7.4 et 7.5).

(cf. Chavanis [46, 55], Roupas [159]). Pour ce qui concerne les systèmes fermioniques, par contre, il a été montré l'existence de la transition de phase seulement au sein de l'ensemble canonique (Bilić & Viollier, [25]).

Le but de ce travail est de compléter les études déjà présentes dans la littérature ainsi que de fournir une description détaillée des transitions de phases dans les systèmes auto-gravitants relativistes. En dépit de son manque de rigueur, dans ce travail, on se servira du modèle de Thomas-Fermi (Bilić & Viollier, [25]), c'est-à-dire que l'on confinera le gaz au moyen de parois externes.

7.2. Equations Fondamentales

On considère une boîte sphérique ayant dimension R, remplie par N fermions ayant la même masse m. Pour cette configuration, l'équilibre gravitationnel est décrit à l'aide du système d'équations TOV (Tolman-Oppenheimer-Volkoff, Tolman [183]), que l'on écrit comme suit (Bilić & Viollier [25]):

$$\begin{aligned} \frac{d\xi}{dr} &= \frac{G}{c^4}\frac{\xi(M_r c^2 + 4\pi P r^3)}{r^2}\Big(1 - \frac{2GM_r}{rc^2}\Big)^{-1} \\ \frac{dM_r}{dr} &= \frac{4\pi\epsilon r^2}{c^2} \end{aligned} \tag{7.1}$$

où ξ est liée à la métrique (dans le cas des configurations sphériques et statiques, elle correspond à la métrique de Schwarzschild) et M_r représente la masse-énergie du système dans une sphère concentrique à la boîte et à distance $r < R$ du centre. P et ϵ indiquent, respectivement, la pression et la densité de masse-énergie; de même G et c sont, respectivement, la constante de gravitation et la vitesse de la lumière. En conséquence de la nature des particules, on écrit la fonction de distribution comme suit:

$$f = \frac{g}{h^3}\frac{1}{e^{(E-\mu_r)/k_B T_r} + 1} \tag{7.2}$$

où E indique l'énergie cinétique de particule individuelle, μ_r et T_r représentent le potentiel chimique et la température[6]. De plus, g, h et k_B sont, respectivement, la dégénérescence quantique (liée à la multiplicité du spin) et les constantes de Planck et Boltzmann. Grâce à la fonction de distribution

[6] À l'intérieur du système, μ_r et T_r sont fonctions locales, qui dépendent de la distance du centre. Cette dépendance est manifestée par les conditions de Tolman [182]:

$$\mu_r = \frac{\mu}{\xi}, \qquad T_r = \frac{T}{\xi} \tag{7.3}$$

ξ est la même quantité présente dans le système TOV (7.1) alors que μ et T représentent le potentiel chimique et la température mesurés par un observateur à distance infinie.

(7.2), on peut définir la densité de particules n (correspondant à la densité de matière, en étant $\rho = mn$), la densité de masse-énergie ϵ et la pression P:

$$n = \int f\, d^3\vec{q} = \frac{g}{h^3} \int \frac{d^3\vec{q}}{e^{(E-\mu_r)/k_B T_r} + 1} \tag{7.4}$$

$$\epsilon = \int f\, E\, d^3\vec{q} = \frac{g}{h^3} \int \frac{E d^3\vec{q}}{e^{(E-\mu_r)/k_B T_r} + 1} \tag{7.5}$$

$$P = \frac{1}{3} \int f\, \vec{q}\, \frac{\partial E}{\partial \vec{q}}\, d^3\vec{q} = \frac{g k_B T_r}{h^3} \int \ln\Big[1 + e^{(\mu_r - E)/k_B T_r}\Big] d^3\vec{q} \tag{7.6}$$

En écrivant l'énergie cinétique comme (q est la quantité de mouvement de la particule)

$$E = \sqrt{m^2c^4 + q^2c^2} = mc^2\sqrt{1+y^2} \qquad \text{où} \qquad y = \frac{q}{mc} \tag{7.7}$$

et en définissant les variables suivantes

$$\alpha = \frac{\mu}{k_B T}, \qquad \xi = \frac{|\mu|}{mc^2} \frac{1}{\sqrt{\Phi + 1}}, \qquad z = e^{-\alpha} \tag{7.8}$$

on peut réécrire les équations (7.4)-(7.6) comme suit:

$$n = \frac{4\pi g m^3 c^3}{h^3} \int_0^\infty y^2 \Big(z e^{|\alpha| \sqrt{\frac{y^2+1}{\Phi+1}}} + 1 \Big)^{-1} dy \tag{7.9}$$

$$\epsilon = \frac{4\pi g m^4 c^5}{h^3} \int_0^\infty y^2 \sqrt{y^2+1} \Big(z e^{|\alpha| \sqrt{\frac{y^2+1}{\Phi+1}}} + 1 \Big)^{-1} dy \tag{7.10}$$

$$P = \frac{4\pi g m^4 c^5}{3h^3} \int_0^\infty \frac{y^4}{\sqrt{y^2+1}} \Big(z e^{|\alpha| \sqrt{\frac{y^2+1}{\Phi+1}}} + 1 \Big)^{-1} dy \tag{7.11}$$

Dans les équations précédentes, on est passé aux coordonnées polaires dans l'espace des impulsions, c'est-à-dire $d^3\vec{q} = 4\pi q^2 dq = 4\pi m^3 c^3 y^2 dy$. D'autre part, si l'on substitue la deuxième égalité (7.8) dans la première équation du système TOV (7.1), on obtient:

$$\begin{aligned} \frac{d\Phi}{dr} &= -\frac{2G}{c^4} \frac{(\Phi+1)(M_r c^2 + 4\pi P r^3)}{r^2} \Big(1 - \frac{2GM_r}{rc^2}\Big)^{-1} \\ \frac{dM_r}{dr} &= \frac{4\pi\epsilon r^2}{c^2} \end{aligned} \tag{7.12}$$

avec les conditions initiales $\Phi(0) = \Phi_0 > -1$ et $M_r(0) = 0$. Le système d'équations (7.12) dépend de R, α et Φ_0 et l'intégration est réalisée à la variation des valeurs de ces paramètres libres. Cependant, l'étude thermodynamique est effectuée en fixant la valeur du nombre des particules. Cette quantité est calculée à l'aide de l'expression suivante:

$$N = \int_0^R 4\pi n r^2 \Big(1 - \frac{2GM_r}{rc^2}\Big)^{-1/2} dr \tag{7.13}$$

qui dépend, par analogie avec le système TOV, de R, α et Φ_0. Comme on l'a dit, l'étude thermodynamique sera faite à nombre de particules fixé, c'est-à-dire $N = N_{spec}$. Cette condition (conservation du nombre baryonique) met des contraintes sur les valeurs de Φ_0, parce que seulement les valeurs de Φ_0 telles que $N(\Phi_0) = N_{spec}$ représenteront des solutions physiques.

La vérification de l'existence des transitions de phase est faite à l'aide de deux fonctions thermodynamiques différentes, selon que l'on se trouve dans un ensemble ou l'autre. Pour le cas micro-canonique, comme l'énergie est fixée, l'étude des transitions de phase est faite en maximisant l'entropie S, alors que dans le cas canonique on minimise l'énergie libre d'Helmholtz F (simplement énergie libre dans la suite). Les expressions de ces deux fonctions sont:

$$S = \frac{k_B|\alpha|}{mc^2}\left[\int_0^R \frac{4\pi(P+\epsilon)r^2dr}{\sqrt{\Phi+1}\sqrt{1-\frac{2GM_r}{rc^2}}} - \mathrm{sgn}(\alpha)Nmc^2\right] \tag{7.14}$$

$$F = Mc^2 + \mu N - \frac{|\mu|}{mc^2}\int_0^R \frac{4\pi(P+\epsilon)r^2dr}{\sqrt{\Phi+1}\sqrt{1-\frac{2GM_r}{rc^2}}} \tag{7.15}$$

Comme on l'a mentionnée précédemment, l'étude thermodynamique sera développée au moyen des séries d'équilibre. En suivant les notations présentes en littérature, on définit l'énergie et la température normalisées comme suit (Chavanis [47]):

$$\Lambda = -\frac{E_b R}{GN^2m^2}\,, \qquad \eta = \frac{GNm^2}{k_B T R} \tag{7.16}$$

Dans l'expression précédente, $E_b = (M - Nm)c^2$ est l'énergie de liaison, définie comme différence entre la masse-énergie et la masse au repos (totales) du système.

Avant de procéder avec l'analyse des résultats, on veut remarquer un point important, par rapport à l'intégration numérique du système TOV (7.12). Afin de travailler avec des nombres plus maniables (et éviter des problèmes d'arrondissement, par exemple), on réécrit les équations en forme *adimensionnelle*. De cette façon, on s'affranchit des dimensions physiques et on peut regarder le problème d'un point de vue mathématique, dans sa plus grande généralité.

On définira des quantités caractéristiques (indiquées par un souscrit $*$) qui gardent les dimensions physiques. De cette façon, on pourra écrire une variable générique comme produit entre sa valeur numérique (indiquée avec une $\sim$ en exposant) et la quantité caractéristique. Comme l'étude thermodynamique est faite selon certaines valeurs précises du rayon R et du nombre de particules N, on réécrira ces deux variables de la façon que l'on vient d'expliquer. En définissant, respectivement, r_* et N_* comme la longueur et le nombre des particules caractéristiques, $\tilde{R}$ et $\tilde{N}$ comme la longueur et le nombre des particules adimensionnels, on obtient:

$$R = \tilde{R}\, r_* \,, \qquad N = \tilde{N}\, N_* \tag{7.17}$$

r_* et N_* sont définis comme suit:

$$r_* = \sqrt{\frac{2}{g}} \frac{hM_{Pl}}{2\pi m^2 c} \,, \qquad N_* = \sqrt{\frac{2}{g}} \frac{M_{Pl}^3}{m^3} \tag{7.18}$$

M_{Pl} est la masse de Planck, qui vaut $M_{Pl} = 2.176 \times 10^{-5}$ g. Pour donner une idée de la portée de l'expression précédente, on suppose que la sphère est peuplée par des neutrons ($m_n = 1.674 \times 10^{-24}$ g et $g = 2$): par l'équation (7.18) on obtient $N_* = 2.196 \times 10^{57}$. Ce nombre indique la quantité de particules à l'intérieur de la sphère de rayon r_*. Si, en particulier, on veut étudier la thermodynamique pour un N et un R fixés, on doit multiplier ce nombre par le résultat numérique afin d'obtenir le "vrai" nombre de particules. Par exemple, si $\tilde{N} = 0.29$, on aura $N = 0.29\ N_* = 6.369 \times 10^{56}$ particules.

7.3. Limite Dégénérée $T \to 0$

Quand la température d'un système fermionique baisse d'une manière considérable, le principe d'exclusion de Pauli se manifeste et les particules ne peuvent plus occuper les mêmes niveaux d'énergie (cf. Huang [105]). Dans cette situation le gaz fermionique est appelé dégénéré, parce que les particules ont tendance à remplir tous les niveaux énergétiques possibles, jusqu'à l'énergie limite ϵ_F, dénommée énergie de Fermi. Dans ce cas, les expressions de quantités thermodynamiques (7.9)-(7.11) se simplifient et les intégrales peuvent être calculées analytiquement:

$$n = \frac{4\pi g m^3 c^3}{h^3} \int_0^{\sqrt{\Phi}} y^2 dy = \frac{4\pi g m^3 c^3}{3h^3} \Phi^{3/2} \tag{7.19}$$

$$\epsilon = \frac{4\pi g m^4 c^5}{h^3} \int_0^{\sqrt{\Phi}} y^2 \sqrt{y^2+1} dy = \frac{\pi g m^4 c^5}{2h^3} \Big[(2\Phi+1)\sqrt{\Phi(\Phi+1)} - \log(\sqrt{\Phi} + \sqrt{\Phi+1}) \Big] \tag{7.20}$$

$$P = \frac{4\pi g m^4 c^5}{3h^3} \int_0^{\sqrt{\Phi}} \frac{y^4 dy}{\sqrt{y^2+1}} = \frac{\pi g m^4 c^5}{6h^3} \Big[(2\Phi-3)\sqrt{\Phi(\Phi+1)} + 3\log(\sqrt{\Phi} + \sqrt{\Phi+1}) \Big] \tag{7.21}$$

Dans les expressions précédentes $\Phi = y_F^2 = (p_F/mc)^2$ (p_F représente la quantité de mouvement associée à l'énergie de Fermi ϵ_F). En substituant ces nouvelles expressions dans le système (7.12), on peut obtenir la relation masse-rayon qui est représentée dans la Figure 7.1. On observe la présence d'une configuration limite, que l'on appelle limite d'Oppenheimer-Volkoff (cf. Ref.[150]).

Les états d'équilibre qui se trouvent au-delà de la limite d'Oppenheimer-Volkoff (à gauche du maximum dans la figure) représentent des états dynamiquement instables, qui ne peuvent pas donner lieu à un

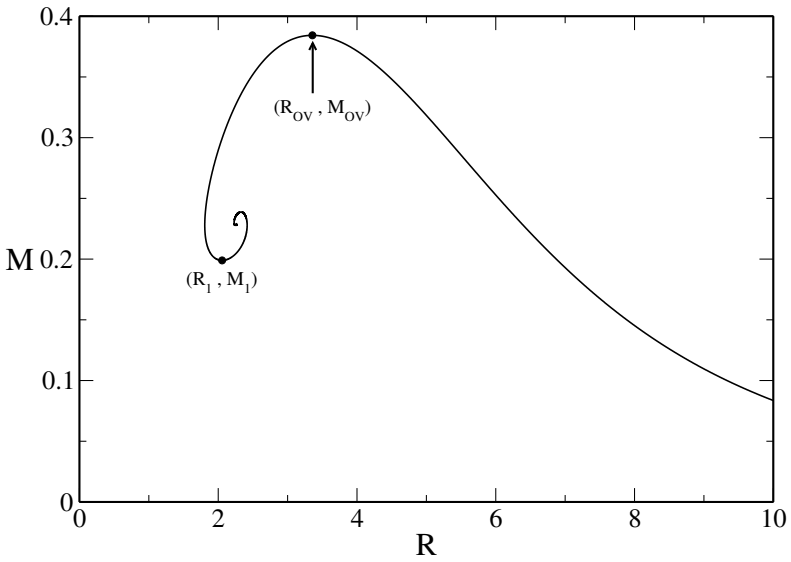

Figure 7.1: *Relation masse-rayon pour des configurations fermioniques dégénérées en Relativité Générale (les quantités sont adimensionnelles). La limite d'Oppenheimer-Volkoff est aussi indiquée. Numériquement on obtient* $R_{OV} = 9.162$ *km et* $M_{OV} = 0.710 M_\odot$ *(*$M_\odot = 1.989 \times 10^{33}$ *g est la masse solaire). Le point identifié par le couple de coordonnées* (R_1, M_1) *donne lieu, dans la série d'équilibre pour* $T \neq 0$ *(cf. Figure 7.6), à une branche secondaire. Numériquement on obtient* $R_1 = 5.611$ *km et* $M_1 = 0.367 M_\odot$.

système physique réel. Cependant, la relation masse-rayon nous permet de déterminer les valeurs minimales des énergies accessibles par le système fermionique dans sa phase condensée (cf. Sec. 7.5).

7.4. Limite Non-Quantique $T \to +\infty$

On commence l'analyse thermodynamique en débutant du cas classique, obtenu dans la limite de haute température ($T \gg 1$). Comme on le sait, la fonction de distribution (7.2) se transforme dans la fonction de distribution de Boltzmann:

$$f = \frac{g}{h^3} e^{(\mu_r - E)/k_B T_r} \tag{7.22}$$

Grâce à l'équation (7.22), les expressions des quantités thermodynamiques (7.9)-(7.11) se simplifient (on peut en effet les exprimer en termes des fonctions de Bessel[7], cf. Abramowitz & Stegun [1]):

[7]Les fonctions de Bessel sont définies de la façon suivante:

$$K_n(b) = \int_0^\infty e^{-b\cosh\theta} \cosh(n\theta) d\theta\,, \qquad \text{avec} \quad n \in \mathbb{N}$$

$$n = \frac{4\pi g m^3 c^3}{h^3} e^{\alpha} \int_0^{\infty} e^{-b\sqrt{y^2+1}} y^2 dy = \frac{4\pi g m^3 c^3}{h^3} \frac{e^{\alpha} K_2(b)}{b} \tag{7.23}$$

$$\epsilon = \frac{4\pi g m^4 c^5}{h^3} e^{\alpha} \int_0^{\infty} e^{-b\sqrt{y^2+1}} y^2 \sqrt{y^2+1} dy = \frac{\pi g m^4 c^5}{h^3} \frac{e^{\alpha}[3K_3(b) + K_1(b)]}{b} \tag{7.24}$$

$$P = \frac{4\pi g m^4 c^5}{3h^3} e^{\alpha} \int_0^{\infty} e^{-b\sqrt{y^2+1}} \frac{y^4 dy}{\sqrt{y^2+1}} = \frac{\pi g m^4 c^5}{h^3} \frac{e^{\alpha}[K_3(b) - K_1(b)]}{b} \tag{7.25}$$

Ces nouvelles quantités thermodynamiques dépendent d'un nouveau paramètre, défini comme suit:

$$b = \frac{|\alpha|}{\sqrt{\Phi + 1}} = \frac{mc^2}{k_B T_r} \tag{7.26}$$

et qui représente l'inverse de la température locale normalisée (les équations TOV peuvent être réécrites et résolues en termes de b). On peut montrer l'existence d'une loi d'échelle qui nous permet de nous affranchir des dimensions de la boîte, en restreignant l'espace de travail à $R = 1\ r_*$. Cette loi d'échelle, qui simplifie notablement le calcul numérique, nous permet de voir comme le gaz classique est indépendant de la taille du système. Pour attendre ce but, on définit la compacité[8] du système:

$$\mathcal{N} = \frac{GNm}{Rc^2} \tag{7.27}$$

L'étude thermodynamique sera faite, donc, pour des valeurs fixées de $\mathcal{N}$ au lieu de N. Il faut souligner que cette simplification est possible seulement dans ce cas et cesse d'être valable pour les fermions. L'existence de cette loi d'échelle constitue une première différence avec le modèle des sphères isothermes relativistes proposé par Roupas [159]. En effet, dans son travail, il trouve des rayons critiques pour instaurer des instabilités thermodynamiques (canoniques et micro-canoniques). Dans notre modèle ces rayons critiques n'existent pas.

Comme précédemment mentionné (cf. Sec. 7.2), dans le cadre du modèle de Thomas-Fermi, l'étude thermodynamique est effectuée à travers la contrainte (dans les nouvelles variables) $\mathcal{N}(\Phi_0) = \mathcal{N}_{spec}$. Dans la Figure 7.2 nous avons représenté cette contrainte d'un point de vue "opératif". Une fois intégré le système (7.12) pour un α fixé (et pour plusieurs valeurs de Φ_0), on fixe une ligne de niveau (dans la figure on montre le cas $\mathcal{N} = 0.1$). Il y aura certains points d'intersection entre la courbe $\mathcal{N}(\Phi_0)$ et la ligne de niveau et ces points représentent ceux qui obéissent à la contrainte $\mathcal{N}(\Phi_0) = 0.1$ (pour la valeur d'α illustrée dans la figure).

Si l'on change de ligne de niveau (pour le même α), on obtiendra des nouveaux points d'intersection, qui représenteront les solutions physiques pour la série d'équilibre associée à la ligne de niveau $\mathcal{N} = \mathcal{N}_{spec}$. Si l'on itère cette procédure en changeant la valeur d'α, pour un $\mathcal{N}$ fixé, on obtient la série d'équilibre

[8] Dans la suite, on se référera à la compacité comme nombre de particules.

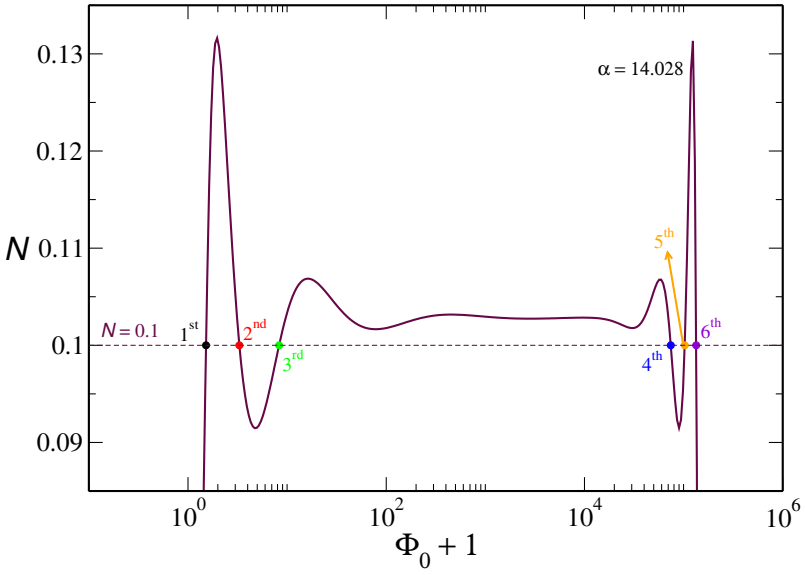

Figure 7.2: *Construction graphique pour obtenir la série d'équilibre. Pour une valeur de $\mathcal{N}$ fixée, on identifie les points d'intersection (six dans le cas ici considéré), entre la courbe $\mathcal{N}(\Phi_0)$ et la ligne de niveau, comme les points obéissent à la contrainte $\mathcal{N}(\Phi_0) = 0.1$.*

complète, paramétrée par le couple de valeurs (α, Φ_0). Dans la Figure 7.3 nous avons représenté deux exemples de courbes caloriques, pour deux valeurs différentes de $\mathcal{N}$.

Le comportement des courbes présente des analogies et des différences avec le cas newtonien. Les deux graphiques montrent la présence d'une double spirale, dont l'origine est différente. La spirale de droite représente la généralisation au cas relativiste de la célèbre spirale obtenue par Lynden-Bell & Wood [133]: ses propriétés thermodynamiques sont identiques à celles de la spirale newtonienne. On voit la présence de deux points critiques, un en énergie (Λ_c) et un en température (η_c).

Si l'on fixe une valeur de la température $\eta = \eta_*$, on identifie deux points, un à gauche et l'autre à droite du point critique η_c. Le point à gauche est placé sur la phase gazeuse de la série d'équilibre et représente une solution physique stable, correspondant à un état d'équilibre "réel". Le point à droite, par contre, correspond à une solution physique instable et ne représente aucun état d'équilibre "réel". Pour cette raison, η_c représente la température critique au-delà de laquelle le système subit un effondrement (selon le sens de la flèche).

Dans l'ensemble micro-canonique, le même phénomène se produit dans le système. Pour une énergie donnée $\Lambda = \Lambda_*$, on a deux états d'équilibre, un au-dessus et l'autre au-dessous de Λ_c. Le point au-dessus représente un état d'équilibre stable (mais, en étant placé à droite de η_c, il est instable dans l'ensemble canonique) alors que le point au-dessous représente un état instable. Par analogie au cas canonique, le système subit l'effondrement gravitationnel si $\Lambda > \Lambda_c$. Ce phénomène est aussi connu

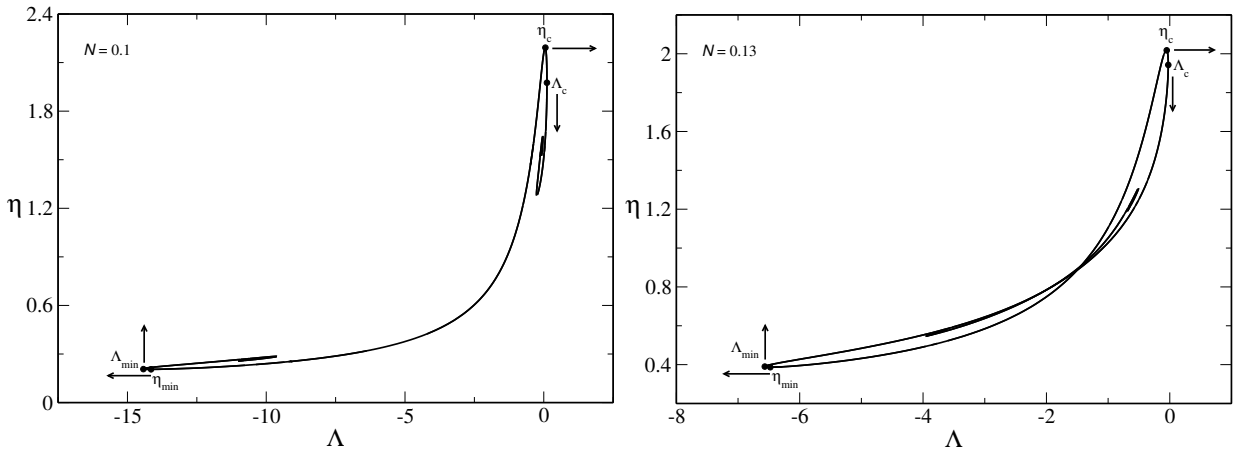

Figure 7.3: ***Gauche**: Série d'équilibre obtenue pour $\mathcal{N} = 0.1$. Il y a quatre points critiques (deux en énergie et deux en température). Les flèches indiquent la direction des effondrements. La spirale de droite représente l'extension de la spirale de Lynden-Bell & Wood [133] à la Relativité Générale. La spirale de gauche représente la contribution de la radiation, qui se manifeste seulement aux échelles relativistes (Chavanis [55], Roupas [159]).* ***Droite**: Série d'équilibre obtenue pour $\mathcal{N} = 0.13$. En contraste avec le cas précédent, le deux spirales ne sont plus séparées mais il y a un point de "jonction". Pour des valeurs de $\mathcal{N}$ plus proches de $\mathcal{N}_{max}$, les deux spirales disparaissent et la série d'équilibre prend la forme d'un huit.*

comme "catastrophe gravotherme" [4, 133]. Il faut aussi souligner que dans la région entre les points η_c et Λ_c la chaleur spécifique est négative[9]. Cet effet fournit la preuve plus évidente de la non-équivalence des ensembles statistiques pour les systèmes auto-gravitants (Thirring [179], Chavanis [53]).

Comme on l'avait anticipé, la spirale de droite étend le modèle newtonien d'Antonov & Lynden Bell à la Relativité Générale dont la présence a, comme unique effet, celui de rendre le système plus instable et d'accélérer le processus d'effondrement gravitationnel[10]. La présence de la spirale de gauche, par contre, est une manifestation des effets relativistes.

En regardant la Figure 7.3, on voit que la spirale de gauche est caractérisée par l'existence de deux points critiques, en énergie (Λ_{min}) et température (η_{min}). Ces points critiques représentent les valeurs minimales de Λ ou η au-delà desquelles le système s'écroule (selon le sens des flèches). Par la figure, on peut aussi remarquer le fait que le comportement des points critiques de la spirale de gauche est inversé par rapport aux points de la spirale de droite.

[9]Par définition, dans l'ensemble canonique, la chaleur specifique ne peut jamais être négative (Huang [105]).

[10]En effet, les valeurs critiques de η_c et Λ_c sont plus petites que les valeurs correspondantes du cas newtonien. Dans l'ensemble canonique l'instabilité thermodynamique se manifeste pour $\eta > 2.525$ (température d'Emden) et dans l'ensemble micro-canonique pour $\Lambda > 0.335$ (limite d'Antonov).

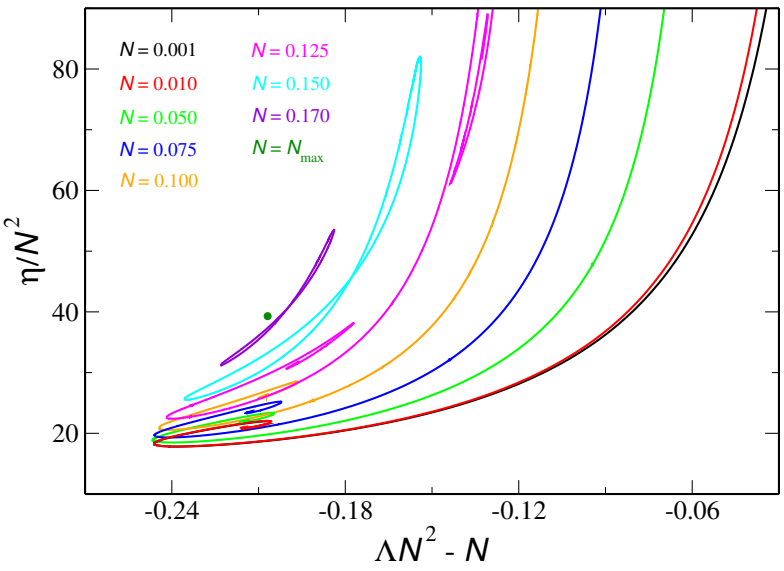

Figure 7.4: *Séries d'équilibre obtenues pour plusieurs valeurs de $\mathcal{N}$. En appliquant la loi d'échelle obtenue dans la limite $\mathcal{N} \to 0$ [cf. équation (7.28)], on voit bien l'existence d'une courbe invariante (ligne noire), qui correspond au cas newtonien. Quand la valeur de $\mathcal{N}$ augmente et les effets relativistes deviennent plus importants, on voit une déviation de la courbe invariante. En particulier, on observe que la spirale de droite se rapproche de celle de gauche et que, pour $\mathcal{N} > \mathcal{N}'_S$, les deux spirales disparaissent et la série d'équilibre devient un huit.*

Si l'on considère les valeurs typiques de Λ_{min} et η_{min}, on voit, en les comparant à celles de Λ_c et η_c, qu'elles sont petites. Selon l'équation (7.16), cela implique que la température T et l'énergie de liaison E_b acquièrent des grandes valeurs. Par conséquent, la masse (et la gravité) associée aux grandes énergies devient grande comparée à la masse au repos du système. Cela montre que la spirale de gauche ne reçoit pas de contribution de la masse au repos mais seulement de l'énergie interne du système qui, dans le cas en considération, se comporte comme le rayonnement (c'est-à-dire photons)[11]. Le graphique de droite de la Figure 7.3 montre une autre particularité, qui n'a pas d'équivalent dans le cas newtonien. Il y a en effet un point de "jonction" des deux spirales, qui ne sont alors plus séparées. Cet effet est explicable en vertu des géométries de la courbe $\mathcal{N}(\Phi_0)$, qui présente plusieurs oscillations (cf. Figure 7.2). Il existe une valeur critique d'α (qui vaut $\alpha = 5.012$) pour laquelle le nombre de particules rejoint sa valeur plus haute ($\mathcal{N} = \mathcal{N}_{max} = 0.1764$, cf. Figure 7.4). La courbe $\mathcal{N}(\Phi_0)$, pour cette valeur critique d'α, donne deux points critiques supplémentaires, associés à la présence du point de jonction des spirales ($\mathcal{N} = \mathcal{N}_S = 0.1279$) et l'apparition d'un huit ($\mathcal{N} = \mathcal{N}'_S = 0.1416$). Dans la limite[12] $\mathcal{N} \to 0$, Λ_{min} and η_{min} suivent le comportement:

[11] On pourrait effectivement montrer que l'équation d'état du fluide, dans ce cas, devient $P = \epsilon/3$.

[12] Quand la valeur de la compacité est petite, on retrouve la gravité newtonienne et la contribution de l'énergie interne

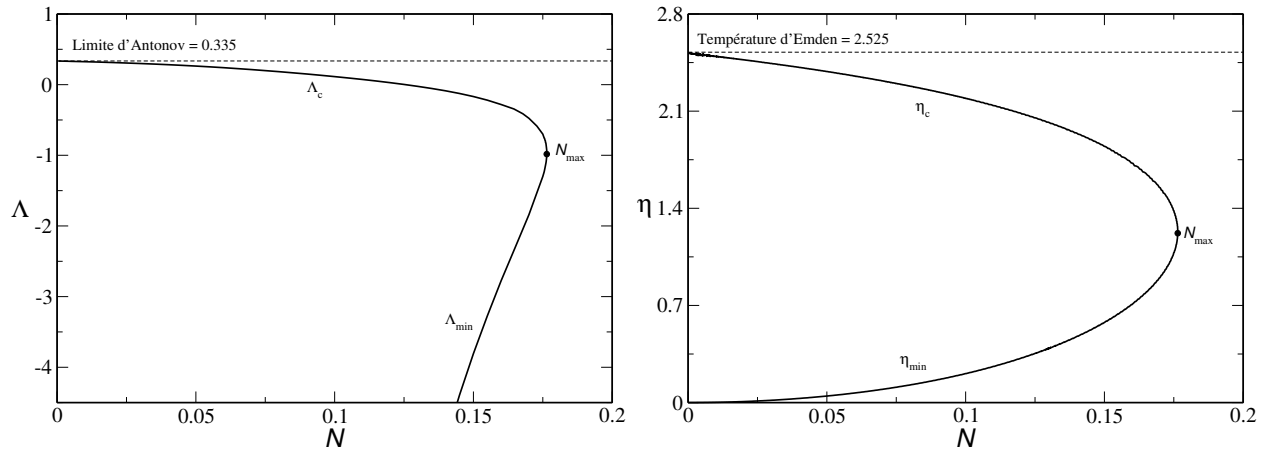

Figure 7.5: ***Gauche**: Diagramme de phase dans l'ensemble micro-canonique. Λ_{min} (quantité toujours négative) diverge pour $\mathcal{N}$ [cf. équation (7.28)] petits (pas montré dans la figure à cause de problèmes d'échelle). Λ_c, par contre, a un comportement opposé, en passant de valeurs négatives à valeurs positives lorsque le nombre de particules devient petit. Dans la limite newtonienne $\mathcal{N} \to 0$ on retrouve la limite d'Antonov. Différemment du cas newtonien, on identifie un point critique, qui concide avec $\mathcal{N}_{max}$ et où Λ acquiert la valeur critique $\Lambda(\mathcal{N}_{max}) = -0.983$. **Droite**: Diagramme de phase dans l'ensemble canonique. Les deux fonctions η_{min} et η_c ont un comportement spéculaire. En partant de $\mathcal{N}_{max}$ [où on l'a $\eta(\mathcal{N}_{max}) = 1.2203$], η_{min} décroît progressivement jusqu'à devenir infinitésimale dans la limite $\mathcal{N} \to 0$ [cf. équation (7.28)]. η_c, par contre, augmente toujours sa valeur jusqu'à la température d'Emden.*

$$\Lambda_{min} \simeq -\frac{0.2463}{\mathcal{N}^2}\,, \qquad \eta_{min} \simeq 17.83\mathcal{N}^2 \tag{7.28}$$

Si l'on normalise Λ et η par les lois d'échelle écrites ci-dessus, on obtient ce qui est représenté en Figure 7.4. On peut voir l'existence d'une courbe invariante (ligne noire), qui représente la série d'équilibre "universelle" associée aux instabilités aux hautes énergies. Quand les effets relativistes deviennent au fur et à mesure plus importants, on peut apprécier une déviation par la courbe invariante. On peut remarquer que la figure résume tous les comportements observés dans notre étude. On observe aussi que, pour $\mathcal{N} = \mathcal{N}_{max}$, la courbe calorique est réduite à un seul point. Dans ce cas, il n'y a aucun effondrement, en impliquant que $\mathcal{N}_{max}$ peut être vu comme le nombre maximal de particules qu'une sphère isotherme peut contenir sans subir un effondrement.

au système devient toujours plus négligeable. Cela explique la raison pour laquelle la spirale de gauche nest jamais attendue en gravité newtonienne.

7.5. Le Cas Général

Dans cette section, on traitera le cas des fermions. Grâce aux résultats obtenus dans les cas newtonien [46] et relativiste [25], on sait que les systèmes fermioniques mettent en évidences l'existence des transitions de phase. Une première différence, par rapport au cas boltzmannien, est la cessation de la validité, due à la présence de la dégénerescence, de la loi d'échelle (7.27). Cela implique, comme on verra dans la suite, l'existence de valeurs précises du rayon de la boîte R où le système fait apparaître les transitions de phase.

L'étude thermodynamique dans le cas des fermions est faite à l'aide de quatre paramètres: le rayon de la boîte R, le nombre de particules N, le potentiel chimique normalisé α et la valeur centrale du potentiel gravitationnel Φ_0. Pour un rayon donné, on intègre le système TOV (7.12) pour différentes valeurs d'α et Φ_0. Ensuite, pour un N donné, on construit la série d'équilibre associée au moyen de la méthode expliquée dans la section précédente.

Les résultats numériques montrent que la transition de phase canonique est supprimée pour un rayon plus petit que le rayon critique canonique R_{CCP}, qui vaut $R_{CCP} = 3.87\ R_{OV}$ (R_{OV} en étant le rayon d'Oppenheimer-Volkoff, cf. Figure 7.1) alors que la transition de phase micro-canonique n'apparaît pas pour $R < R_{MCP}$, où $R_{MCP} = 27.4\ R_{OV}$ est le rayon critique micro-canonique. Dans la suite, on étudiera séparément les deux cas. Le cas canonique sera analysé en considérant une boîte sphérique dont la dimension est $R = 50\ r_* \simeq 14.9\ R_{OV}$ alors que le cas micro-canonique sera analysé pour $R = 600\ r_* \simeq 179\ R_{OV}$. Pour ce dernier, il faut aussi souligner que la valeur du rayon est telle que les effets relativistes ne jouent aucun rôle et le système a retrouvé le comportement newtonien.

7.5.1. Ensemble Canonique: $R = 50\ r_*$

Il faut d'abord distinguer le cas au-dessous du cas au-dessus de la limite d'Oppenheimer-Volkoff. Cette distinction est nécessaire, parce que cela nous permet de comprendre si la gravité du système soit newtonienne ou einsteinienne. La manifestation de la transition de phase n'est pas influencée par la Relativité Générale, parce qu'elle est plus liée à la nature des particules qu'au niveau de gravité. Cependant, comme on le verra, il y a des nouveautés par rapport au cas newtonien.

Dans la Figure 7.6 nous avons représenté la série d'équilibre obtenue pour $N = 0.29\ N_*$. D'abord, on remarque la présence de deux branches distinguées, délimitées par les énergies Λ_{max} et Λ'_{max}. Cette dernière, qui n'a pas d'équivalent dans le cas newtonien, est constituée par des états d'équilibre instables qui ne représentent aucun système physique. L'origine de cette branche est purement relativiste et associée au point tournant (R_1, M_1) de la relation masse-rayon à $T = 0$ (cf. Figure 7.1).

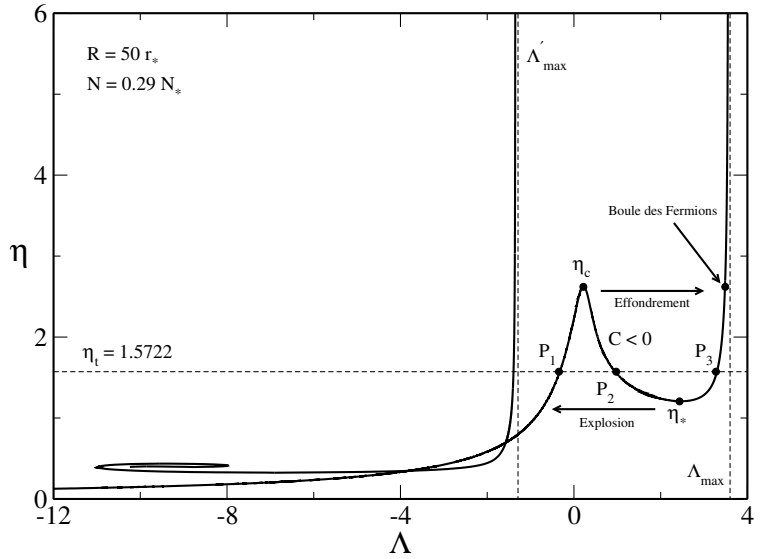

Figure 7.6: *Série d'équilibre des fermions auto-gravitants obtenue pour $N = 0.29\ N_*$ et $R = 50\ r_*$. La branche secondaire, délimitée par l'énergie Λ'_{max}, est instable et est montrée à but illustratif. La branche principale (qui termine à Λ_{max}) montre l'existence de la transition de phase canonique. Pour une température donnée, on trouve plusieurs solutions physiques dont la nature est variée.*

Si l'on se focalise sur la branche principale, on voit que plusieurs solutions peuvent exister pour une température donnée (points P_1, P_2 et P_3). Cela est la raison pour laquelle on parle de transition de phase (la ligne en tiré dans la figure correspond à la température de transition pour $N = 0.29\ N_*$). En même temps, la courbe nous permet d'identifier deux points critiques en températures, η_c et η_* respectivement. La partie de la courbe qui termine à η_c forme ce que l'on appelle la "phase gazeuse". A la température critique η_c, le système est destiné à subir un effondrement (isotherme) et, en suivant le sens de la flèche, à former ce que l'on appelle la "phase condensée" (qui émerge au point η_*).

Quand le système rejoint la phase condensée, il acquiert une structure similaire à celle d'une étoile naine blanche, c'est-à-dire un objet compact entouré d'une atmosphère très diluée (une boule des fermions). Les points du type P_3 appartiennent donc à la phase condensée alors que les points P_2 sont des points de selle, instables. Du point de vue micro-canonique, dans la région comprise entre η_c et η_*, la chaleur spécifique est négative.

La température de transition η_t est définie comment la valeur de la température pour laquelle l'énergie libre de la phase gazeuse égalise l'énergie libre de la phase condensée. Dans le diagramme de l'énergie libre (cf. Figure 7.8), cela donne lieu à un point de croisement.

Les points appartenant à la phase gazeuse ayant une température $\eta < \eta_t$ sont des minimas globaux d'énergie libre (mGEL) et représentent des états d'équilibre stables. Les points ayant $\eta_t < \eta < \eta_c$

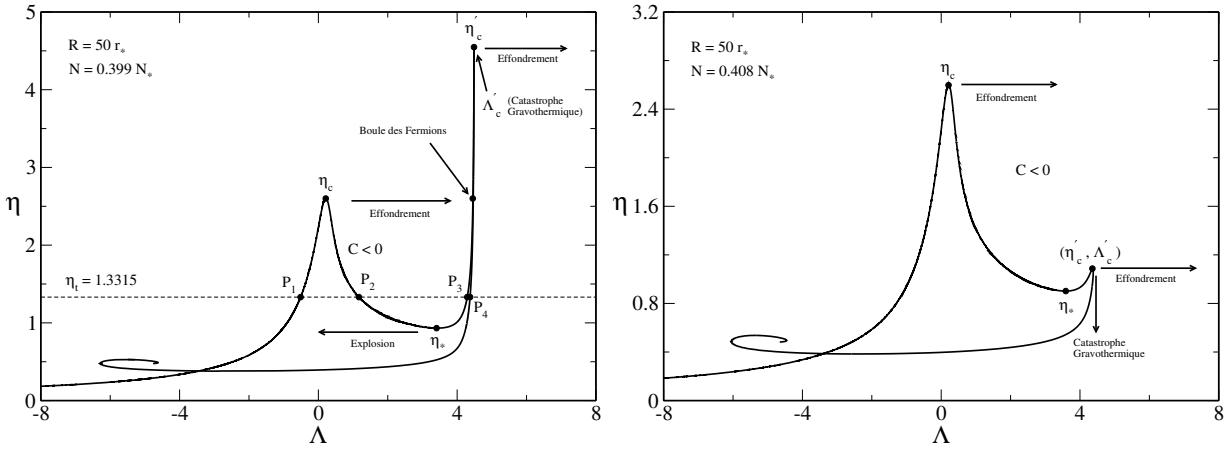

Figure 7.7: ***Gauche**: Série d'équilibre des fermions auto-gravitants obtenue pour $N = 0.399\ N_*$ et $R = 50\ r_*$. Différemment du cas $N < N_{OV}$, la phase condensée s'achève à la température critique η_c' et à l'énergie Λ_c'. Le système montre deux effondrements, aux points η_c et η_c', respectivement. La température de transition η_t est aussi indiquée.* ***Droite**: Série d'équilibre des fermions auto-gravitants obtenue pour $N = 0.408\ N_*$ et $R = 50\ r_*$. En contraste avec le cas précédent, il n'y a pas de transition de phase, même si le système montre l'existence de trois effondrements aux points η_c, η_c' et Λ_c', respectivement. L'extension de la phase condensée est notablement réduite par rapport au cas précédent.*

sont des minimas locaux d'énergie libre (mLEL) et correspondent à des états d'équilibre *métastables*. Cela veut dire qu'ils sont destinés à subir un effondrement gravitationnel. En même temps, on peut montrer que la vie moyenne de ces états est proportionnelle au nombre des particules, c'est-à-dire $\tau_{vie} \sim e^{2\lambda N(\eta_c - \eta)^{3/2}}$ (cf. Chavanis [52]). Dans la limite thermodynamique $N \to +\infty$, on voit que τ_{vie} diverge exponentiellement, en impliquant que la transition de phase ne se manifeste pas pratiquement. Par conséquent, les états métastables peuvent, en principe, représenter des systèmes physiques réels. Les points appartenant à la phase condensée ont une nature inversée par rapport aux points de la phase gazeuse.

Dans la Figure 7.7 nous avons représenté deux exemples de série d'équilibre au-dessus de la limite d'Oppenheimer-Volkoff[13] $N > N_{OV}$. La courbe illustrée dans le graphique de gauche montre l'existence de la transition de phase mais, différemment du cas précédent, on voit la présence d'une nouvelle température critique (η_c'), qui permet au système de subir un deuxième effondrement. En nous trouvant dans la situation $N > N_{OV}$, la structure de la phase condensée est plus similaire à une étoile à neutrons qu'une étoile naine blanche (stable dans le cas du point P_3 et instable dans le cas du

[13] $N_{OV} = 0.39853\ N_* = 8.752 \times 10^{56}$ particules.

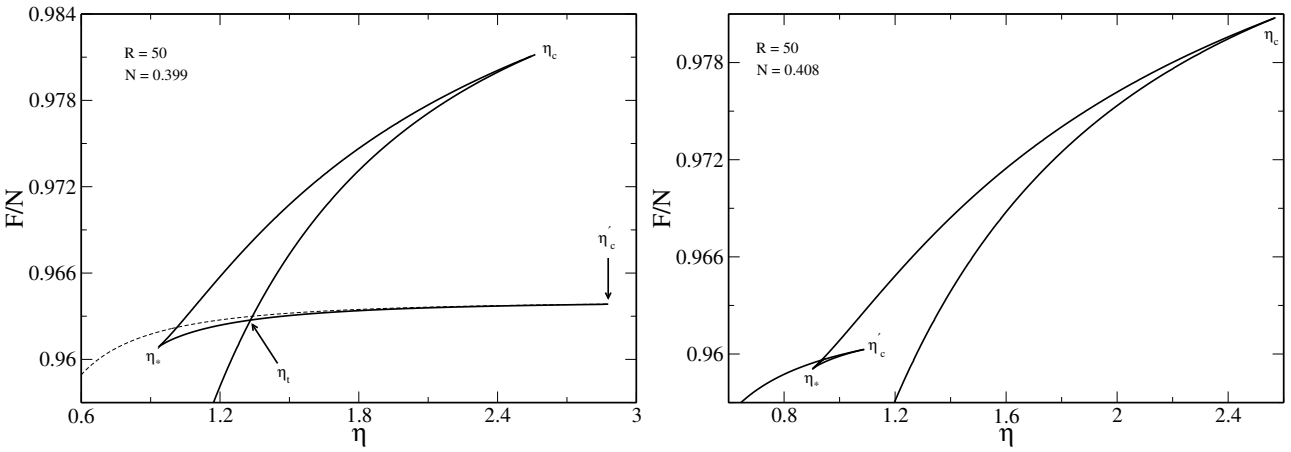

Figure 7.8: ***Gauche**: Energie libre par fermion en fonction de la température η. La courbe montre bien l'existence de la transition de phase, indiquée par le point de croisement entre les phases gazeuse et condensée. La partie de la courbe en tiré se réfère à des états instables. Les points critiques η_c, η_* et η_c' sont aussi indiqués.* ***Droite**: La diminution de η_c' a comme conséquence l'extinction de la transition de phase (il n'y a plus le point de croisement entre phase gazeuse et condensée). Cela implique l'existence d'une valeur critique de N, au-dessus de laquelle la transition de phase est supprimée.*

point P_4).

Jusqu'à l'apparition de la phase condensée, les propriétés de la série d'équilibre sont les mêmes que celles qui sont observées dans le cas $N = 0.29\ N_*$. Cependant, la présence d'une deuxième température critique (effet dont l'origine est purement relativiste) a des conséquences importantes pour l'existence de la transition de phase. Le fait que η_c' possède une valeur finie pour $N = N_{OV} + \delta$ (avec $\delta \to 0$) implique que, pour des N encore plus grands, sa valeur se réduit (ce que l'on voit dans le graphique de droite en Figure 7.7).

Une diminution d'η_c' comporte une réduction de l'extension spatiale de la phase condensée dans la série d'équilibre (cf. graphique de droite en Figure 7.7). Pour cette raison, il semble peu probable que les énergies libres du gaz et du condensé peuvent encore s'égaliser et la transition de phase risque d'être *supprimée*. Afin de vérifier cette conjecture, dans la Figure 7.8 nous avons représenté les énergies libres associées aux courbes caloriques obtenues pour $N = 0.399\ N_*$ et $N = 0.408\ N_*$.

Si l'on regarde le graphique de gauche en Figure 7.8, l'existence de la transition de phase est garantie. Il y a en effet un point de croisement entre les branches gazeuse (branche verticale qui s'achève à η_c) et condensée (branche horizontale comprise entre η_* et η_c'). Si maintenant on focalise notre attention sur le graphique de droite, on voit l'absence du point de croisement entre les deux phases. Par conséquent, la transition de phase n'a pas lieu. Le point de croisement qui apparaît dans la figure montre l'existence

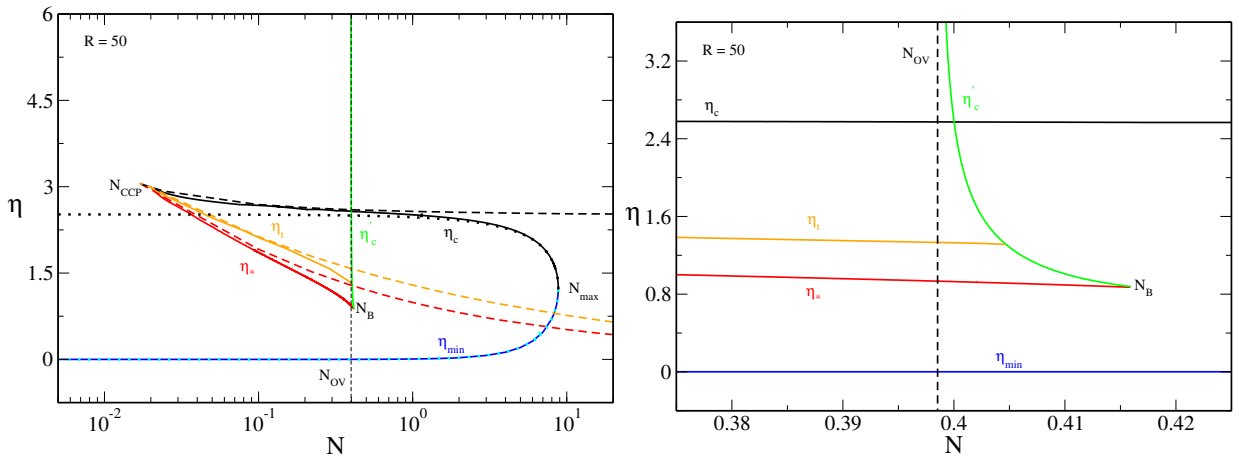

Figure 7.9: *Diagramme de phase dans l'ensemble canonique pour $R = 50\ r_*$. Le point critique N_{CCP} correspond au point critique canonique, où la transition de phase se manifeste. Le point critique N_B est défini par l'égalité $\eta_* = \eta'_c$. Dans ce cas, le système fermionique retrouve le comportement classique.* ***Gauche****: Les lignes pleines représentent les résultats relativistes alors que les lignes en tiré correspondent aux résultats newtoniens. Les corrections relativistes deviennent appréciables pour $N \sim 0.1\ N_*$ et dévient par le comportement newtonien lorsque l'on se rapproche de N_B. Les lignes en pointillés représentent η_c et η_{min} obtenus dans le cas classique.* ***Droite****: Agrandissement du diagramme de phase en proximité du point critique N_B. On voit comme la température de transition η_t (ligne orange) joint η'_c (ligne verte) pour $N < N_B$.*

d'une transition de phase entre des états instables et donc pas physiquement pertinent.

Dans l'ensemble micro-canonique, par contre, on voit que l'énergie limite (asymptotique) Λ_{max} a été remplacée par l'énergie critique Λ'_c (où le système subit la catastrophe gravotherme). Entre les points η'_c et Λ'_c il y a une petite région où la chaleur spécifique est une deuxième fois négative. De surcroît, pour des grandes valeurs de N, les séries d'équilibre retrouvent progressivement le comportement classique en devenant des spirales.

7.5.2. Ensemble Micro-canonique: $R = 600\ r_*$

Quand on agrandit la taille du système, la série d'équilibre modifie sa forme. Dans le cas $R = 100\ r_*$, pour $N \sim 1.5\ N_*$ (mais cette estimation est réduite lorsque R augmente) on voit que, après le point η_c, la descente de la courbe n'est plus continue mais présente une "interruption". En d'autres termes, on trouve que l'énergie présente un maximum et un minimum locaux, de façon analogue à ce que l'on a observé dans le cas canonique avec les points η_c et η_*. Afin de mieux montrer ce nouveau phénomène, qui correspond à l'apparition de la transition de phase micro-canonique, on a représenté

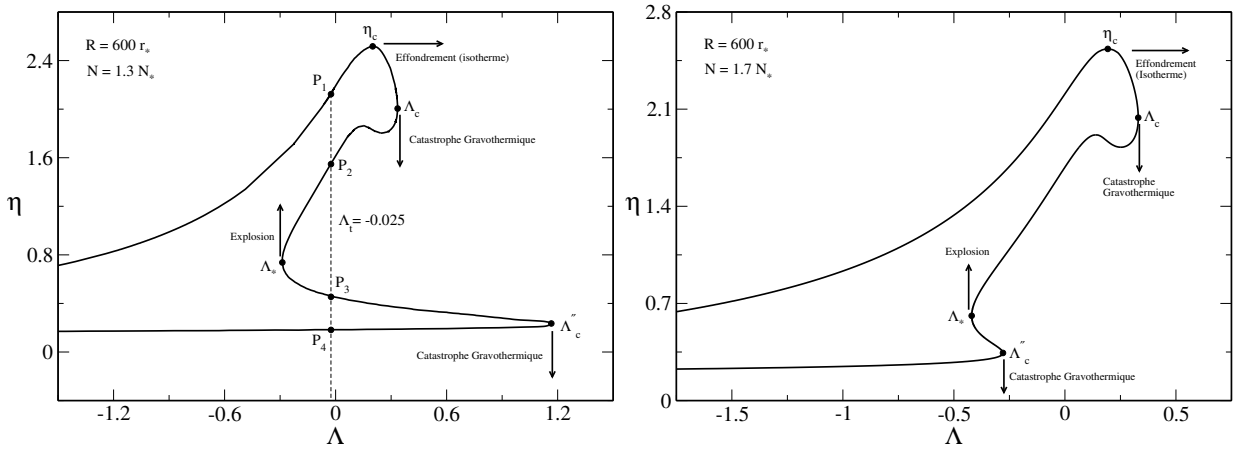

Figure 7.10: ***Gauche**: Série d'équilibre des fermions auto-gravitants obtenue pour $N = 1.3\ N_*$ et $R = 600\ r_*$. Le système montre l'existence de deux effondrements, aux points Λ_c et Λ_c'' (catastrophe gravotherme) respectivement. l'énergie de transition Λ_t est aussi indiquée. **Droite**: Série d'équilibre de fermions auto-gravitants obtenue pour $N = 1.7\ N_*$ et $R = 600\ r_*$. En contraste avec le cas précédent, il n'y a pas de transition de phase, bien que le système montre l'existence de deux effondrements aux points Λ_c et Λ_c'', respectivement.*

dans la Figure 7.10 deux exemples de série d'équilibre dans le cas $R = 600\ r_*$.

L'interprétation physique de la courbe peut être facilement obtenue à la lumière de l'analyse du cas canonique. En effet, si l'on invertit les axes, on retrouve une courbe très similaire à celles-là montrées dans la section précédente. Si l'on regarde le graphique de gauche de la Figure 7.10, on voit l'existence de plusieurs solutions pour une énergie donnée (cf. la ligne verticale en tiré dans la figure). Après la température critique η_c, la courbe montre l'existence de trois points critiques en énergie Λ_c, Λ_* et Λ_c''. Le point Λ_c représente l'énergie critique au-delà de laquelle la catastrophe gravotherme a lieu. Différemment du cas boltzmannien, ici le système s'effondre sur un nouvel état d'équilibre (points du type P_3). Par analogie au cas canonique, ce nouvel état d'équilibre représente la phase condensée, dont sa structure est formé d'un noyau "dur" entouré par une atmosphère diluée. L'énergie critique Λ_* correspond à l'énergie critique d'émersion de la phase condensée. Entre ces deux points critiques, la chaleur spécifique est négative. L'énergie critique Λ_c'' est l'équivalent micro-canonique de la température η_c'. En particulier, Λ_c'' est l'évolution des points Λ_{max} et Λ_c' et peut être vu comme la valeur de l'énergie où le deuxième effondrement isotherme (à la température η_c') cesse d'exister. Comme Λ_c'' tire son origine de cette température, on peut sattendre un comportement similaire par rapport à l'extinction de la transition de phase micro-canonique (voir ci-dessous).

L'énergie de transition Λ_t est déterminée comment la valeur de l'énergie pour laquelle l'entropie de

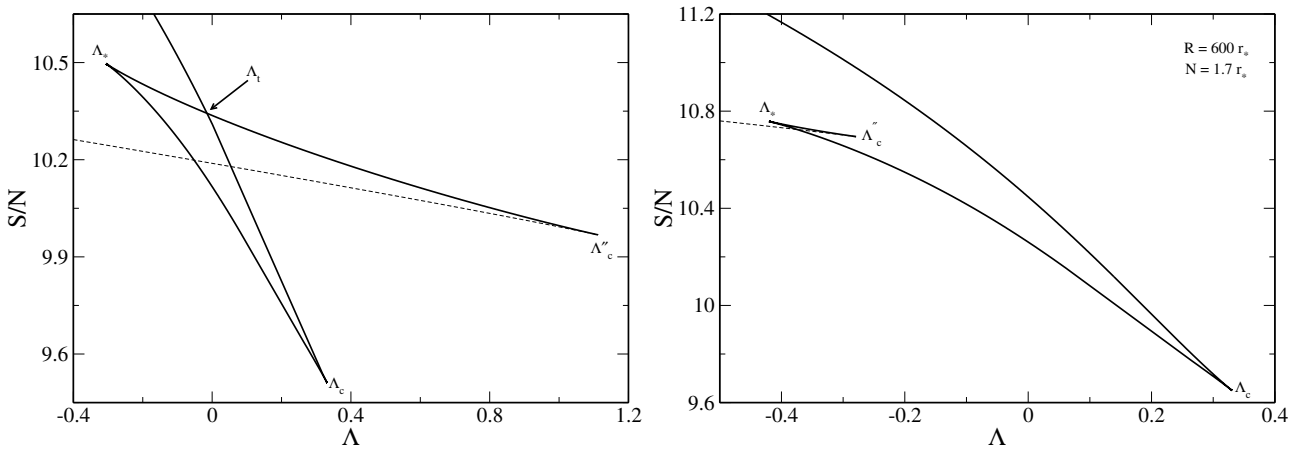

Figure 7.11: ***Gauche**: Entropie par fermion en fonction de l'énergie Λ. La courbe montre bien l'existence de la transition de phase, indiquée par le point de croisement entre les phases gazeuse et condensée. La partie de la courbe en tiré se réfère à des états instables. Les points critiques Λ_c, Λ_* et Λ_c'' sont aussi indiqués.* ***Droite**: La diminution de Λ_c'' a comme conséquence l'extinction de la transition de phase. En termes de la construction de Maxwell, les aires délimitées par l'énergie de transition et le plateau correspondant aux deux phases ne s'égalisent pas.*

la phase gazeuse (branche supérieure, points P_1) égalise l'entropie de la phase condensée (branche inférieure, points P_3). Dans le diagramme de l'entropie (cf. Figure 7.11) cela donne lieu à un point de croisement. Selon leur position par rapport à l'énergie de transition, la nature des points constituant la série d'équilibre est différente.

Les points appartenant à la phase gazeuse sont des maximas globaux d'entropie (MGE) si $\Lambda < \Lambda_t$ et maximas locaux d'entropie (MLE) si $\Lambda > \Lambda_t$. En particulier, les points MGE sont stables alors que les états MLE sont *métastables*. De façon analogue au cas canonique, les états métastables ont une vie moyenne infinie dans la limite thermodynamique $N \to +\infty$ (en effet on a $\tau_{vie} \sim e^{2\lambda' N(\Lambda_c - \Lambda)^{3/2}}$, cf. Chavanis [52]) et, donc, ils peuvent représenter des états physiques réels. Les points classifiés comme P_2 et P_4, par contre, sont des points de selle instables. Les points appartenant à la phase condensée sont (MLE) si $\Lambda < \Lambda_t$ et (MGE) si $\Lambda > \Lambda_t$ (comme dans le cas canonique, ces points ont nature inversée par rapport aux points formant la phase gazeuse).

C'est la nature métastable des points MLE de la phase gazeuse qui donne lieu à l'effondrement au point Λ_c. De même, les états métastables dans la phase condensée dirigent le système vers une explosion[14]. Si l'on augmente la valeur de N, on obtient une situation comme celle illustrée dans le graphique de

[14]Dans le cas canonique on observe la même propriété: effondrement si $\eta > \eta_c$ pour le gaz et explosion si $\eta < \eta_*$ pour le condensé.

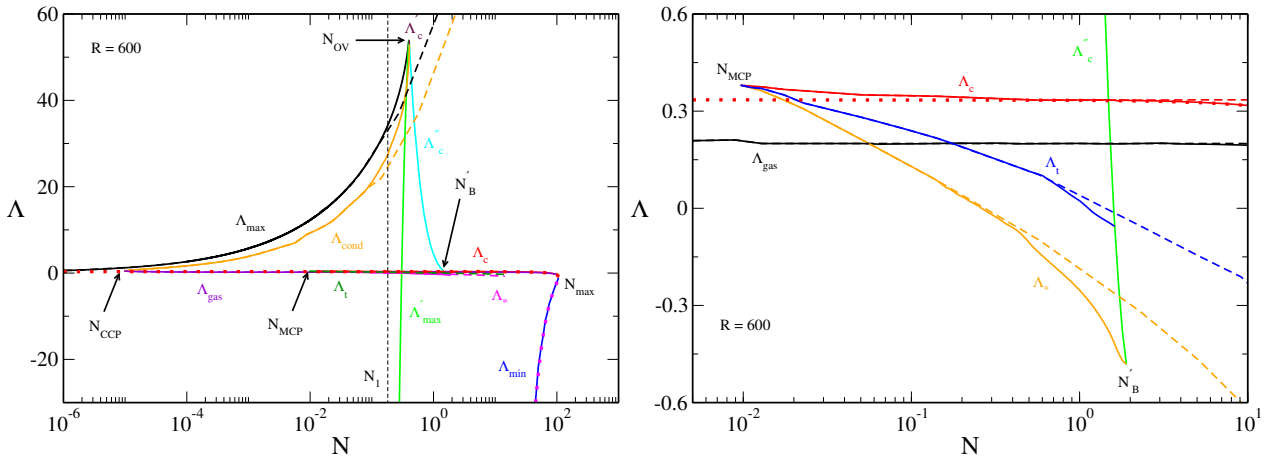

Figure 7.12: *Diagramme de phase dans l'ensemble micro-canonique pour $R = 600\ r_*$. Les points critiques N_{CCP} et N_{MCP} correspondent aux points critiques canonique et micro-canonique. Le point critique N'_B est défini par l'égalité $\Lambda_* = \Lambda''_c$. Dans ce cas, le système fermionique retrouve le comportement classique.* ***Gauche****: Les lignes pleines représentent les résultats relativistes alors que les lignes en tiré correspondent aux résultats newtoniens. Les corrections relativistes deviennent appréciables pour $N \sim 0.3\ N_*$ et dévient du comportement newtonien lorsque l'on se rapproche de N'_B. Les lignes en pointillés représentent η_c et η_{min} obtenus dans le cas classique.* ***Droite****: Agrandissement du diagramme de phase en proximité du point critique N'_B. On voit comme l'énergie de transition Λ_t (ligne bleue) joint Λ''_c (ligne verte) pour $N < N'_B$.*

droite de la Figure 7.10. Il y a les effondrements aux points η_c (ensemble canonique) et aux points Λ_c et Λ''_c (ensemble micro-canonique) mais il ny a pas évidence de transition de phase.

En effet, comme on l'a déjà vu dans l'ensemble canonique, il y a un moment où l'entropie du gaz n'est plus égale à celle du condensé et la transition de phase est supprimée. En Figure 7.11 nous avons représenté les entropies associées aux séries d'équilibre montrées en Figure 7.10. On voit que, dans le graphique de droite, la branche condensée ne croise pas la branche gazeuse. Cela montre que, aussi dans l'ensemble micro-canonique, la Relativité Générale garantit l'extinction de la transition de phase.

Dans la Figure 7.12 nous avons représenté le diagramme de phase dans l'ensemble micro-canonique. A cause de la présence des deux types de transition, on identifie deux points critiques, N_{CCP} et N_{MCP} correspondant, respectivement, à l'apparence des transitions canonique et micro-canonique. La présence de N_{CCP} est justifiée en vertue de la disparition de la phase gazeuse (Λ_{gas}) et de l'émersion de la phase condensée (Λ_{cond}). La figure (comme dans le cas canonique) peut être interprétée, en allant de gauche à droite, en suivant le niveau de dégénérescence et gravité du système.

Pour petites valeurs de N, le système est "quantique", en exhibant les transitions de phase (d'où la

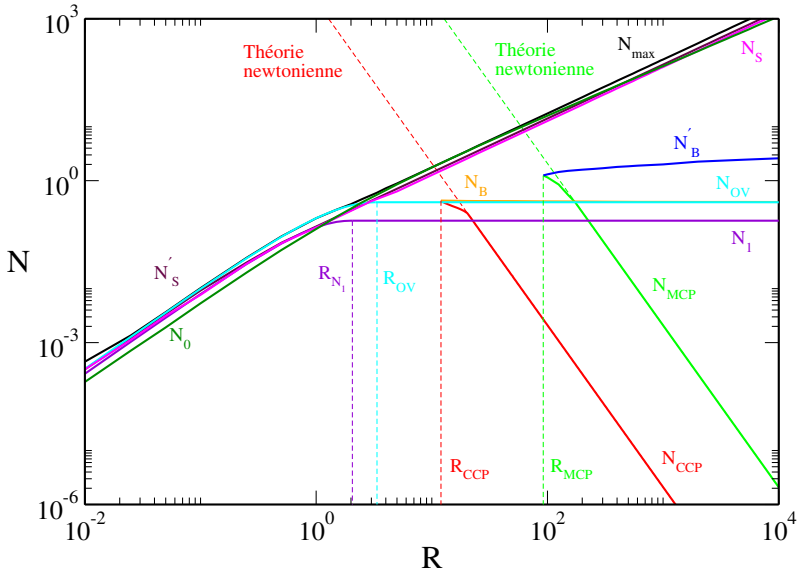

Figure 7.13: *"Diagramme de phase des diagrammes de phase". La figure montre le comportement des différents points critiques en fonction du rayon de la boîte. Les lignes en tiré représentent les prédictions newtoniennes. Les rayons critiques R_{CCP} et R_{MCP} définissent les moments où les transitions de phase (canonique et micro-canonique) apparaissent. La figure nous permet d'apprécier comme les corrections relativistes à la théorie newtonienne sont, généralement, de petite entité.*

présence des points N_{CCP} et N_{MCP}). Par contre, le niveau de gravité est faible et le système peut être considéré newtonien (à confirmation de ça, il y a le fait que les courbe relativistes et newtoniennes concident). En procédant vers la droite, les effets dus à la Relativité Générale deviennent toujours plus considérables et l'on peut apprécier les déviations de la théorie newtonienne. Si l'on regarde le graphique de droite de la Figure 7.12, on peut voir ces différences.

On peut noter comme, autour du point critique micro-canonique (N_{MCP}), les courbes représentant les fonctions Λ_c, Λ_* et Λ_t suivent parfaitement le comportement newtonien (dans le cas de Λ_c on voit aussi une subtile discrépance par rapport au Λ_c évalué dans le cas boltzmannien, cf. Sec. 7.4). Les corrections relativistes[15] deviennent importantes pour $N \sim 0.45\ N_*$ (pour Λ_c elles interviennent pour des valeurs de N ben plus grandes). Les courbes Λ_* et Λ_t se dirigent vers le nouveau point critique N'_B (qui n'est pas contemplé dans le cadre de la théorie newtonienne). Plus précisément, à cause de la violation du plateau de Maxwell, seulement Λ_* converge vers N'_B (où il rejoint Λ'_c). Comme on le voit dans la figure, Λ_t "arrête" son chemin auparavant.

Afin de résumer tous les phénomènes observés dans notre étude, nous avons construit le "diagramme de

[15]En fait, à cause de la petite intensité des champs gravitationnels pour $R = 600r_*$, on pourrait considérer ces corrections plutôt à niveau post-newtonien que relativiste.

phase des diagrammes de phase" (cf. Figure 7.13), dans lequel nous avons représenté le comportement des points critiques en fonction du rayon de la boîte. En regardant le diagramme, on peut identifier trois régions: grandes valeurs de N et R (en haut et à droite dans la figure), petites valeurs de N et grandes valeurs de R (en bas et à droite dans la figure), petites valeurs de N et R (en bas et à gauche dans la figure). Il manque la région des petits rayons et grands N (en haut et à gauche dans la figure) qui, comme on le voit, est vide.

Pour $N, R \to +\infty$, le gaz fermionique a les mêmes propriétés du gaz classique: donc, grandes valeurs de N et R correspondent à la limite non-quantique $\hbar \to 0$ (ou $T \to +\infty$). Les fonctions N_{max}, N_0, N_S et N'_S représentent la généralisation, au cas fermionique, des homologues points critiques déjà analysés dans le cas boltzmannien. En particulier, N_0 correspond au maximum de la courbe $N(\Phi_0)$ obtenue pour $\alpha = 0$. On voit que, quand le rayon de la boîte devient plus petit, il y a une déviation par l'originaire comportement boltzmannien [correspondant à la loi d'échelle (7.27)].

C'est à remarquer que N_0 n'est pas parallèle à N_{max}, N_S et N'_S. La raison se trouve dans la différente définition de ce point. N_{max}, N_S et N'_S dépendent par un α "universel" alors que N_0 est fonction de R (chaque rayon a "sa propre configuration" $\alpha = 0$). C'est intéressant à noter aussi que la fonction N_{max} traverse le diagramme, en nous permettant de déterminer une région peuplée par des systèmes réels (au-dessous de N_{max}) et une région interdite (au-dessus de N_{max}), vide. En effet, cette dernière représenterait des systèmes physiques au-delà de N_{max} qui, comme on le sait, sont destinés à un effondrement gravitationnel à cause de leur nature instable.

Si l'on diminue progressivement N, les effets quantiques commencent à se manifester (pour $N < N'_B$, ligne bleue dans la figure) et le gaz fermionique montre ses propriétés typiques dues à la dégénérescence. Par un point de vue gravitationnel, le système est encore newtonien mais, en même temps, l'extinction des transitions de phase montre que les premières corrections relativistes influencent le comportement et la nature du gaz.

Si l'on continue à baisser N et, en même temps, à réduire les dimensions de la boîte, on arrive dans la région dans laquelle les transitions de phase micro-canonique et canonique apparaissent (lignes verte et rouge). C'est dans cette petite région où on l'observe la présence des corrections apportées, à la théorie newtonienne, de la Relativité Générale (cf. lignes en tiré et lignes en traits pleins).

Enfin, pour $R < R_{CCP}$, le système fermionique devient très relativiste et, pour $R < R_{OV}$, on voit aussi que la limite d'Oppenheimer-Volkoff N_{OV} n'est plus constante mais elle devient une fonction du rayon. Cela arrive lorsque le gaz fermionique est emprisonné dans une boîte de dimension $R < R_{OV}$. Dans ce dernier cas, on peut apprécier comme les fonctions N_{max}, N_0, N_S, N'_S, N_{OV} et N_1 sont infinitésimales dans la limite $R \to 0$. De plus, le gaz fermionique est complètement dégénéré.

Appendices

A

The Graphical Construction of the Caloric Curve

In this Section we show the method used to obtain the series of equilibria, i.e. the curve $\eta = \eta(\Lambda)$. When relativistic effects are present, the definition (1.27) of Λ given in Sec. 1.3 must be changed. Introducing the binding energy (3.143) that here we rewrite as

$$E_b = (M - Nm)c^2\,, \tag{A.1}$$

we get the new definition of Λ (we write also the definition of η for completeness)

$$\Lambda = -\frac{E_b R}{GN^2m^2} = -\frac{(\tilde{M} - \tilde{N})\tilde{R}}{\tilde{N}^2}\,, \qquad \eta = \frac{GNm^2}{k_B T R} = \frac{\tilde{N}}{\tilde{T}\tilde{R}}\,, \tag{A.2}$$

where we have introduced the dimensionless variables defined in Sec. 2.3. From Eq.(A.2) we see that Λ and η depend on global quantity that are obtained from the numerical integration of the TOV system (2.59). For a given value of the radius R, indeed, the integration of the TOV system depends on α and Φ_0. This means that also the points in the series of equilibria are determined by the pair $[\alpha, \Phi_0]$. In the framework of the Thomas-Fermi model [24, 25], the caloric curve is obtained for a given value of the baryon number in the interval $[0, N_{max}]$, i.e. $N = N_{spec}$. This can be obtained by the constraint of the baryon number conservation

$$N(\Phi_0) = \int_0^R 4\pi n r^2 \Big(1 - \frac{2GM_r}{rc^2}\Big)^{-1/2} dr = N_{spec} \tag{A.3}$$

which determines a condition on Φ_0. In fact, only the value of Φ_0 for which the equality (A.3) is satisfied can be considered as physical solutions to obtain the caloric curve for $N = N_{spec}$.

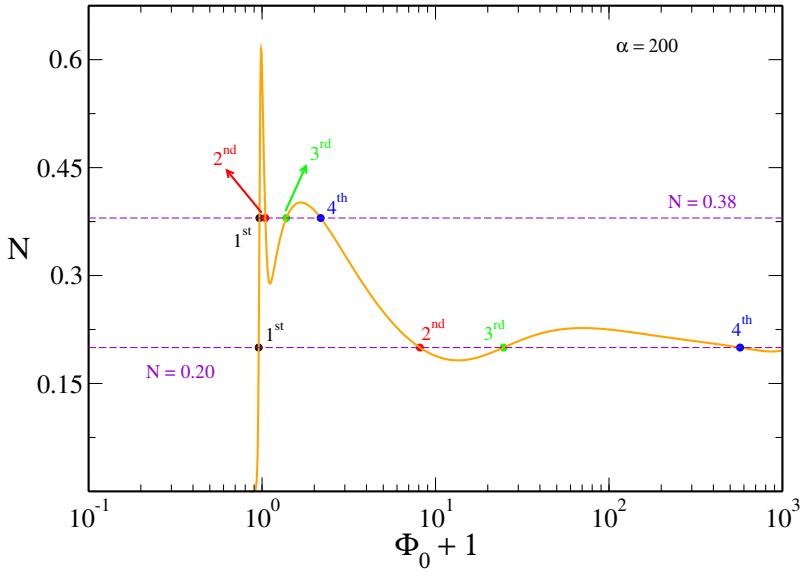

Figure A.1: *Representation (for two values of N and $R = 50$) of the method used to find the points satisfying the constraint of the baryon number conservation* (A.3). *The intersection points (ordered from the left to the right) are indicated by the full circles. The value of α is also indicated.*

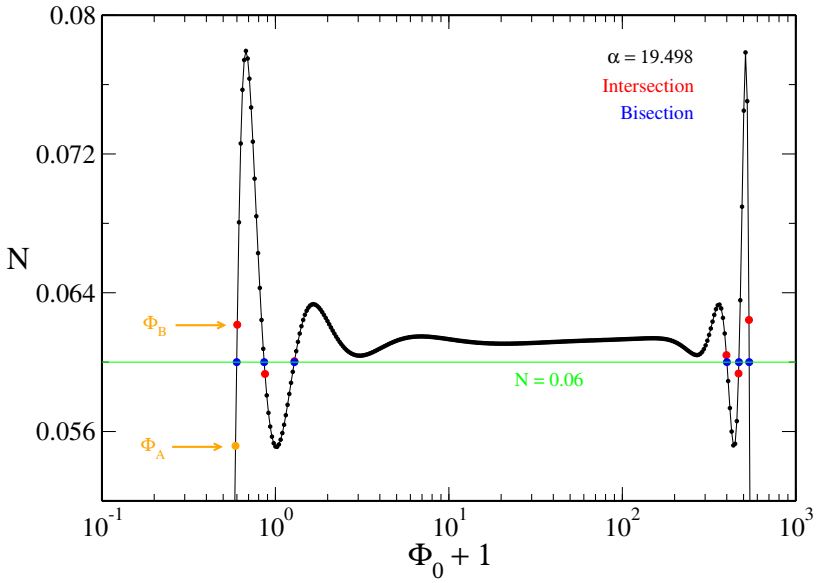

Figure A.2: *Particles number N versus the central value of the gravitational potential Φ_0. The line level $N = 0.06$ identifies six intersection points (red circles), not perfectly superimposed over the line level. To solve this problem, we have applied the bisection method, by "bringing" the red points onto the line level (blue points). Defining the interval $[\Phi_A, \Phi_B]$ (as indicated), the middle point Φ_C is computed. If $N(\Phi_c) = 0.06$ the solution is found, otherwise the procedure is iterated.*

The points obeying to the constraint (A.3) can be obtained by means of a graphical construction (see Fig. A.1). For given values of the cavity radius R and of the normalized chemical potential α, the TOV system is solved for several values of Φ_0. If we plot the baryon number versus Φ_0, we obtain a curve similar to that represented in Fig. A.1 (orange line). The choice of a particular value of N is equivalent to fix a line level at the height $N = N_{spec}$ (in Fig. A.1 we have represented two examples). In both of cases shown in the figure, the line level intersects the curve $N = N(\Phi_0)$ in four points[1], that are the unique solutions of the Thomas-Fermi model in this case. This implies that, to obtain the complete series of equilibria, α must vary in the interval $[\alpha_{min}, \alpha_{max}]$ (see Sec. 4.3).

From the figure, we note also that the first intersection is always placed before the maximum of the curve $N = N(\Phi_0)$. As we known ([25], see also Sec. 5.2), the ascending part of the curve $N = N(\Phi_0)$ corresponds to the gaseous phase of the caloric curve. Thanks to this last argument, we may think that the graphical construction could be used to get the nature of the physical states belonging to the series of equilibria. This is not *in general* true.

Furthermore, from a numerical point of view, we observe that the points of the curve $N = N(\Phi_0)$ are not perfectly aligned with the line level $N = N_{spec}$. This is a consequence of the fact that the number of values of Φ_0 is *discrete* and not continuous (see Fig. A.2). To obtain the "good" point, let us define the interval $[\Phi_A, \Phi_B]$, where Φ_A and Φ_B are the closest points to the line level (see Fig. A.2) and compute the point Φ_C such that

$$\Phi_C = \frac{\Phi_A + \Phi_B}{2} \,. \tag{A.4}$$

Integrating the TOV system (2.59) with the initial condition $\Phi(0) = \Phi_C$, we get an evaluation of the particles number $N(\Phi_C)$. If $|N(\Phi_C) - N_{spec}| \leq \delta$ (where δ is an error threshold defined *a priori*) we have obtained the "good" point and the procedure is arrested. If, vice-versa, $|N(\Phi_C) - N_{spec}| > \delta$ we define a new interval $[\Phi_A, \Phi_C]$ or $[\Phi_C, \Phi_B]$ (this depends on the position of Φ_C with respect to the line level) and iterate the procedure until the error condition is satisfied.

[1]The number of intersections is not limited *a priori*. As we have seen in Chaps. 4 and 5, for $\alpha_{min} \leq \alpha \leq \alpha_{max}$, indeed, the number of intersections goes from 1 to $+\infty$.

B

Basic Formulae for a Polytropic Equation of State

We consider a Newtonian self-gravitating system described by a polytropic EOS of the form

$$P = K\rho^{\gamma}\,, \qquad \gamma = 1 + \frac{1}{n}\,, \tag{B.1}$$

where K is the polytropic constant and γ (or n) is the polytropic index. Substituting this equation of state into the fundamental equation of equilibrium (3.33), we obtain

$$\frac{K(n+1)}{r^2}\frac{d}{dr}\Big(r^2\frac{d\rho^{1/n}}{dr}\Big) = -4\pi G\rho. \tag{B.2}$$

Introducing the variables θ and ξ defined by

$$\rho = \rho_0\theta^n\,, \qquad \xi = \left[\frac{4\pi G\rho_0^{1-1/n}}{K(n+1)}\right]^{1/2} r\,, \tag{B.3}$$

(ρ_0 is the central density) we can put Eq.(B.2) under the form

$$\frac{1}{\xi^2}\frac{d}{d\xi}\Big(\xi^2\frac{d\theta}{d\xi}\Big) = -\theta^n \tag{B.4}$$

with the conditions $\theta(0) = 1$ and $\theta'(0) = 0$. This is the Lane-Emden equation of index n. For $0 < n < 5$, the density vanishes at a normalized radius ξ_1 such that $\theta(\xi_1) = 0$ [41]. The mass and the radius are given in terms of the central density by

$$M = -4\pi\rho_0\left[\frac{K(n+1)}{4\pi G\rho_0^{1-1/n}}\right]^{3/2}\Big(\xi^2\frac{d\theta}{d\xi}\Big)_{\xi_1}\,, \qquad R = \left[\frac{K(n+1)}{4\pi G\rho_0^{1-1/n}}\right]^{1/2}\xi_1\,. \tag{B.5}$$

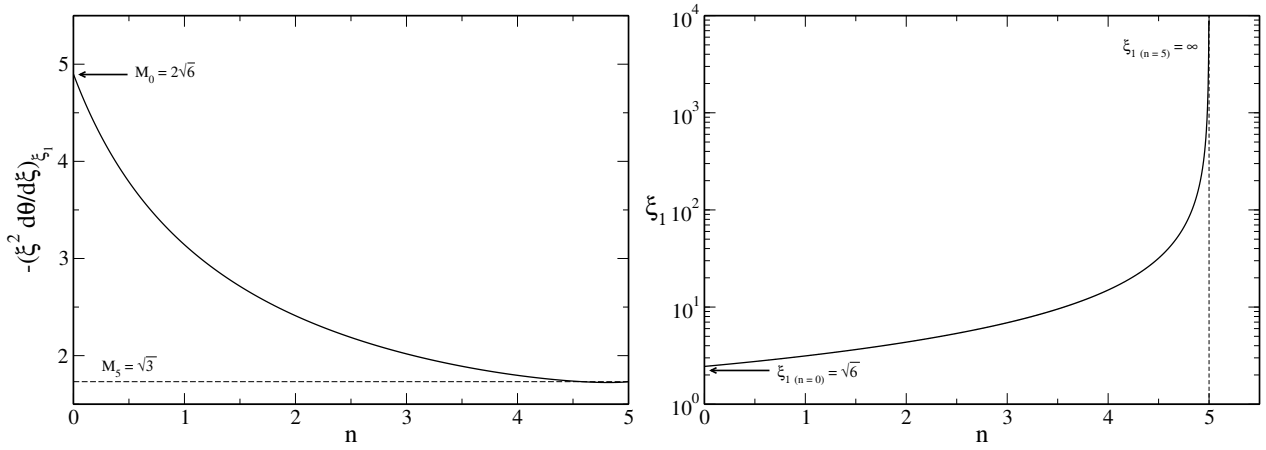

Figure B.1: ***Left Panel****: Total dimensionless mass as a function of the polytropic index, for several polytropic configurations. M_0 is the mass associated with the polytrope $n = 0$ whereas M_5 the mass associated with the polytrope $n = 5$.* ***Right Panel****: Total dimensionless radius ξ_1 versus the polytropic index* n*, for several polytropic configurations. The limiting values corresponding to the cases $n = 0$ and $n = 5$ are also indicated. In particular, for $n > 5$, both the mass and radius diverge.*

Eliminating the central density in the foregoing expressions, we obtain the mass-radius relation

$$M^{(n-1)/n} R^{(3-n)/n} = \frac{K(n+1)}{(4\pi)^{1/n} G} \omega_n^{(n-1)/n}, \qquad \omega_n = -\xi_1^{(n+1)/(n-1)} \theta_1' \,. \tag{B.6}$$

For $n = 3/2$, we have $\xi_1 = 3.65375$ and $\omega_{3/2} = 132.3843$. For $n = 3$, we have $\xi_1 = 6.89685$ and $\omega_3 = 2.01824$. The central density ρ_0 and the average density $\overline{\rho} = 3M/4\pi R^3$ are related to each other by

$$\frac{\overline{\rho}}{\rho_0} = \frac{3\omega_n}{\xi_1^{2n/(n-1)}}. \tag{B.7}$$

The potential energy of a polytropic star is given by the Betti-Ritter formula[1] [41]

$$W = -\frac{3}{5-n} \frac{GM^2}{R} \,. \tag{B.8}$$

The moment of inertia of a polytropic star is given by

$$I = \frac{MR^2}{\xi_1^{(3n-5)/(n-1)} \omega_n} \int_0^{\xi_1} \theta^n \xi^4 \, d\xi \,. \tag{B.9}$$

Using the Ledoux formula (3.76) together with Eqs.(B.8) and (B.9), we find that the fundamental pulsation of a polytropic star of index n is (approximately) given by

[1] For an extension of this formula to the planetary systems see Ref.[191]

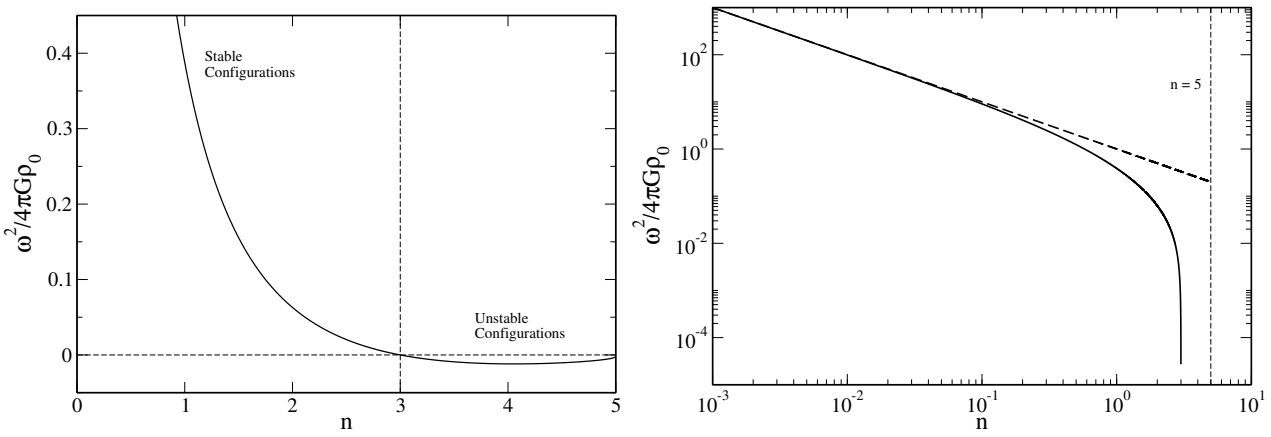

Figure B.2: ***Left Panel****: Pulsations as a function of the polytropic index, for several polytropic configurations.* ***Right Panel****: Comparison between the asymptotic expression* (B.14) *and the exact solution* (B.11).

$$\frac{\omega^2}{4\pi G\overline{\rho}} = \frac{3-n}{(5-n)n}\frac{\xi_1^{(3n-5)/(n-1)}\omega_n}{\int_0^{\xi_1}\theta^n\xi^4\,d\xi}\,. \tag{B.10}$$

Using the relation (B.7) between the average density and the central density, we get

$$\frac{\omega^2}{4\pi G\rho_0} = \frac{3(3-n)}{(5-n)n}\frac{\xi_1^{(n-5)/(n-1)}\omega_n^2}{\int_0^{\xi_1}\theta^n\xi^4\,d\xi}\,. \tag{B.11}$$

Alternatively, if we use Eq.(3.74), we obtain

$$\frac{\omega^2}{4\pi G\rho_0} = \frac{3(3-n)}{n(n+1)}\frac{\int_0^{\xi_1}\theta^{n+1}\xi^2\,d\xi}{\int_0^{\xi_1}\theta^n\xi^4\,d\xi}\,. \tag{B.12}$$

Comparing Eqs.(B.11) and (B.12), we find the relation

$$\int_0^{\xi_1}\theta^{n+1}\xi^2\,d\xi = \frac{n+1}{5-n}\xi_1^3|\theta_1'|^2\,, \tag{B.13}$$

well-known in the theory of polytropes [41]. Physically, it corresponds to the virial theorem (3.75). From Eq.(B.11), in the limit $n \to 0$, we have

$$\frac{\omega^2}{4\pi G\rho_0} \sim \frac{9}{5n}\frac{\xi_1^5\omega_0^2}{\int_0^{\xi_1}\xi^4 d\xi} = \frac{9\omega_0^2}{n} = \frac{1}{n}\,. \tag{B.14}$$

We arrive to the same result by also considering Eq.(B.12): indeed we have

$$\frac{\omega^2}{4\pi G\rho_0} \sim \frac{9}{n}\frac{\int_0^{\xi_1}\theta\xi^2 d\xi}{\int_0^{\xi_1}\xi^4 d\xi} = \frac{15}{\xi_1^2}\Big(1-\frac{\xi_1^2}{10}\Big)\frac{1}{n} = \frac{1}{n}\,, \tag{B.15}$$

where, in the last passage, we have used the analytical[2] solution of $\theta = \theta(\xi)$ for the polytrope $n = 0$. For the polytropic EOS (B.1), the internal energy is given by

$$U = \int \rho \int_0^\rho \frac{P(\rho')}{\rho'^2}\, d\rho'\, d^3\vec{r} = \frac{1}{\gamma - 1} \int P\, d^3\vec{r}. \tag{B.17}$$

According to the virial theorem, we have

$$W + 3 \int P\, d^3\vec{r} = 0\,. \tag{B.18}$$

Therefore,

$$U = -\frac{W}{3(\gamma - 1)} = -\frac{n}{3} W = \frac{n}{5 - n} \frac{GM^2}{R}\,. \tag{B.19}$$

The free energy is defined by $F = U + W$: therefore, we have

$$F = \frac{\gamma - 4/3}{\gamma - 1} W = \Big(1 - \frac{n}{3}\Big) W = \frac{n - 3}{5 - n} \frac{GM^2}{R}\,. \tag{B.20}$$

According to the Poincaré argument, the system is stable if $F < 0$, i.e. if $\gamma > 4/3$. For $\gamma = 4/3$ we have $F = 0$. Using the Ledoux formula the pulsation is given by

$$\omega^2 = -3(\gamma - 1) \frac{F}{I}\,. \tag{B.21}$$

The speed of sound is defined by $c_s^2 = P'(\rho)$. For a polytropic EOS, we have

$$c_s^2 = \gamma \frac{P}{\rho}\,. \tag{B.22}$$

As a result, Eq.(B.21) can be written as

$$\omega^2 = -3\Big(3 - \frac{4}{\gamma}\Big) \frac{\langle c_s^2 \rangle}{\langle r^2 \rangle}\,, \tag{B.23}$$

where $\langle X \rangle = \int \rho X\, d^3\vec{r} / \int \rho\, d^3\vec{r}$. This is the time required for a sound wave to travel through the weighted radius $\langle r^2 \rangle^{1/2}$ with the weighted speed $\langle c_s^2 \rangle^{1/2}$.

[2]There exist analytical solutions of Eq.(B.4) only for $n = 0, 1$ and 5 (for the details of the calculations see Ref.[41]):

$$\begin{aligned} n = 0: &\qquad \theta = 1 - \frac{\xi^2}{6}\,, \\ n = 1: &\qquad \theta = \frac{\sin \xi}{\xi}\,, \\ n = 5: &\qquad \theta = \Big(1 + \frac{\xi^2}{3}\Big)^{-1/2}\,. \end{aligned} \tag{B.16}$$

C

Oppenheimer-Volkoff Equation of State

In this section we show that Oppenheimer-Volkoff[1] equation of state (see Ref.[150]) is a particular case of the EOS (3.110). Let be

$$\begin{aligned} \epsilon_{OV} &= K(\sinh t - t)\,, \\ P_{OV} &= \frac{K}{3}\Big[\sinh t - 8\sinh\Big(\frac{t}{2}\Big) + 3t\Big]\,, \end{aligned} \tag{C.1}$$

where K and t are defined by

$$K = \frac{\pi m^4 c^5}{4h^3} = \frac{3A}{4}\,, \qquad t = 4\log\Big(x + \sqrt{x^2+1}\Big) \qquad \Longleftrightarrow \qquad x = \sinh\Big(\frac{t}{4}\Big)\,, \tag{C.2}$$

[A and x are defined by Eqs.(3.30) and (3.6), respectively]. For the moment, let us consider only the mass-energy density ϵ. Substituting t in Eq.(3.110) and also imposing $q = 1$, we get

$$\epsilon_{CT} = A\bigg\{8\sinh^3\Big(\frac{t}{4}\Big)\cosh\Big(\frac{t}{4}\Big) - \sinh\Big(\frac{t}{4}\Big)\cosh\Big(\frac{t}{4}\Big)\Big[2\sinh^3\Big(\frac{t}{4}\Big) - 3\Big] - \frac{3t}{4}\bigg\}\,. \tag{C.3}$$

Now, introducing $z = t/4$ and rearranging the terms, we have

$$\begin{aligned} \epsilon_{CT} &= A\Big[3\sinh z\cosh z\,(2\sinh^2 z + 1) - 3z\Big] = 3A\Big[\frac{1}{2}\sinh(2z)(\cosh^2 z + \sinh^2 z) - z\Big] = \\ &= \frac{3A}{2}\Big[\sinh(2z)\cosh(2z) - 2z\Big] = \frac{3A}{4}\Big[\sinh(4z) - 4z\Big] = K(\sinh t - t)\,, \end{aligned} \tag{C.4}$$

where, in the last passage, we have reintroduced t and used the first equality of Eq.(C.2). Eq.(3.110) (for $q = 1$) thus coincides with the first of Eq.(C.1). Concerning the pressure, we proceed in a different way. Let us consider

[1] In this Section "OV" stands for Oppenheimer & Volkoff and "CT" for Chandrasekhar & Tooper.

$$\begin{aligned}\sinh t &= \sinh\Big(4\cdot\frac{t}{4}\Big) = 4\sinh\Big(\frac{t}{4}\Big)\cosh\Big(\frac{t}{4}\Big)\Big[\cosh^2\Big(\frac{t}{4}\Big)+\sinh^2\Big(\frac{t}{4}\Big)\Big]\,,\\ \sinh\Big(\frac{t}{2}\Big) &= \sinh\Big(2\cdot\frac{t}{4}\Big) = 2\sinh\Big(\frac{t}{4}\Big)\cosh\Big(\frac{t}{4}\Big)\,.\end{aligned} \tag{C.5}$$

Substituting the equalities (C.5) in the second of (C.1) and using Eq.(C.2), we have

$$\begin{aligned}P_{OV} &= \frac{K}{3}\left\{4\sinh\Big(\frac{t}{4}\Big)\cosh\Big(\frac{t}{4}\Big)\Big[\cosh^2\Big(\frac{t}{4}\Big)+\sinh^2\Big(\frac{t}{4}\Big)\Big]-16\sinh\Big(\frac{t}{4}\Big)\cosh\Big(\frac{t}{4}\Big)+3t\right\} =\\ &= \frac{4K}{3}\left[x\sqrt{x^2+1}(2x^2-3)+3\log\Big(x+\sqrt{x^2+1}\Big)\right] = Af(x)\,,\end{aligned} \tag{C.6}$$

that corresponds to the second of Eqs.(3.110).

D

Evaluation of Λ_{max} and Λ'_{max} in the Fully Degenerate Limit

In the limit of low temperatures, the Fermi - Dirac distribution function (2.29) becomes a step function delimited by its natural cutoff, the Fermi energy ϵ_F [see also Eq.(1.22)]. Consequently, the thermodynamic quantities (2.54), (2.55) and (2.56) become

$$\tilde{n} = \frac{\Phi\sqrt{\Phi}}{3\pi^2}\,, \tag{D.1}$$

$$\tilde{\epsilon} = \frac{(2\Phi+1)\sqrt{\Phi(\Phi+1)} - \log(\sqrt{\Phi}+\sqrt{\Phi+1})}{8\pi^2}\,, \tag{D.2}$$

$$\tilde{P} = \frac{(2\Phi-3)\sqrt{\Phi(\Phi+1)} + 3\log(\sqrt{\Phi}+\sqrt{\Phi+1})}{24\pi^2}\,, \tag{D.3}$$

where $y_F = \sqrt{\Phi}$ (y_F here represents the dimensionless Fermi momentum[1]). Analogous to Sec. 3.3.1, the integration of the TOV system is arrested at the point $r = R$ where the density vanishes, implying $\Phi(R) = 0$ [see Eq.(D.1)]. The result of the numerical integration is depicted in Fig. D.1. According to the formalism outlined in Chap. 2, the values of radius, mass and particles number at the OV limit are, respectively, $\tilde{R}_{OV} = 3.3569$, $\tilde{M}_{OV} = 0.38426$ and $\tilde{N}_{OV} = 0.39853$ (moreover $\Phi_0 = 0.69502$). Are these values consistent with those obtained in Sec. 3.3? Yes, they are. Recalling the definitions of r_* [for $g = 2$, see Eq.(2.57)] and a_{rel} [for $q = 1$, see Eq.(3.111)] we have

$$a_{rel} = \frac{c^2}{(32\pi GA)^{1/2}} = \sqrt{\frac{3h^3}{32\pi^2 Gm^4 c}} = \sqrt{\frac{3\hbar^3}{4\pi Gm^4 c}} = \frac{\sqrt{3\pi}}{2} r_* \tag{D.4}$$

[1]The definition of y_F corresponds to that of x in Eq.(3.110).

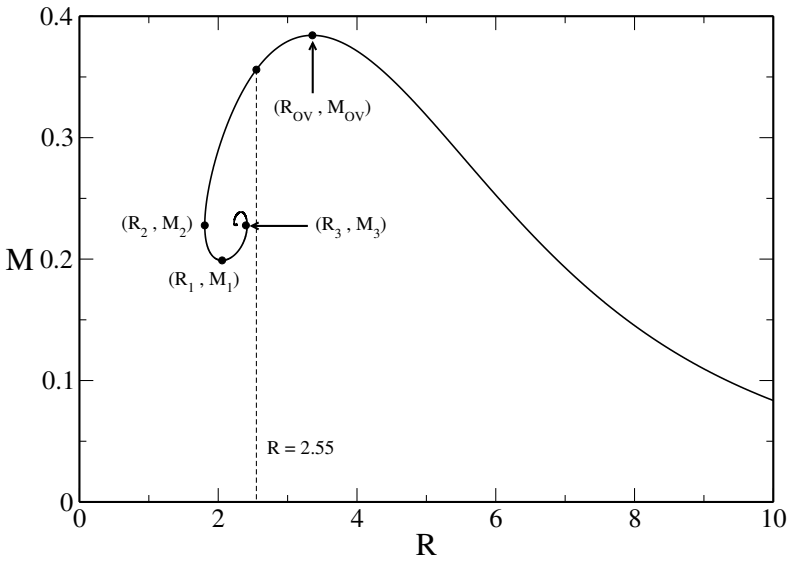

Figure D.1: *Total radius versus total mass for fermionic configurations in the degenerate limit. The three turning points (R_{OV}, M_{OV}) = (3.3569, 0.38426), (R_1, M_1) = (2.0556, 0.19893), (R_2, M_2) = (1.8063, 0.22776) and (R_3, M_3) = (2.3986, 0.22776) are also indicated. The line level $R = 2.55$ represents an example of application of the Thomas Fermi model to the degenerate configurations (see Appendix E).*

[we have used the definition of A, see Eq.(3.30)]. Combining Eqs.(3.111) and (2.57), we get

$$\tilde{r} = \frac{r}{r_*} = \frac{\sqrt{3\pi}}{2}\frac{r}{a_{rel}} = \frac{\sqrt{3\pi}}{2}\eta\,. \tag{D.5}$$

By applying Eq.(D.5) to the expression of the mass-energy (2.59), we obtain

$$\begin{aligned}\tilde{M} &= \int_0^{\tilde{R}} 4\pi\tilde{\epsilon}\tilde{r}^2 d\tilde{r} = \frac{\sqrt{3\pi}}{2}\int_0^{\eta_1}\frac{3[(2\Phi+1)\sqrt{\Phi(\Phi+1)}-\log(\sqrt{\Phi}+\sqrt{\Phi+1})]}{8}\eta^2 d\eta = \\ &= \frac{\sqrt{3\pi}}{2}\int_0^{\eta_1}\Big[x^3+\frac{g(x)}{8}\Big]\eta^2 d\eta = \frac{\sqrt{3\pi}}{2}v_1\,,\end{aligned} \tag{D.6}$$

where we have used Eq.(D.2) and $x = \sqrt{\Phi}$. For what concerns the baryonic number, we have

$$\begin{aligned}\tilde{N} &= \int_0^{\tilde{R}} 4\pi\tilde{n}\tilde{r}^2\Big(1-\frac{2\tilde{M}_r}{\tilde{r}}\Big)^{-1/2}d\tilde{r} = \frac{4}{3\pi}\Big(\frac{\sqrt{3\pi}}{2}\Big)^3\int_0^{\eta_1}\Phi\sqrt{\Phi}\eta^2\left(1-2\frac{\frac{\sqrt{3\pi}}{2}v}{\frac{\sqrt{3\pi}}{2}\eta}\right)^{-1/2}d\eta = \\ &= \frac{\sqrt{3\pi}}{2}\int_0^{\eta_1}x^3\eta^2\Big(1-\frac{2v}{\eta}\Big)^{-1/2}d\eta = \frac{\sqrt{3\pi}}{2}\tilde{N}_{B1}\,.\end{aligned} \tag{D.7}$$

Now, if we take the values at the OV limit obtained in Sec. 3.3, we have

$$\begin{aligned}\tilde{R}_{OV} &= \frac{\sqrt{3\pi}}{2}\eta_1 = 3.3309\,,\\ \tilde{M}_{OV} &= \frac{\sqrt{3\pi}}{2}v_1 = 0.38427\,,\\ \tilde{N}_{OV} &= \frac{\sqrt{3\pi}}{2}N_{B1} = 0.39854\,,\end{aligned} \tag{D.8}$$

which are in perfect agreement with the values previously listed (moreover $\Phi_0 = x_0^2 = 0.69222$)[2]. In Fig. D.1, we have represented the mass radius relation: each point of the curve is identified by the pair (R, M). If we want to evaluate the binding energy associated with the points forming the curve, we cannot apply the definition (A.2) of Λ, because of the presence of the box radius[3]. To solve this problem, we define

$$\Lambda_D = \frac{\Lambda}{\tilde{R}} = \frac{\tilde{N} - \tilde{M}}{\tilde{N}^2}\,. \tag{D.9}$$

In Fig. D.2 we have represented Λ_D as a function of the baryon number N. If we fix a generic line level, we obtain one (or more) intersection points, according to the value of N. If we consider the case $N_{spec} < N_1$, we obtain one only intersection which identifies a critical value of energy. Looking at the figure, we see that this value $\Lambda_D(N_{spec})$ represents a limit, that is, the system cannot reach a value of energy larger than $\Lambda_D(N_{spec})$.

In Chap. 5 we have seen that, when the fermionic system is cooled down below the transition temperature, the condensed phase emerges. In this case, the fermionic system takes the "core-halo" structure and its structure is equivalent to that of a degenerate fermionic configuration. Further, the condensed phase is delimited by the energy Λ_{max} which represents the maximum value achievable by Λ. As previously discussed, the maximal accessible energy for a degenerate configuration corresponds to Λ_D. This implies that

$$\Lambda_D = \frac{\Lambda_{max}}{R}\,. \tag{D.10}$$

Thanks to this result, we can get a "theoretical" evaluation of Λ_{max} by means of Fig. D.2, for any value of $N_{spec} < N_{OV}$. We stress that the function Λ_D is universal, because independent of the cavity radius R. If we now consider a line level $N_1 < N_{spec} < N_2$, we obtain two intersections, corresponding to two critical values of the energy Λ_D. As we have seen, the intersection with the upper branch corresponds to the energy Λ_{max}. The intersection with the lower branch corresponds instead to Λ'_{max}.

[2]The biggest difference found concerns the radius R_{OV}: we have a discard of 0.78%.

[3]We remind that each point of the curve has *its own radius*. The radius in Eq.(A.2) is the cavity radius.

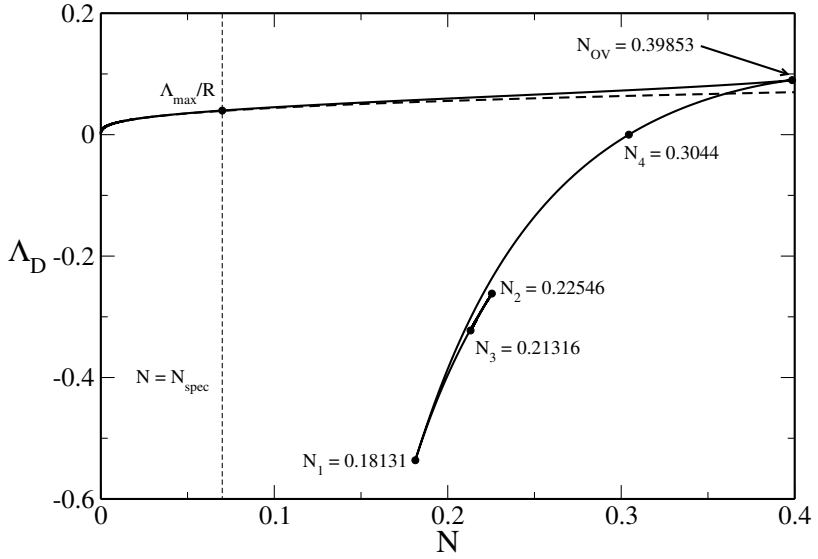

Figure D.2: *Normalized binding energy Λ_D versus the total particles number* N. *The points N_1, N_2 and N_3 represent specific values of N related to the number of intersection points that a generic line level can identify (an example is also shown). For $N = N_1$ the series of equilibria displays the secondary unstable branch delimited by the critical energy Λ'_{max}. N_2 and N_3 are associated with the appearance (and disappearance) of (unstable) branches of higher order. N_4, by contrast, is the value of N corresponding to $\Lambda = 0$ and N_{OV} indicates the OV limit. The dashed line is the nonrelativistic approximation* (D.22).

This explains the reason why in Newtonian gravity the series of equilibria do not display this secondary branch: its origin is exclusively relativistic.

For a line level $N_2 < N_{spec} < N_3$, there are three intersection points corresponding to the critical energies Λ_{max}, Λ'_{max} and Λ''_{max}. As the reader can understand, for $N \to 0.21585$[4], the number of intersection points increases and we obtain several critical values of Λ_D, corresponding to unstables branches in the caloric curve. In the limit $N \to N_{OV}$, Λ_{max} and Λ'_{max} can be expressed by the approximated relations

$$\begin{aligned} \Lambda_{D\,max} &\sim 0.0898 - 0.2739\,(N_{OV} - N)^{1/2}\,, \\ \Lambda'_{D\,max} &\sim 0.0898 - 0.3708\,(N_{OV} - N)^{1/2}\,. \end{aligned} \tag{D.11}$$

The Newtonian gravity is recovered for $\Phi \to 0$ (equivalently $N \to 0$). In this limit, the thermodynamic quantities (D.1), (D.2) and (D.3) become

[4]This value of N corresponds to the point at the center of the spiral of the mass-radius relation depicted in Fig. D.1.

$$\tilde{n} = \frac{\Phi^{3/2}}{3\pi^2}\,, \tag{D.12}$$

$$\tilde{\epsilon} \sim \frac{\Phi^{3/2}}{3\pi^2} = \tilde{n}\,, \tag{D.13}$$

$$\tilde{P} =\sim \frac{\Phi^{5/2}}{15\pi^2} = \frac{\pi\sqrt[3]{9\pi}}{5}\tilde{n}^{5/3}\,. \tag{D.14}$$

Eq.(D.14) shows that the EOS is that of a polytropic with $n = 3/2$ (or $\gamma = 5/3$, see also Sec. 3.1). Furthermore, Eq.(D.13) implies $\tilde{M} \simeq \tilde{N}$, so in the following we write $\tilde{N}$ instead of $\tilde{M}$. The TOV system (2.59) becomes

$$\begin{aligned} &\frac{d\Phi}{d\tilde{r}} \sim -\frac{2\tilde{N}_r}{\tilde{r}^2}\,, \\ &\frac{d\tilde{N}_r}{d\tilde{r}} \sim 4\pi\tilde{n}\,\tilde{r}^2 = \frac{4\Phi^{3/2}}{3\pi}\,\tilde{r}^2\,. \end{aligned} \tag{D.15}$$

Isolating the mass on the r.h.s of the first of (D.15), deriving both members and substituting the second of (D.15), one has

$$\frac{1}{\tilde{r}^2}\frac{d}{d\tilde{r}}\Big(\tilde{r}^2\frac{d\Phi}{d\tilde{r}}\Big) = -\frac{8\Phi^{3/2}}{3\pi} \tag{D.16}$$

with the conditions $\Phi(0) = \Phi_0$ and $\Phi'(0) = 0$. By defining $\Phi = \Phi_0\,\theta$ and $\tilde{r} = a\xi$ we get

$$\frac{1}{\xi^2}\frac{d}{d\xi}\Big(\xi^2\frac{d\theta}{d\xi}\Big) = -\theta^{3/2} \qquad \text{where} \qquad a = \sqrt[4]{\frac{9\pi^2}{64\Phi_0}} \tag{D.17}$$

which corresponds to the Lane - Emden equation for the polytrope $n = 3/2$, with the initial conditions $\theta(0) = 1$ and $\theta'(0) = 0$. The radius of the configuration solution of Eq.(D.16) is

$$\tilde{R} = a\xi_1 = \frac{\xi_1\sqrt{3\pi}}{2\sqrt{2}}\Phi_0^{-1/4} \simeq 3.96579\,\Phi_0^{-1/4} \tag{D.18}$$

where $\xi_1 = 3.65375$ is the radius solution of Eq.(D.17). The total mass is

$$\tilde{N} = \int_0^{\tilde{R}} 4\pi\tilde{n}\tilde{r}^2 d\tilde{r} = \frac{4\Phi_0^{3/2}a^3}{3\pi}\int_0^{\xi_1}\theta^{3/2}\xi^2 d\xi = \frac{M_{3/2}}{4}\sqrt{\frac{3\pi}{2}}\,\Phi_0^{3/4} \simeq 1.47292\,\Phi_0^{3/4} \tag{D.19}$$

where $M_{3/2} = 2.71406$ is the total mass of the configuration solution of Eq.(D.17). The previous relation can be inverted, in order to obtain Φ_0 as a function of $\tilde{N}$:

$$\Phi_0 = \Big(\frac{4\sqrt{2}}{M_{3/2}\sqrt{3\pi}}\Big)^{4/3}\tilde{N}^{4/3} \simeq 0.59671\,\tilde{N}^{4/3}\,. \tag{D.20}$$

Thanks to the previous equation, the radius (D.18) can be expressed as a function of the total mass

$$\tilde{R} = a\xi_1 = \frac{\xi_1\sqrt{3\pi}}{2\sqrt{2}}\Phi_0^{-1/4} = \frac{\xi_1 M_{3/2}^{1/3}}{2}\Big(\frac{3\pi}{2}\Big)^{2/3}\tilde{N}^{-1/3} \simeq 4.51221\, N^{-1/3} \tag{D.21}$$

As it is known (see Sec. 3.2.3), the binding energy $E_b = -F$ so the expression of Λ_D becomes

$$\Lambda_D = \frac{\Lambda}{\tilde{R}} = \frac{\tilde{F}}{\tilde{N}^2} = \frac{3\tilde{N}^2}{7\tilde{N}^2\tilde{R}} = \frac{3}{7\tilde{R}} = \frac{3}{7}\frac{2}{\xi_1 M_{3/2}^{1/3}}\Big(\frac{2}{3\pi}\Big)^{2/3}\tilde{N}^{1/3} \simeq 0.09498\,\tilde{N}^{1/3} \tag{D.22}$$

which is represented by the dashed line in Fig. D.2.

E

Spatial Confinement in the Fully Degenerate Limit

The TOV system (2.59) can be integrated for *every* value of the box radius, even smaller than R_{OV}. In this Section we study the case of a degenerate fermionic gas bound in a box. Let us start by considering the mass-radius relation $M = M(R)$ shown in Fig. D.1. The vertical line $R = 2.55$ represents an example of the application of the Thomas-Fermi model. For $R \geq R_{OV}$, we are placed on the stable part of the OV limiting curve and the thermodynamics, for these radii, is the same studied in Chap. 5. There exists one only solution between the OV curve and the line level $R = R_{spec}$, which only effect is to "cut" the mass-radius relation.

By contrast, if we consider the case $R < R_{OV}$ (see the vertical line in Fig. D.1), we see that the mass-radius relation has a different limiting configuration, identified by the line level and the OV curve. More precisely, if the box radius is smaller than the OV radius, the system is not able to reach the usual OV limit but an "adjusted" OV limit, which value is $M_{lim} = M(R < R_{OV}) < M_{OV}$. If we decrease the value of the cavity radius, we can see that the line level can intersect the OV curve in more than one point for $R_2 < R_{spec} < R_3$. For $R_{spec} < R_2$ there are not intersections between the line level and the OV curve.

The consequences of the application of the Thomas-Fermi model can be seen in Fig. E.1, where we have represented the function $N = N(\Phi_0)$. Let us firstly consider the case of small radii (more precisely $R < R_2$; see the left panel in Fig. E.1), corresponding to the absence of intersection between the line level and the OV curve. As we see, the first four curves represented in the figure are detached by the OV curve. This shows that every box of radius $R < R_2$ has *its own OV limiting curve*, characterized

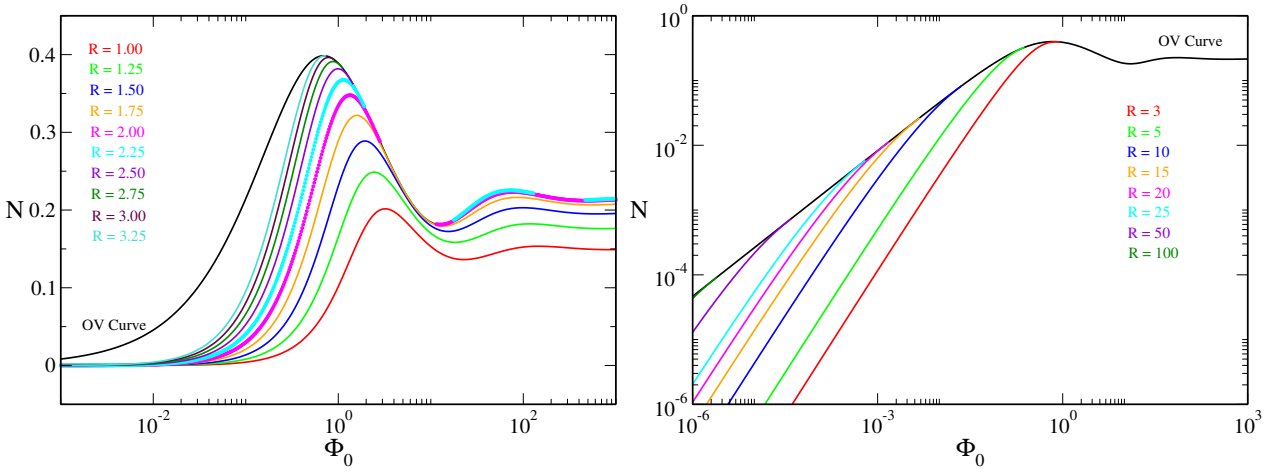

Figure E.1: *Total particle number versus Φ_0, for fermionic degenerate configurations placed within a box of radius $R < R_{OV}$ (left panel) and $R > R_{OV}$ (right panel). The OV curve is represented by the black line.*

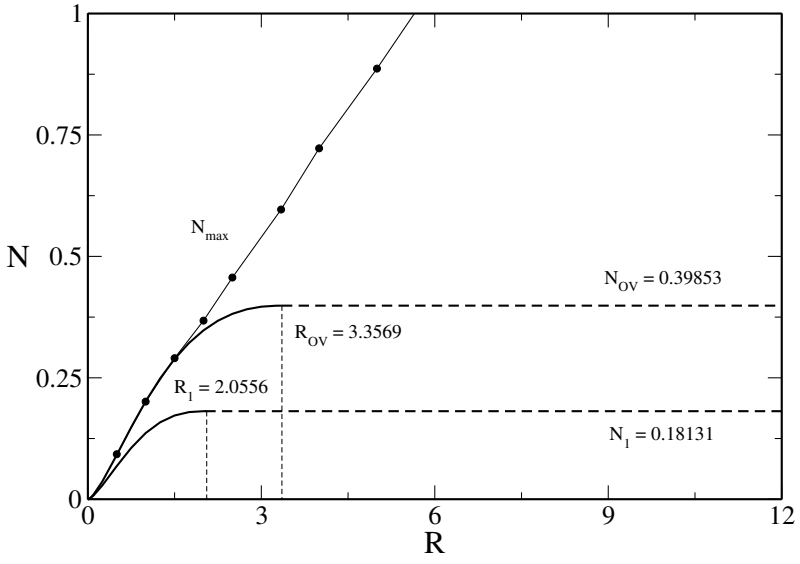

Figure E.2: *Representation of the functions $N_{max} = N_{max}(R)$, $N_{OV}^{box} = N_{OV}^{box}(R)$ and $N_1^{box} = N_1^{box}(R)$. The three functions tend to zero in the limit $R \to 0$.*

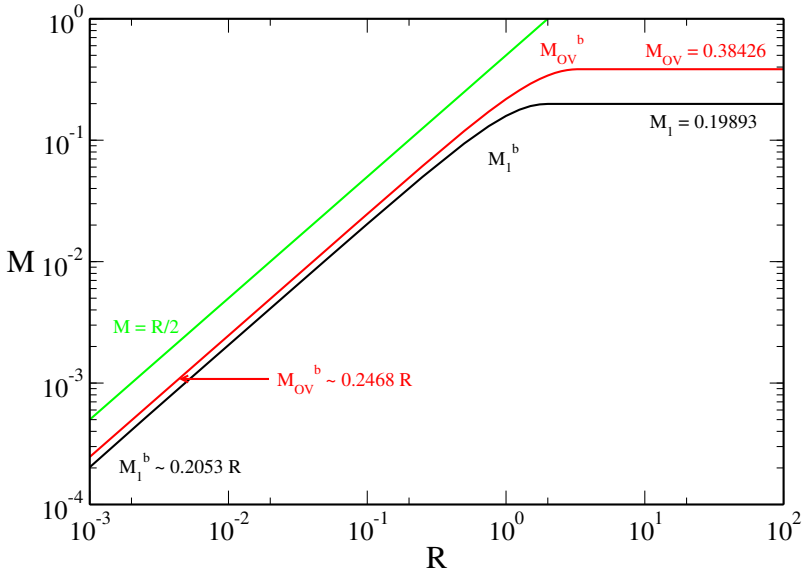

Figure E.3: *The same as the preceding figure, but representing the total mass. The black line represents the mass associated with N_1^{box}, the red one the mass corresponding to N_{OV}^{box}. The green line represents the black hole limit $M = R/2$. For small values of the radius, the three functions are infinitesimal. It is remarkable the fact that, from a physical point of view, the degenerate encapsulated configurations can exist.*

by a critical point, analogous to the usual OV limit. The typical values are, of course, smaller than the usual OV limit.

The first four curves (red, green, blue and orange line) in Fig. E.1 do not intersect the OV curve in any point, although they present the same behaviour: monotonic increase until the achievement of the maximum (the "own" OV limit) followed by several and several oscillations.

For $R_2 \leq R < R_3$ we observe a changement of regime, because the line level intersects the OV curve in more than one point. If, in particular, we consider the case $R = 2$ (magenta line in Fig. E.1), we see that the curve $N = N(\Phi_0)$ is made by two separated parts, that create a "hole" in the curve. In reality, the "hole" is compensated by the OV curve (in the figure the black line is hidden by the others). From a physical point of view, this means that the system "stabilizes" only reaching the OV curve, although the cavity radius is smaller than R_{OV}.

The "hole-space" solution disappears for $R = R_3$ (corresponding to the fourth turning point of the spiral, see Fig. D.1). Further, by still looking at Fig. E.1, we observe that the curves obtained for $R > R_3$ do not present the local minimum identified by the point N_1 (see Appendix D). This feature is explained by virtue of fact that the line level does not intersect anymore the OV curve in the region of the spiral. The right panel of Fig. E.1 shows the case $R > R_{OV}$ (we have kept the curve obtained for

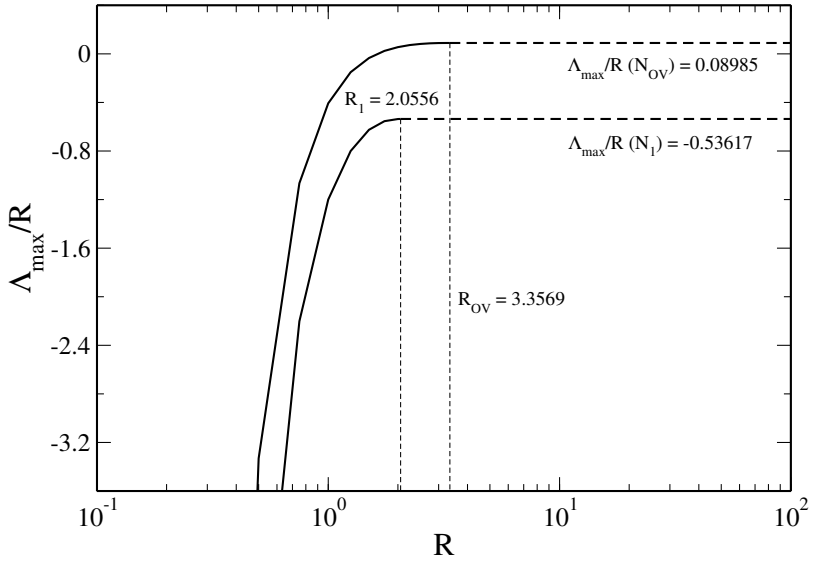

Figure E.4: Λ_{max} *and* Λ'_{max}*, as a function of the radius.*

$R = 3$ for comparison). The reader can easily see that the space solution is destined to progressively reduce. The degenerate limiting curve recovers the OV limiting curve and the Thomas-Fermi model gives the same results obtained in the preceding Section for $T = 0$.

In Fig. E.2 we have represented N_{OV}^{box} (i.e. the OV limiting configuration delimited by the box) as a function of R. The reader can see that the deviations from the OV limiting configuration start at $R = R_{OV}$. Moreover, for decreasing values of the box radius, N_{OV}^{box} decreases as well and converges to zero in the limit $R \to 0$. The curve N_1^{box} presents the same behaviour as N_{OV}^{box}. The deviations from the usual OV limiting curve start for $R = R_1$. In the limit $R \to 0$ we see that $N_1^{box} \to 0$. To have a more precise idea, we have also plotted the function $N_{max} = N_{max}(R)$. We can observe a deviation from the usual Boltzmannian behaviour (the scaling N/R is not anymore preserved).

Since we consider spheres having $R < R_{OV}$ or, also, very small values of R, the question about the physical pertinence of these solutions naturally arises. We can see if these configurations can or not physically exist, by considering the Schwarzschild radius R_S associated with each value of M intersected by the line level R_{spec}. For this reason, in Fig. E.3, we have represented the total mass, associated with N_{OV}^{box} and N_1^{box}, as a function of the radius R (the BH limit, represented by the green line, is shown for comparison). Looking at the figure, we see that the black and the red lines, i.e. $M(N_{OV}^{box})$ and $M(N_1^{box})$ respectively, are parallel with respect to the BH line. This implies that we never reach the Schwarzschild limit and that the solutions found represent physical states. From the figure it is evident a scaling property in the limit $R \to 0$. We have

$$
\begin{aligned}
N_{OV}^{b} &\sim 0.3104 R^{3/2}\,, \\
N_{1}^{b} &\sim 0.2492 R^{3/2}\,, \\
M_{OV}^{b} &\sim 0.2468 R\,, \\
M_{1}^{b} &\sim 0.2053 R\,.
\end{aligned}
\tag{E.1}
$$

Finally, in Fig. E.4, we have plotted the normalized binding energies associated with the points N_{OV}^{box} and N_{1}^{box}. Differently from the baryon number and the total mass, Λ_{max}/R and Λ'_{max}/R diverge in the limit $R \to 0$ [see Eq.(D.9)].

Bibliography

[1] M. Abramowitz and I.A. Stegun. *Handbook of mathematical functions: with formulas, graphs, and mathematical tables*, volume 55. Courier Corporation, 1964.

[2] W. Anderson. Über die Grenzdichte der Materie und der Energie. *Zeit. f. Phys.*, 56:851–856, November 1929.

[3] J. Antoniadis, P. C. C. Freire, N. Wex, T. M. Tauris, R. S. Lynch, M. H. van Kerkwijk, M. Kramer, C. Bassa, V. S. Dhillon, T. Driebe, J. W. T. Hessels, V. M. Kaspi, V. I. Kondratiev, N. Langer, T. R. Marsh, M. A. McLaughlin, T. T. Pennucci, S. M. Ransom, I. H. Stairs, J. van Leeuwen, J. P. W. Verbiest, and D. G. Whelan. A Massive Pulsar in a Compact Relativistic Binary. *Science*, 340:448, April 2013.

[4] V. A. Antonov. Remarks on the Problem of Stability in Stellar Dynamics. *Sov. Astr.*, 4:859, April 1961.

[5] V. A. Antonov. *Solution of the problem of stability of stellar system Emden's density law and the spherical distribution of velocities*. 1962.

[6] V. A. Antonov. Most probable phase distribution in spherical star systems and conditions for its existence. In J. Goodman and P. Hut, editors, *Dynamics of Star Clusters*, volume 113 of *IAU Symposium*, page 525, 1985.

[7] V. A. Antonov. On the Instability of Stationary Spherical Models with Purely Radial Motion. In P. T. de Zeeuw, editor, *Structure and Dynamics of Elliptical Galaxies*, volume 127 of *IAU Symposium*, page 549, 1987.

[8] V. A. Antonov. Solution of the Problem of Stability of a Stellar System with Emden's Density

Law and a Spherical Distribution of Velocities. In P. T. de Zeeuw, editor, *Structure and Dynamics of Elliptical Galaxies*, volume 127 of *IAU Symposium*, page 531, 1987.

[9] R. Antonucci. Unified models for active galactic nuclei and quasars. *Ann. Rev. Astron. Astrophys.*, 31:473–521, 1993.

[10] K. Arun, S. B. Gudennavar, and C. Sivaram. Dark matter, dark energy, and alternate models: A review. *Advances in Space Research*, 60:166–186, July 2017.

[11] M. Axenides, G. Georgiou, and Z. Roupas. Gravothermal catastrophe with a cosmological constant. *Phys. Rev. D*, 86(10):104005, November 2012.

[12] M. Axenides, G. Georgiou, and Z. Roupas. Gravitational instabilities of isothermal spheres in the presence of a cosmological constant. *Nucl. Phys. B*, 871:21–51, June 2013.

[13] W. Baade and F. Zwicky. On Super-novae. *Proc. Nat. Ac. Sci.*, 20:254–259, May 1934.

[14] W. Baade and F. Zwicky. Remarks on Super-Novae and Cosmic Rays. *Phys. Rev.*, 46:76–77, July 1934.

[15] T. Banks, W. Fischler, A. Kashani-Poor, R. McNees, and S. Paban. Entropy of the stiffest stars. *Class. Quant. Grav.*, 19:4717–4728, September 2002.

[16] J. M. Bardeen, B. Carter, and S. W. Hawking. The four laws of black hole mechanics. *Comm. Math. Phys.*, 31:161–170, June 1973.

[17] H. Baumgardt, G. De Marchi, and P. Kroupa. Evidence for Primordial Mass Segregation in Globular Clusters. *Astrophys. J.*, 685:247–253, September 2008.

[18] J. D. Bekenstein. Black Holes and Entropy. *Phys. Rev. D*, 7:2333–2346, April 1973.

[19] S. J. Bell and A. Hewish. Angular Size and Flux Density of the Small Source in the Crab Nebula at 81.5 Mc/s. *Nat.*, 213:1214–1216, March 1967.

[20] M. J. Benacquista and J. M. B. Downing. Relativistic Binaries in Globular Clusters. *Liv. Rev. in Rel.*, 16:4, March 2013.

[21] G. Bertone. *Particle Dark Matter : Observations, Models and Searches*. Cambridge University Press, 2010.

[22] N. Bilić, F. Munyaneza, and R. D. Viollier. Stars and halos of degenerate relativistic heavy-neutrino and neutralino matter. *Phys. Rev. D*, 59(2):024003, January 1999.

[23] N. Bilić and R. D. Viollier. Gravitational phase transition of fermionic matter. *Phys. Lett. B*, 408:75–80, February 1997.

[24] N. Bilić and R. D. Viollier. General-Relativitstic Thomas-Fermi Model. *Gen. Rel. Grav.*, 31:1105, August 1999.

[25] N. Bilić and R. D. Viollier. Gravitational phase transition of fermionic matter in a general-relativistic framework. *Eur. Phys. J. C*, 11:173–180, November 1999.

[26] J. Binney and S. Tremaine. *Galactic Dynamics: 2nd Edition*. Princeton University Press, 2008.

[27] G. S. Bisnovatyi-Kogan and M. Merafina. Self-Gravitating Gas Spheres in a Box and Relativistic Clusters: Relation between Dynamical and Thermodynamical Stability. *Astrophys. J*, 653:1445–1453, December 2006.

[28] G. S. Bisnovatyi-Kogan, M. Merafina, R. Ruffini, and E. Vesperini. Stability of dense stellar clusters against relativistic collapse. *Astrophys. J*, 414:187–199, September 1993.

[29] G. S. Bisnovatyi-Kogan, M. Merafina, R. Ruffini, and E. Vesperini. Stability of Dense Stellar Clusters against Relativistic Collapse. II. Maxwellian Distribution Functions with Different Cutoff Parameters. *Astrophys. J*, 500:217, June 1998.

[30] W. B. Bonnor. Boyle's Law and gravitational instability. *Mon. Not. R. Astron. Soc.*, 116:351, 1956.

[31] L. Bonolis. Stellar structure and compact objects before 1940: Towards relativistic astrophysics. *Eur. Phys. J. H*, 42, June 2017.

[32] H. Bradt. *Astrophysics Processes*. September 2008.

[33] R. H. Brans, C. & Dicke. Mach's Principle and a Relativistic Theory of Gravitation. *Phys. Rev.*, 124:925–935, November 1961.

[34] H. A. Buchdahl. General Relativistic Fluid Spheres. *Phys. Rev.*, 116:1027–1034, November 1959.

[35] A. Campa, T. Dauxois, D. Fanelli, and S. Ruffo. *Physics of Long-Range Interacting Systems*. Oxford University Press, 2014.

[36] A. Campa, T. Dauxois, and S. Ruffo. Statistical mechanics and dynamics of solvable models with long-range interactions. *Phys. Rep.*, 480:57–159, September 2009.

[37] S. Capozziello and V. Faraoni. *Beyond Einstein Gravity: A Survey of Gravitational Theories for Cosmology and Astrophysics*. Springer Science+Business Media B.V., 2011.

[38] M. Catelan and H. A. Smith. *Pulsating Stars*. Wiley, 2015.

[39] M. Champion, A. Alastuey, T. Dauxois, and S. Ruffo. Validity conditions of the hydrostatic approach for self-gravitating systems: a microcanonical analysis. *J. Phys. A: Math. Theor.*, 47(22):225001, June 2014.

[40] S. Chandrasekhar. The Maximum Mass of Ideal White Dwarfs. *Astrophys. J*, 74:81, July 1931.

[41] S. Chandrasekhar. *An introduction to the study of stellar structure*. Chicago University Press, 1939.

[42] S. Chandrasekhar. The Dynamical Instability of Gaseous Masses Approaching the Schwarzschild Limit in General Relativity. *Astrophys. J*, 140:417, August 1964.

[43] S. Chandrasekhar and R. F. Tooper. The Dynamical Instability of the White-Dwarf Configurations Approaching the Limiting Mass. *Astrophys. J*, 139:1396, May 1964.

[44] P.-H. Chavanis. On the 'coarse-grained' evolution of collisionless stellar systems. *Mon. Not. R. Astron. Soc.*, 300:981–991, November 1998.

[45] P. H. Chavanis. Gravitational instability of finite isothermal spheres. *Astron. Astrophys.*, 381:340–356, January 2002.

[46] P. H. Chavanis. Gravitational instability of finite isothermal spheres in general relativity. Analogy with neutron stars. *Astron. Astrophys.*, 381:709–730, January 2002.

[47] P.-H. Chavanis. Phase transitions in self-gravitating systems: Self-gravitating fermions and hard-sphere models. *Phys. Rev. E*, 65(5):056123, May 2002.

[48] P. H. Chavanis. Gravitational instability of isothermal and polytropic spheres. *Astron. Astrophys.*, 401:15–42, April 2003.

[49] P.-H. Chavanis. Generalized Fokker-Planck equations and effective thermodynamics. *Phys. A*, 340:57–65, September 2004.

[50] P.-H. Chavanis. Generalized thermodynamics and kinetic equations: Boltzmann, Landau, Kramers and Smoluchowski. *Phys. A*, 332:89–122, February 2004.

[51] P.-H. Chavanis. Statistical mechanics and thermodynamic limit of self-gravitating fermions in D dimensions. *Phys. Rev. D*, 69(6):066126, June 2004.

[52] P. H. Chavanis. On the lifetime of metastable states in self-gravitating systems. *Astron. Astrophys.*, 432:117–138, March 2005.

[53] P. H. Chavanis. Phase Transitions in Self-Gravitating Systems. *Int. J. Mod. Phys. B*, 20:3113–3198, 2006.

[54] P.-H. Chavanis. White dwarf stars in D dimensions. *Phys. Rev. D*, 76(2):023004, July 2007.

[55] P. H. Chavanis. Relativistic stars with a linear equation of state: analogy with classical isothermal spheres and black holes. *Astron. Astrophys.*, 483:673–698, June 2008.

[56] P.-H. Chavanis. Relativistic self-gravitating Bose-Einstein condensates and cold baryons with a stiff equation of state. *Eur. Phys. J. Plus*, 130:181–205, November 2015.

[57] P.-H. Chavanis and T. Harko. Bose-Einstein condensate general relativistic stars. *Phys. Rev. D*, 86(6):064011, September 2012.

[58] P.-H. Chavanis, M. Lemou, and F. Méhats. Models of dark matter halos based on statistical mechanics: The classical King model. *Phys. Rev. D*, 91(6):063531, March 2015.

[59] P.-H. Chavanis, M. Lemou, and F. Méhats. Models of dark matter halos based on statistical mechanics: The fermionic King model. *Phys. Rev. D*, 92(12):123527, December 2015.

[60] P. H. Chavanis and M. Rieutord. Statistical mechanics and phase diagrams of rotating self-gravitating fermions. *Astron. Astrophys.*, 412:1–17, December 2003.

[61] P.-H. Chavanis, C. Rosier, and C. Sire. Thermodynamics of self-gravitating systems. *Phys. Rev. D*, 66(3):036105, September 2002.

[62] P.-H. Chavanis and C. Sire. Anomalous diffusion and collapse of self-gravitating Langevin particles in D dimensions. *Phys. Rev. E*, 69(1):016116, January 2004.

[63] P.-H. Chavanis and J. Sommeria. Degenerate equilibrium states of collisionless stellar systems. *Mon. Not. Astron. Soc.*, 296:569–578, May 1998.

[64] P. Coles and F. Lucchin. *Cosmology: The Origin and Evolution of Cosmic Structure, Second Edition*. July 2002.

[65] G. W. Collins. *The Fundametals of Stellar Astrophysics*. Freeman, July 1989.

[66] K. J. Daniel, D. C. Heggie, and A. L. Varri. An approximate analytic model of a star cluster with potential escapers. *Mon. Not. Roy. Astron. Soc.*, 468:1453–1473, June 2017.

[67] U. Das and B. Mukhopadhyay. New Mass Limit of White Dwarfs. *Int. J. Mod. Phys. D*, 22:42004, September 2013.

[68] U. Das, B. Mukhopadhyay, and A. R. Rao. A Possible Evolutionary Scenario of Highly Magnetized Super-Chandrasekhar White Dwarfs: Progenitors of Peculiar Type Ia Supernovae. *Astrophys. J.*, 767:L14, April 2013.

[69] T. Dauxois, S. Ruffo, E. Arimondo, and M. Wilkens. *Dynamics and Thermodynamics of Systems with Long-Range Interactions*. Springer-Verlga, 2002.

[70] P. A. M. Dirac. On the Theory of Quantum Mechanics. *Proc. R. Soc. Lon. Ser. A*, 112:661–677, October 1926.

[71] P. A. M. Dirac. The Cosmological Constants. *Nat.*, 139:323, February 1937.

[72] A. Drago, A. Lavagno, and G. Pagliara. Can very compact and very massive neutron stars both exist? *Phys. Rev. D*, 89(4):043014, February 2014.

[73] R. Ebert. Über die Verdichtung von H I-Gebieten. Mit 5 Textabbildungen. *Zeit. f. Astrophys.*, 37:217, 1955.

[74] A. S. Eddington. *The Internal Constitution of the Stars*. Cambridge University Press, 1926.

[75] G. F. R. Ellis. 100 Years of General Relativity. *ArXiv e-prints*, September 2015.

[76] E. D. Fackerell. Relativistic, Spherically Symmetric Star Clusters.IV. a Sufficient Condition for Instability of Isotropic Clusters against Radial Perturbations. *Astrophys. J.*, 160:859, June 1970.

[77] E. D. Fackerell. Relativistic, Spherically Symmetric Star Clusters. V. a. Relativistic Version of Plummer's Model. *Astrophys. J.*, 165:489, May 1971.

[78] E. D. Fackerell and K. G. Suffern. The structure and dynamic instability of isothermal relativistic star clusters. *Aus. J. Phys.*, 29:311–328, August 1976.

[79] J. Faulkner. Unstable degenerates revisited. *Astrophys. J.*, 408:600–602, May 1993.

[80] J. Faulkner and J. R. Gribbin. Stability and Radial Vibration Periods of the Hamada-Salpeter White Dwarf Models. *Nature*, 218:734–736, May 1968.

[81] E. Fermi. Zur Quantelung des idealen einatomigen Gases. *Zeit. f. Phys.*, 36:902–912, November 1926.

[82] G. Fontaine, P. Brassard, S. Charpinet, S. K. Randall, and V. Van Grootel. An overview of white dwarf stars. In *European Physical Journal Web of Conferences*, volume 43 of *European Physical Journal Web of Conferences*, page 05001, March 2013.

[83] R. H. Fowler. On dense matter. *MNRAS*, 87:114–122, December 1926.

[84] G. Fragione. Gravity and thermodynamics: fundamental principles and gravothermal instability. In *J. Phys. Conf. Ser.*, volume 566 of *Journal of Physics Conference Series*, page 012024, December 2014.

[85] D. A. Frail, S. R. Kulkarni, R. Sari, S. G. Djorgovski, J. S. Bloom, T. J. Galama, D. E. Reichart, E. Berger, F. A. Harrison, P. A. Price, S. A. Yost, A. Diercks, R. W. Goodrich, and F. Chaffee. Beaming in Gamma-Ray Bursts: Evidence for a Standard Energy Reservoir. *Astrophys. J.*, 562:L55–L58, November 2001.

[86] R. Genzel, F. Eisenhauer, and S. Gillessen. The Galactic Center massive black hole and nuclear star cluster. *Rev. Mod. Phys.*, 82:3121–3195, October 2010.

[87] C. Gilbert. Dirac's cosmology and the general theory of relativity. *Mon. Not. Roy. Astron. Soc.*, 116:684, 1956.

[88] E. Gourgoulhon. BOOK REVIEW: Numerical Relativity: Solving Einstein's Equations on the Computer Numerical Relativity: Solving Einstein's Equations on the Computer. *Class. Quant. Grav.*, 28(22):229002, April 2011.

[89] A. W. Graham. Galaxy Bulges and Their Massive Black Holes: A Review. *Galactic Bulges*, 418:263, 2016.

[90] R. G. Gratton, E. Carretta, and A. Bragaglia. Multiple populations in globular clusters. Lessons learned from the Milky Way globular clusters. *Astron. Astrophys. Rev.*, 20:50, February 2012.

[91] N. Guicciardini and G. Introzzi. *The Fermi-Dirac Statistics: a Simultaneous Discovery, in "The Foundations of Quantum Mechanics - Historical Analysis and Open Questions", edited by C. Garola and A. Rossi*, volume 71. Springer, 1995.

[92] Marshal H. and G. R. Burbidge E. Margaret Burbidge Hans E. Suess Harold C. Urey Lawrence H. Aller P. Ledoux Th. Walraven Armin J. Deutsch E. Schatzman Cecilia Payne-Gaposchkin F. Zwicky Wrubel, H. C. Arp. *Handbüch der Physik: Astrophysik II: Sternaufbau*. 1958.

[93] F. Halzen and A. D. Martin. *Quarks and leptons : an introductory course in modern particle physics*. 1984.

[94] T. Hamada and E. E. Salpeter. Models for Zero-Temperature Stars. *Astrophys. J.*, 134:683, November 1961.

[95] B. K. Harrison, K. S. Thorne, M. Wakano, and J. A. Wheeler. *Gravitation Theory and Gravitational Collapse*. 1965.

[96] S. W. Hawking. Black hole explosions? *Nat.*, 248:30–31, March 1974.

[97] M. Hazewinkel. *Sturm - Liouville Theory: Enciclopedia of Mathematics*. Springer - Verlag, 2001.

[98] M. Hénon. L'évasion des étoiles hors des amas isolés. *Ann. Astrophys.*, 23:668, February 1960.

[99] P. Hertel, H. Narnhofer, and W. Thirring. Thermodynamic functions for fermions with gravostatic and electrostatic interactions. *Comm. Math. Phys.*, 28:159–176, June 1972.

[100] P. Hertel and W. Thirring. A soluble model for a system with negative specific heat. *Ann. Phys.*, 63:520–533, April 1971.

[101] P. Hertel and W. Thirring. Free energy of gravitating fermions. *Comm. Math. Phys.*, 24:22–36, March 1971.

[102] A. Hewish, S. J. Bell, J. D. H. Pilkington, P. F. Scott, and R. A. Collins. Observation of a Rapidly Pulsating Radio Source. *Nat.*, 217:709–713, February 1968.

[103] J. Hjorth and J. Madsen. Violent Relaxation and Stability of Elliptical Galaxies. In I. J. Danziger, W. W. Zeilinger, and K. Kjär, editors, *European Southern Observatory Conference and Workshop Proceedings*, volume 45 of *European Southern Observatory Conference and Workshop Proceedings*, page 263, 1993.

[104] G. Horwitz and J. Katz. Steepest-descent technique and stellar equilibrium statistical mechanics. I - Newtonian clusters in a box. *Astrophys. J.*, 211:226–243, January 1977.

[105] K. Huang. *Statistical Mechanics, 2nd Edition*. April 1987.

[106] G. Ingrosso, M. Merafina, and R. Ruffini. Systems of self-gravitating bosons with a cut-off in their distribution function. Newtonian treatment. *N. Cim. B Ser.*, 105:977–983, September 1990.

[107] J. R. Ipser. Relativistic, Spherically Symmetric Star Clusters. II. Sufficient Conditions for Stability against Radial Perturbations. *Astrophys. J*, 156:509, May 1969.

[108] J. R. Ipser. Relativistic, Spherically Symmetric Star Clusters. III. Stability of Compact Isotropic Models. *Astrophys. J*, 158:17, October 1969.

[109] J. R. Ipser and K. S. Thorne. Relativistic, Spherically Symmetric Star Clusters. I. Stability Theory for Radial Perturbations. *Astrophys. J*, 154:251, October 1968.

[110] P. Jetzer. Boson stars. *Phys. Rep.*, 220:163–227, November 1992.

[111] D. Jiulin. The nonextensive parameter and Tsallis distribution for self-gravitating systems. *Europhys. Lett.*, 67:893–899, September 2004.

[112] V. M. Kaspi. Grand unification of neutron stars. *Proc. Nat. Ac. Sci.*, 107:7147–7152, April 2010.

[113] J. Katz. On the number of unstable modes of an equilibrium. *Mon. Not. R. Astron. Soc.*, 183:765–770, June 1978.

[114] J. Katz. Stability limits for 'isothermal' cores in globular clusters. *Mon. Not. Roy. Astron. Soc.*, 190:497–507, February 1980.

[115] J. Katz. Thermodynamics and Self-Gravitating Systems. *ArXiv Astrophysics e-prints*, December 2002.

[116] D. C. Kennedy and S. A. Bludman. Variational Principles for Stellar Structure. *Astrophys. J*, 484:329–340, July 1997.

[117] M. Kilic, C. Allende Prieto, W. R. Brown, and D. Koester. The Lowest Mass White Dwarf. *Astrophys. J.*, 660:1451–1461, May 2007.

[118] I. R. King. The structure of star clusters. I. an empirical density law. *Astron. J.*, 67:471, October 1962.

[119] I. R. King. The structure of star clusters. II. Steady-state velocity distributions. *Astron. J.*, 70:376, June 1965.

[120] I. R. King. The structure of star clusters. III. Some simple dynamical models. *Astron. J.*, 71:64, February 1966.

[121] R. Kippenhahn, A. Weigert, and A. Weiss. *Stellar Structure and Evolution.* 2012.

[122] O. Klein. On the Thermodynamical Equilibrium of Fluids in Gravitational Fields. *Rev. of Mod. Phys.*, 21:531–533, July 1949.

[123] D. Koester and G. Chanmugam. REVIEW: Physics of white dwarf stars. *Rep. Prog. Phys.*, 53:837–915, July 1990.

[124] A. V. Kolesnichenko. Power distributions for self-gravitating astrophysical systems based on nonextensive Tsallis kinetics. *Sol. Sy. Res.*, 51:127–144, March 2017.

[125] J. R. Kuhn and L. Kruglyak. Non-Newtonian forces and the invisible mass problem. *Astrophys. J*, 313:1–12, February 1987.

[126] L. D. Landau and Lifshitz E. M. *Statistical Physics, 3rd Edition, Part 1.* January 1980.

[127] N. R. Lebovitz. On Schwarzschild's Criterion for the Stability of Gaseous Masses. *Astrophys. J.*, 142:229, July 1965.

[128] P. Ledoux. On the Vibrational Stability of Gaseous Stars. *Astrophys. J.*, 94:537, November 1941.

[129] P. Ledoux and C. L. Pekeris. Radial Pulsations of Stars. *Astrophys. J.*, 94:124, July 1941.

[130] Y. Levin, R. Pakter, F. B. Rizzato, T. N. Teles, and F. P. C. Benetti. Nonequilibrium statistical mechanics of systems with long-range interactions. *Phys. Rep.*, 535:1–60, February 2014.

[131] J. F. Luciani and R. Pellat. On the Antonov criterion for gravothermal instability. *Astrophys. J.*, 317:241–245, June 1987.

[132] D. Lynden-Bell. Statistical mechanics of violent relaxation in stellar systems. *Mon. Not. R. Astron. Soc.*, 136:101, 1967.

[133] D. Lynden-Bell and R. Wood. The gravo-thermal catastrophe in isothermal spheres and the onset of red-giant structure for stellar systems. *MNRAS*, 138:495, 1968.

[134] C. H. F. Melo, P. de Laverny, N. C. Santos, G. Israelian, S. Randich, J. D. Do Nascimento, Jr., and J. R. de Medeiros. On the nature of lithium-rich giant stars. Constraints from beryllium abundances. *Astron. Astronphys.*, 439:227–235, August 2005.

[135] M. Membrado, A. F. Pacheco, and J. Sanudo. A description of semidegenerate self-gravitating spheres of fermions. *Astrophys. J.*, 390:88–95, May 1992.

[136] M. Merafina. Dynamical evolution of globular clusters: Recent developments. *Int. J. Mod. Phys. D*, 26:1730017, 2017.

[137] M. Merafina and G. Alberti. Self-gravitating Newtonian models of fermions with anisotropy and cutoff energy in their distribution function. *Phys. Rev. D*, 89(12):123010, June 2014.

[138] M. Merafina and G. Alberti. Self-gravitating relativistic models of fermions with anisotropy and cutoff energy in their distribution function. *Phys. Rev. D*, 92(2):023005, July 2015.

[139] M. Merafina and R. Ruffini. Systems of selfgravitating classical particles with a cutoff in their distribution function. *Astron. Astrophys.*, 221:4–19, August 1989.

[140] M. Merafina and D. Vitantoni. Data Analysis of Globular Cluster Harris Catalogue in View of the King Models and Their Dynamical Evolution. I. Theoretical model. In *Multifrequency Behaviour of High Energy Cosmic Sources*, pages 231–234, November 2014.

[141] M. Merafina and D. Vitantoni. Data Analysis of Globular Cluster Harris Catalogue in View of the King Models and Their Dynamical Evolution. II. Observational Evidences. In *Multifrequency Behaviour of High Energy Cosmic Sources*, pages 235–239, November 2014.

[142] M. Milgrom. A modification of the Newtonian dynamics as a possible alternative to the hidden mass hypothesis. *Astrophys. J*, 270:365–370, July 1983.

[143] C. W. Misner and H. S. Zapolsky. High-Density Behavior and Dynamical Stability of Neutron Star Models. *Phys. Rev. Lett.*, 12:635–637, June 1964.

[144] G. Narain, J. Schaffner-Bielich, and I. N. Mishustin. Compact stars made of fermionic dark matter. *Phys. Rev. D*, 74(6):063003, September 2006.

[145] Y. Nazé, A. Ud-Doula, M. Spano, G. Rauw, M. De Becker, and N. R. Walborn. New findings on the prototypical Of?p stars. *Astron. Astrophys.*, 520:A59, September 2010.

[146] K. Nomoto, C. Kobayashi, and N. Tominaga. Nucleosynthesis in Stars and the Chemical Enrichment of Galaxies. *Ann. Rev. Astron. Astrophys.*, 51:457–509, August 2013.

[147] I. D. Novikov. Delayed Explosion of a Part of the Fridman Universe and Quasars. *Astron. Zh.*, 41:1075, 1964.

[148] I. D. Novikov. Delayed Explosion of a Part of the Fridman Universe and Quasars. *Sov. Astron.*, 8:857, June 1965.

[149] J. R. Oppenheimer and R. Serber. On the Stability of Stellar Neutron Cores. *Phys. Rev.*, 54:540–540, October 1938.

[150] J. R. Oppenheimer and G. M. Volkoff. On Massive Neutron Cores. *Phys. Rev.*, 55:374–381, February 1939.

[151] T. Padmanabhan. Antonov instability and gravothermal catastrophe - Revisited. *Astrophys. J. Suppl.*, 71:651–664, November 1989.

[152] T. Padmanabhan. Statistical mechanics of gravitating systems. *Phys. Rep.*, 188:285–362, April 1990.

[153] W. Pauli. Über den Zusammenhang des Abschlusses der Elektronengruppen im Atom mit der Komplexstruktur der Spektren. *Zeit. f. Phys.*, 31:765–783, February 1925.

[154] A. Pesci. Entropy of gravitating systems: scaling laws versus radial profiles. *Class. Quant. Grav.*, 24:2283–2300, May 2007.

[155] L. Piersanti, S. Gagliardi, I. Iben, Jr., and A. Tornambé. Carbon-Oxygen White Dwarf Accreting CO-Rich Matter. II. Self-Regulating Accretion Process up to the Explosive Stage. *Astrophys. J.*, 598:1229–1238, December 2003.

[156] L. Piersanti, S. Gagliardi, I. Iben, Jr., and A. Tornambé. Carbon-Oxygen White Dwarfs Accreting CO-rich Matter. I. A Comparison between Rotating and Nonrotating Models. *Astrophys. J*, 583:885–901, February 2003.

[157] J.D. Pryce. *Numerical Solutions of Sturm - Liouville Problems*. Clarendon Press, 1993.

[158] C. E. Rhoades and R. Ruffini. Maximum Mass of a Neutron Star. *Phys. Rev. Lett.*, 32:324–327, February 1974.

[159] Z. Roupas. Relativistic gravothermal instabilities. *Class. Quant. Grav.*, 32(13):135023, July 2015.

[160] Z. Roupas. Thermal mass limit of neutron cores. *Phys. Rev. D*, 91(2):023001, January 2015.

[161] Z. Roupas, B. Kocsis, and S. Tremaine. Isotropic Nematic Phase Transitions in Gravitational Systems. *Astrophys. J.*, 842:90, June 2017.

[162] C. Rovelli. Notes for a brief history of quantum gravity. *ArXiv General Relativity and Quantum Cosmology e-prints*, June 2000.

[163] J. A. Rueda and R. Ruffini. On the Einstein-Maxwell Equations of Equilibrium for White Dwarfs and Neutron Stars. *Int. J. Mod. Phys. D*, 22:1360007, September 2013.

[164] R. Ruffini and S. Bonazzola. Systems of Self-Gravitating Particles in General Relativity and the Concept of an Equation of State. *Phys. Rev.*, 187:1767–1783, November 1969.

[165] R. Ruffini and L. Stella. On semi-degenerate equilibrium configurations of a collisionless self-gravitating Fermi gas. *Astron. Astrophys.*, 119:35–41, March 1983.

[166] A. Sandage. *The Hubble Atlas of Galaxies*. 1961.

[167] R. H. Sanders. Anti-gravity and galaxy rotation curves. *Astron. Astrophys.*, 136:L21–L23, July 1984.

[168] B. M. Schaefer. The role of cosmology in modern physics. *ArXiv e-prints*, January 2017.

[169] M. Schönberg and S. Chandrasekhar. On the Evolution of the Main-Sequence Stars. *Astrophys. J.*, 96:161, September 1942.

[170] K. Schwarzschild. On the Gravitational Field of a Mass Point According to Einstein's Theory. *Abh. Konigl. Preuss. Akad. Wissenschaften Jahre 1906,92, Berlin,1907*, 1916, 1916.

[171] S. L. Shapiro and S. A. Teukolsky. *Black holes, white dwarfs, and neutron stars: The physics of compact objects*. Wiley, 1983.

[172] C. Sire and P.-H. Chavanis. Thermodynamics and collapse of self-gravitating Brownian particles in D dimensions. *Phys. Rev. E*, 66(4):046133, October 2002.

[173] J. Smoller and B. Temple. On the Oppenheimer-Volkoff Equations in General Relativity. *Arch. Rat.l Mech. Anal.*, 142:177–191, 1998.

[174] J. Solà, E. Karimkhani, and A. Khodam-Mohammadi. Higgs potential from extended Brans-Dicke theory and the time-evolution of the fundamental constants. *Class. Quant. Grav.*, 34(2):025006, January 2017.

[175] M. C. Sormani and G. Bertin. Gravothermal catastrophe: The dynamical stability of a fluid model. *Astron. Astrophys.*, 552:A37, April 2013.

[176] L. Spitzer. *Dynamical evolution of globular clusters*. 1987.

[177] E. Stoner. The Equilibrium of Dense Stars. *Phil. Mag. and J. Sci.*, 9:944–963, January 1930.

[178] K. G. Suffern and E. D. Fackerell. The dynamic instability of isothermal relativistic star clusters. *Astrophys. J*, 203:477–480, January 1976.

[179] W. Thirring. Systems with negative specific heat. *Zeit. f. Phys.*, 235:339–352, August 1970.

[180] R. C. Tolman. On the Weight of Heat and Thermal Equilibrium in General Relativity. *Phys. Rev.*, 35:904–924, April 1930.

[181] R. C. Tolman. Effect of Inhomogeneity on Cosmological Models. *Proc. Nat. Ac. Sci.*, 20:169–176, March 1934.

[182] R. C. Tolman. *Relativity, Thermodynamics, and Cosmology.* Clarendon Press, 1934.

[183] R. C. Tolman. Static Solutions of Einstein's Field Equations for Spheres of Fluid. *Phys. Rev.*, 55:364–373, February 1939.

[184] R. C. Tolman and P. Ehrenfest. Temperature Equilibrium in a Static Gravitational Field. *Phys. Rev.*, 36:1791–1798, December 1930.

[185] S. Tremaine. The Statistical Mechanics of Planet Orbits. *Astrophys. J.*, 807:157, July 2015.

[186] H. M. van Horn. Crystallization of White Dwarfs. *Astrophys. J.*, 151:227, January 1968.

[187] E. Vangioni-Flam. *Astrophysical Ages and Dating Methods.* IAP astrophysics meeting. Editions Frontieres, 1990.

[188] R. D. Viollier, F. R. Leimgruber, and D. Trautmann. Halos of heavy neutrinos around baryonic stars. *Phys. Lett. B*, 297:132–137, December 1992.

[189] R. D. Viollier, D. Trautmann, and G. B. Tupper. Supermassive neutrino stars and galactic nuclei. *Phys. Lett. B*, 306:79–85, May 1993.

[190] S. Weinberg. *Gravitation and Cosmology: Principles and Applications of the General Theory of Relativity.* Wiley, July 1972.

[191] S. Yabushita. Extension of the Betti-Ritter formula to the gravitational energy of the planets. *Mon. Not. R. Astron. Soc.*, 128:249, 1964.

[192] D. G. Yakovlev, P. Haensel, G. Baym, and C. Pethick. Lev Landau and the concept of neutron stars. *Phys. Usp.*, 56:289–295, March 2013.

Statistical Mechanics of Self-Gravitating Systems in General Relativity

The statistical mechanics of self-gravitating systems constitutes one of the most fascinating and puzzling fields of research. Due to the long-range nature of the gravitational force, the usual notion of statistical equilibrium is modified, making of this study an out-of-equilibrium problem. As a consequence, these systems exhibit some peculiar features such as the occurrence of phase transitions associated with a gravitational collapse. The work presented in this thesis aims at providing a detailed description of the phase transitions in a general relativistic framework by considering, in particular, the case of self-gravitating fermions. The thesis is conceptually divided in three parts, according to the degeneracy level of the system. We firstly focus our attention on the case of degenerate fermions ($T = 0$), by studying in detail the gravitational equilibrium. Successively, considering the high temperature limit ($T \gg 1$), we show the existence of two kinds of gravitational collapse in the series of equilibria. Finally, we explore the general case, by illustrating the occurrence of the gravitational phase transitions, in both microcanonical and canonical ensembles.

Keywords: *General Relativity, Thermodynamics, Fermions, Phase Transitions*

Mécanique Statistique des Systèmes Auto-gravitants en Relativité Générale

La mécanique statistique des systèmes auto-gravitants constitue un des plus fascinants et mystérieux champs de recherche. A cause de la nature à longue-portée de la force gravitationnelle la notion usuelle d'quilibre statistique est modifiée, faisant de cette étude un problème hors-équilibre. Par conséquent, ces systèmes exhibent certaines propriétés particulières comme, par exemple, l'existence de transitions de phase associées à un effondrement gravitationnel. Le travail prsenté dans cette thèse a comme but une description détaillée des transitions de phase dans un cadre général relativiste en considérant, en particulier, le cas des fermions auto-gravitants. La thèse est conceptuellement divisée en trois parties, selon le niveau de dégénerescence du système. D'abord, nous focalisons notre attention sur le cas des fermions dégénérés ($T = 0$), en étudiant en détail l'équilibre gravitationnel. Ensuite, en considérant la limite de haute température ($T \gg 1$), nous montrons l'existence de deux types d'effondrement gravitationnel dans les séries d'équilibre. Enfin, nous explorons le cas général, en illustrant la présence des transitions de phase gravitationnelles, et dans l'ensemble microcanonique et dans l'ensemble canonique.

Mots-Clés: *Relativité Générale, Thermodynamique, Fermions, Transitions de Phase*